2018

Crystal Engineering, Syntheses and Structural Evaluations of Coordination Networks

Afsaneh Khansari
University of Wollongong

Crystal Engineering, Syntheses and Structural Evaluations of Coordination Networks

Afsaneh Khansari

This thesis is presented as part of the requirement for the Degree of Doctor of Philosophy in Chemistry

UNIVERSITY OF WOLLONGONG AUSTRALIA

School of Chemistry

University of Wollongong

Wollongong

Australia

2018

Declaration

I, Afsaneh Khansari, declare that this thesis, submitted in partial fulfilment of the requirements for the award of Doctor of Philosophy, in the School of Chemistry, University of Wollongong, is wholly my own work unless otherwise referenced or acknowledged. The document has not been submitted for qualifications at any other academic institution.

Afsaneh Khansari

29th March 2018

Acknowledgements

I would like to express my special appreciation and thanks to my supervisor, Dr. Christopher Richardson for his continuous support of my PhD research. Thanks for your unlimited time for interpretation and discussion of the data. Thanks for your guidance, advice, insightful comments during the research and writing of this thesis.

I would also like to acknowledge the University of Wollongong for the scholarship and financial support to undertake this research.

I must also thank Prof. Shane Telfer, for his great assistance and valued collaboration in crystallography through my PhD research. His expertise is very admirable.

I would also thank Dr. Pawel Wagner, for his great assistance and providing me the facilities in his laboratory to synthesise porphyrin starting materials.

I would also like thank to Dr. David Turner for the synchrotron single crystal structures of two compounds, and Dr. Luke Liu for the geometric surface area calculations.

I am grateful to the following staff in the School of Chemistry, Dr. Celine Kelso, for her help with GC-MS analysis and to Dr. Phil Barker for his helpful discussions over NMR spectroscopy.

I would also thank the following staff at University of Wollongong's Innovation Campus, Mr. Tony Romeo and Dr. Mitchell Nancarrow, for help with SEM-EDS analysis, and Dr. Andrew Nattestad for assistance with photoluminescence spectroscopy.

I would like to say thanks to my current and past labmates in the Richardson research group for the many helpful scientific discussions. I would like to thank Timothy Ablott for his help to proof read my thesis.

Finally, words cannot express how grateful I am to my beloved family. I am extremely grateful to my parents, my sisters and brothers, and my partner who experienced all the ups and downs of my research. Thanks for their love, caring, understanding and unconditional support, especially over the last 5 years. I am endlessly grateful for them.

Table of Contents

Abbreviations

bcNO	Benzo[*c*]cinnoline-*N*-oxide
BET	Brunauer, Emmett and Teller
bpdc	4,4′-Biphenyl-dicarboxylate
bpy	4,4'-Bipyridine
btc	Benzene-1,3,5-tricarboxylate
CMOFs	Homochiral Metal-Organic Frameworks
CP	Coordination Polymer
DA-H_2P	5,15-Di(4-pyridylethynyl)-10,20-diphenylporphyrin
DEF	*N,N′*-Diethylformamide
DMF	*N,N′*-Dimethylformamide
DMOF-1-NH_2	DABCO Metal-Organic Framework-1-NH_2
DMSO	Deuterated dimethyl sulfoxide
DPNI	*N,N′*-Di-(4-pyridyl)-1,4,5,8-naphthalenetetracarboxydiimide
DPT	Di-(4-pyridyl)tetrazine
EtOAc	Ethyl acetate
EtOH	Ethanol
F-H_2P	5,15-Dipyridyl-10,20-bis(pentafluorophenyl)]porphyrin
GC-MS	Gas Chromatography–Mass Spectrometry
H_2bc	Benzo[*c*]cinnoline-3,8-dicarboxylic acid
H_2bdc	1,4-Benzenedicarboxylic acid
H_2bpdc	4,4'-Biphenyldicarboxylic acid
H_2bpdc-$(NH_2)_2$	2,2'-Diamino-[1,1'-biphenyl]-4,4'-dicarboxylic acid
H_2bpdc-$(NO_2)_2$	2,2'-Dinitro-[1,1'-biphenyl]-4,4'-dicarboxylic acid
H_2bpdc-N$(allyl)_2$	2-(Diallylamino)-[1,1'-biphenyl]-4, 4'-dicarboxylic acid
H_2bpdc-NH_2	1,1'-Biphenyl]-4,4'-dicarboxylic acid
H_2bpdc-NHallyl	2-(Allylamino)-[1,1'-biphenyl]-4,4'-dicarboxylic acid
H_2bpdc-NMe_2	2-(Dimethylamino)-[1,1'-biphenyl]-4,4'-dicarboxylic acid
H_2fdc	9-Fluorenone-2,7-dicarboxylic acid
H_2ndc	2,6-Naphthalenedicarboxylic acid
H_2tdc	2,5-Thiophenedicarboxylic acid
H_2tpdc	4,4',4"-Terphenyldicarboxylic acid
H_2TPPCO_2Me	5,10,15,20-Tetrakis(4-methoxycarbonylphenyl)porphyrin
H_3dbba	3-(2′,5′-Dicarboxyphenyl)benzoic acid
H_4cdacs	1,2-Cyclohexanediamino-*N,N′*-bis(5-carboxysalicylidene)

H_4TCPP	*meso*-Tetra(4-carboxyphenyl)porphine
HKUST-1	Hong Kong University of Science and Technology-1
iCap Q-ICP-MS	Quadrupole-Inductively Coupled Plasma-Mass Spectrometer
ICP-OES	Inductively Coupled Plasma-Optical Emission Spectroscopy
IRMOF	Isoreticular Metal-Organic Framework
M(TCPP)	Metallated tetra-(4-carboxyphenyl) porphyrin
Me_2bpdc	Dimethyl [1,1'-biphenyl]-4,4'-dicarboxylate
Me_2bpdc-NO_2	Dimethyl 2-nitro-[1,1'-biphenyl]-4,4'-dicarboxylate
MeI	Methyl iodide
MeOH	Methanol
MIL	Materials of Institute Lavoisier
MOF	Metal-Organic Framework
MRI	Magnetic Resonance Imaging
MS	Mass Spectrometry
MTV-MOF	Multivariate-Metal-Organic Framework
MUF	Massey University Metal-Organic Framework
NMR	Nuclear Magnetic Resonance
PCN	Porous Coordination Network
PCP	Porous Coordination Polymer
PhIO	Iodosylbenzene
PL	Photoluminescence
PPF	Porous Porphyrin Framework
PSM	Post-Synthetic Modification
PXRD	Powder X-Ray Diffraction
RPMs	Robust Porphyrinic Materials
SALE	Solvent Assisted Linker Exchange
$ScCO_2$	Supercritical CO_2
SCXRD	Single Crystal X-Ray Crystallography
SEM-EDS	Scanning Electron Microscopy-Energy Dispersive X-ray Spectroscopy
tdc	Thiophene-2,5-dicarboxylate
TFA	Trifluoroacetic acid
TG-DSC	Thermogravimetric and Differential Scanning Calorimetry
TG-DTA	Thermogravimetric and Differential Thermal Analysis
THB	1,2,3-trihydroxybenzene
UiO	University of Oslo
UMCM	University of Michigan Crystalline Material
ZIF	Zeolitic Imidazolate Framework

Abstract

The first part of this thesis (Chapter 3 and Chapter 4), focuses on crystal engineering of multi-metal coordination networks in the aim of developing synthetic strategies to construct porous tandem catalysts. The second part (Chapter 5 and Chapter 6) concerns the synthesis and characterisation of Zn- and Sr-based materials using functionalised biphenyl dicarboxylate linkers.

A thorough study of conditions to grow coordination networks from a racemic salen ligand, *rac*-1,2-cyclohexanediamino-*N*,*N'*-bis(5-carboxysalicylidene) (H_4cdacs), metallated with Cu, VO, Fe and Mn, is reported in Chapter 3. This led to only a small number of successful syntheses. These include a coordination polymer starting from the metallolinker VO(H_2cdacs) and a highly open structure, starting from FeCl(H_2cdacs), that features heptazinc secondary building unit and unique (cdacs)Fe-O-Fe(cdacs) bridges. The preparation of networks from copper and manganese cdacs complexes were pursued but results that were anticipated based on literature reports were not obtained. The preparation of multi-metal VO(cdacs)-Zn(cdacs) network was attempted but was not successful and similar results to those found here were found in the literature during the course of this work.

Chapter 4 describes the crystal engineering of single-metal and multi-metal MOFs using metallated tetra-(4-carboxyphenyl) porphyrin linkers [M(TCPP)s] as building blocks. The syntheses of the MOFs were performed using conditions developed in this work. The structures and compositions of the frameworks were fully characterised using single crystal and powder X-ray techniques, ICP-MS, SEM-EDS and ^{1}H NMR spectroscopy. A multi-metal Mn/Ni(TCPP) MOF was successfully engineered, and SCXRD showed the accessible and catalytically active metal centres in the porphyrin units. A family of multi-metal Co/Ni(TCPP) MOFs were also synthesised through control of reaction stoichiometries, and the resultant crystals formed a mixture of two structures. These MOFs proved unstable to activation for further analysis using gas sorption. Structural collapse also occurred upon using Mn/Ni(TCPP) MOF in catalytic reaction.

In Chapter 5, amine-functionalised biphenyl carboxylate linkers were used to construct isostructural but multivariate Zn-based MOFs. A novel C-N bond cleavage phenomenon was discovered. The impact of the amine functional groups on the topologies and properties of the resultant frameworks were investigated. The MOFs were characterised by single crystal and powder methods, TGA and ^{1}H NMR spectroscopy. The carbon dioxide gas sorption properties were also studied with regards to their functional groups. The potential for post-synthetic modification was investigated for converting diallyl amine groups to dimethylamine groups.

In Chapter 6, six nitro- and amine-functionalised linkers were synthesised and used to construct Sr-based coordination networks. Four porous and two non-porous coordination networks were formed. It was found that the size and the number of the substituents play a vital role in porosity of these materials, as larger substituents resulted in more open structures. Different binding modes were observed for Sr-carboxylate coordination, and therefore, the binding modes of these materials were classified. Activation procedures and gas sorption properties of the materials were also exami

Chapter 1

Introduction

1 Introduction

1.1 Porous Solids

Over recent years, interest in man-made porous materials has increased significantly due to their interesting applications. Porous materials are defined as solids which contain pores, channels or cavities. They are divided into three categories depending on pore size; macroporous (pores > 50 nm), mesoporous (pores between 2–50 nm) and microporous (pores < 2 nm). Figure 1.1 shows three categories of porous material; organic polymers, inorganic solids (e.g. zeolites) and hybrid materials that contain an organic and an inorganic component. Such materials seek to combine the best aspects of their parent materials into the hybrid. Additionally, the other common example of porous organic solids are porous carbons. Perhaps the newest of these porous hybrid materials are metal-organic frameworks (MOFs). The term MOF has been popularised by Omar Yaghi and is a result of his many seminal and ground-breaking contributions to the area. There are other terms used in the literature, such as porous coordination polymers (PCPs),[1] and porous coordination networks (PCNs),[2] and these have been defined and used by other research groups. In this thesis, the term MOF and coordination network are used.

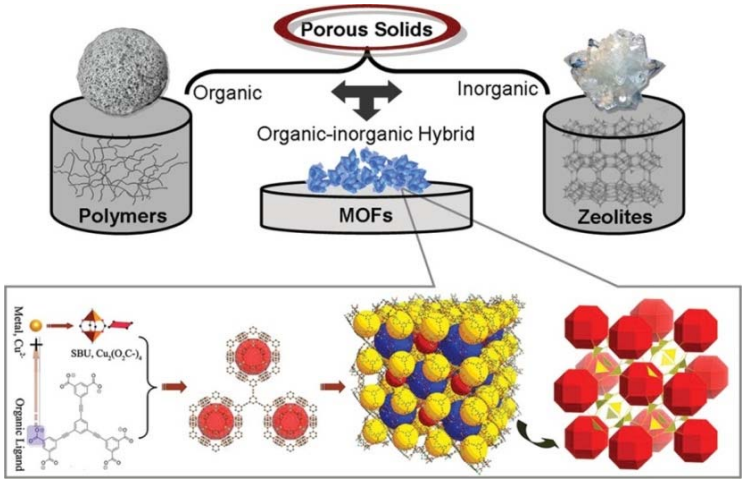

Figure 1.1 A figure showing the hybrid nature of MOFs at the intersection of organic and inorganic porous materials. Reprinted with permission from Li, J.-R.; Sculley, J.; Zhou, H.-C. *Chemical Reviews* 2012, 112 (2), 869-932. Copyright (2011) American Chemical Society.[3]

MOFs contain organic molecules that link metal ions or clusters (known as secondary building units (SBUs)) by coordination bonds into crystalline reticular frameworks. The formation of MOFs is shown schematically in Figure 1.2. Most MOFs are microporous and arguably their most impressive property is their porosity. The surface areas of the most porous MOFs are reported to ca. 6000 m^2g^{-1}, but the majority of MOFs have surface areas ca. 2000 m^2g^{-1} and these are still appreciably higher than zeolites and only activated carbons with microporosity are comparable.[4,5] MOFs are seen as attractive due to other advantages. For instance, compared to activated carbon and to zeolites, the sheer number of combinations of organic and inorganic components lead to the formation of a wider and more chemically diverse range of porous compounds. To some extent, MOFs also have easy synthesis procedures and have a much higher potential in the design and functionalisation of the structure, which offers further potential for targeted physical and chemical applications.

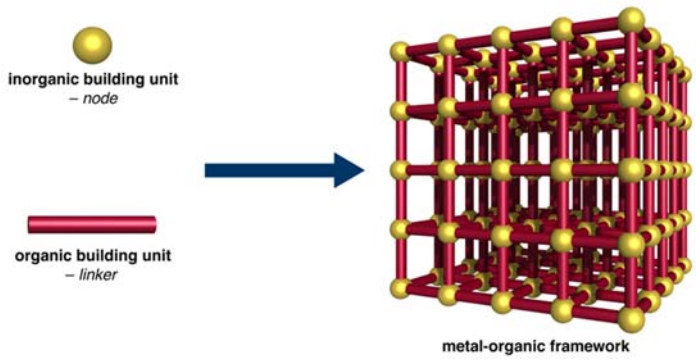

Figure 1.2 A general schematic for the formation of a MOF. Reprinted from http://www.ccb.tu-dortmund.de/fb03/en/Fields_of_research/AC/Henke/Research/index.html.

As Figure 1.3 shows, the number of publications has been increasing for MOFs while the numbers of publications featuring the term coordination polymer (CP) seems to have levelled off. Possibly one contributing reason for this may be authors preferences for using the term MOF to describe their material. The high interest in these materials has been generated by the large variety of structures and their promising properties for applications in gas storage,[6] drug delivery,[7] heterogeneous asymmetric catalysis,[8] chemical sensing,[9] separation,[10] ion-exchange[11] and biomedical imaging.[12] MOF materials can also show great physical properties such as enantioselectivity,[13]

luminescence[14] and magnetism[15] that can be potentially harnessed for applications. Therefore, the applications of MOFs are established based on their pore sizes and their properties to act as hosts.

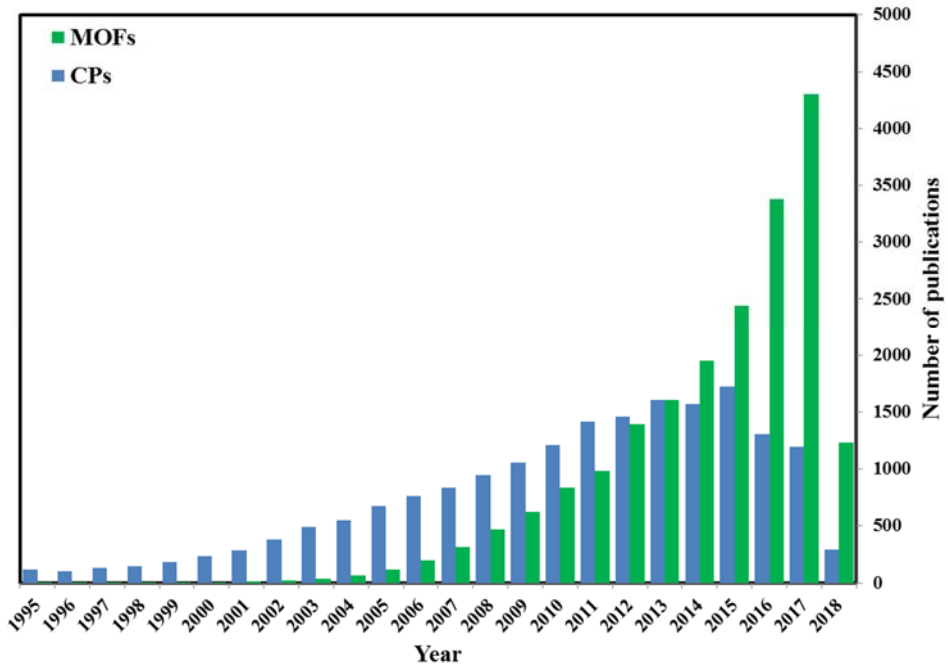

Figure 1.3 The number of publications featuring the term MOFs and CPs from 1995–2018. Data sourced from SciFinder on 12-March-2018.

1.1.1 General background and highlight of interest in MOFs

MOFs have been around since the early 1960s; however, interest in these materials was really launched towards the end of the last century by Robson, Férey, Kitagawa, Yaghi, Lee and Moore. In 1990, Robson and co-workers introduced the design of a crystalline porous framework, $[N(CH_3)_4][CuZn(CN)_4]$, in which guest molecules could be exchanged within the pores.[16] In 1999, Yaghi and co-workers reported the synthesis of MOF-5, which was formed by a solvothermal reaction between 1,4-benzenedicarboxylic acid (H_2bdc) and $Zn(NO_3)_2 \cdot 6H_2O$ in a mixture of *N,N′*-dimethylformamide (DMF) and chlorobenzene in the presence of H_2O_2. Single crystal X-ray diffraction showed the structure formed through the bridging of bdc^{2-} linkers between octahedral $Zn_4O(CO_2)_6$ clusters to form a 3D framework, as shown in Figure

1.4. The $Zn_4O(CO_2)_6$ clusters have four tetrahedral ZnO_4 units connected by six carboxylates and a central μ_4-oxido atom. MOF-5 is widely regarded as the first demonstration of permanent porosity in this class of material, with nitrogen sorption studies at 77 K revealing Type I isotherm behaviour and a Langmuir surface area of 2,900 m^2g^{-1}.[17]

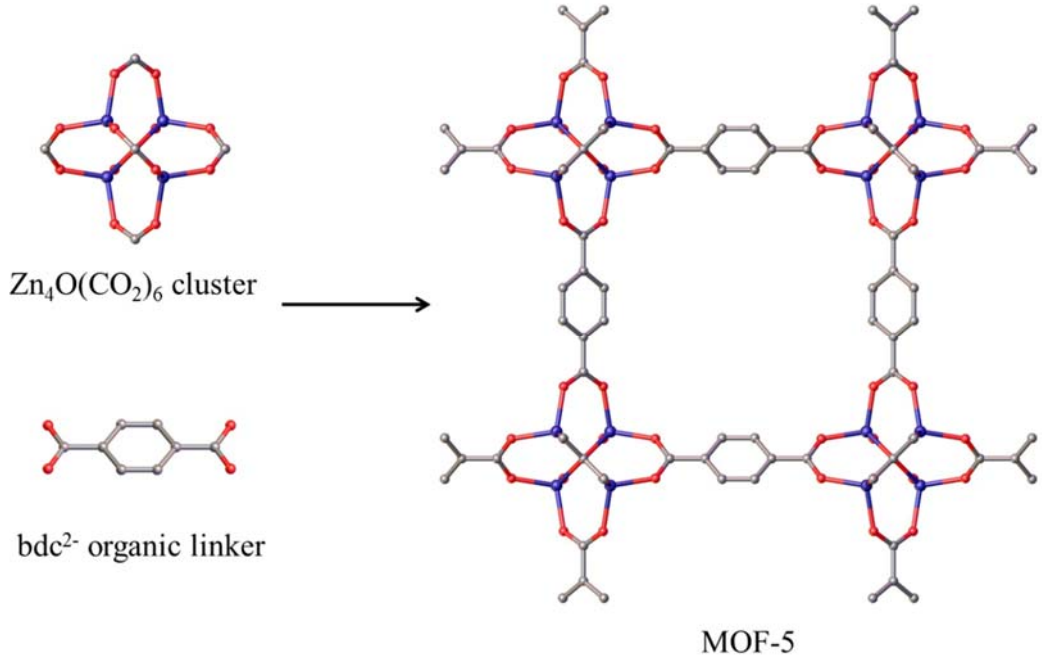

Figure 1.4 A scheme showing part of the structure of MOF-5.

MOF-5 has become a truly iconic MOF alongside a select group that includes Cu_3btc_2 (btc = benzene-1,3,5-tricarboxylate), also known as HKUST-1 (HKUST = Hong Kong University of Science and Technology), reported by Williams and co-workers in 1999,[18] the chromium(III) terephthalate framework, MIL-101Cr (MIL = Materials Institute Lavoisier), reported by Férey in 2005,[19] and UiO-66 (UiO = University of Oslo), a zirconium(IV) terephthalate framework, reported by Lillerud in 2008.[20] These MOFs all feature aryl carboxylate-based organic linkers. This type of linker has been widely used due to the ease in which they combine with a range of different metal ions to construct MOFs. These linkers, in combination with different metal ions, such as transition metal ions and alkaline earth metal ions, lead to SBUs with different coordination numbers

and geometries that depend largely on the charge and coordination preferences of the metal ions. Some examples of common SBUs are provided in Figure 1.5. The versatility of carboxylates is notable as the nature of binding of carboxylates to *d*-block and *s*-block ions is very different. The bonding between carboxylate oxygens and *d*-block ions is covalent in character, whereas the bonding of *s*-block metal ions with carboxylate oxygens is primarily ionic, due to the large differences in electronegativity.[21] Also, the high coordination numbers of many *s* block metals result in very different node structures than what is observed for the *d* block elements.

Carboxylate-connected infinite chain SBUs are commonly reported for *s*-block metal ions (e.g. Mg, Ca, Sr and Ba)[22, 23] and rare-earth metal ions[24] and also observed for *d*-block metal ions.[25] Each metal centre in the chain is a polyhedral unit and linked to adjacent members by edge-, point-, or face-sharing of the polyhedra. Of course, many other binding moieties have been employed to construct MOFs, including *N*-heterocyclics, sulfonates[26] and phosphonates.[27, 28]

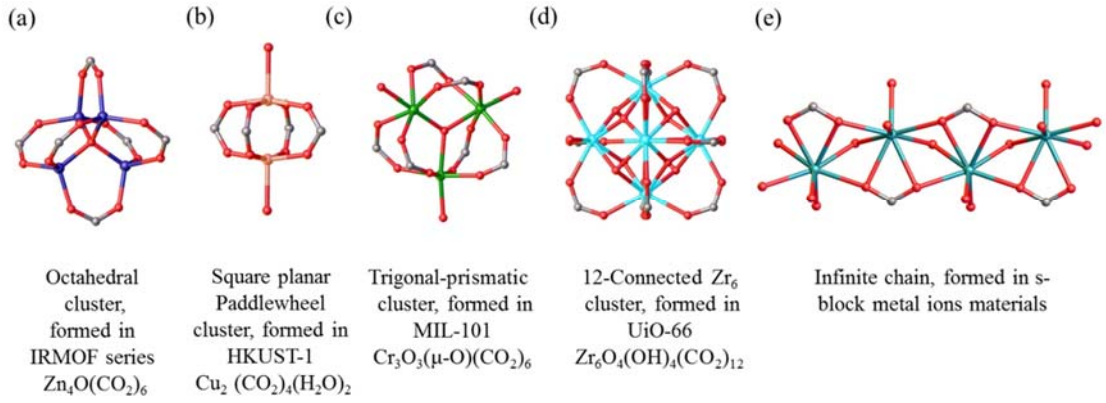

Figure 1.5 A view of different types of SBUs in MOFs.

Yaghi and co-workers published a seminal paper which described the principle of reticular chemistry.[29] One of the guiding principles of reticular chemistry for MOFs is preserving the framework topology while modulating the pore size. Yaghi and his co-workers synthesised sixteen isoreticular metal-organic frameworks (IRMOFs 1–16) under solvothermal conditions by reactions between $Zn(NO_3)_2 \cdot 6H_2O$ and functionalised aryl dicarboxylates. They established that the topology of the framework could be

maintained while the bdc linker was functionalised by various tag groups (bdc-R where R = -H, -Br, -NH_2, -OC_3H_7, -OC_5H_{11}, -C_2H_4, and -C_4H_4) and while the dicarboxylate linker was lengthened to 2,6-naphthalenedicarboxylic acid (2,6-H_2ndc), 4,4'-biphenyldicarboxylic acid (H_2bpdc) and 4,4',4"-terphenyldicarboxylic acid (H_2tpdc).[30] Figure 1.6 shows the binding of $bpdc^{2-}$ linkers between octahedral $Zn_4O(CO_2)_6$ clusters to form IRMOF-10.

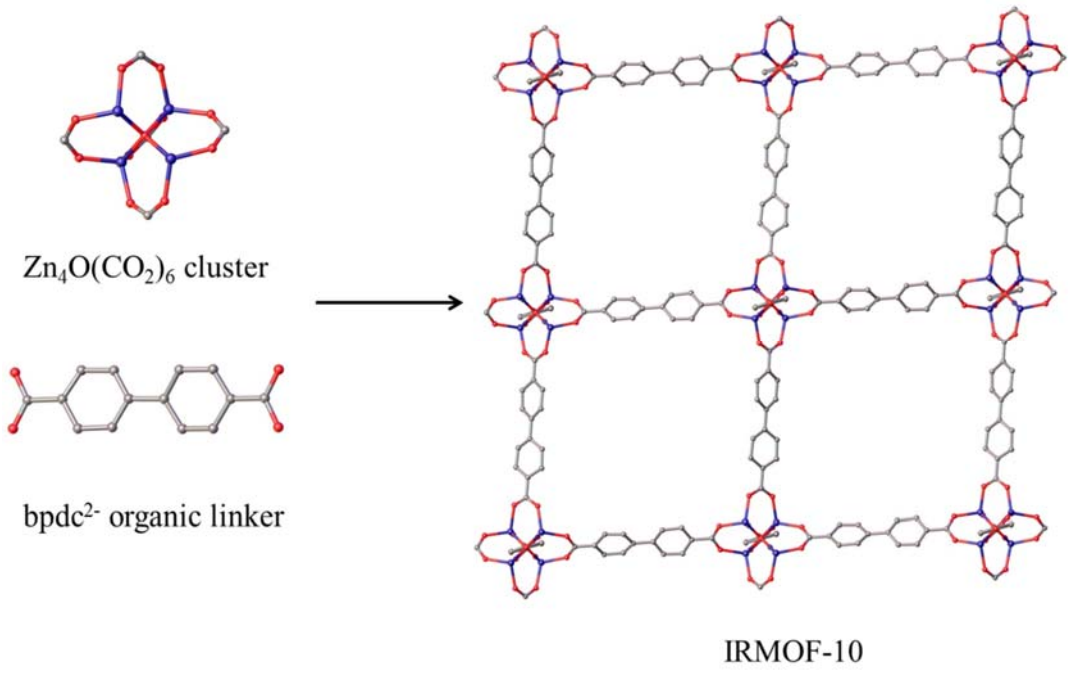

Figure 1.6 A scheme showing part of the structure of IRMOF-10 along the crystallographic *a*-axis.

Furthermore, interpenetrated and non-interpenetrated frameworks formed in the IRMOF series depending on the length of the linear linker and the conditions of synthesis.[30] Interpenetration is where multiple frameworks form in the same crystal, as shown in Figure 1.7, for two-fold interpenetration. There are no chemical bonds between the frameworks, and the frameworks would not be able to be separated without cleaving bonds. The most well-known interpenetrated/non-interpenetrated IRMOF pair is IRMOF-9/IRMOF-10.

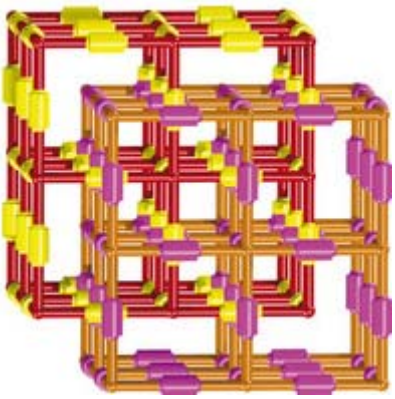

Figure 1.7 A representative schematic structure of two-fold interpenetration in a cubic framework topology. Reprinted with permission from Jiang, H. L.; Makal, T. A.; Zhou, H. C., *Coordination Chemistry Reviews* 2013, 257 (15-16), 2232-2249. Copyright (2013) Elsevier. [31]

While many different methods have been employed to synthesise MOFs, including sonochemistry,[32] mechanochemistry[33] and microwave heating,[34] the classical method is a solvothermal reaction, and it is here that solvent molecules can play significant roles as space-filling templates. The topologies and structures of MOFs created solvothermally are also dependent on reactant concentration, water content, temperature, reaction time, molar reactant ratios and pH. In terms of the IRMOF-9/IRMOF-10 pair, the overwhelming majority of are interpenetrated IRMOF-9 type (*vide infra* Chapter 5). Sumby and Doonan showed the size of the solvent was critical in forming isoreticular hydroxyl-functionalised IRMOF-9/IRMOF-10 frameworks. Interpenetrated structures were obtained in DMF, while non-interpenetrated structures were produced in the larger sized solvent, *N,N′*-diethylformamide (DEF).[35]

Telfer and co-workers reported one of the most important studies in this area on interpenetrated, non-interpenetrated and partially interpenetrated MUFs (MUF = Massey University Metal-Organic Framework) that are isotopological with IRMOF-9/IRMOF-10 frameworks. The team showed an uncommon interpenetration behaviour in the resultant frameworks where the first framework was partially occupied by the second framework. They also showed the degree of the interpenetration is controllable by the solvent size and synthesis time. The team introduced the term “autocatenation process”—a process by which non-interpenetrated crystals convert to an interpenetrated

form in a single-crystal-to-single-crystal transformation. Three methods were suggested for autocatenation (i) a solvothermal process, (ii) desolvation of the crystals, and (iii) mechanical shearing. These methods were examined on the non-interpenetrated α-MUF-9 and α-MUF-10 crystals (IRMOF-10 type), and each showed full conversion of the crystals to the interpenetrated form (IRMOF-9 type).[36]

Interpenetrated IRMOF structures have smaller pore sizes and volumes compared to non-interpenetrated analogues. This can be advantageous or disadvantageous depending on the potential point of use. For example, smaller pore sizes generally lead to higher adsorption enthalpies for gases, which might then be desirable for applications in gas storage or separation but potentially limiting for the admission of large molecules if the MOF were to be used as a heterogeneous catalyst. Indeed, the tightly controlled pore sizes of MOFs endow them with the ability to select guests based on size, for any application.[37, 38]

1.2 Pre- and Post-synthetic functionalisation of MOFs

The chemical functionalisation of the bridging organic linkers contributes strongly to the surface properties of porous MOFs. Hence, the introduction of functional groups into the structures of the bridging ligands and their incorporation into MOFs is an efficient way to tune host-guest interactions within the pores. In the last two decades, the design and synthesis of MOF structures containing functionalised organic linkers has undergone explosive development. Two different ways have been established for the functionalisation of organic linkers. The first way is to pre-functionalise the ligand with the specific substituent or group and use this ligand in the synthesis of the MOF (Figure 1.8a). The second method is to perform a post-synthetic modification (PSM) on the ligand once it is fixed in the lattice of the MOF crystal (Figure 1.8b). The literature on post-synthetic MOF chemistry has been comprehensively reviewed[39, 40, 41, 42] and extends to many other types of post-synthetic processes.

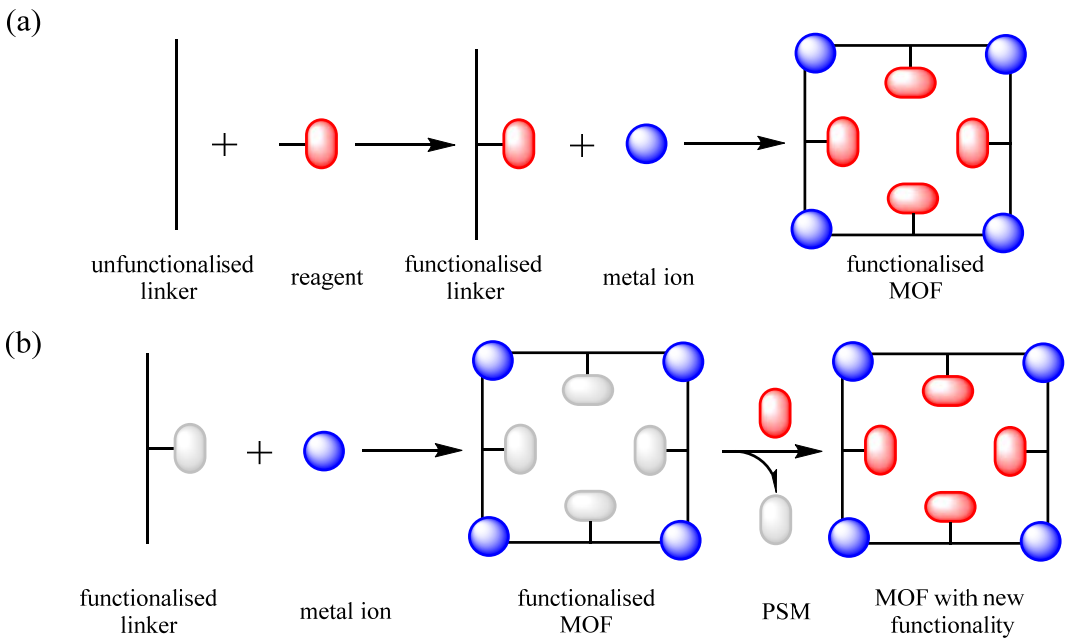

Figure 1.8 (a) 'Pre-functionalisation' of the organic linker followed by incorporation of the functionalised linker into a MOF structure and (b) incorporation of the functionalised linker into a MOF structure followed by PSM.

The pre-functionalisation approach has been particularly successful in the IRMOF series, where MOFs with quite a range of chemical functionality, such as amine,[30] alkoxy,[35] and halides,[43] have been synthesised. The principle advantage of the pre-functionalisation approach is the simplicity and direct nature of obtaining MOFs with the desired chemical functionality, as well as being a shorter sequence to obtain target MOFs than post-synthetic methods.

Limitations of the direct approach are encountered when organic linkers with large substituents are used, as due to their steric profile binding to metal ions during network formation is impeded or inhibited, and when the chemical functionality is incompatible with the conditions of network nucleation and growth. Post-synthetic modification overcomes many of these issues, and has become an important tool for the chemistry of MOFs. Post-synthetic modification enables the preparation of MOFs that could otherwise not be made and can be applied to the organic linker or metal node. It is also an approach to make MOFs with identical topologies, but with differing functionality.

PSM has been performed on MOFs containing primary aryl amine pendant groups, in particular, to introduce salicyl,[44] amide,[45] imine,[46] and urea[47] functional groups but there is very little work reported on alkylated amine derivatives, however. Figure 1.9 shows PSM of the amine groups in IRMOF-3, DMOF-1-NH_2 (DABCO MOF-1-NH_2), and UMCM-NH_2 (UMCM = University of Michigan Crystalline Material) to amides by reaction with alkyl anhydrides, ($[CH_3(CH_2)_nCO]_2O$, n = 0, 2, 4, 8, 12, 18). This study showed the relationships between pore size and reagent size and the degree of conversion, as larger anhydrides gave lower conversions. It also demonstrated the impact functionalisation had on the physical properties. For example, the MOFs carrying longer chain alkyl amides became more hydrophobic.[48] Modifications of azido,[49] aldehyde,[50] hydroxyl[51] and alkyne functionalities[52] have also been reported in the literature.

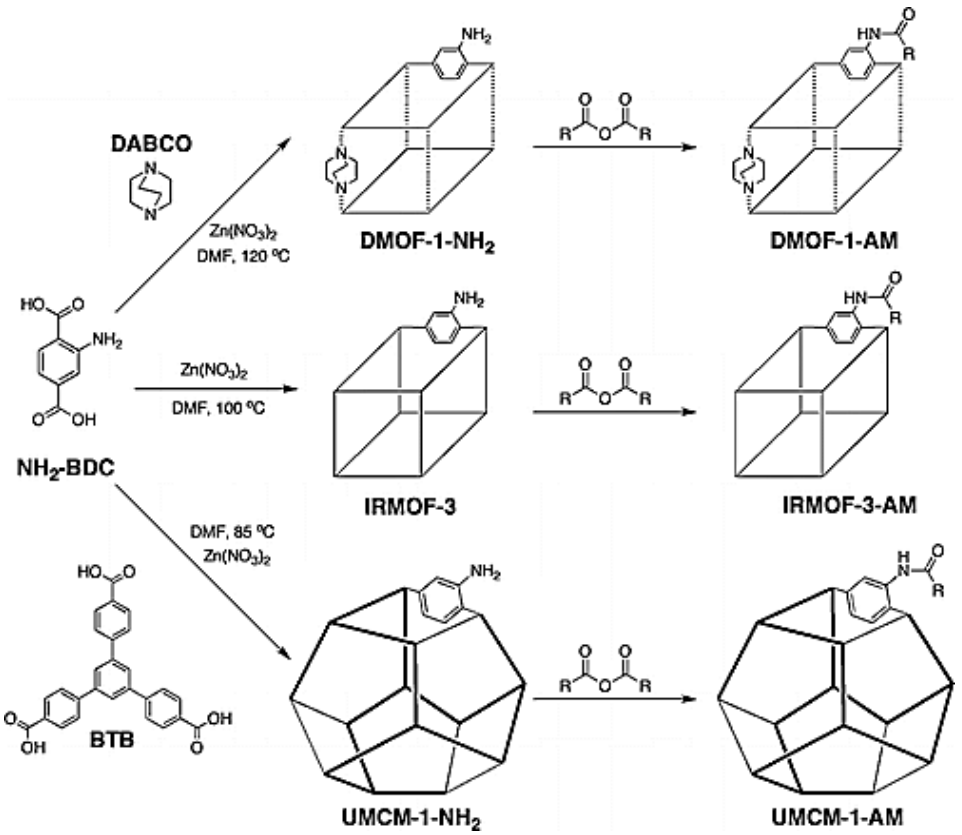

Figure 1.9 Synthesis and PSM of DMOF-1-NH_2, IRMOF-3, and UMCM-1-NH_2 (DABCO and BTB linkers are displayed by dashed and bold lines in the scheme, respectively). Reprinted with permission from Wang, Z.; Tanabe, K. K.; Cohen, S. M., *Inorganic Chemistry* 2009, *48* (1), 296-306. Copyright (2009) American Chemical Society.[48]

1.3 The design of multivariate MOFs: linker mixtures and multiple metals

There is the possibility to design and synthesise MOFs containing multiple, differently functionalised, organic linkers and to create MOF structures with more than one type of metal in the framework nodes. Conceivably, multiple-metal nodes can be prepared by direct solvothermal synthesis containing two metal ions in the reaction mixture, as shown schematically in Figure 1.10a. Zhang and co-workers used this method in a solvothermal reaction to construct bimetallic Cu/Co ZIF-8 (ZIF = Zeolitic Imidazolate Framework). Gas sorption studies on this material revealed higher H_2 and CO_2 uptake capacities for Cu/Co-ZIF-8 compared to Co-ZIF-8. The Cu/Co MOF was active as a visible-light-driven photocatalyst, which was a new property induced into the structure.[53] In general, however, it has proved much more satisfactory to employ post-synthetic metal exchange protocols as this gives better control over incorporation. Dinca and co-workers have looked at this in some IRMOF materials.[54]

Like the synthesis procedure of multi-metal nodes, it is possible to introduce at least two differently functionalised linkers and one type of metal ion into one MOF structure in a direct synthesis, as shown schematically in Figure 1.10b. The direct solvothermal synthesis of MOFs from mixtures of linkers is far more common than multi-metal nodes.

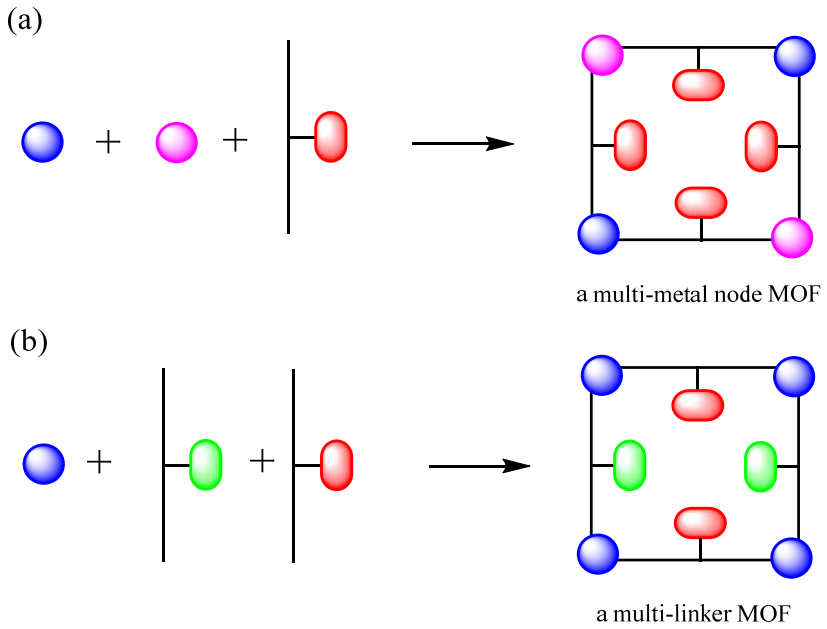

Figure 1.10 A schematic diagram of synthesis of (a) a multi-metal node MOF and (b) a multi-linker MOF.

Burrows and co-workers demonstrated the possibility of incorporation of two linkers within one framework. Multi-component IRMOF-9 was synthesised using H_2bpdc-CHO and H_2bpdc-OMe linkers in 1 : 1 feed ratio in synthesis. The ^{1}H NMR analysis showed the formula of $[Zn_4O(bpdc\text{-}CHO)_{0.3}(bpdc\text{-}OMe)_{2.7}]$ for the resultant framework.[50] They also suggested deliberate doping of MOF structures was possible and could be used to control levels of catalyst incorporation, for example.

Yaghi demonstrated that it was possible to co-polymerise up to eight differently functionalised linkers (-H, $-NH_2$, -Br, $-(Cl)_2$, $-NO_2$, $-(CH_3)_2$, $-(OC_3H_5)_2$, $-(OC_7H_7)_2$ and $-C_4H_4$) in MOF-5-type structures and coined the term 'multivariate' or MTV-MOFs. The gas sorption studies for MTV-MOF-5-AHI (containing $-NO_2$, $-(OC_3H_5)_2$, and $-(OC_7H_7)_2$ groups) showed 400% better selectivity for CO_2/CO compared to MOF-5. This result showed introducing more than one linker in a MOF structure increases a specific property or induces a new property.[55] There are now many examples of MTV-MOFs made from multiple linkers.[56, 57] The method was suggested by Burrows as a way of selectively doping catalytic functionality into MOFs.[50]

An alternative to the de novo synthesis of MTV-MOFs is Solvent Assisted Linker Exchange (SALE).[58] This method works based on the lability of ligands in the MOF lattice and several examples have showed this works from the outer to the inner of the crystal, as the MOF is recreated. At intermediate levels of exchange, the materials can be considered as core-shell structures,[59] as shown schematically in Figure 1.11.

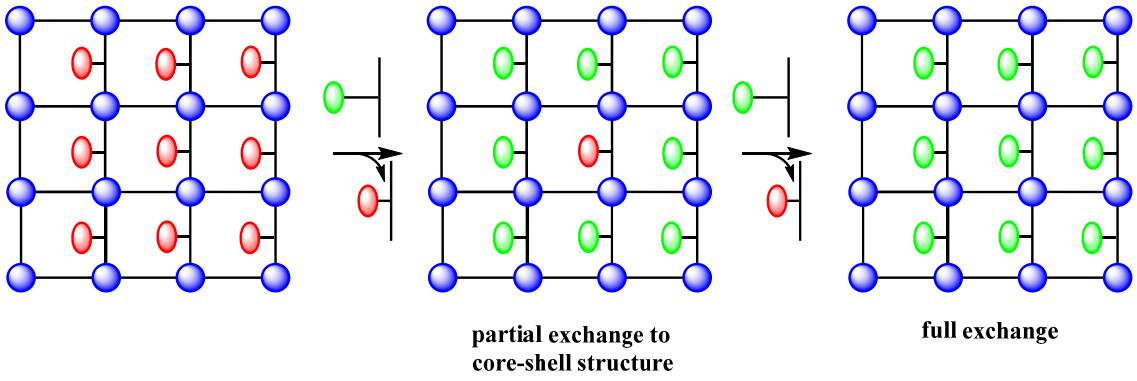

Figure 1.11 A generic scheme of SALE in MOFs.

1.4 Multi-metallic MOFs as Advanced Heterogeneous Catalysts

From the outset of the field, MOFs have been identified as materials holding great promise for heterogeneous catalysis. The solid-yet-porous nature of MOFs endows them with advantages in handling, and control for separating and recycling from reaction mixtures, and in reducing traces of metal in product streams. But it is the utilisation of the pore space as nano-dimensional reaction vessels that has stimulated research in this area. Fujita and co-workers established one of the first reports of a MOF demonstrating substrate shape selectivity in the cyanosilylation of aldehydes, in 1994.[60]

Reports until around 2009 were largely focused on catalysis at the metal node in MOFs. This type of reactivity can be greatly affected by saturation of the nodes by organic linkers or by solvents and the development of MOFs with open metal centres was a major step forward for the area.

The advent of post-synthetic chemistry led to rapid advances in MOF catalysis. An example is the post-synthetic metalation and reactivity of bpy-UiO-67 (Figure 1.12).

Lin and co-workers used $[Ir(COD)(OMe)]_2$ and $[Pd(CH_3CN)_4](BF_4)_2$ to afford bpy-UiO-67-Ir and bpy-UiO-67-Pd, respectively. The catalytic activity of bpy-UiO-Ir was investigated for borylation of arene substrates (85−96% yields) and catalytic activity of bpy-UiO-Pd for dehydrogenation of substituted cyclohexenones to phenols (83−91% yields) (Figure 1.12b and c). The activities of bpy-UiO-67-Ir and bpy-UiO-67-Pd were reported to be at least 1250 times that of their homogeneous counterparts and showed good stability and recyclability.[61] Cohen and co-workers incorporated $Ru(bpy)_2^{2+}$ units and examined the resultant MOF as a photocatalyst for the aerobic oxidation of arylboronic acids (Figure 1.12d).[62] The bpy-UiO-67-$Mn(CO)_3Br$ MOF was shown to be an efficient photocatalyst for CO_2 reduction with a higher turn-over number and selectivity compared to comparable homogeneous systems (Figure 1.12e).[63]

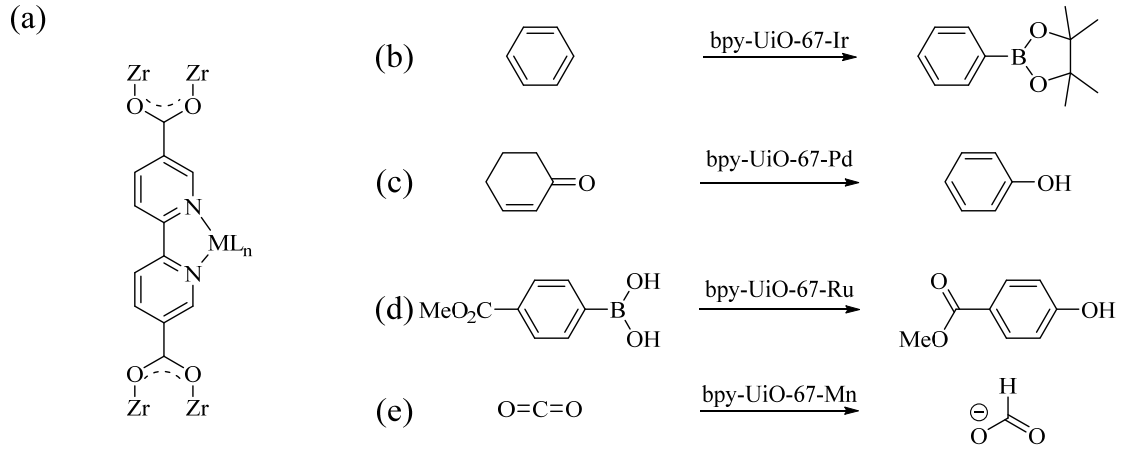

ML_n = Ir(COD)(OMe), $Pd(DMSO)_2(BF_4)_2$, $Ru(bpy)_2$ and $Mn(CO)_3Br$

Figure 1.12 (a) Metalated bpy-UiO-67 derivatives and (b) borylation, (c) dehydrogenation of substituted cyclohexenones, (d) aerobic arylboronic acid oxidation and (e) photocatalytic CO_2 reduction.

1.4.1 Heterogeneous Asymmetric Metal Organic Framework Catalysts

A remarkable development was the establishment of MOFs to act as asymmetric heterogeneous catalysts. Amongst the first reports were a microporous Ti-based MOF for a stereoselective Diels-Alder reaction,[64] the homochiral MOF D-POST-1 for enantioselective transesterification[65] and a lanthanide bisphosphonate-based MOF for the first asymmetric aldehyde cyanosilylation reaction and in the separation of ring opening of *meso*-carboxylic anhydrides.[66] Since these reports around the turn of the century, many research groups have demonstrated the capability of porous MOFs as useful materials for asymmetric catalysis in epoxidation,[67] epoxide ring opening,[68] Diels-Alder,[69] Aldol,[70] sulfoxidation,[71] CO_2 insertion,[72] asymmetric organometallic additions[73] and aldehyde cyanosilylation reactions.[74]

Metalloligand MOFs, that is MOFs featuring a linker binding a metal, feature heavily as catalysts. Such MOFs can be made directly from pre-metallated linkers or by post-synthetic metalation, which has become a facile method.[75] Among the most active asymmetric MOF catalysts are those based on metallated Schiff base linkers, more commonly known as metallosalens, such as that shown in Figure 1.13. Direct incorporation of these metallolinkers into MOF structures has been looked at by a few research groups, and the performance of the resultant MOFs were studied as heterogeneous catalysts. [69, 71] Metalloporphyrins (Figure 1.13) are also popular targets as metallolinkers to construct MOFs. Many excellent properties have been reported by some research groups for MOFs containing metalloporphyrin linkers, such as robust structure, high surface area, and high thermal and chemical stabilities.[2, 76, 77] Additionally, by implantation of appropriate metal ions in the porphyrin linkers, they act as catalyst for a wide variety of organic transformations.[78, 79]

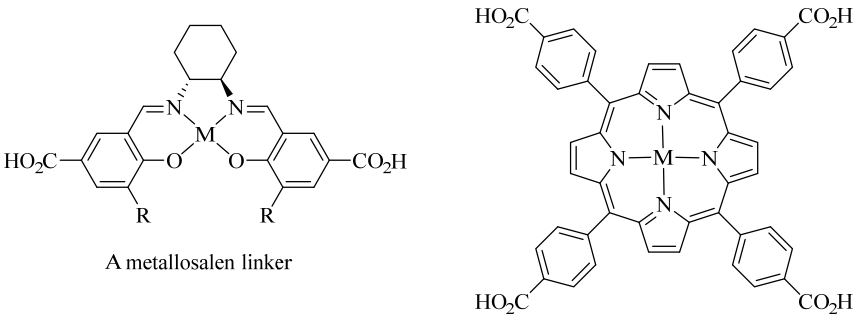

Figure 1.13 Typical chemical structures of metallosalen and metalloporphyrin linkers.

1.4.2 Advanced MOF Catalysis: Synergism and Tandem Reactivity

A strategy that can be taken to increase the efficiency of catalysis is the incorporation of two or more distinct Lewis acid or Brønsted acid-base catalytic sites in one framework, by direct synthesis or by PSM. The resultant MOFs can then act to catalyse two different reactions consecutively. The idea of this one-step procedure involving two catalytic transformations is called tandem catalysis.[80] There are some advantages to performing syntheses using tandem catalysts, mainly focused on increasing the catalytic efficiency of the process, and consequently saving time, materials and energy.

There are two examples of tandem catalysis based around MIL-101 scaffolds. The bifunctional Brønsted acid-base catalyst, MTV MIL-101(Cr)-NH_2-SO_3H, was generated by co-polymerisation of H_2bdc-NO_2, H_2bdc-SO_3H and chromium(III), coupled with a post-synthetic reduction step. It was used for a tandem reaction of benzaldehyde dimethylacetal with nitromethane to *trans*-1-nitro-2-phenylethylene through benzaldehyde as the intermediate (Scheme 1.1a).[81] A bifunctional Lewis acid-Brønsted base MIL-101(Al)-NH_2 catalyst was active in the tandem reaction from styrene epoxide to the malononitrile derivative shown in Scheme 1.1b. The first process is the Lewis acid catalysed Meinwald rearrangement and then a Lewis base Knoevenagel condensation.[82] The arrangements of the ligands in the structures of these MOFs are likely to be randomised. This is likely a common feature to MOFs made from one type of ligand and where these act in the same structural role.

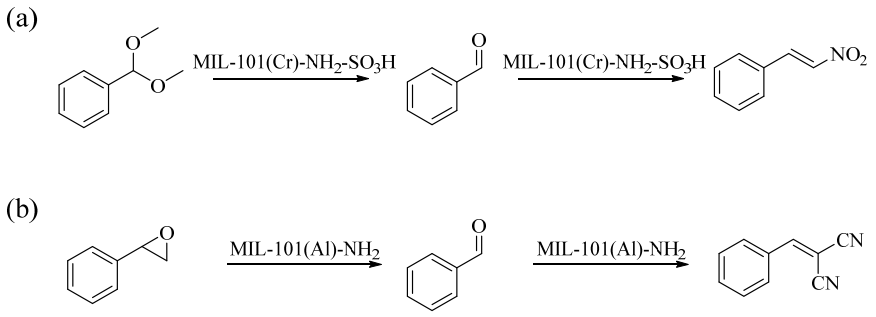

Scheme 1.1 Tandem reactions of (a) benzaldehyde dimethylacetal to *trans*-1-nitro-2-phenylethylene using MIL-101(Cr)-NH_2-SO_3H and (b) styrene epoxide to 2-benzylidenemalononitrile using MIL-101(Al)-NH_2.

1.4.2.1 Pore surface engineering

A current topic in the field of MOFs is pore surface engineering.[83] This is where the chemical functionality that lines the porous channels and spatial relationships are controlled. The advantage MOFs hold over other porous materials stems from their modular construction from molecular components. This gives the opportunity to use both organic and coordination chemistry to predesign MOF components for modification of pore shape and functionality through a strategy of crystal engineering. In principle, this leads to locating functional groups within the frameworks at defined positions and (ii) the installation of multifunctional groups can be precisely placed at desired within the MOFs.

Surface engineering was demonstrated by Telfer and co-workers on MUF-77 by installation of a catalytic site and a modulator in the same pore system and applied towards asymmetric aldol reactions. A series of ditopic terephthalate and biphenyldicarboxylate ligands were designed with C_2 symmetry aiming to align with the symmetry of the pore environment and carrying prolinyl groups as organocatalytic sites for asymmetric aldol reactions. The implementation of the modulators exhibited significant effects on the reaction rate and the enantiomeric excess of the aldol products.[83] The chemical structure of multifunctional MUF-77 and the reaction catalysed by the MOF are shown in Figure 1.14. This example is different from the previous MIL-101 examples by virtue of the differing types of ligands that have defined

and ordered positions in the MOF structure because of their different structural roles. This enables the units to work synergistically.

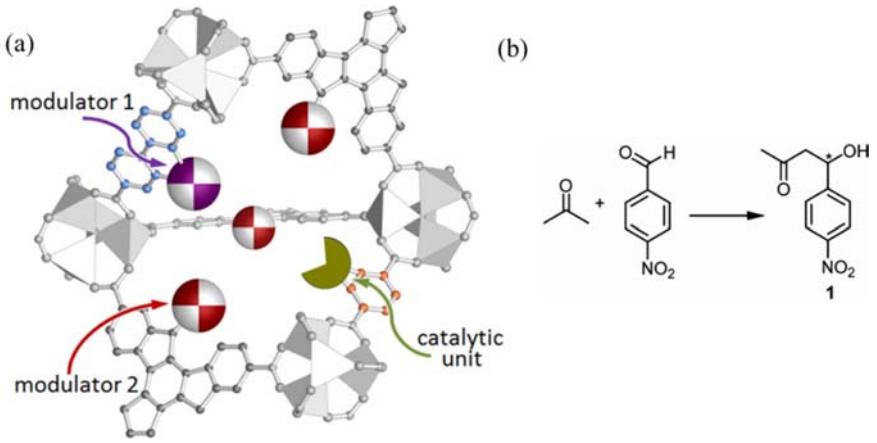

Figure 1.14 (a) Chemical structure of multifunctional MUF-77 and (b) the reaction catalysed by MUF-77. Reprinted with permission from Liu, L.; Zhou, T.-Y.; Telfer, S. G. *Journal of the American Chemical Society* 2017, *139* (39), 13936-13943. Copyright (2017) American Chemical Society. [84]

Pore surface engineering by arranging multiple organic functional groups has been looked at by several research groups.[84, 85] However, there is not much work done on MOFs containing multi-metalloligands and this area is still underdeveloped. Hence, the development of multi-metalloligand MOFs as capable tandem or synergistic catalysts remains a significant challenge. Co-polymerisation of two metalloligands with different metal centres within one framework would be considered as a possible method to enhance catalytic performance of the MOFs. To create such MOF structures with complex functionality first requires developing the synthetic methods.

1.5 Thesis coverage

Chapter 2 lists the instrumentation used in the work described in this thesis and gives the general methods that were used for the preparation of samples for various analytical methods.

Chapter 3 concerns the synthesis and characterisation of metallosalen-based coordination networks based on racemic metalloligand complexes of 1,2-cyclohexanediamino-*N,N'*-bis(5-carboxysalicylidene) (H_4cdacs). The synthesis of single metallolinker MOFs was examined to establish synthetic conditions before investigating multi-metallolinker systems. It was found that each metallosalen linker was crystallised in a different synthesis condition, therefore, assembling and co-polymerisation of two different metallolinkers in one structure was problematic.

The theme of metalloligands and the assembly of multi-metalloligand coordination networks continues in Chapter 4. Described in this chapter is the modulation of metalloporphyrin-based porous MOFs in the Porous Porphyrin Framework (PPF) series and an extension of the methodology developed to metalloporphyrin-based zirconium-materials, which are members of the Porous Coordination Network (PCN) series. The catalytic ability of many of these MOFs was tested in oxygen transfer reactions to alkenes (epoxidation).

The focus shifted to the synthesis and study of an isoreticular series of zinc MOFs containing amine-functionalised biphenyl dicarboxylate (bpdc) linkers in Chapter 5. The effects of the substituent on the structure and properties in this series of porous MOFs was examined by single crystal and powder X-ray diffraction, and by gas adsorption. Some novel reactivity of the amine functional groups was found during MOF synthesis, as a result many are multivariate MOFs. In addition, a rare case of autocatenation of a MOF structure was found.

In Chapter 6, the synthesis and characterisation of Sr-based materials of nitro- and amine-functionalised bpdc linkers is reported. A wide variety of structural types were found including coordination networks with very large 1D channels (> 2 nm) as well as

densely-packed materials with no apparent porosity. The structures were characterised by diffraction methods and selected examples were studied by gas adsorption and for their photoluminescence properties.

The thesis is concluded in Chapter 7 and some areas are identified for future work.

1.6 References

1. Uemura, T.; Kitagawa, S., Controlled polymerization by incarceration of monomers in nanochannels. In *Functional metal-organic frameworks: Gas storage, separation and catalysis*, Schröder, M., Ed. Springer Berlin Heidelberg: Berlin, Heidelberg, 2010; pp 155-173.
2. Feng, D.; Gu, Z. Y.; Li, J. R.; Jiang, H. L.; Wei, Z.; Zhou, H. C., Zirconium-metalloporphyrin PCN-222: Mesoporous metal-organic frameworks with ultrahigh stability as biomimetic catalysts. *Angewandte Chemie - International Edition* **2012,** *51* (41), 10307-10310.
3. Li, J.-R.; Sculley, J.; Zhou, H.-C., Metal-organic frameworks for separations. *Chemical Reviews* **2012,** *112* (2), 869-932.
4. Farha, O. K.; Yazaydin, A. Ö.; Eryazici, I.; Malliakas, C. D.; Hauser, B. G.; Kanatzidis, M. G.; Nguyen, S. T.; Snurr, R. Q.; Hupp, J. T., De novo synthesis of a metal-organic framework material featuring ultrahigh surface area and gas storage capacities. *Nature Chemistry* **2010,** *2* (11), 944-948.
5. Furukawa, H.; Ko, N.; Go, Y. B.; Aratani, N.; Choi, S. B.; Choi, E.; Yazaydin, A. O.; Snurr, R. Q.; O'Keeffe, M.; Kim, J.; Yaghi, O. M., Ultrahigh porosity in metal-organic frameworks. *Science* **2010,** *329* (5990), 424-428.
6. Millward, A. R.; Yaghi, O. M., Metal-organic frameworks with exceptionally high capacity for storage of carbon dioxide at room temperature. *Journal of the American Chemical Society* **2005,** *127* (51), 17998-17999.
7. Luo, Z.; Wang, R.; Gu, C.; Li, F.; Han, Y.; Li, B.; Liu, J., A metal-organic framework with unusual nanocages: Drug delivery. *Inorganic Chemistry Communications* **2017,** *76*, 91-94.
8. Xia, Q.; Liu, Y.; Li, Z.; Gong, W.; Cui, Y., A Cr(salen)-based metal-organic framework as a versatile catalyst for efficient asymmetric transformations. *Chemical Communications* **2016,** *52* (89), 13167-13170.
9. Zhao, X.; Wang, Y.; Hao, X.; Liu, W., Fluorescent molecule incorporated metal-organic framework for fluoride sensing in aqueous solution. *Applied Surface Science* **2017,** *402*, 129-135.
10. Devic, T.; Horcajada, P.; Serre, C.; Salles, F.; Maurin, G.; Moulin, B.; Heurtaux, D.; Clet, G.; Vimont, A.; Grenéche, J. M.; Le Ouay, B.; Moreau, F.; Magnier, E.; Filinchuk, Y.; Marrot, J.; Lavalley, J. C.; Daturi, M.; Férey, G., Functionalization in flexible porous solids: Effects on the pore opening and the host-guest interactions. *Journal of the American Chemical Society* **2010,** *132* (3), 1127-1136.
11. Kumar, P.; Pournara, A.; Kim, K. H.; Bansal, V.; Rapti, S.; Manos, M. J., Metal-organic frameworks: Challenges and opportunities for ion-exchange/sorption applications. *Progress in Materials Science* **2017,** *86*, 25-74.
12. Chowdhury, M. A., Metal-organic-frameworks for biomedical applications in drug delivery, and as MRI contrast agents. *Journal of Biomedical Materials Research - Part A* **2016**.
13. Liu, J.; Wang, F.; Ding, Q. R.; Zhang, J., Synthesis of an enantipure tetrazole-based homochiral Cu(I),(II)-MOF for enantioselective separation. *Inorganic Chemistry* **2016,** *55* (24), 12520-12522.

14. Cao, Y. Y.; Guo, X. F.; Wang, H., High sensitive luminescence metal-organic framework sensor for hydrogen sulfide in aqueous solution: A trial of novel turn-on mechanism. *Sensors and Actuators, B: Chemical* **2017,** *243*, 8-13.
15. Feng, X.; Chen, H.; Jiang, F., In-situ ethylenediamine-assisted synthesis of a magnetic iron-based metal-organic framework MIL-53(Fe) for visible light photocatalysis. *Journal of Colloid and Interface Science* **2017,** *494*, 32-37.
16. Hoskins, B. F.; Robson, R., Design and construction of a new class of scaffolding-like materials comprising infinite polymeric frameworks of 3D-linked molecular rods. A reappraisal of the $Zn(CN)_2$ and $Cd(CN)_2$ structures and the synthesis and structure of the diamond-related frameworks $[N(CH_3)_4]$ $[Cu^{I}Zn^{II}KCN_4]$. *Journal of the American Chemical Society* **1990,** *112* (4), 1546-1554.
17. Li, H.; Eddaoudi, M.; O'Keeffe, M.; Yaghi, O. M., Design and synthesis of an exceptionally stable and highly porous metal-organic framework. *Nature* **1999,** *402* (6759), 276-279.
18. Chui, S. S. Y.; Lo, S. M. F.; Charmant, J. P. H.; Orpen, A. G.; Williams, I. D., A chemically functionalizable nanoporous material $[Cu_3(TMA)_2$ $(H_2O)_3](n)$. *Science* **1999,** *283* (5405), 1148-1150.
19. Férey, C.; Mellot-Draznieks, C.; Serre, C.; Millange, F.; Dutour, J.; Surblé, S.; Margiolaki, I., Chemistry: A chromium terephthalate-based solid with unusually large pore volumes and surface area. *Science* **2005,** *309* (5743), 2040-2042.
20. Cavka, J. H.; Jakobsen, S.; Olsbye, U.; Guillou, N.; Lamberti, C.; Bordiga, S.; Lillerud, K. P., A new zirconium inorganic building brick forming metal-organic frameworks with exceptional stability. *Journal of the American Chemical Society* **2008,** *130* (42), 13850-13851.
21. Yang, L.-M.; Vajeeston, P.; Ravindran, P.; Fjellvag, H.; Tilset, M., Revisiting isoreticular MOFs of alkaline earth metals: a comprehensive study on phase stability, electronic structure, chemical bonding, and optical properties of A-IRMOF-1 (A = Be, Mg, Ca, Sr, Ba). *Physical Chemistry Chemical Physics* **2011,** *13* (21), 10191-10203.
22. Lo, S. H.; Liu, H. K.; Zhan, J. X.; Lin, W. C.; Kao, C. C.; Lin, C. H.; Zima, V., Assembly of a water-insoluble strontium metal-organic framework with luminescent properties. *Inorganic Chemistry Communications* **2011,** *14* (10), 1602-1605.
23. Douvali, A.; Papaefstathiou, G. S.; Gullo, M. P.; Barbieri, A.; Tsipis, A. C.; Malliakas, C. D.; Kanatzidis, M. G.; Papadas, I.; Armatas, G. S.; Hatzidimitriou, A. G.; Lazarides, T.; Manos, M. J., Alkaline earth metal ion/dihydroxy-terephthalate MOFs: structural diversity and unusual luminescent properties. *Inorganic Chemistry* **2015,** *54* (12), 5813-5826.
24. Guo, L.-R.; Tang, X.-L.; Ju, Z.-H.; Zhang, K.-M.; Jiang, H.-E.; Liu, W.-S., Lanthanide metal-organic frameworks constructed by asymmetric 2-nitrobiphenyl-4,4'-dicarboxylate ligand: syntheses, structures, luminescence and magnetic investigations. *CrystEngComm* **2013,** *15* (44), 9020-9031.
25. Zhang, N.; Sun, Y. J.; Yang, H.; Zhang, J. Y.; Gao, E. Q., Solvothermal synthesis, structures, and magnetic properties of Ni(II) compounds directed by *N,N'*-bridging auxiliary ligands. *Inorganica Chimica Acta* **2015,** *428*, 37-43.
26. Wang, H.; Hou, X. Y.; Wang, X.; Fu, F., Structural diversity and luminescent properties of metal-organic frameworks based on a rare sulfonate and imidazole co-ligand system. *Jiegou Huaxue* **2016,** *35* (9), 1427-1437.

27. Maity, D. K.; Haque, F.; Dutta, B.; Bhattacharya, B.; Ghoshal, D., Syntheses and characterization of three diphenyl phosphate based Cu(II) complexes and the effect of non-covalent interactions on their supramolecular framework. *Journal of Chemical Sciences* **2016,** *128* (12), 1861-1869.
28. Shimizu, G. K. H.; Vaidhyanathan, R.; Taylor, J. M., Phosphonate and sulfonate metal organic frameworks. *Chemical Society Reviews* **2009,** *38* (5), 1430-1449.
29. Ockwig, N. W.; Delgado-Friedrichs, O.; O'Keeffe, M.; Yaghi, O. M., Reticular chemistry: Occurrence and taxonomy of nets and grammar for the design of frameworks. *Accounts of Chemical Research* **2005,** *38* (3), 176-182.
30. Eddaoudi, M.; Kim, J.; Rosi, N.; Vodak, D.; Wachter, J.; O'Keeffe, M.; Yaghi, O. M., Systematic design of pore size and functionality in isoreticular MOFs and their application in methane storage. *Science* **2002,** *295* (5554), 469-472.
31. Jiang, H. L.; Makal, T. A.; Zhou, H. C., Interpenetration control in metal-organic frameworks for functional applications. *Coordination Chemistry Reviews* **2013,** *257* (15-16), 2232-2249.
32. Masoomi, M. Y.; Bagheri, M.; Morsali, A., Porosity and dye adsorption enhancement by ultrasonic synthesized Cd(II) based metal-organic framework. *Ultrasonics Sonochemistry* **2017,** *37*, 244-250.
33. Julien, P. A.; Užarević, K.; Katsenis, A. D.; Kimber, S. A. J.; Wang, T.; Farha, O. K.; Zhang, Y.; Casaban, J.; Germann, L. S.; Etter, M.; Dinnebier, R. E.; James, S. L.; Halasz, I.; Friščić, T., In situ monitoring and mechanism of the mechanochemical formation of a microporous MOF-74 framework. *Journal of the American Chemical Society* **2016,** *138* (9), 2929-2932.
34. Firmino, A. D. G.; Mendes, R. F.; Ananias, D.; Vilela, S. M. F.; Carlos, L. D.; Tomé, J. P. C.; Rocha, J.; Almeida Paz, F. A., Microwave synthesis of a photoluminescent metal-organic framework based on a rigid tetraphosphonate linker. *Inorganica Chimica Acta* **2017,** *455*, 584-594.
35. Rankine, D.; Avellaneda, A.; Hill, M. R.; Doonan, C. J.; Sumby, C. J., Control of framework interpenetration for in situ modified hydroxyl functionalised IRMOFs. *Chemical Communications* **2012,** *48* (83), 10328-10330.
36. Ferguson, A.; Liu, L.; Tapperwijn, S. J.; Perl, D.; Coudert, F. X.; Van Cleuvenbergen, S.; Verbiest, T.; Van Der Veen, M. A.; Telfer, S. G., Controlled partial interpenetration in metal-organic frameworks. *Nature Chemistry* **2016,** *8* (3), 250-257.
37. Song, F.; Wang, C.; Falkowski, J. M.; Ma, L.; Lin, W., Isoreticular chiral metal-organic frameworks for asymmetric alkene epoxidation: Tuning catalytic activity by controlling framework catenation and varying open channel sizes. *Journal of the American Chemical Society* **2010,** *132* (43), 15390-15398.
38. Falkowski, J. M.; Wang, C.; Liu, S.; Lin, W., Actuation of asymmetric cyclopropanation catalysts: Reversible single-crystal to single-crystal reduction of metal-organic frameworks. *Angewandte Chemie - International Edition* **2011,** *50* (37), 8674-8678.
39. Cohen, S. M., Postsynthetic methods for the functionalization of metal-organic frameworks. *Chemical Reviews* **2012,** *112* (2), 970-1000.
40. Tanabe, K. K.; Cohen, S. M., Postsynthetic modification of metal-organic frameworks - A progress report. *Chemical Society Reviews* **2011,** *40* (2), 498-519.

41. Gui, B.; Meng, X.; Xu, H.; Wang, C., Postsynthetic modification of metal-organic frameworks through click chemistry. *Chinese Journal of Chemistry* **2016,** *34* (2), 186-190.
42. Evans, J. D.; Sumby, C. J.; Doonan, C. J., Post-synthetic metalation of metal-organic frameworks. *Chemical Society Reviews* **2014,** *43* (16), 5933-5951.
43. Babarao, R.; Coghlan, C. J.; Rankine, D.; Bloch, W. M.; Gransbury, G. K.; Sato, H.; Kitagawa, S.; Sumby, C. J.; Hill, M. R.; Doonan, C. J., Does functionalisation enhance CO_2 uptake in interpenetrated MOFs? An examination of the IRMOF-9 series. *Chemical Communications* **2014,** *50* (24), 3238-3241.
44. Liu, B.; Jie, S.; Bu, Z.; Li, B.-G., A MOF-supported chromium catalyst for ethylene polymerization through post-synthetic modification. *Journal of Molecular Catalysis A: Chemical* **2014,** *387*, 63-68.
45. Wang, Z.; Cohen, S. M., Postsynthetic covalent modification of a neutral metal-organic framework. *Journal of the American Chemical Society* **2007,** *129* (41), 12368-12369.
46. Wang, J.; Xia, T.; Zhang, X.; Zhang, Q.; Cui, Y.; Yang, Y.; Qian, G., A turn-on fluorescent probe for Cd^{2+} detection in aqueous environments based on an imine functionalized nanoscale metal-organic framework. *RSC Advances* **2017,** *7* (86), 54892-54897.
47. Dugan, E.; Wang, Z.; Okamura, M.; Medina, A.; Cohen, S. M., Covalent modification of a metal-organic framework with isocyanates: probing substrate scope and reactivity. *Chemical Communications* **2008,** (29), 3366-3368.
48. Wang, Z.; Tanabe, K. K.; Cohen, S. M., Accessing postsynthetic modification in a series of metal-organic frameworks and the influence of framework topology on reactivity. *Inorganic Chemistry* **2009,** *48* (1), 296-306.
49. Yi, X.-C.; Xi, F.-G.; Qi, Y.; Gao, E.-Q., Synthesis and click modification of an azido-functionalized Zr(IV) metal-organic framework and a catalytic study. *RSC Advances* **2015,** *5* (2), 893-900.
50. Burrows, A. D.; Frost, C. G.; Mahon, M. F.; Richardson, C., Post-synthetic modification of tagged metal-organic frameworks. *Angewandte Chemie - International Edition* **2008,** *47* (44), 8482-8486.
51. Deshpande, R. K.; Waterhouse, G. I. N.; Jameson, G. B.; Telfer, S. G., Photolabile protecting groups in metal-organic frameworks: Preventing interpenetration and masking functional groups. *Chemical Communications* **2012,** *48* (10), 1574-1576.
52. Li, B.; Gui, B.; Hu, G.; Yuan, D.; Wang, C., Postsynthetic modification of an alkyne-tagged zirconium metal-organic framework via a "click" reaction. *Inorganic Chemistry* **2015,** *54* (11), 5139-5141.
53. Yang, H.; He, X.-W.; Wang, F.; Kang, Y.; Zhang, J., Doping copper into ZIF-67 for enhancing gas uptake capacity and visible-light-driven photocatalytic degradation of organic dye. *Journal of Materials Chemistry* **2012,** *22* (41), 21849-21851.
54. Brozek, C. K.; Dincă, M., Ti^{3+}-, $V^{2+/3+}$-, $Cr^{2+/3+}$-, Mn^{2+}-, and Fe^{2+}-Substituted MOF-5 and Redox Reactivity in Cr- and Fe-MOF-5. *Journal of the American Chemical Society* **2013,** *135* (34), 12886-12891.
55. Deng, H.; Doonan, C. J.; Furukawa, H.; Ferreira, R. B.; Towne, J.; Knobler, C. B.; Wang, B.; Yaghi, O. M., Multiple functional groups of varying ratios in metal-organic frameworks. *Science* **2010,** *327* (5967), 846-850.

56. Lee, S. J.; Doussot, C.; Baux, A.; Liu, L.; Jameson, G. B.; Richardson, C.; Pak, J. J.; Trousselet, F.; Coudert, F.-X.; Telfer, S. G., Multicomponent metal-organic frameworks as defect-tolerant materials. *Chemistry of Materials* **2016,** *28* (1), 368-375.
57. Bryant, M. R.; Burrows, A. D.; Kepert, C. J.; Southon, P. D.; Qazvini, O. T.; Telfer, S. G.; Richardson, C., Mixed-component sulfone-sulfoxide tagged zinc IRMOFs: In situ ligand oxidation, carbon dioxide, and water sorption studies. *Crystal Growth & Design* **2017,** *17* (4), 2016-2023.
58. Lalonde, M. B.; Mondloch, J. E.; Deria, P.; Sarjeant, A. A.; Al-Juaid, S. S.; Osman, O. I.; Farha, O. K.; Hupp, J. T., Selective solvent-assisted linker exchange (SALE) in a series of zeolitic imidazolate frameworks. *Inorganic Chemistry* **2015,** *54* (15), 7142-7144.
59. Boissonnault, J. A.; Wong-Foy, A. G.; Matzger, A. J., Core–shell structures arise naturally during ligand exchange in metal-organic frameworks. *Journal of the American Chemical Society* **2017,** *139* (42), 14841-14844.
60. Fujita, M.; Kwon, Y. J.; Washizu, S.; Ogura, K., Preparation, clathration ability, and catalysis of a two-dimensional square network material composed of cadmium(II) and 4,4′-bipyridine. *Journal of the American Chemical Society* **1994,** *116* (3), 1151-1152.
61. Manna, K.; Zhang, T.; Lin, W., Postsynthetic metalation of bipyridyl-containing metal-organic frameworks for highly efficient catalytic organic transformations. *Journal of the American Chemical Society* **2014,** *136* (18), 6566-6569.
62. Yu, X.; Cohen, S. M., Photocatalytic metal-organic frameworks for the aerobic oxidation of arylboronic acids. *Chemical Communications* **2015,** *51* (48), 9880-9883.
63. Fei, H.; Sampson, M. D.; Lee, Y.; Kubiak, C. P.; Cohen, S. M., Photocatalytic CO_2 reduction to formate using a Mn(I) molecular catalyst in a robust metal-organic framework. *Inorganic Chemistry* **2015,** *54* (14), 6821-6828.
64. Sawaki, T.; Dewa, T.; Aoyama, Y., Immobilization of soluble metal complexes with a hydrogen-bonded organic network as a supporter. A simple route to microporous solid Lewis acid catalysts. *Journal of the American Chemical Society* **1998,** *120* (33), 8539-8540.
65. Seo, J. S.; Whang, D.; Lee, H.; Jun, S. I.; Oh, J.; Jeon, Y. J.; Kim, K., A homochiral metal-organic porous material for enantioselective separation and catalysis. *Nature* **2000,** *404* (6781), 982-986.
66. Evans, O. R.; Ngo, H. L.; Lin, W., Chiral porous solids based on lamellar lanthanide phosphonates. *Journal of the American Chemical Society* **2001,** *123* (42), 10395-10396.
67. Ruano, D.; Díaz-García, M.; Alfayate, A.; Sánchez-Sánchez, M., Nanocrystalline M-MOF-74 as heterogeneous catalysts in the oxidation of cyclohexene: Correlation of the activity and redox potential. *ChemCatChem* **2015,** *7* (4), 674-681.
68. Blandez, J. F.; Santiago-Portillo, A.; Navalón, S.; Giménez-Marqués, M.; Álvaro, M.; Horcajada, P.; García, H., Influence of functionalization of terephthalate linker on the catalytic activity of UiO-66 for epoxide ring opening. *Journal of Molecular Catalysis A: Chemical* **2016,** *425*, 332-339.
69. Bandini, M.; Cozzi, P. G.; Umani-Ronchi, A., [Cr(Salen)] as a 'bridge' between asymmetric catalysis, Lewis acids and redox processes. *Chemical Communications* **2002,** (9), 919-927.

70. Demuynck, A. L. W.; Goesten, M. G.; Ramos-Fernandez, E. V.; Dusselier, M.; Vanderleyden, J.; Kapteijn, F.; Gascon, J.; Sels, B. F., Induced chirality in a metal-organic framework by postsynthetic modification for highly selective asymmetric aldol reactions. *ChemCatChem* **2014,** *6* (8), 2211-2214.
71. Yang, Z.; Zhu, C.; Li, Z.; Liu, Y.; Liu, G.; Cui, Y., Engineering chiral Fe(salen)-based metal-organic frameworks for asymmetric sulfide oxidation. *Chemical Communications* **2014,** *50* (63), 8775-8778.
72. Gao, W. Y.; Wojtas, L.; Ma, S., A porous metal-metalloporphyrin framework featuring high-density active sites for chemical fixation of CO_2 under ambient conditions. *Chemical Communications* **2014,** *50* (40), 5316-5318.
73. Ma, L.; Falkowski, J. M.; Abney, C.; Lin, W., A series of isoreticular chiral metal-organic frameworks as a tunable platform for asymmetric catalysis. *Nat Chem* **2010,** *2* (10), 838-846.
74. Li, Y. P.; Zhang, L. J.; Ji, W. J., Synthesis, characterization, crystal structure of magnesium compound based 3, 3′, 5, 5′-azobenzentetracarboxylic acid and application as high-performance heterogeneous catalyst for cyanosilylation. *Journal of Molecular Structure* **2017,** *1133*, 607-614.
75. Burgun, A.; Crees, R. S.; Cole, M. L.; Doonan, C. J.; Sumby, C. J., A 3D diamondoid MOF catalyst based on in situ generated $[Cu(L)_2]$ N-heterocyclic carbene (NHC) linkers: hydroboration of CO_2. *Chemical Communications* **2014,** *50* (79), 11760-11763.
76. Morris, W.; Volosskiy, B.; Demir, S.; Gándara, F.; McGrier, P. L.; Furukawa, H.; Cascio, D.; Stoddart, J. F.; Yaghi, O. M., Synthesis, structure, and metalation of two new highly porous zirconium metal-organic frameworks. *Inorganic Chemistry* **2012,** *51* (12), 6443-6445.
77. Jiang, H. L.; Feng, D.; Wang, K.; Gu, Z. Y.; Wei, Z.; Chen, Y. P.; Zhou, H. C., An exceptionally stable, porphyrinic Zr metal-organic framework exhibiting pH-dependent fluorescence. *Journal of the American Chemical Society* **2013,** *135* (37), 13934-13938.
78. Xie, M.-H.; Yang, X.-L.; Wu, C.-D., A metalloporphyrin functionalized metal-organic framework for selective oxidization of styrene. *Chemical Communications* **2011,** *47* (19), 5521-5523.
79. Wang, X. S.; Chrzanowski, M.; Wojtas, L.; Chen, Y. S.; Ma, S., Formation of a metalloporphyrin-based nanoreactor by postsynthetic metal-ion exchange of a polyhedral-cage containing a metal-metalloporphyrin framework. *Chemistry - A European Journal* **2013,** *19* (10), 3297-3301.
80. Wasilke, J.-C.; Obrey, S. J.; Baker, R. T.; Bazan, G. C., Concurrent Tandem Catalysis. *Chemical Reviews* **2005,** *105* (3), 1001-1020.
81. Lee, Y.-R.; Chung, Y.-M.; Ahn, W.-S., A new site-isolated acid-base bifunctional metal-organic framework for one-pot tandem reaction. *RSC Advances* **2014,** *4* (44), 23064-23067.
82. Srirambalaji, R.; Hong, S.; Natarajan, R.; Yoon, M.; Hota, R.; Kim, Y.; Ho Ko, Y.; Kim, K., Tandem catalysis with a bifunctional site-isolated Lewis acid-Bronsted base metal-organic framework, NH_2-MIL-101(Al). *Chemical Communications* **2012,** *48* (95), 11650-11652.

83. Liu, L.; Zhou, T.-Y.; Telfer, S. G., Modulating the performance of an asymmetric organocatalyst by tuning its spatial environment in a metal-organic framework. *Journal of the American Chemical Society* **2017,** *139* (39), 13936-13943.
84. Li, X.; Zhang, B.; Tang, L.; Goh, T. W.; Qi, S.; Volkov, A.; Pei, Y.; Qi, Z.; Tsung, C.-K.; Stanley, L.; Huang, W., Cooperative multifunctional catalysts for nitrone synthesis: Platinum nanoclusters in amine-functionalized metal–organic frameworks. *Angewandte Chemie International Edition* **2017,** *56* (51), 16371-16375.
85. Azarifar, D.; Ghorbani-Vaghei, R.; Daliran, S.; Oveisi, A. R., A multifunctional zirconium-based metal-organic framework for the one-pot tandem photooxidative passerini three-component reaction of alcohols. *ChemCatChem* **2017,** *9* (11), 1992-2000.

Chapter 2

Materials and instrumentation

2 Materials and instrumentation

2.1 Materials

All the chemical reagents used in experiments were of analytical grade and were used as received without further purification and were purchased from Sigma Aldrich or Ajax Finechem Pty Ltd.

2.2 Instrumentation

2.2.1 Nuclear Magnetic Resonance (NMR) spectroscopy

^{1}H NMR and ^{13}C NMR spectra were recorded using three NMR spectrometers; Mercury Vx 300 MHz NMR spectrometer operating at 300 MHz for ^{1}H and 75.5 MHz for ^{13}C, Inova and VNMRS PS54 500 MHz NMR spectrometers operating at 500 MHz for ^{1}H and 125 MHz for ^{13}C and Bruker 400 MHz spectrometer operating at 400 MHz for ^{1}H and 100 MHz for ^{13}C. The NMR data were processed using Mestronova software, version 6.0.2.

^{1}H NMR spectra were referenced to the residual *protio* peaks at 7.26 ppm for $CDCl_3$ and 2.50 ppm for d_6-DMSO. ^{13}C NMR spectra were referenced to the solvent peaks at 77.7 ppm for $CDCl_3$ and 39.6 ppm for d_6-DMSO.

2.2.1.1 Sample preparation for organic molecules for ^{1}H NMR and ^{13}C NMR spectroscopy

Approximately 5–8 mg of organic compounds in ester or acid forms were dissolved in 500 μL of $CDCl_3$ or d_6-DMSO, and then used for ^{1}H NMR spectroscopy. A similar procedure was used for ^{13}C NMR spectroscopy, with approximately 20–25 mg of the compound dissolved in the same amounts of solvent.

2.2.1.2 Sample preparation of coordination networks for ^{1}H NMR and ^{13}C NMR spectroscopy

Approximately 5–8 mg of each compound was digested in 500 μL of d_6-DMSO and 3 μL of 35% DCl in D_2O. The solution was used for ^{1}H NMR analysis after the crystals dissolved.

2.2.2 Mass Spectrometry (MS)

Mass spectra were recorded on a Shimadzu LCMS-2010EV electrospray ionisation (ESI) mass spectrometer. The data were processed using MassLynx software, version 4.1. Elemental composition was calculated with the software's inbuilt elemental calculation tool.

2.2.2.1 Sample preparation for organic molecules and coordination complexes

Each solution was made in MeOH/H_2O with a concentration of 0.1 $mgmL^{-1}$ concentration and then analysed by ESI in negative or positive ion mode.

2.2.2.2 Sample preparation for coordination networks

Approximately 20 mg of coordination network was digested in MeOH (1 mL) and 1 M HCl (1 mL). Upon dilution the precipitate that formed was filtered off and air dried. MS samples were dissolved in MeOH/H_2O (1 : 1, 0.1 $mgmL^{-1}$) and the solution was analysed by ESI in negative or positive ion mode.

2.2.3 Powder X-Ray Diffraction (PXRD)

PXRD patterns were collected on a GBC-MMA X-ray diffractometer with samples mounted on 1" SiO_2 substrates. Typically, as-synthesised samples were loaded on the plate with small amounts of solvent (DMF or DMF/H_2O or DEF) to keep them damp. PXRD data were recorded in the 2θ range of 2–30 (for zirconium based MOFs, chapter 5) and 3–30 for other materials reported in this thesis with a step size of 0.02° at 1° per minute. The data were processed using Traces version 6.6 software.

2.2.4 Thermogravimetric and Differential Thermal Analysis (TG-DTA)

TG-DTA traces were recorded using a Shimadzu DTG-60 simultaneous Thermogravimetric and Differential Thermal Analyser, equipped with a FC-60A Flow Rate controller and TA-60WS Thermal Analyser. Measuring parameters of 10 °C per min under N_2 flow (20 cm^3min^{-1}) were used. Data analysis was performed on Ta60 version 2.20 software system. Traces were recorded by loading approximately 5 mg of sample on a platinum pan for strontium based materials in the range between room temperature to 700 °C, or on an aluminium pan for other materials reported in this thesis, in the range between room temperature to 550 °C.

2.2.5 Thermogravimetric and Differential Scanning Calorimetry (TG-DSC)

TG-DSC analyses were performed using a NETZSCH STA 449 F3 Jupiter simultaneous Thermogravimetric and Differential Scanning Calorimeter equipped with a multi-channel temperature controller (TRG 004). Measuring parameters of 10 °C per min under N_2 flow (20 cm^3min^{-1}) were used. Data analysis was carried out on NETZSCH Proteus® version 6.1.0 software system. The masses and heating protocols were the same as stated in 2.2.4.

2.2.6 Single Crystal X-Ray Crystallography

Single-crystal X-ray diffraction (SCXRD) data were collected on a Rigaku Spider diffractometer equipped with a MicroMax MM007 rotating anode generator (Cu Kα radiation, λ =1.54180 Å), high-flux Osmic multilayer mirror optics, and a curved image-plate detector. Most data were collected at 292 K and low temperature collections were also carried out. The data were integrated and scaled and averaged with FS Process. The crystal structures were solved by direct methods using SHELXS-97 and refined against F2 on all data by full-matrix least-squares with SHELXL-97 (SHELX-97 program package, Sheldrick, Universität Göttingen, 1997). The crystal structure images were produced by $Olex^2$ software, version 1.2.9 or Mercury software version 3.8. All data solution and refinement was carried out by Professor Shane Telfer of Massey University, unless otherwise indicated.

2.2.7 Elemental Microanalysis

Elemental microanalysis was carried out using a PerkinElmer CHNS/O Elemental Analyser (Model PE2400) with a PerkinElmer AD-6 Ultra Micro Balance. The analysis was performed by Chemical Analysis Facility at Macquarie University.

2.2.8 Photoluminescence Spectroscopy (PL)

Photoluminescence measurements were carried out using a Fluorolog FL3-212 spectrophotometer (Model Horiba Jobin Yvon) equipped with 450 W Xe lamp as excitation source.

2.2.9 Inductively Coupled Plasma Optical Emission Spectroscopy (ICP-OES)

ICP-OES measurements were carried out using a PerkinElmer Optima instrument (Model 8000) equipped with a CCD detector. The data were processed using OPTIMA Syngistix Software, version 1.0.1.

2.2.9.1 Sample preparation for (ICP-OES)

The samples were solvent exchanged to dry CH_2Cl_2, followed by vacuum drying to remove the volatiles. The samples were then digested with 5 mg of each MOF in 1 mL HNO_3 70% at 70 °C for 12 hours in an oil bath. Dilutions were carried out as required using ultra-pure dilute HNO_3 solutions.

2.2.10 Quadrupole-Inductively Coupled Plasma-Mass Spectrometer (iCap Q-ICP-MS)

ICP-MS measurements were performed using an iCap Q-ICP-MS ThermoFisher instrument and then the data were processed using Qtegra software. The analysis was carried out by staff at the Wollongong Isotope Geochronology Laboratory at the University of Wollongong. Typical sample preparation involved weighing greater than 5.00 mg of each sample to digest in 1 mL of 70% HNO_3 at 70 °C for 12 hours in an oil bath. Samples were diluted in ultrapure 0.3M HNO_3 to ppb levels for analysis. The residual deviations on results obtained were 1% of final sample values from ICP-MS analysis. Errors from the weighing and analysis are around 1-2%.

2.2.11 Gas Chromatography–Mass Spectrometry (GC-MS)

GC-MS chromatographs were obtained using a Xevo-QTOFMS Autosampler Agilent 7683 series fitted with an Agilent DB-5MS column (30 m × 250 μm × 0.25 μm) under N_2 gas flow (30 $mLmin^{-1}$) in constant flow mode. A 1 μL sample volume in CH_2Cl_2 (HPLC grade) was injected in split mode with split ratio of 20 : 1 with the inlet temperature set to 280 °C. The initial oven temperature was set to 45 °C with 1 minute equi1ibrium time followed by a 30 $°Cmin^{-1}$ ramp to temperature set point of 300 °C. The mass range was set to scan the 40–1050 *m/z* range with 6.5 minutes scan time. The data were analysed by MassLynx software, version 4.0.

2.2.12 Scanning Electron Microscopy-Energy-Dispersive X-ray Spectroscopy (SEM-EDS)

All microscopy was performed using a JEOL JSM-6490LV operated at 15 kV accelerating voltage. EDS elemental analysis was performed using Oxford Instruments AZtec suite from an Oxford X-max^N 80mm^2 SDD.

2.3 Activation methods of the MOFs

2.3.1 Freeze Drying

Freeze drying was carried out using a Christ Alpha 1-2 LD plus Freeze Dryer at –53 °C under vacuum of 0.18–0.33 mbar between one and sixteen hours. The samples were used immediately for gas sorption after bringing back to room temperature for further activation by vacuum treatment at or above room temperature.

2.3.2 Supercritical CO_2 Point Dryer

$ScCO_2$ processing was performed using a Leica EM CPD030 Critical Point Dryer. After solvent exchange to an appropriate solvent, the crystals were transferred directly from the solution to a mesoporous capsule and placed in the critical point dryer and soaked in liquid CO_2 (3 × 15 minutes) to exchange residual solvent, then the chamber temperature and pressure was raised to 40 °C and 100 bar for a further period of time (typically 8 hours). The CO_2 was then vented off over a period of 18 hours. The crystals were transferred to a dry, modified Schlenk tube fitted with a gas tight valve and prefilled by

N_2 gas and transferred immediately to gas sorption station for further activation by heating under vacuum.

In this thesis, the solvent exchange procedure and type of solvent being used are described for each MOF in the appropriate chapter.

2.3.3 Gas sorption studies

Gas adsorption studies were carried out using a Quantachrome Autosorb MP instrument using high purity He (99.999%), N_2 (99.999%) and CO_2 (99.995%) gasses. The data were analysed using ASiQwin version 3.0 software.

Specific surface areas were determined by calculating the volumetric amount of gas adsorbed using Brunauer, Emmett and Teller (BET) theory, equation:[1]

$$\frac{P}{Va(\mathrm{P}-P°)} = \frac{1}{VmC} + \frac{(C-1)}{VmC} \times (\frac{P}{P°})$$

where:

Va is the volume of gas adsorbed at P

Vm is the volume of gas required to form monolayer

C is the BET constant

P/P^o is the relative pressure of adsorbate

The BET equation was used to calculate all surface areas reported in this thesis. The recommendations of Rouquerol were followed for selection of the points for the BET surface areas.[2]

Heat of adsorption was calculated by CO_2 adsorption measurements using at least two temperatures, and by employing the Clausius-Clapeyron equation:[3]

$$Q_{st} = -\Delta H_{Ads} = -R\left(\frac{d\ln P}{d\frac{1}{T}}\right) > 0$$

Selectivity of CO_2 over N_2 was evaluated by the quantity of CO_2 adsorbed at 0.15 bar and divided by the quantity of N_2 adsorbed at 0.85 bar. It can be calculated by The Ideal Adsorbed Solution Theory (IAST) of Myers and Prausnitz via the formula below:[4]

$$S = \frac{\mathrm{q1/q2}}{p1/p2}$$

2.4 References

1. Brunauer, S.; Emmett, P. H.; Teller, E., Adsorption of Gases in Multimolecular Layers. *Journal of the American Chemical Society* **1938,** *60* (2), 309-319.
2. Rouquerol, J.; Llewellyn, P.; Rouquerol, F., Is the BET equation applicable to microporous adsorbents? In *Studies in Surface Science and Catalysis*, 2006; Vol. 160, pp 49-56.
3. Vlugt, T. J. H.; García-Pérez, E.; Dubbeldam, D.; Ban, S.; Calero, S., Computing the heat of adsorption using molecular simulations: The effect of strong Coulombic interactions. *Journal of Chemical Theory and Computation* **2008,** *4* (7), 1107-1118.
4. Myers, A. L.; Prausnitz, J. M., Thermodynamics of mixed-gas adsorption. *AIChE Journal* **1965,** *11* (1), 121-127.

Chapter 3

Crystal Engineering of Metallosalen-based Coordination Networks

3 Introduction

One of the advanced aspects of MOFs is their amenability to rational design through crystal engineering. The rapidly expanding interest in the rational design and crystal engineering of MOFs arises from the desire to introduce specific physical and chemical properties. In the crystal engineering approach, pore surface properties can be tuned by direct introduction of organic linkers carrying specific functional groups[1] or via PSM.[2] An ultimate aim is to control the pore size and functionalities, and consequently generate MOFs with specific properties for targeted applications. The crystal engineering of MOFs using rational design plays a vital role in the development of these materials for specific applications, such as size selective heterogeneous catalysis[3] and gas sorption technology for shape-selective separation of specific gases.[4]

Crystal engineering also provides a platform for the rational design and construction of frameworks with a predictable final topology. Ideally, the choice of metal nodes and organic linkers could be used to determine the final topology of the MOF.[5, 6, 7] Although the structural components of MOFs can be rationally designed, it is still challenging to predict the final structure and topology. However, there are special cases reported in the literature; recently Eddaoudi and colleagues published work that shows for edge-transitive structures that have highly connected nodes, predetermined topologies can be predicted.[8] Organic linkers with identical coordination moieties often adopt different conformations, resulting in MOFs with different topologies and therefore properties[9] and also that metal ions form different SBUs with different structural properties.[10] Finally, the use of the same metal nodes and organic linkers lead to differing structures under different synthetic conditions.[11] These complications make the process of rationally designing MOFs very challenging, and therefore, true design is rare.

3.1 Crystal engineering of MOFs based on salen-type complexes as metalloligands

In the last few years, metallosalen-type complexes with different metal centres have become prominent organic linkers to construct MOFs for different applications. Chiral salen-type ligands are established as catalysts for transformations in synthetic organic chemistry and for molecular separations because of preparatory ease; salens have a modular structure amenable to straight forward structural modification, easy complexation with a wide range of metal ions, good solubility in common organic solvents and good stability.[12, 13] The use of metallosalen-type linkers for MOFs is still underexplored. Metallosalen-type linkers typically have more flexibility and are less rigid compare to other aromatic organic linkers and often give unique topologies and pore shapes.[14] There are a few reports in the literature of metallosalen based MOFs as heterogeneous catalysts,[15, 16] magnetic resonance imaging (MRI) agents,[17] and for gas storage/separation.[18] However, in some cases, the MOFs suffered from severe diffusion limitations for gas sorption measurements.[19]

Lin and co-workers reported a very important crystal engineering study of chiral Mn-salen-based MOFs in 2010.[20] The rational design of isoreticular homochiral MOFs (CMOFs) with cubic network topologies using Mn(salen)Cl derived dicarboxylate ligands as linkers and $Zn_4(\mu_4\text{-}O)(CO_2)_6$ nodes in different solvent systems was accomplished. The effect of the solvent as a space-filling template was investigated on the structures of the CMOFs. Control over the structure and pore size was achieved depending on the solvent used, with interpenetrated structures of $Zn_4O(L^1)_3 \cdot 20DMF \cdot 2H_2O$ (CMOF-1), $Zn_4O(L^2)_3 \cdot 42DMF$ (CMOF-3) and $Zn_4O(L^3)_3 \cdot 38DMF \cdot 11EtOH$ (CMOF-5) obtained in DMF and EtOH mixtures, while non-interpenetrated $Zn_4O(L^1)_3 \cdot 22DEF \cdot 4H_2O$ (CMOF-2) and $Zn_4O(L^2)_3 \cdot 37DEF \cdot 23EtOH \cdot 4H_2O$ (CMOF-4) (the structures of $H_2L^{1\text{-}3}$ and CMOF-1-5 are shown in Figure 3.1) were obtained in DEF and EtOH solvent mixtures. The catalytic activity of CMOFs 1-5 for the epoxidation of alkenes was examined using 1*H*-indene as a substrate and 2-(*tert*-butyl-sulfonyl)iodosylbenzene as the terminal oxidant.

Interestingly, the rate of conversion was dependent on the CMOF channel sizes and increased as follows: CMOF-1 < CMOF-5 < CMOF-3 < CMOF-2 < CMOF-4. In this study, the rational structural design of these MOFs was successful wherein variation of the linker length changed the size of the channels and the solvent templates controlled catenation.

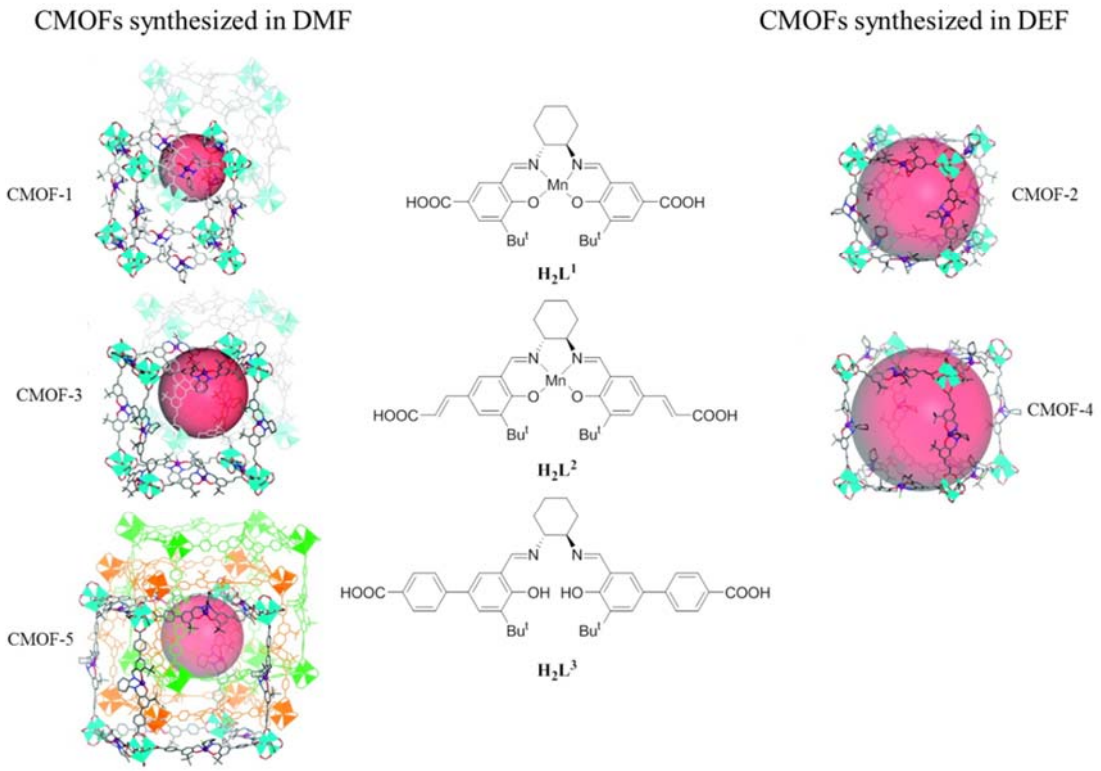

Figure 3.1 The structures of H_2L^{1-3} and CMOF-1-5. Reprinted with permission from Song, F.; Wang, C.; Falkowski, J. M.; Ma, L.; Lin, W. *Journal of the American Chemical Society* 2010, *132* (43), 15390-15398. Copyright (2010) American Chemical Society.

The CMOF system with salen-derived dicarboxylate ligands and $Zn_4O(CO_2R)_6$ nodes seems particularly suitable for further elaboration. Different metallated salens could be introduced through direct synthesis, forming MOF catalysts with dual active sites.

Most crystal engineering studies of MOFs in the literature concern systems containing only one functional group or a single type of metal ion in a node. As explained in section 1.4.2, a crystal engineering approach allows for the design of MOFs containing multiple organic linkers with different functional groups or metal centres. Introducing two or more

different functionalities in one framework allows for the modification of the surface environment within a single material. Such approaches ideally must come with enhanced synthetic efficiency, that is, taking less time and effort, and also benefit tuning the MOF towards a particular application.

The strategy of incorporating two differently functionalised linkers or different metal centres into coordination frameworks can be applied to the synthesis of catalysts for tandem catalytic reactions, where each linker/metal centre could be chosen based on its property and function. The group of Cui reported such a crystal engineering approach in the synthesis of a multi-metal (Cr/VO) salen-based MOF for tandem catalysis.[21] The team used a direct synthetic approach toward constructing a mixed-metal MOF using the dipyridyl salen ligand shown in Figure 3.2a, that was metallated with Cr and VO. Interestingly, this proved unsuccessful with no Cr(salen) incorporation. Therefore, SALE was employed to introduce Cr(salen) in a pre-made VO(salen) MOF to afford the multi-metal material (Figure 3.2c). Inductively coupled plasma-mass spectrometry/optical emission spectroscopy (ICP-MS/OES) indicated 40% Cr incorporation in the multi-metal Cr/VO(salen) MOF, confirming a successful linker exchange and functionality modification of the MOF. Presumably, however, Cr is located at the edges of the new MOF particle as the exchange process takes place and a core-shell ensemble is formed. If the design of a tandem MOF catalyst was for sequential reactions, then simply using two singly-metallated MOFs would be just as efficient. If, however, the metals are to work synergistically then a core shell structure is not advantageous. A synergistic multi-metal catalyst would need the metals dispersed through the structure and the best way to do this might be through direct synthesis.

This example shows that much work is still needed in the design and synthesis of bimetallic MOF catalysts with high complexity.

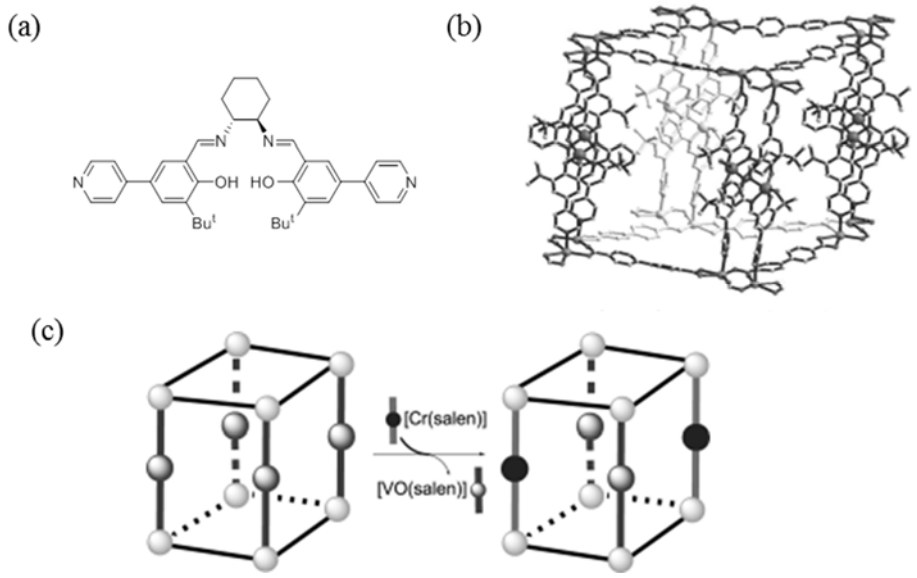

Figure 3.2 (a) The chemical structure of the VO(salen) as linker, b) 3D pillared-layer structure of VO(salen) MOF and (c) SALE procedure of VO(salen) MOF to Cr/VO(salen) MOF. From Xi, W.; Liu, Y.; Xia, Q.; Li, Z.; Cui, Y. *Chemistry - A European Journal* 2015, *21* (36), 12581-12585, Copyright © 2015 by John Wiley & Sons, Inc. Reprinted by permission of John Wiley & Sons, Inc.

3.2 Outline and rationale

The primary aim of this chapter was to show the rational design of racemic multi-metal metallosalen MOFs and to develop and implement new and easy approaches to the synthesis of bimetallic frameworks with permanent porosity and large channel sizes. The synthesis of single metallolinker coordination networks was examined to establish synthetic conditions using *rac*-1,2-cyclohexanediamino-*N,N′*-bis(5-carboxysalicylidene) (H_4cdacs) (Figure 3.3) metallated with Cu, VO, Fe and Mn before investigating a vanadium/zinc multi-metallolinker system using VO(H_2cdacs) and Zn(H_2cdacs).

Racemic H_4cdacs was used for the study as it contains a central *N,N′*-salicylidene core that could be metallated with specifically selected, catalytically competent metal ions. Salens metallated with VO,[22] Mn,[23] Ru,[24] Ti[25] and Fe[26] function as oxidants and Cu,[27] Ni,[28] Zn[29] and Co[30] as Lewis acid catalysts in organic transformations. Thus, the appropriate combination of two metals allows for the development of a bifunctional framework as an advanced material for tandem catalysis. Upon metallation H_4cdacs to M(H_2cdacs), it becomes a near-linear bridging ligand by the positioning of the carboxylic acid groups and be able to form reticular lattices observed in the literature.[16, 31] In this chapter, the synthesis of MOFs using M(H_2cdacs) (M = Cu, VO, Fe and Mn) linkers and multi-metal VO(cdacs)-Zn(cdacs) are described.

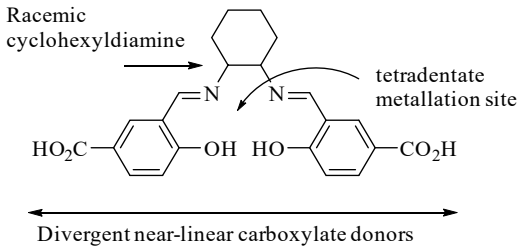

Figure 3.3 The chemical structure of H_4cdacs.

3.3 Synthesis and characterisation of metallosalen coordination networks

3.3.1 Synthesis of the ligand and complexes

The term salen is generally used to describe the class of [O,N,N,O]-tetradentate bis-Schiff base ligands. The common synthesis procedure to prepare salen-type ligands is a reaction between two equivalents of a salicylaldehyde with a diamine in an alcoholic solvent at room temperature or in refluxing conditions. In this study, H_4cdacs was previously prepared in the Richardson research group.

3.3.1.1 Syntheses and characterisation of VO(H_2cdacs), Fe(H_2cdacs)Cl, Mn(H_2cdacs)Cl and Zn(H_2cdacs)

There are several conditions reported in the literature for metallating salen ligands with VO units in alcoholic solvents starting from molecular complexes such as $VO(acac)_2$[32] or metal salts, such as $VOSO_4$.[33] Here, this complexation was accomplished using $VOSO_4$ in MeOH at 60 °C for 5 hours. The product, VO(H_2cdacs), was isolated as a pink solid in 83% yield after evaporation of most of the solvent and filtration (Scheme 3.1a).

Fe(H_2cdacs) was synthesised based on a solvothermal reaction procedure reported in the literature, with the substitution of $FeCl_3 \cdot 6H_2O$ for anhydrous $FeCl_3$.[31] Anhydrous $FeCl_3$ and H_4cdacs were refluxed in EtOH at 70 °C for 7 hours before the EtOH was removed under low pressure, and water was added to precipitate a red solid that was collected by filtration with 60% yield (Scheme 3.1b). Mn(H_2cdacs)Cl was synthesised similarly to Fe(H_2cdacs) using $MnCl_2 \cdot 4H_2O$ to afford an olive green solid with 61% yield (Scheme 3.1c). Zn(H_2cdacs) was obtained similarly to VO(H_2cdacs) using $Zn(CH_3COO)_2 \cdot 2H_2O$ in place of the vanadium salt to afford a yellow solid with 96% yield (Scheme 3.1d).

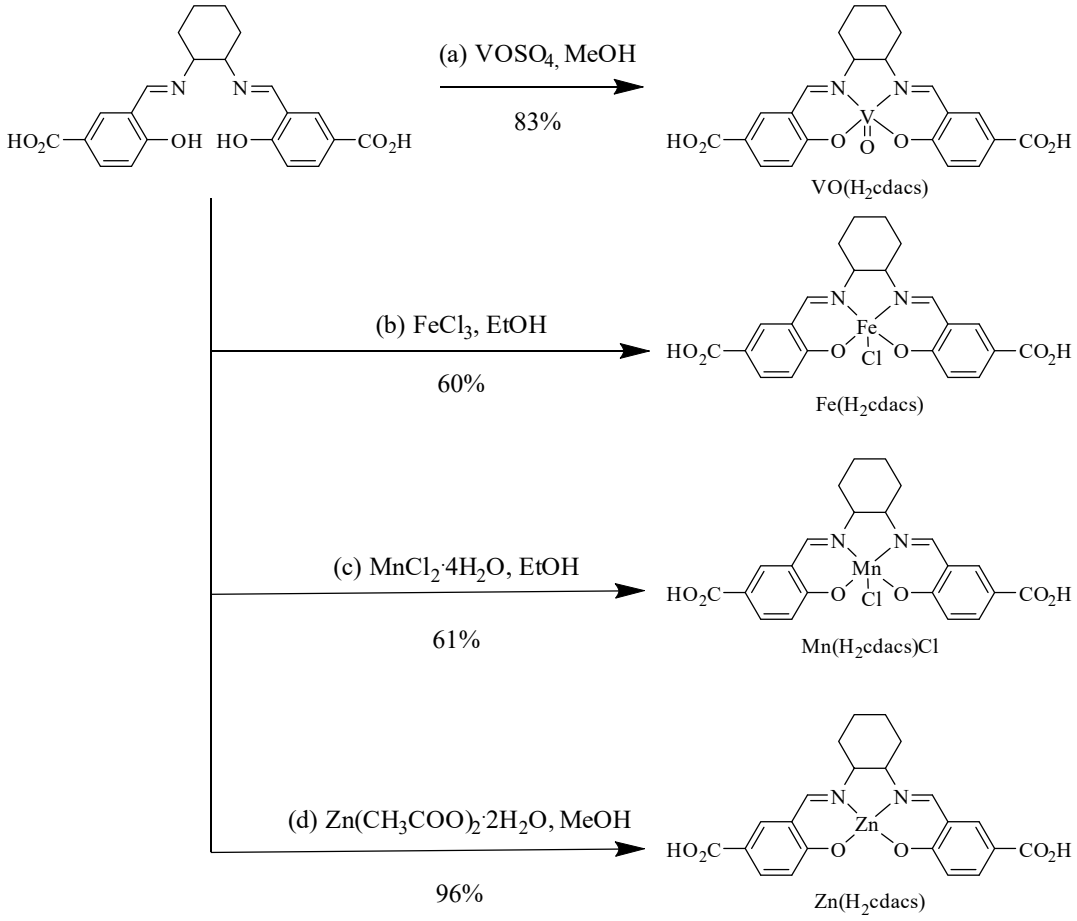

Scheme 3.1 The synthetic pathways to VO(H_2cdacs), Fe(H_2cdacs), Mn(H_2cdacs)Cl and Zn(H_2cdacs).

3.3.2 Syntheses and structures of single metallosalen-linked coordination networks

Two different synthetic methodologies were applied to make metallosalen-based materials. In the first methodology, H_4cdacs and one equivalent of divalent metal acetate salt (M = Cu, Ni and Zn) were first reacted to form the metallosalen M(H_2cdacs) (M = Cu, Ni and Zn) *in situ*. Then $Zn(NO_3)_2 \cdot 6H_2O$ was added as a source for the metal nodes. The reactions were carried out in 1 : 1, 1 : 2 and 1 : 3 ratios of M(H_2cdacs) (M = Cu, Ni and Zn) to $Zn(NO_3)_2 \cdot 6H_2O$, respectively, in DMF, DMA, or NMP and in mixed solvent systems of these polar high boiling point amides in combination with H_2O, MeOH or EtOH. The amide solvents were chosen due to their ability to decompose to their

corresponding amines under heating, which then deprotonate carboxylic acid groups and help crystal nucleation.[34] The reactions were performed between 65 °C and 100 °C from 16 hours up to one week, in line with published reports for the synthesis of salen-type MOFs.[16, 20, 35, 36]

A wide range of behaviours were observed, such as precipitation, decomposition, the formation of amorphous compounds and of gels. Reactions that were carried out in DMA and NMP solvent systems were not successful at any temperature, as the formation of amorphous compounds and powdery solids were observed. Additionally, reactions performed in DMF containing H_2O, MeOH and EtOH were also unsuccessful across all temperatures as the reactions resulted in precipitates.

Reactions in DMF gave much better results. Reactions performed at 100 °C in DMF gave precipitates and decomposition instead of crystal growth, suggesting this temperature is too high for the reactions.[34] Therefore, the reactions were performed at 65 °C and 80 °C to avoid decomposition and to possibly encourage slow nucleation to grow X-ray quality crystals. Reactions at 65 °C did not produce crystals for any of the metallated M(H_2cdacs) (M = Cu, Ni and Zn) complexes. The reactions at 80 °C showed different behaviours; the reaction between Cu(H_2cdacs) and $Zn(NO_3)_2 \cdot 6H_2O$ in all ratios (1 : 1, 1 : 2 and 1 : 3, respectively) resulted in the formation of crystals (Table 3.1, entries 1–3). Only precipitates formed from the reactions where Ni(H_2cdacs) was generated *in situ* (Table 3.1, entries 4–6) whereas all reactions of the Zn(H_2cdacs) linker resulted in the formation of gels (Table 3.1, entries 7–9). The term cdacs-CPs 1-3 are used here for Cu(H_2cdacs) materials that formed from the reaction with $Zn(NO_3)_2 \cdot 6H_2O$ in the ratios of 1 : 1, 1 : 2 and 1 : 3, respectively. Tables of *in situ* one-step syntheses performed at 65 °C, 80 °C and at 100 °C are provided in Appendix 1, Table A1.1–1.3.

Table 3.1 A summary of the *in situ* one-step syntheses performed in DMF solvent at 80 °C.

Entry	Metal acetate salt*	Metal acetate : $Zn(NO_3)_2 \cdot 6H_2O$ ratio	Product type
1	Cu	1 : 1	Crystals
2	Cu	1 : 2	Crystals
3	Cu	1 : 3	Crystals
4	Ni	1 : 1	Powder
5	Ni	1 : 1	Powder
6	Ni	1 : 3	Powder
7	Zn	1 : 1	Gel
8	Zn	1 : 2	Gel
9	Zn	1 : 3	Gel

*$Zn(CH_3COO)_2 \cdot 2H_2O$; $Ni(CH_3COO)_2 \cdot 4H_2O$; $Cu(CH_3COO)_2 \cdot H_2O$

Single crystal X-ray diffraction analysis was performed on cdacs-CPs 1-3 in order to determine the structures of the compounds. The crystals were extremely mechanically fragile and sensitive to X-rays, and proved unsuitable for crystallography. Thus, it was problematic to provide structural information, and therefore, the crystal structures remain undefined for the compounds.

The results of the *in situ* metalation and crystal growth methodology were disappointing and not in line with descriptions and literature procedures.[31] It was speculated that there might be small amounts of unreacted metal from the metalation reactions present that might be proving harmful to the growth of crystals, even though great care was taken in providing an equimolar amount. On this basis, a second synthetic approach was pursued. The change was simply to metalate H_4cdacs and isolate the M(H_2cdacs) complexes before using these complexes in MOF-forming reactions. This ensured that no amounts of free metal from the metallosalen would be present, at least at the start of the reaction. A wider range of pre-made M(H_2cdacs) metallolinkers (where M = Cu, Ni, VO, MnCl and FeCl) were reacted with $Zn(NO_3)_2 \cdot 6H_2O$ in DMF in mixed systems of these solvents with H_2O, MeOH and EtOH. The solvent systems were chosen based on the results of the *in situ* method; hence NMP and DMA were not used in the second approach.

Some factors from the *in situ* methodology were taken into account for reactions starting from pre-formed cdacs complexes. DMF solvent and reaction temperatures between 80 °C and 100 °C were clearly giving the best results. The reactions were conducted at lower concentrations to slow down crystal growth and the use of HNO_3 as a modulator was explored. HNO_3 was chosen as it can act as a competitive ligand and influence the carboxylic acid-carboxylate anion equilibrium for M(H_2cdacs). Although modulators can promote the formation of frameworks with high crystallinity, they can also inhibit crystal growth.[37]

3.3.3 Syntheses and single crystal X-ray diffraction studies

The reaction of VO(H_2cdacs) with $Zn(NO_3)_2 \cdot 6H_2O$ in the ratio 1 : 2, respectively, at 100 °C in a solvent mixture of DMF and water containing HNO_3 as modulator gave small blue crystals (Table 3.2, entry 1). Single crystal synchrotron X-ray diffraction studies showed that the structure crystallises in the monoclinic space group *C*2/*c* with an asymmetric unit containing one zinc(II) ion bound to a complete $VO(cdacs)^{1-}$ linker and one coordinated DMF molecule (Figure 3.4a).

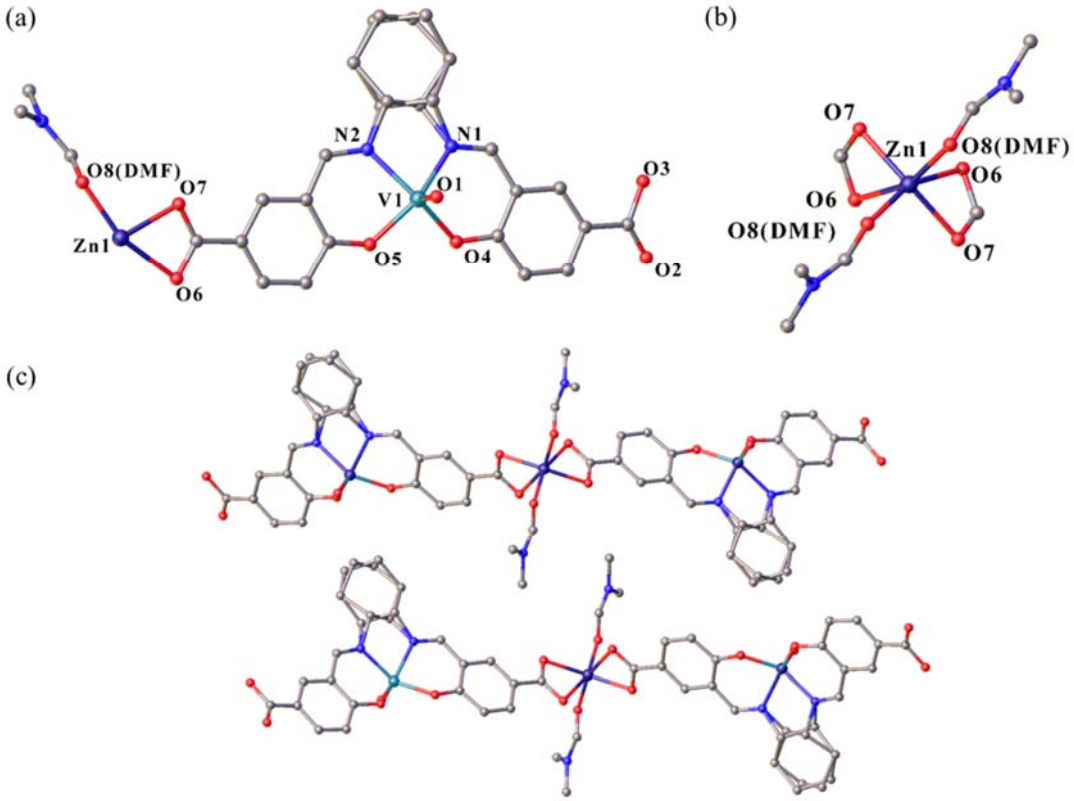

Figure 3.4 (a) Asymmetric unit of $Zn[VO(cdacs)_2(DMF)_2]$, (b) a perspective view of the distorted octahedral SBU and (c) a view of $Zn[VO(cdacs)DMF]_n$ in the 1D coordination polymer parallel to the crystallographic *b*-axis. Hydrogen atoms are not shown for clarity. Selected bond lengths: V1-O1 1.608(2), V1-O4 1.9231(17), V1-O5 1.9313(18),V1-N1 2.058(2), V1-N2 2.062(2), Zn1-O8(DMF) 2.008(2), Zn1-O7 2.1072(18) and Zn1-O6 2.2456(18). Atoms labelled with superscripted I correspond to the symmetry element 1-Y+X, X-1 ½1/2 ½

The SBUs of this structure are single six-coordinate zinc(II) ions that bind four oxygen atoms of two bridging $VO(cdacs)^{1-}$ units (via O6 and O7) and two coordinated DMF

molecules (O8), forming a distorted octahedral coordination environment, as shown in Figure 3.4b. $Zn[VO(cdacs)_2(DMF)_2]$ forms into a coordination polymer, as viewed along the *b*-axis in Figure 3.4c, wherein two $VO(cdacs)^{2-}$ ligands are twisted around the Zn atom by 89.19°. $Zn[VO(cdacs)_2(DMF)_2]$ units are repeat parallel to each other to create $Zn[VO(cdacs)_2DMF_2]_n$. Elemental analysis confirmed a formula of $Zn[VO(cdacs)]\cdot 3DMF\cdot 4H_2O$ for this compound.

$Fe(H_2cdacs)Cl$ was reacted with a threefold excess of $Zn(NO_3)_2\cdot 6H_2O$ in a DMF-water solvent mixture with HNO_3 as modulator to give red coloured needle crystals and a powdery phase (Table 3.2, entry 2). To increase crystal formation over the powder, reactions were subsequently performed in a scratched conical flask instead of a reaction tube. This was helpful in increasing the amount of crystals; however, a small amount of powdery material was always observed in the final product. Synchrotron single crystal X-ray crystallography studies showed the red crystals form in the monoclinic space group *C*2/*c* with an asymmetric unit consisting of three $Fe(cdacs)^+$ linkers and three and a half Zn atoms, and could be formulated as $Zn_7(OH)_4[Fe(cdacs)\text{-}\mu\text{-oxido-}Fe(cdacs)]_3$ (Figure 3.5a). In the asymmetric unit, two $Fe(cdacs)^+$ units are connected by a μ_2-oxido atom to form a $[Fe(cdacs)]_2[\mu_2\text{-O}]$ sub-unit. All Fe-Cl bonds have been hydrolysed by water and exist as Fe-O in the structure. The SBU clusters are heptanuclear and crystallise over a centre of inversion, and consist of five ZnO_4 tetrahedra and two ZnO_6 octahedra (Figure 3.5b and c). Four-coordinate Zn1 and Zn4 bind three bridging carboxylate groups of $Fe(cdacs)^+$ linkers and to one μ_3-hydroxido atom in tetrahedral coordination geometries. Zn3 is also four coordinated tetrahedral, binding to two μ_3-hydroxido and two carboxylate ligands. The coordination number and geometry of Zn2 is different; there are three oxygen atoms from three bridging Fe(cdacs) carboxylates and one μ_3-hydroxido atom in equatorial positions. A second μ_3-hydroxido atom and one Fe(cdacs) carboxylate linker are bound in axial positions to complete the octahedral coordination sphere. Six SBU clusters are bridged by six $Fe(cdacs)^+$ metallolinkers into 1D hexagonal channels to create large 1D hexagonal channels of width ca. 28 Å that run along the *c*-axis (Figure 3.5d).

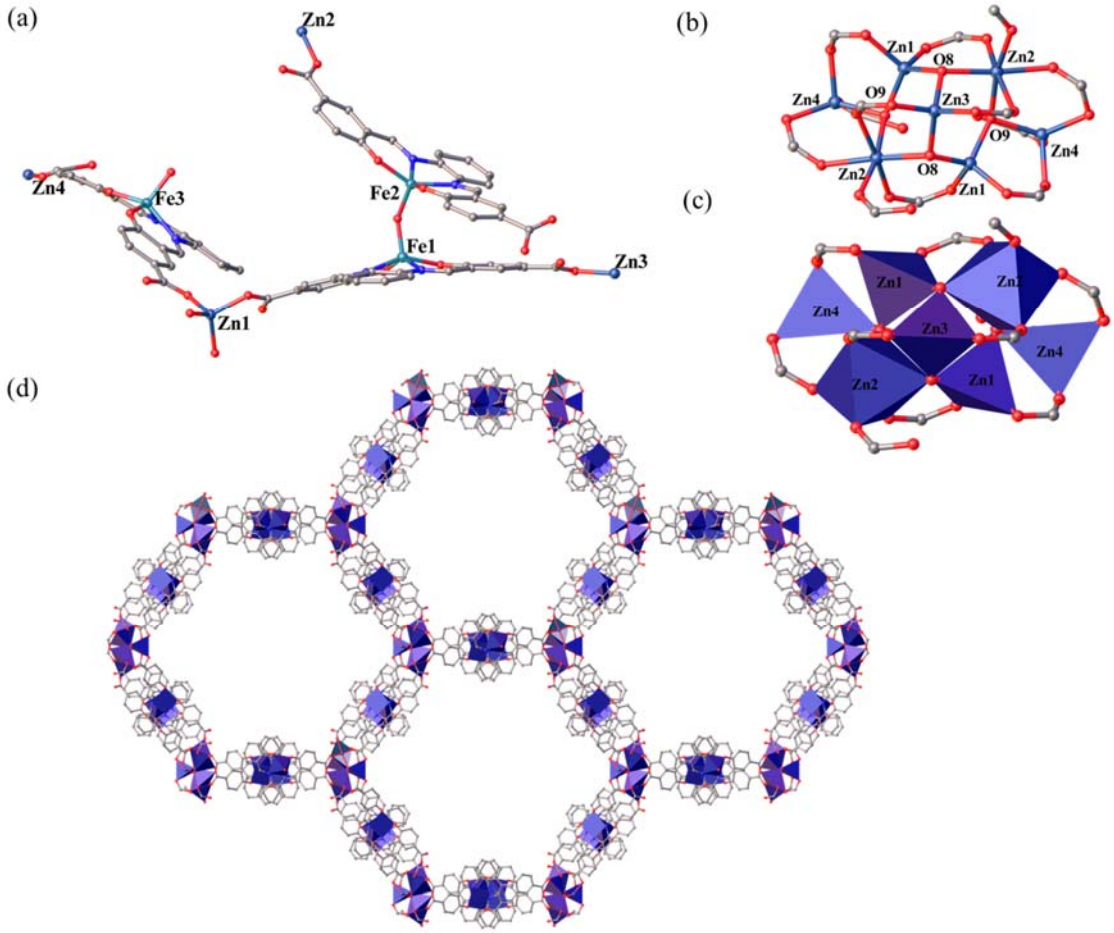

Figure 3.5 (a) The asymmetric unit of $Zn_7(OH)_4[Fe(cdacs)\text{-}\mu\text{-oxido-}Fe(cdacs)]_3$, (b) and (c) the heptanuclear SBU of $Zn_7(OH)_4[Fe(cdacs)\text{-}\mu\text{-oxido-}Fe(cdacs)]_3$ in ball and stick representation and in polyhedral representation, respectively, and (d) perspective view of the expanded structure parallel to the crystallographic *c*-axis. Hydrogen atoms are not shown for clarity.

Crystals formed when $Mn(H_2cdacs)Cl$ was reacted with three equivalents of zinc(II) in a DMF-MeOH solvent system (Table 3.2, entry 3). This procedure largely followed the synthesis described by Lin and co-workers for a MOF with [Ru(*tert*-butyl-salen)$(py)_2$] linkers and $[Zn_4(\mu_4\text{-}O)(O_2C)_6]$ SBUs and a pcu topology.[38] Many attempts to obtain the structure by single crystal X-ray studies were made but were only successful in revealing a cubic unit cell. The experimental PXRD pattern of this framework (discussed in section 3.2.5) indicates that a similar structure to $Zn_4(\mu_4\text{-}O)[(Ru(tert\text{-butyl-salen})(py)_2Cl]_3\cdot(DEF)_{19}\cdot(DMF)_5\cdot(H_2O)_{17}$ MOF may be formed. The elemental analysis

gave the formula of $Zn_4O[Mn(cdacs)Cl]_2 \cdot 6DMF \cdot 5H_2O$ for the framework, which is consistent with the formula for the asymmetric unit for the structure reported by Lin.

Many different synthesis conditions were applied to grow MOF crystals using Ni(H_2cdacs) and Cu(H_2cdacs) metallolinkers, but the formation of crystal was not successful.

Table 3.2 Synthesis conditions to form $Zn[VO(cdacs)_2(DMF)_2]$ and $Zn_7(OH)_4[Fe(cdacs)\text{-}\mu\text{-oxido-}Fe(cdacs)]_3$, $Zn_4O[Mn(cdacs)Cl]_2 \cdot 6DMF \cdot 5H_2O$ from pre-made organic linkers.

Entry	M(H_2cdacs)	Metallosalen : $Zn(NO_3)_2 \cdot 6H_2O$ ratio	Solvent system	Temp. (°C)	Product morphology
1	VO	1 : 2	DMF/H_2O	100	Needles
2	FeCl	1 : 3	DMF/H_2O	100	Needles
3	MnCl	1 : 3	DMF/MeOH	100	Cubic blocks

3.3.4 Synthesis of a multi-metal coordination polymer

One objective of this study was to investigate the rational design of bifunctional frameworks by incorporation of two metallolinkers, and where the resulting material could act as a dual active catalyst for tandem organic transformations. With this goal in mind, VO(H_2cdacs) and Zn(H_2cdacs) were chosen as metallolinkers based on their ability to act as a catalytic transfer oxidant and a Lewis acid, respectively.

The reaction of equimolar proportions of VO(H_2cdacs) and Zn(H_2cdacs) was carried out at 100°C in DMF containing 33% water with two equivalents of $Zn(NO_3)_2 \cdot 6H_2O$. This resulted in a mixture of tiny blue needle crystals and tiny yellow circular disk crystals, in addition to some precipitated material, as observed under an optical microscope. The blue needle crystals showed the same morphology as $Zn[VO(cdacs)_2(DMF)_2]$. However, PXRD of the crystal mixture did not show the presence of this compound. The existence of two morphologies was problematic and due to the tiny size of the crystals, it was difficult to separate them and analyse each to investigate their bulk composition and

structure. Other conditions were investigated while maintaining the DMF-water solvent system to grow a multi-linker framework. The concentration, ratio of ligand to zinc(II), and the temperature were varied but these changes did not yield better results and the presence of a modulator also saw no improvement. Changing the solvents to DEF or DMSO gave no improvements as only precipitates formed. The time and temperature also has a strong effect on growing MOFs and on their morphologies.[39] Therefore, these two parameters were also investigated but with no further improvement.

3.3.5 Powder X-ray diffraction

The recorded PXRD data for cdacs-CPs 1-3 show very similar patterns for all three materials (Figure 3.6a–c), suggesting they all have the same structure. The peaks are very broad and with low relative intensity, indicating the structures are not highly crystalline materials or that they have lost considerable crystallinity in obtaining the PXRD data. An un-indexed intense peak at a 2θ value of 16.32° can be seen in the PXRD pattern of cdacs-CP-2 that is not present in the other samples (Figure 3.6). This could be an impurity in this particular sample or a reflection that is subject to orientational effects. As the structure of the material is not known it is impossible to specify which effect is responsible.

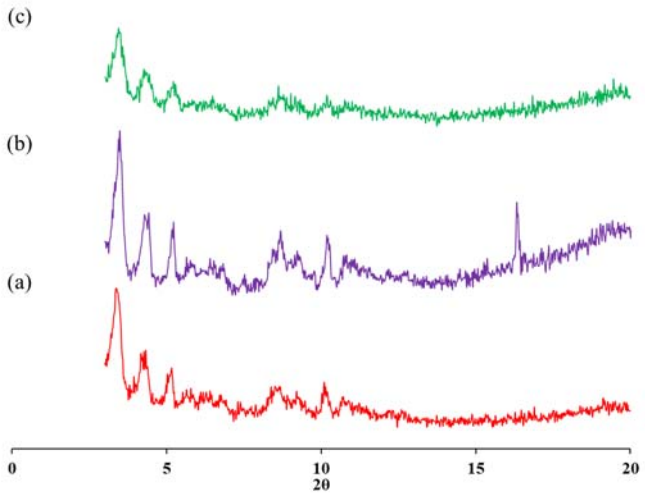

Figure 3.6 PXRD patterns for (a) cdacs-CP-1, (b) cdacs-CP-2 and (c) cdacs-CP-3.

The PXRD pattern of as-synthesised $Zn[VO(cdacs)_2(DMF)_2]$ showed that all but one of the peak positions match between the experimental and the simulated pattern (Figure 3.7a). An un-indexed intense peak at a 2θ value of 5.06° can be observed, which is not seen in the simulated pattern. At this point it is not known why this peak is present. Due to the needle morphology, $Zn[VO(cdacs)_2(DMF)_2]$ may suffer from preferred orientation on the flat plate that was used to collect PXRD data on this sample, and therefore, some difference in intensities compared to the simulated pattern are evident.

The experimental PXRD pattern of $Zn_7(OH)_4$[Fe(cdacs)-μ-oxido-Fe(cdacs)]$_3$ closely matches the theoretical pattern simulated from the SCXRD studies at 2θ values 3.2 ° and 6.04°; however, peak splitting also occurs in the experimental trace, indicating the presence of an additional Zn species or a change of symmetry in the materials. As discussed in section 3.3, the crystals of $Zn_7(OH)_4$[Fe(cdacs)-μ-oxido-Fe(cdacs)]$_3$ showed needle crystals in addition to the formation of a powdery phase. Thus, the peaks at the 2θ values of 11.78° and 12.12° might be as a result of the powder phase

In the experimental PXRD pattern of $Zn_4O[Mn(cdacs)Cl]_2 \cdot 6DMF \cdot 5H_2O$, a degree of crystallinity can be observed. Therefore, the experimental PXRD trace was compared to a trace from a metallosalen-type MOF reported in the literature, and showed it closely matched with the $Zn_4(\mu_4\text{-}O)[(Ru(tert\text{-butyl-salen})(py)_2Cl]_3 \cdot (DEF)_{19} \cdot (DMF)_5 \cdot (H_2O)_{17}$ MOF.[38]

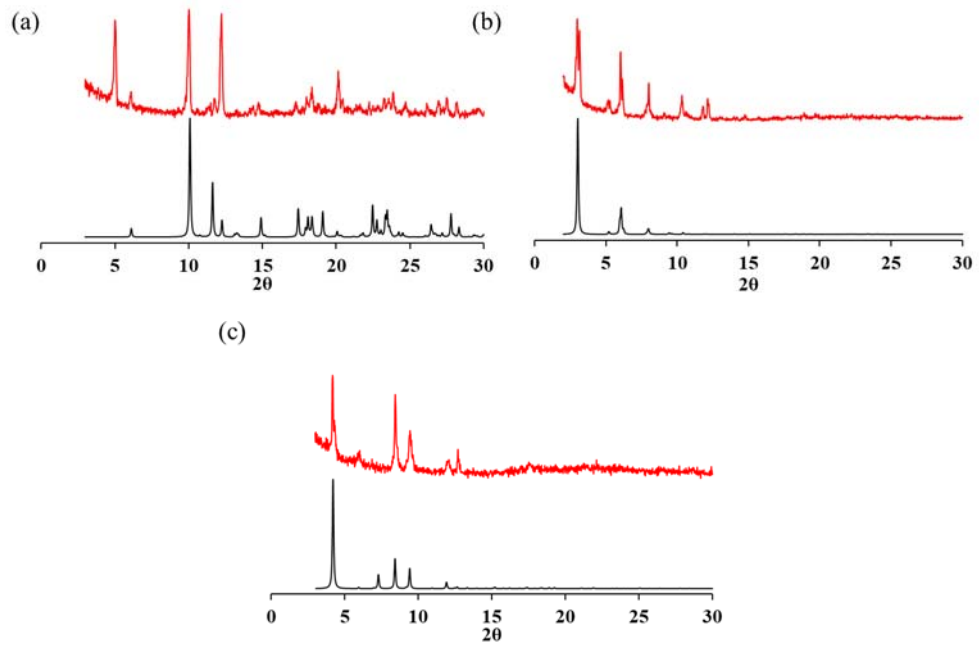

Figure 3.7 PXRD patterns for (a) Zn[VO(cdacs)$_2$(DMF)$_2$], (b) $Zn_7(OH)_4$[Fe(cdacs)-μ-oxido-Fe(cdacs)]$_3$ and (c) $Zn_4O[Mn(cdacs)Cl]_2 \cdot 6DMF \cdot 5H_2O$, simulated (black; bottom); 'as-synthesised' (red; top).

TGA-DTA data for cdacs-CPs 1–3, Zn[VO(cdacs)] DMF, $Zn_7(OH)_4$[Fe(cdacs)-μ-oxido-Fe(cdacs)$_3$ and $Zn_4O[Mn(cdacs)Cl]_2 \cdot 6DMF \cdot 5H_2O$ are presented in Appendix 1, Figure A1.1.

3.4 Conclusion

In the present study, the syntheses of single metallosalen coordination networks were attempted by a one-pot *in situ* metalation to form the Cu(H_2cdacs), Ni(H_2cdacs) and Zn(H_2cdacs) linkers then MOF synthesis and secondly by using a wider range of pre-formed metallosalen complexes. A wide range of synthesis conditions were explored (metal ratios, solvent systems, temperatures, time) with the only success being a copper metallosalen coordination network. Unfortunately, the crystals were unsuitable for crystallography, and therefore, the crystal lattice is undiscovered for this compound.

Pre-metallated salen linkers (VO(H_2cdacs), Mn(H_2cdacs)Cl and Fe(H_2cdacs)Cl) were prepared and used to grow single-metallosalen coordination networks. Single crystal X-ray crystallography revealed the structure of a coordination polymer $Zn[VO(cdacs)_2(DMF)_2]$ and a 3D framework with large ~28 Å 1D pores of $Zn_7(OH)_4[(Fe(cdacs)\text{-}\mu\text{-oxido-}Fe(cdacs)]_3$. The synthesis of this network remains to be optimised to produce sufficient material for further investigation of its porosity. X-ray analysis of Mn(H_2cdacs)Cl was only successful in determining a cubic unit cell for this material. Comparison of the experimental PXRD pattern of this material with similar metallosalen-type MOF reported in the literature showed a good match and based on the elemental analysis result, the framework formulated as $Zn_4O[Mn(cdacs)Cl]_2 \cdot 6DMF \cdot 5H_2O$.

One of the aims of the study was to co-polymerise differently metallated salens into a porous coordination network, which would then have dual active sites suitable for tandem catalysis. The synthesis of a multi vanadium-zinc network was investigated but was ultimately not successful. Although the shape, size, and coordination functionalities of the metallolinkers are similar, the differences toward the synthetic conditions could be problematic in the formation of multi-metal metallosalen structures, and therefore the linkers do not incorporate within one structure. This was also observed by Cui in his study on bimetallic salen-MOF catalysts. This result raises some questions over the generality of this approach or whether this is unique to metallosalens.

3.5 Experimental

3.5.1 Syntheses of complexes

3.5.1.1 Synthesis of VO(H2cdacs)

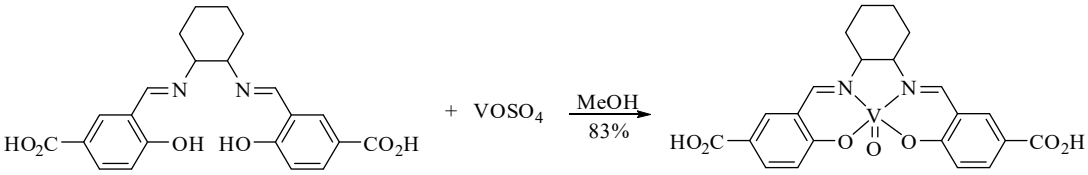

Scheme 3.2 Synthesis of $VO(H_2cdacs)$.

$VOSO_4$ (132 mg, 0.812 mmol) in MeOH (3.5 mL) was added drop wise to H_4cdacs (256 mg, 0.624 mmol) suspended in hot MeOH (17.5 mL) and the reaction mixture was heated with stirring at 60 °C for 5 h. The reaction mixture was cooled to RT and most of the solvent was removed by rotary evaporation and a pink solid was collected by filtration, washed with MeOH and air dried. Yield 0.247 g (83%). m/z (ESI) 474.10 ([M – H]–; $[C_{22}H_{20}N_2O_7V - H]^-$ requires 474.34).

3.5.1.2 Synthesis of Fe(H2cdacs)Cl

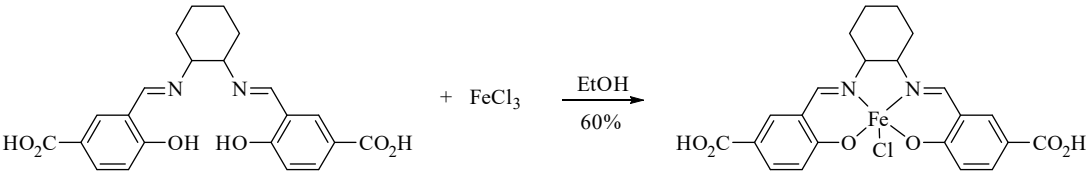

Scheme 3.3 Synthesis of $Fe(H_2cdacs)Cl$.

$FeCl_3$ (81 mg, 0.50 mmol) dissolved in EtOH (10 mL) was added drop wise to H_4cdacs (205 mg, 0.500 mmol) suspended in EtOH (30 mL). The reaction mixture was heated with stirring at 70 °C for 7 h. The reaction mixture was cooled to RT and most of the solvent was removed by rotary evaporation, and then the product was collected by filtration as a red powder, washed with 1:1 EtOH and H_2O and air dried. Yield 0.150 g (60%). m/z (ESI) 464.00 $([M - Cl]^+$; $[C_{22}H_{21}FeN_2O_6 - Cl]^+$ requires 464.26).

3.5.1.3 Synthesis of Mn(H2cdacs)Cl

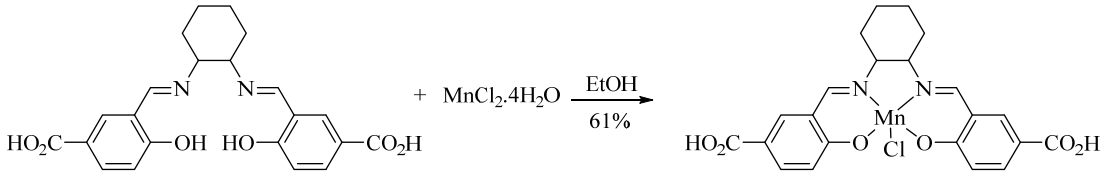

Scheme 3.4 Synthesis of $Mn(H_2cdacs)Cl$.

$MnCl_2 \cdot 4H_2O$ (147 mg, 0.743 mmol) in EtOH (10 mL) was added drop wise to H_4cdacs (205 mg, 0.500 mmol) suspended in EtOH (10 mL) and the reaction mixture was heated with stirring at 70 °C for 7 h. The solvent was removed by rotary evaporation and the residue was diluted with water (30 mL). The green solid was collected by filtration, washed with water and EtOH (1:1) and air dried. Yield 0.151 g (61%). m/z (ESI) 463.00. ($[M - Cl]^-$; $[C_{22}H_{21}MnN_2O_6 - Cl]^-$ requires 463.35).

3.5.1.4 Synthesis of Zn(H2cdacs)

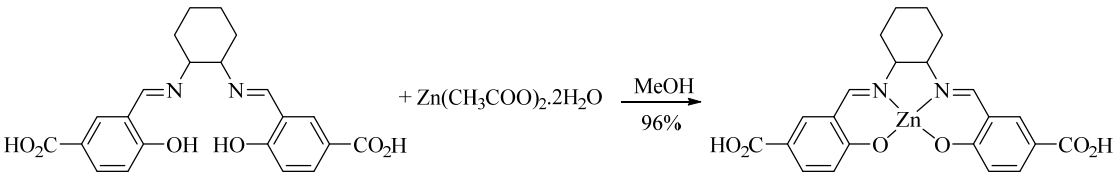

Scheme 3.5 Synthesis of $Zn(H_2cdacs)$.

$Zn(CH_3COO)_2 \cdot 2H_2O$ (219 mg, 1.00 mmol) in MeOH (3.5 mL) was added drop wise to H_4cdacs (256 mg, 0.624 mmol) suspended in hot MeOH (17.5 mL) and the reaction mixture was heated with stirring at 60 °C for 5 h. The reaction mixture was cooled to RT and most of the solvent was removed by rotary evaporation, and then the pale product was collected by filtration as a red powder, washed with MeOH and air dried. Yield 0.283 g (96%). m/z (ESI) 472.00 ($[M - H]^-$; $[C_{22}H_{20}N_2O_6Zn - H]^-$ requires 472.78).

3.5.2 Syntheses of Coordination Networks

3.5.2.1 Synthesis of cdacs-CPs 1-3

$Cu(OAc)_2 \cdot H_2O$ (5.0 mg, 0.010 mmol) and H_4cdacs (5.0 mg, 0.010 mmol) were suspended in dry DMF (1 mL) in a 4 mL vial and the mixture was stirred and heated at 80 °C for 0.5 h. The solution was cooled to RT and $Zn(NO_3)_2 \cdot 6H_2O$ (cdacs-CP-1: 3.7 mg, 0.010 mmol; cdacs-CP-2: 7.3 mg, 0.020 mmol; cdacs-CP-3: 11.0 mg, 0.030 mmol) was added. The reaction mixture was capped and heated at 80 °C for 24 hours. The crystals that formed were washed and stored in fresh DMF. Yield: 2.1 mg (cdacs-CP-1); 1.9 mg (cdacs-CP-2); 2.3 mg (cdacs-CP-3).

3.5.2.2 Synthesis of $Zn[VO(cdacs)_2(DMF)_2]$

$VO(H_2$cdacs) (5.0 mg, 0.010 mmol) and $Zn(NO_3)_2 \cdot 6H_2O$ (5.95 mg, 0.0200 mmol) were suspended in DMF (1 mL) and water (0.5 mL) in a 4 mL vial. 2 M HNO_3 (5 µL, 0.05 mmol) was added to the reaction mixture, and the vial was capped and heated at 100 °C for 24 hours. Needle shaped blue crystals were collected by filtration and washed with dry DMF. Yield 2.3 mg (19%). Found C, 44.29%, H, 5.63%, N, 8.71%. $Zn[VO(cdacs)] \cdot 3DMF \cdot 4H_2O$ requires C, 44.86%, H, 5.71%, N, 8.44%.

3.5.2.3 Synthesis of $Zn_7(OH)_4[Fe(cdacs)$-µ-oxido-$Fe(cdacs)]_3$

$Fe(H_2$cdacs)Cl (5.0 mg, 0.010 mmol) and $Zn(NO_3)_2 \cdot 6H_2O$ (8.9 mg, 0.030 mmol) were suspended in a mixture of dry DMF (1 mL) and water (0.5 mL) in a 4 mL vial. 2 M HNO_3 (5 µL, 0.05 mmol) was then added to the reaction mixture, and the vial was capped and then heated at 100 °C for 24 hours. Small needle-shaped red crystals and a powdery red precipitate were co-harvested before washing with dry DMF. Yield 2.1 mg (37%).

3.5.2.4 Synthesis of $Zn_4O[Mn(cdacs)Cl]_2 \cdot 6DMF \cdot 5H_2O$

$Mn(H_2$cdacs)Cl (5.0 mg, 0.010 mmol) and $Zn(NO_3)_2 \cdot 6H_2O$ (5.95 mg, 0.0200 mmol) were suspended in a mixture of dry DMF (1 mL) and MeOH (0.5 mL) in a 4 mL vial. 2 M HNO_3 (5 µL, 0.05 mmol) was then added to the reaction mixture, and the vial was capped

and heated at 100 °C for 24 hours. Cubic olive green crystals were collected before washing with dry DMF. Yield 1.8 mg (15%). Found C, 40.97%, H, 5.39%, N, 7.71%. $Zn_4O[Mn(cdacs)Cl]_2 \cdot 6DMF \cdot 5H_2O$ requieres C, 41.01%, H, 4.88%, N, 7.71%.

3.5.2.5 Synthesis of multi-metal VO(cdacs)-Zn(cdacs)

$VO(H_2cdacs)$ (2.5 mg, 0.0050 mmol), $Zn(H_2cdacs)$ (2.5 mg, 0.0050 mmol), and $Zn(NO_3)_2 \cdot 6H_2O$ (5.95 mg, 0.0200 mmol) were suspended in DMF (1.5 mL) in a 4 mL vial. 2 M HNO_3 (5 μL, 0.05 mmol) was added to the reaction mixture, and the vial was capped and then heated at 100 °C for 24 hours. The mixture of needle shaped blue crystals and circular disk-shaped yellow crystals were collected by filtration and washed with dry DMF. Yield 1.5 mg

3.6 References

1. Zhang, J., Enhancement of gas sorption and separation performance via ligand functionalization within highly stable zirconium-based metal-organic frameworks. *Crystal Growth & Design 17* (4), 2131-2139.
2. Hassan, H. M. A.; Betiha, M. A.; Mohamed, S. K.; El-Sharkawy, E. A.; Ahmed, E. A., Salen- Zr(IV) complex grafted into amine-tagged MIL-101(Cr) as a robust multifunctional catalyst for biodiesel production and organic transformation reactions. *Applied Surface Science* **2017,** *412*, 394-404.
3. Zhang, W.; Lu, G.; Cui, C.; Liu, Y.; Li, S.; Yan, W.; Xing, C.; Chi, Y. R.; Yang, Y.; Huo, F., A family of metal-organic frameworks exhibiting size-selective catalysis with encapsulated Noble-metal nanoparticles. *Advanced Materials* **2014,** *26* (24), 4056-4060.
4. First, E. L.; Gounaris, C. E.; Floudas, C. A., Predictive framework for shape-selective separations in three-dimensional zeolites and metal-organic frameworks. *Langmuir* **2013,** *29* (18), 5599-5608.
5. Eddaoudi, M.; Kim, J.; Rosi, N.; Vodak, D.; Wachter, J.; O'Keeffe, M.; Yaghi, O. M., Systematic design of pore size and functionality in isoreticular MOFs and their application in methane storage. *Science* **2002,** *295* (5554), 469-472.
6. Liu, T. F.; Feng, D.; Chen, Y. P.; Zou, L.; Bosch, M.; Yuan, S.; Wei, Z.; Fordham, S.; Wang, K.; Zhou, H. C., Topology-guided design and syntheses of highly stable mesoporous porphyrinic zirconium metal-organic frameworks with high surface area. *Journal of the American Chemical Society* **2015,** *137* (1), 413-419.
7. Cmarik, G. E.; Kim, M.; Cohen, S. M.; Walton, K. S., Tuning the adsorption properties of UiO-66 via ligand functionalization. *Langmuir* **2012,** *28* (44), 15606-15613.
8. Pereira, C. F.; Simões, M. M.; Tomé, J. P.; Almeida Paz, F. A., Porphyrin-based metal-organic frameworks as heterogeneous catalysts in oxidation reactions. *Molecules* **2016,** *21* (10).
9. Wang, X.-S.; Ma, S.; Forster, P. M.; Yuan, D.; Eckert, J.; López, J. J.; Murphy, B. J.; Parise, J. B.; Zhou, H.-C., Enhancing H_2 uptake by "close-packing" alignment of open copper sites in metal-organic frameworks. *Angewandte Chemie - International Edition* **2008,** *47* (38), 7263-7266.
10. Zhang, M.; Chen, Y.-P.; Zhou, H.-C., Structural design of porous coordination networks from tetrahedral building units. *CrystEngComm* **2013,** *15* (45), 9544-9552.
11. Mohapatra, B.; Venkatesh, V.; Verma, S., Crystal engineering with 2-aminopurine containing a carboxylic acid pendant. *Crystal Growth & Design* **2014,** *14* (10), 5042-5052.
12. Kalow, J. A.; Doyle, A. G., Mechanistic investigations of cooperative catalysis in the enantioselective fluorination of epoxides. *Journal of the American Chemical Society* **2011,** *133* (40), 16001-16012.
13. Sammis, G. M.; Jacobsen, E. N., Highly enantioselective, catalytic conjugate addition of cyanide to α,β-unsaturated imides. *Journal of the American Chemical Society* **2003,** *125* (15), 4442-4443.
14. Bhunia, A.; Dey, S.; Moreno, J. M.; Diaz, U.; Concepcion, P.; Van Hecke, K.; Janiak, C.; Van Der Voort, P., A homochiral vanadium-salen based cadmium bpdc MOF

with permanent porosity as an asymmetric catalyst in solvent-free cyanosilylation. *Chemical Communications* **2016,** *52* (7), 1401-1404.
15. Xia, Q.; Liu, Y.; Li, Z.; Gong, W.; Cui, Y., A Cr(salen)-based metal-organic framework as a versatile catalyst for efficient asymmetric transformations. *Chemical Communications* **2016,** *52* (89), 13167-13170.
16. Yang, Z.; Zhu, C.; Li, Z.; Liu, Y.; Liu, G.; Cui, Y., Engineering chiral Fe(salen)-based metal-organic frameworks for asymmetric sulfide oxidation. *Chemical Communications* **2014,** *50* (63), 8775-8778.
17. Yuan, G.; Zhu, C.; Liu, Y.; Cui, Y., Nano- and microcrystals of a Mn-based metal-oligomer framework showing size-dependent magnetic resonance behaviors. *Chemical Communications* **2011,** *47* (11), 3180-3182.
18. Das, M. C.; Guo, Q.; He, Y.; Kim, J.; Zhao, C.-G.; Hong, K.; Xiang, S.; Zhang, Z.; Thomas, K. M.; Krishna, R.; Chen, B., Interplay of metalloligand and organic ligand to tune micropores within isostructural mixed-metal organic frameworks (M′MOFs) for their highly selective separation of chiral and achiral small molecules. *Journal of the American Chemical Society* **2012,** *134* (20), 8703-8710.
19. Zhu, C.; Yuan, G.; Chen, X.; Yang, Z.; Cui, Y., Chiral nanoporous metal-metallosalen frameworks for hydrolytic kinetic resolution of epoxides. *Journal of the American Chemical Society* **2012,** *134* (19), 8058-8061.
20. Song, F.; Wang, C.; Falkowski, J. M.; Ma, L.; Lin, W., Isoreticular chiral metal-organic frameworks for asymmetric alkene epoxidation: Tuning catalytic activity by controlling framework catenation and varying open channel sizes. *Journal of the American Chemical Society* **2010,** *132* (43), 15390-15398.
21. Xi, W.; Liu, Y.; Xia, Q.; Li, Z.; Cui, Y., Direct and post-synthesis incorporation of chiral metallosalen catalysts into metal-organic frameworks for asymmetric organic transformations. *Chemistry - A European Journal* **2015,** *21* (36), 12581-12585.
22. Ghorbani-Choghamarani, A.; Shiri, L.; Azadi, G., Preparation and characterization of oxovanadium(IV)-glycine imine immobilized on magnetic nanoparticles and its catalytic application for selective oxidation of sulfides to sulfoxides. *Research on Chemical Intermediates* **2016,** *42* (6), 6049-6060.
23. Wang, Y.; Fan, Y.; Jian, J.; Pan, Y.; Zhao, L.; Jing, X.; Zhou, S.; Chen, X.; Du, Q.; Wang, L.; Wu, X.; Fu, X., Synthesis of chiral salen Mn (III) complex immobilized on phenoxy-modified AlPS-PVPA as catalysts for epoxidation of olefins. *Acta Chimica Sinica* **2017,** *75* (7), 715-722.
24. Khokhar, M. D.; Shukla, R. S.; Jasra, R. V., Selective oxidation of methane by molecular oxygen catalyzed by a bridged binuclear ruthenium complex at moderate pressures and ambient temperature. *Journal of Molecular Catalysis A: Chemical* **2009,** *299* (1), 108-116.
25. Hao, L.; Lu, Y.; He, Z.; Lan, Q.; Wang, E., Synthesis, structure, and characterization of two 1-D homometallic coordination polymers based on carboxylate-functionlized salen ligands. *Journal of Coordination Chemistry* **2015,** *68* (15), 2682-2690.
26. Olivo, G.; Lanzalunga, O.; DiStefano, S., Non-heme lmine-based iron complexes as catalysts for oxidative processes. *Advanced Synthesis & Catalysis* **2016,** *358* (6), 843-863.

27. Azam, M.; Dwivedi, S.; Al-Resayes, S. I.; Adil, S. F.; Islam, M. S.; Trzesowska-Kruszynska, A.; Kruszynski, R.; Lee, D.-U., Cu(II) salen complex with propylene linkage: An efficient catalyst in the formation of CX bonds (X = N, O, S) and biological investigations. *Journal of Molecular Structure* **2017,** *1130*, 122-127.
28. Routaray, A.; Mantri, S.; Nath, N.; Sutar, A. K.; Maharana, T., Nickel(II) complex catalyzed ring-opening polymerization of lactide. *Polyhedron* **2016,** *119*, 335-341.
29. (a) Brunauer, S.; Emmett, P. H.; Teller, E., Adsorption of gases in multimolecular layers. *Journal of the American Chemical Society* **1938,** *60* (2), 309-319; (b) Lang, X.-D.; Yu, Y.-C.; He, L.-N., Zn-salen complexes with multiple hydrogen bonding donor and protic ammonium bromide: Bifunctional catalysts for CO_2 fixation with epoxides at atmospheric pressure. *Journal of Molecular Catalysis A: Chemical* **2016,** *420*, 208-215.
30. Kobayashi, T.; Shimura, T.; Kurita, Y.; Katsumata, Y.; Kezuka, S., Chiral cobalt(II)-salen-catalyzed Michael addition of amines to β-substituted nitroalkenes. *Tetrahedron Letters* **2014,** *55* (17), 2818-2821.
31. Li, J.; Yang, J.; Liu, Y.-Y.; Ma, J.-F., Two heterometalli-organic frameworks composed of iron(III)-salen-based ligands and d^{10} metals: gas sorption and visible-light photocatalytic degradation of 2-chlorophenol. *Chemistry – A European Journal* **2015,** *21* (11), 4413-4421.
32. Galloni, P.; Coletti, A.; Floris, B.; Conte, V., Electrochemical properties of VO salen complexes. *Inorganica Chimica Acta* **2014,** *420* (Supplement C), 144-148.
33. Carter, E.; Fallis, I. A.; Kariuki, B. M.; Morgan, I. R.; Murphy, D. M.; Tatchell, T.; Van Doorslaer, S.; Vinck, E., Structure and pulsed EPR characterization of *N,N′*-bis(5-tert-butylsalicylidene)-1,2-cyclohexanediamino-vanadium(IV) oxide and its adducts with propylene oxide. *Dalton Transactions* **2011,** *40* (28), 7454-7462.
34. Zhao, D.; Timmons, D. J.; Yuan, D.; Zhou, H.-C., Tuning the topology and functionality of metal-organic frameworks by ligand design. *Accounts of Chemical Research* **2011,** *44* (2), 123-133.
35. Zhu, C.; Chen, X.; Yang, Z.; Du, X.; Liu, Y.; Cui, Y., Chiral microporous Ti(salan)-based metal–organic frameworks for asymmetric sulfoxidation. *Chemical Communications* **2013,** *49* (64), 7120-7122.
36. Zhang, T.; Song, F.; Lin, W., Blocking bimolecular activation pathways leads to different regioselectivity in metal-organic framework catalysis. *Chemical Communications* **2012,** *48* (70), 8766-8768.
37. Marshall, R. J.; Hobday, C. L.; Murphie, C. F.; Griffin, S. L.; Morrison, C. A.; Moggach, S. A.; Forgan, R. S., Amino acids as highly efficient modulators for single crystals of zirconium and hafnium metal-organic frameworks. *Journal of Materials Chemistry A* **2016,** *4* (18), 6955-6963.
38. Falkowski, J. M.; Wang, C.; Liu, S.; Lin, W., Actuation of asymmetric cyclopropanation catalysts: Reversible single-crystal to single-crystal reduction of metal-organic frameworks. *Angewandte Chemie - International Edition* **2011,** *50* (37), 8674-8678.
39. Zhang, J.; Bu, X., Temperature dependent charge distribution in three-dimensional homochiral cadmium camphorates. *Chemical Communications* **2008,** *8* (4), 444-446.

Chapter 4

Crystal Engineering of Multi-Metalloporphyrin Metal-Organic Frameworks

4 Introduction

Porphine is a conjugated macrocyclic compound, which upon *meso*-substitution, followed by metalation becomes a porphyrin and metalloporphyrin, respectively (Figure 4.1). Porphyrins and metalloporphyrins have been heavily studied with significant achievements in the field of organic and inorganic chemistry and engineering functional materials.[1] Metalloporphyrins have been widely used in organic synthesis in C-O, C-N, and C-C bond formation reactions.[2, 3] These compounds are also the catalysts in plants and other photosystems due to their photo-physicochemical properties.

The applications and properties of metalloporphyrins are highly developed and it is an enticing prospect to incorporate metalloporphyrins as large square-planar building blocks in well-ordered, chemically stabile, high surface area materials, such as MOFs.[4, 5] Such metalloporphyrin-based MOFs could be utilised for a wide range of applications and play roles in catalysis,[6, 7] photovoltaics[8] and the adsorption of gases.[9, 10]

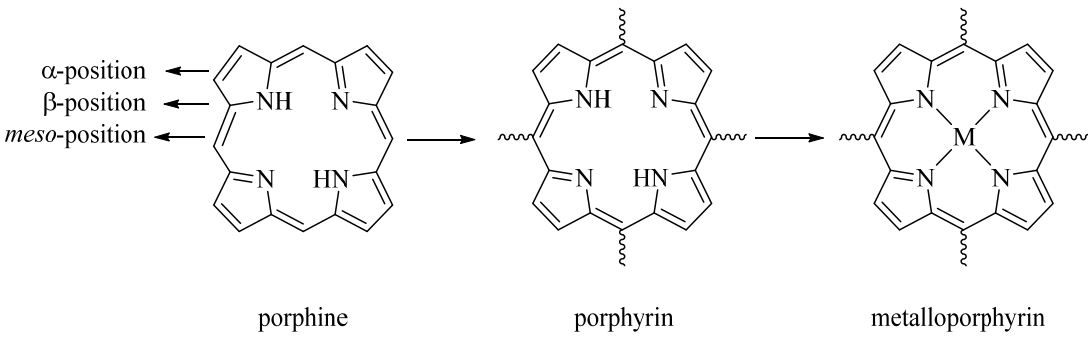

Figure 4.1 Structures of porphine and generalised structures of a porphyrin and a metalloporphyrin.

With the desire to achieve specific arrangements of defined functionality to control the surface properties of MOFs, a crystal engineering approach to construct multi-linker MOFs has attracted attention recently.[11] Mixtures of linkers integrated into a single framework is conceptually an efficient approach to achieve multifunctional MOFs with cooperative properties. Recent success in designing and constructing MOFs using metalloporphyrin organic linkers have been reported in the literature.[12, 13, 14] However, there are few reports regarding the synthesis of multi-porphyrin-linker MOFs.[15]

The first metalloporphyrin MOF was reported by Robson and co-workers in 1991. A palladium-metallated tetrapyridyl porphyrin was incorporated into a 3D framework structure with Cd centres as the metal nodes (Figure 4.2). The structure was the first heterometallic porphyrin framework with different metals in the porphyrin and node.[16] Within a short time, Fleischer reported 1D chain networks with a series of pyridyl-based porphyrins with Zn in both the porphyrin centre and framework node.[17] Further leading studies in this field have been done by Suslick,[18, 19] Goldberg,[20, 21] Hupp,[22, 23] Zhou,[24, 25] Ma[26, 27] and Wu.[9, 28]

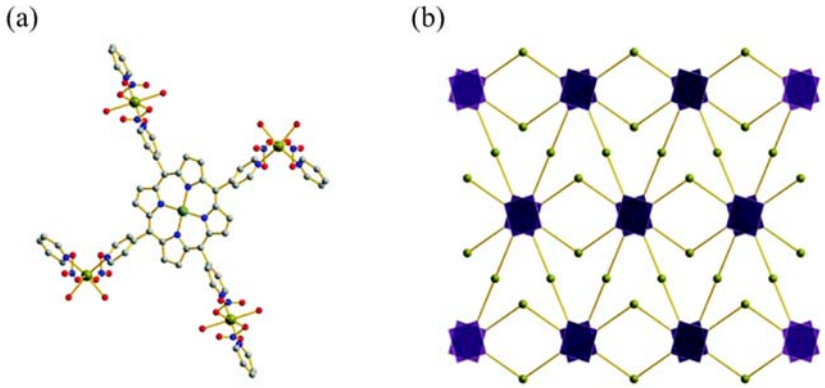

Figure 4.2 A view of (a) the Pd(porphyrin) linker coordinated to the Cd centres, and (b) a schematic view of the 3D framework.[16] Reproduced from Gao, W.-Y.; Chrzanowski, M.; Ma, S. *Chemical Society Reviews* 2014, *43* (16), 5841-5866. with permission from The Royal Society of Chemistry.[29]

4.1 Pillared Porphyrin MOFs

Another approach to the crystal engineering of MOFs is through the implantation of pillars in MOF structures. Conceptually, this enhances the possibility of modifying pore size and potentially increases the porosity in the MOF. However, in some cases, introducing pillars can restrict the accessibility of the pores compared with single linker MOFs.[30] Pillared-porphyrin MOFs have been paid attention recently by different research groups.[31, 32]

Hupp and co-workers reported a crystal engineering study into mixed-metalloporphyrin-linker MOFs, which they termed Robust Porphyrinic Materials (RPMs). By incorporating tetra-(4-carboxyphenyl)porphyrin or its metallated derivatives (M(TCPP), M = 2H, Al, Pd and Fe) and metallated dipyridyl porphyrin ligands (M = 2H and Mn),

six isoreticular RPMs were formed through rational design. It should be noted that the metalloporphyrins act in different structural roles and that their occupancy in the frameworks are crystallography defined. The organic linkers and a representative view of the RPM structure are shown in Figure 4.3a and b and Table 4.1 summarises the combinations of metal centres. Only two RPM frameworks possess different metalloporphrin sites, with one containing Pd/Mn and the other containing Fe/Mn. The catalytic activity of the Mn-RPM MOF was studied for alkene epoxidation and alkane hydroxylation, in which the framework showed very low selectivity.[33]

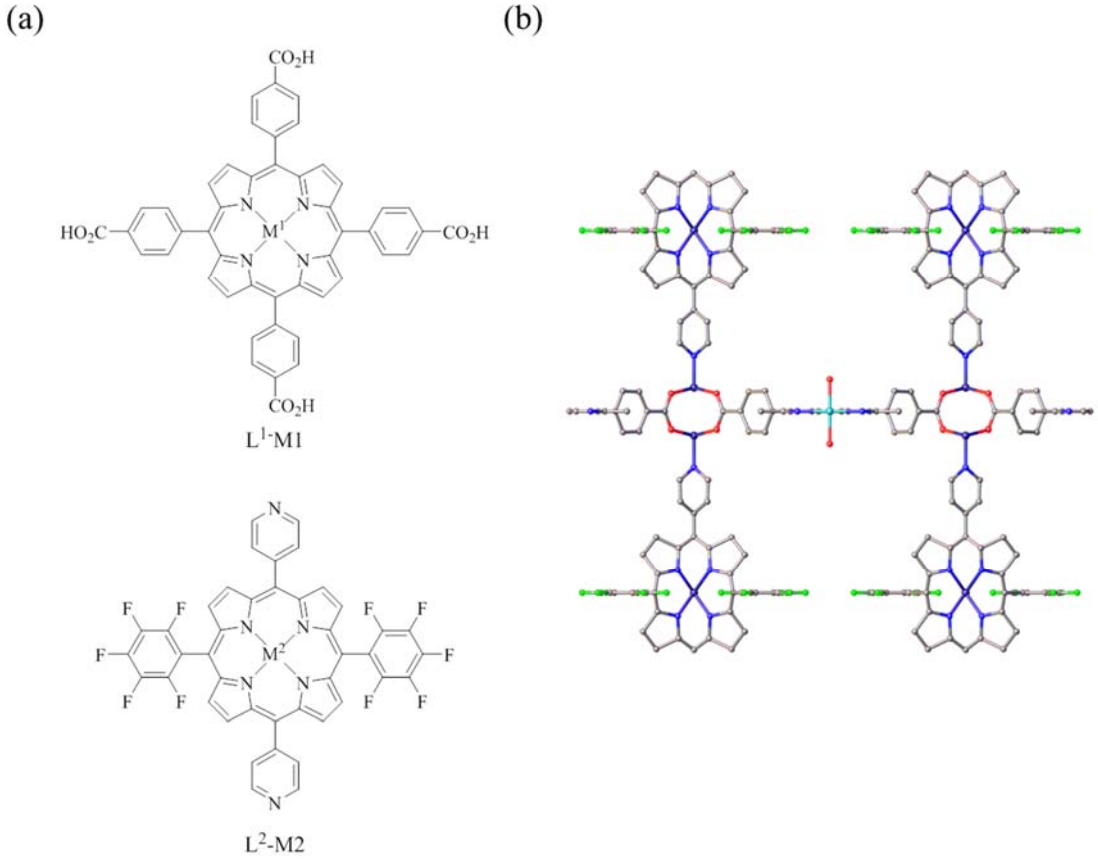

Figure 4.3 (a) The structures of the porphyrin linkers used to construct multi-linker RPMs, and (b) a representative view of the RPM structures.

Table 4.1 The mixtures of metal centres found in the RPMs.

L^1-M^1	L^2-M^2	RPM	Metal(s)
M^1 = 2 H	M^2 = 2 H	ZnZn	No metal
2H	Mn	ZnMn	Mn
Al	2H	AlZn	Al
Pd	Mn	PdMn	Pd and Mn
Fe	2H	FeZn	Fe
Fe	Mn	FeMn	Fe and Mn

Hupp and co-workers also described the synthesis of two porphyrin-pillared MOFs, which they named F-MOF and DA-MOF. As shown in Figure 4.4, F-MOF and DA-MOF were synthesised using 5,15-dipyridyl-10,20-bis(pentafluorophenyl)]porphyrin (F-H_2P) and 5,15-di(4-pyridylethynyl)-10,20-diphenylporphyrin (DA-H_2P) as pillars, respectively, and 1,2,4,5-tetrakis(4-carboxyphenyl)benzene. The MOFs were studied for molecular-exciton migration, in which they were proposed to be efficient components for light-harvesting and energy-transport.[34]

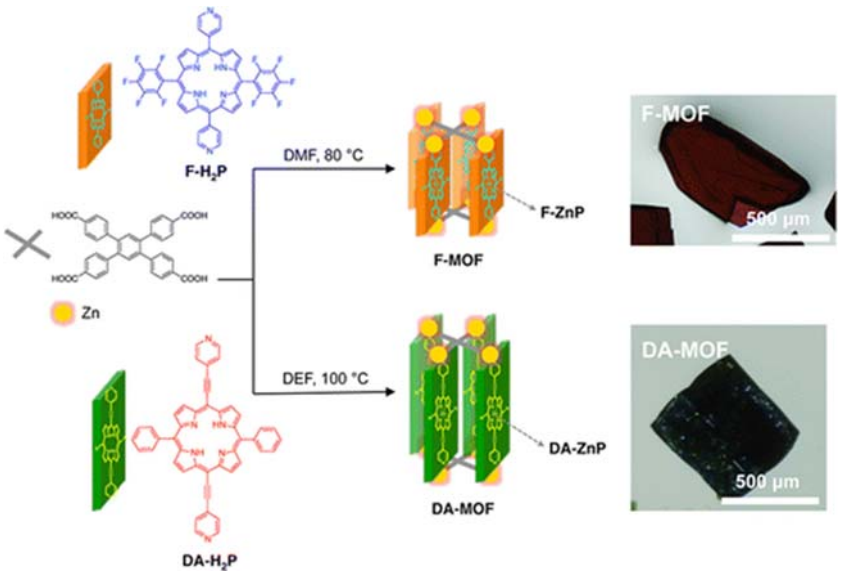

Figure 4.4 Syntheses and schematic topologies of F-MOF and DA-MOF with images of the crystals at right. Adapted with permission from Son, H. J.; Jin, S.; Patwardhan, S.; Wezenberg, S. J.; Jeong, N. C.; So, M.; Wilmer, C. E.; Sarjeant, A. A.; Schatz, G. C.; Snurr, R. Q.; Farha, O. K.; Wiederrecht, G. P.; Hupp, J. T. *Journal of the American Chemical Society* 2013, *135* (2), 862-869. Copyright (2013) American Chemical Society.

Choe and co-workers demonstrated pore surface engineering using bridging bidentate pyridyl-based pillars and metallated tetra-(4-carboxyphenyl) porphyrin linkers [M(TCPP)s] in a series they termed Porphyrin-Paddlewheel Frameworks (PPFs). The team demonstrated the pillars highly influence the pore size and structure dimensionality in these frameworks. The rational design of PPF materials is associated with the well-established propensity of M(TCPP)s and metal paddlewheel [$M_2(CO_2)_4$] building blocks to form 2D sheets. The PPF family of materials are then built up by coordination of M(TCPP) linkers and $M_2(CO_2)_4$ SBUs (M = Zn and Co) in the sheets with various pillaring linkers to make 3D networks. There exist two available sites for the pillars to connect the 2D layers; the axial positions of the paddlewheel clusters and the metal centres of the metalloporphyrins. This leads to three possible stacking patterns of paddlewheel-to-paddlewheel (AA′), paddlewheel-to-porphyrin (AB) and metalloporphyrin-to-metalloporphyrin (BB′) in these pillared-layer MOFs, as displayed in Figure 4.5a–c. In PPF type materials, AA′ and AB stacking patterns were seen, but BB′ connectivity was not observed. BB′ stacking has been reported by Goldberg and co-workers in other porphyrin frameworks.[20]

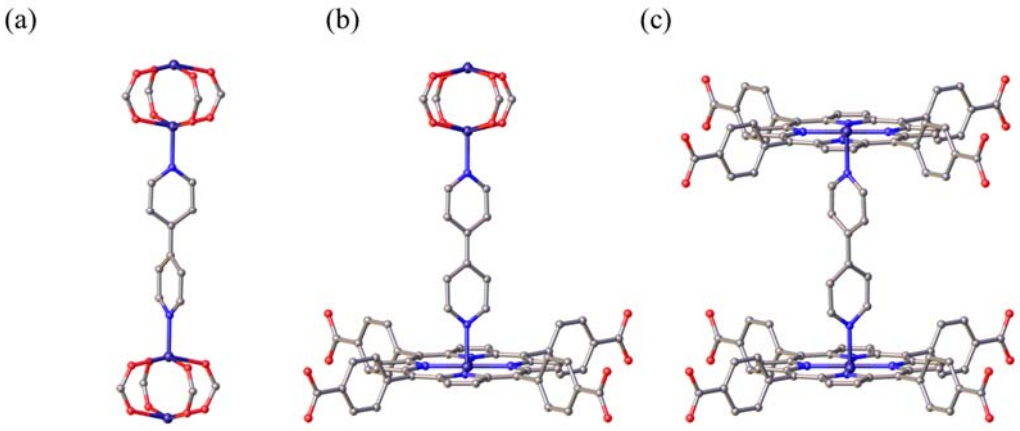

Figure 4.5 Representative views of (a) paddlewheel-to-paddlewheel (AA′), (b) paddlewheel-to-metalloporphyrin (AB) and (c) metalloporphyrin-to-metalloporphyrin (BB′) connections.

PPF-1 is a 2D layered compound from Zn(TCPP) and $Zn_2(CO_2)_4$ and has a **sql** topology.[35] 3D pillared structures were constructed from M(TCPP) linkers with Zn and Co paddlewheel nodes and 4,4'-bipyridine (bpy) as the pillar. The resultant MOFs showed three different stacking patterns and topologies, arising from the coordination

preferences of the metal bound in the porphyrin and presence of pillaring linkers. Thus, the topologies are controlled by the metalloporphyrin linkers. The PPF-3 structure forms with cobalt, manganese and iron metallated TCPPs and has an AB stacking pattern. PPF-4 has an ABBA stacking pattern (M(TCPP); M = Zn) in which bpy pillaring alternates between 2D layers. The PPF-5 structure is formed using metalloporphyrins that have no propensity for axial coordination (M(TCPP); M = VO, Ni, Pt and Pd) and forms with an AA′ stacking pattern where bpy connects only the paddlewheel units. Based on this observation, Choe and co-workers suggested the accessible metal centres in PPF-5 structures could be used for catalytic reactions.[36, 30]

Using a methyl-substituted bpy pillar, some control over PPF framework topology was gained for metalloporphyrins with preference for being six-coordinate (M(TCPP); M = Co, Mn, Fe). The methyl-substituted bpy pillars preferred coordinating to paddlewheel nodes rather than the metalloporphyrin centres for steric reasons, leading to AA′ connections.[32] Changing the length of pillaring ligands gave control over stacking orientation and pore size in the PPF series. Using the longer pillars di(4-pyridyl)tetrazine (DPT) and *N*,*N*′-di-(4-pyridyl)-1,4,5,8-naphthalenetetracarboxydiimide (DPNI) (Figure 4.6) in combination with M(TCPP) linkers gave structures analogous to PPF-4, but with larger pores and AB bilayer stacking patterns, and to PPF-5, but with interpenetration.[37] All PPF structures are summarised in Appendix 2, Table A2.1.

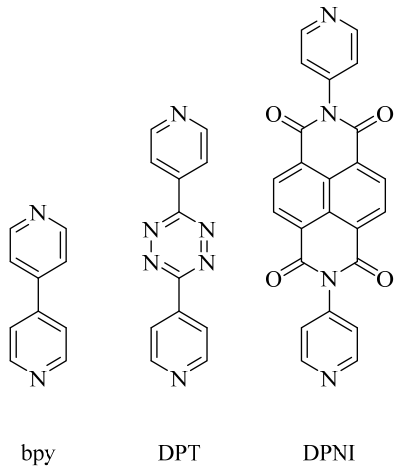

Figure 4.6 Chemical structures of bpy, DPT and DPNI.

4.2 Rationale and Outline

The aim of this chapter was to explore crystal engineering in the relatively underexplored area of multi-metalloporphyrin frameworks. The PPF series was identified as a good target for making complex multi-metalloligand frameworks due its seemingly modular nature. A further aim was to try and engineer porphyrin frameworks having accessible and catalytically active metal centres in the porphyrin units. This meant that PPFs with paddlewheel-to-paddlewheel (AA′) associations were primary targets.

This chapter details an examination of the PPF series in which a number of PPFs were synthesised and structurally and compositionally evaluated in detail by a range of techniques. New members with catalytic potential were discovered. Particular effort was paid to the hybridisation of the PPF-3 and PPF-5 structure types using mixtures of metalloporphyrin linkers. Single and bimetallic PPF-1 compounds were also synthesised and structurally and compositionally evaluated. Metal compositions in bulk samples were analysed by ICP-MS and further characterisation using SEM-EDS was performed to investigate metal compositions of individual crystal faces. The catalytic ability of selected samples was also evaluated in epoxidation reactions.

4.3 Syntheses and characterisation of Pillared Porphyrin Frameworks

4.3.1 Syntheses of metalloporphyrin complexes

5,10,15,20-Tetrakis(4-methoxycarbonylphenyl)porphyrin (H_2TPPCO_2Me) was synthesised using a modified procedure reported by Adler and co-workers where methyl 4-formylbenzoate and pyrrole were added to near-boiling propionic acid and then refluxed for 40 minutes.[38] The product was isolated in 15% yield after filtration, silica gel chromatography and crystallisation.

Metalloporphyrin complexes ($M(TPPCO_2Me)$; where M = Ni, MnCl and Co) were synthesised based on procedures reported by Zhou and co-workers with slight changes (Scheme 4.1).[10] A coloured baseline component that was present after each of the metalation procedures was removed by heating the products in boiling methanol and pure products were recollected by filtration, whereas Zhou used an extractive procedure for purification. The complexes were hydrolysed as described by Zhou (2 M KOH in MeOH/THF) to give Ni(TCPP), Mn(TCPP)Cl and Co(TCPP) in excellent yields.

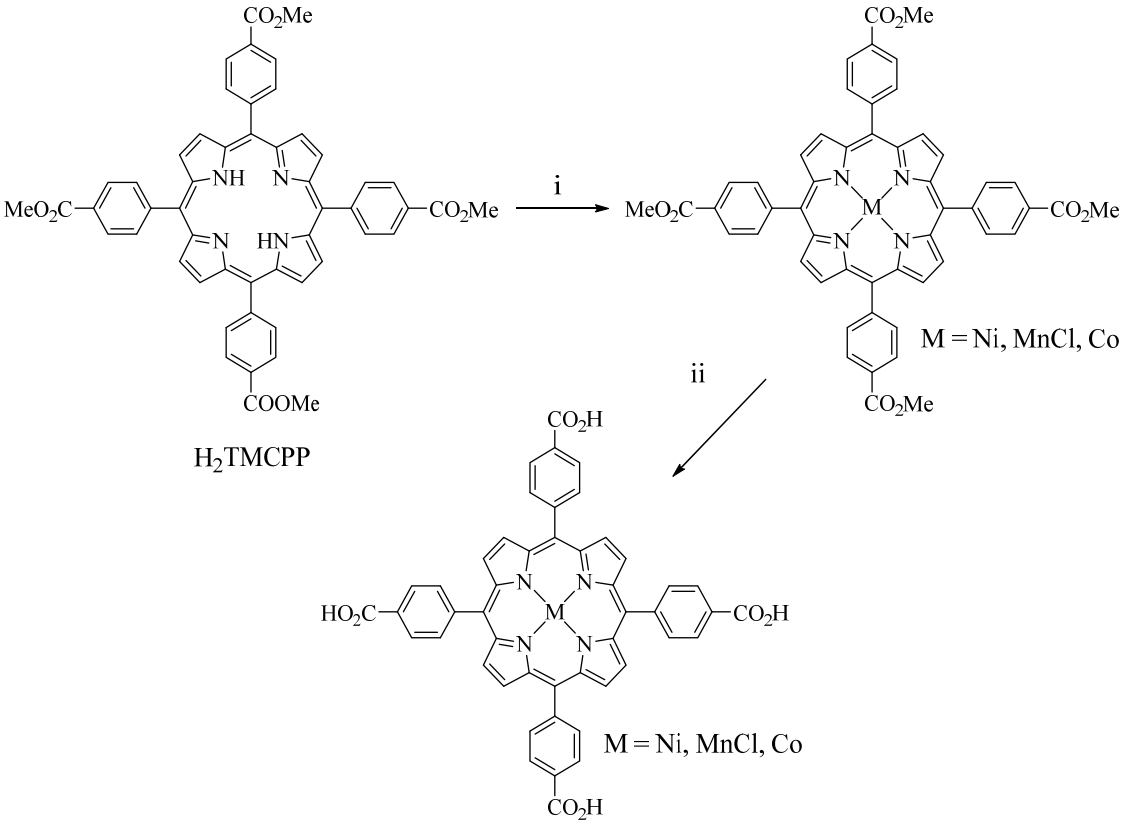

Scheme 4.1 The synthetic path to M(TCPP) complexes, (i) metal salt ($NiCl_2 \cdot 6H_2O$ / $MnCl_2 \cdot 4H_2O$ / $CoCl_2 \cdot 6H_2O$), DMF, reflux, 6 hours, and (ii) 2 M KOH in MeOH/THF, reflux, 12 hours. Yields: Ni(TCPP) (92%), Mn(TCPP)Cl (92%) and Co(TCPP) (94%).

4.3.2 Syntheses and structural description of PPF-1 type MOFs

Crystals of PPF-1(Ni) and PPF-1(MnCl) were synthesised under solvothermal reaction conditions by heating the respective metalloporphyrin linker, Ni(TCPP) or Mn(TCPP)Cl, and $Zn(NO_3)_2 \cdot 6H_2O$ in DEF containing TFA as a modulator at 85 °C for 12 hours. Multi-metal PPF-1(Ni/Mn) was synthesised similarly but using a 1 : 1 ratio of Ni(TCPP) and Mn(TCPP)Cl in the synthesis.

Single crystal X-ray diffraction analyses were carried out on PPF-1(Ni) and PPF-1(Ni/Mn). The structures consist of dizinc paddlewheel SBUs where the axial positions are occupied by water molecules to give $Zn_2(carboxylate)_4(H_2O)_2$ clusters, as shown in Figure 4.7a. The tetratopic metalloporphyrins combine with the paddlewheel clusters to form the expected 2D sheet structure. These were identified as PPF-1 type structures, consistent with those reported by Choe. A representative view of the PPF-1(Ni) structure is shown in Figure 4.7b.

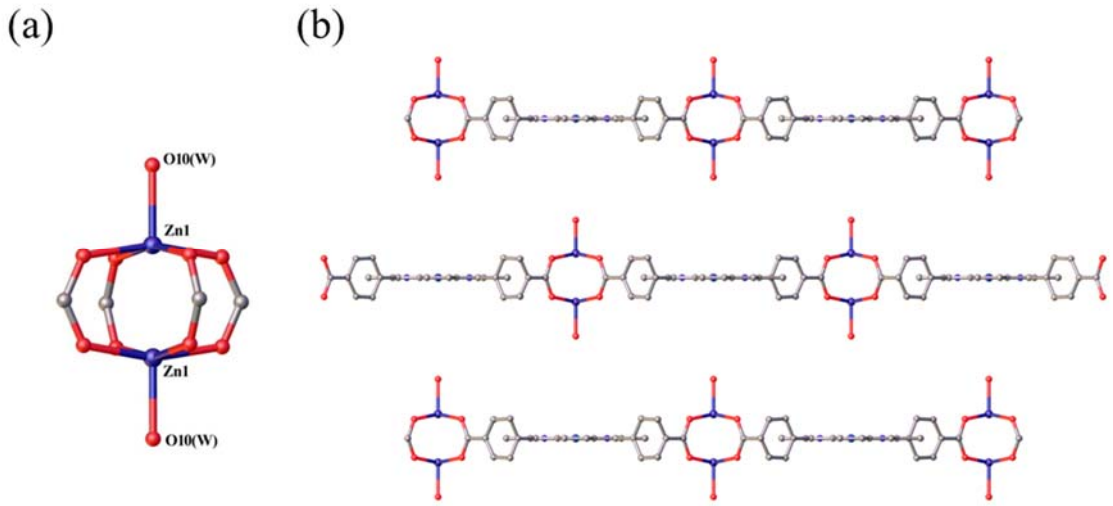

Figure 4.7 (a) Paddlewheel SBU in zinc PPF-1-type MOFs and (b) representative view of the 2D layers of PPF-1 structures, as viewed parallel to the *b*-axis.

Phase purity and crystallinity of all samples were confirmed by powder X-ray diffraction. PXRD was recorded on a quartz plate in Bragg-Brentano geometry (Method 1) and the sample preparation described in 2.2.3 and by using a single crystal X-ray diffractometer with sample rotation around the φ axis (Method 2).

The calculated and experimental PXRD patterns of PPF-1(Ni) and PPF-1(Mn/Ni) are presented in Figure 4.8. The PXRD traces recorded using Method 1, are near identical and show strong preferred orientation (red and purple dotted lines). Major peaks at 2θ values of 9.16° and 18.25° are present but a peak at 7.44° is missing compared to the patterns calculated from the single crystal structures. The miller planes are systematic absences in the PXRD patterns and this is consistent with the observations and data reported by Choe.[35] The plate-like crystal morphology of these samples (see section 4.5.1 for representative SEM images of these samples) often do not arrange completely randomly on the plate and this leads to systematic error in the peak intensities. When these samples were recorded using Method 2, matches to all the calculated peak positions were found (solid red and purple lines). The PXRD pattern of PPF-1(MnCl) recorded using Method 1 showed a degree of crystallinity and evidence of strong preferred orientation, as shown in Figure 4.8 (green, dotted line). PPF-1(MnCl) was positively identified by comparison of the experimental powder pattern with that calculated from the X-ray crystal structures of PPF-1(Ni) and PPF-1(Mn/Ni).

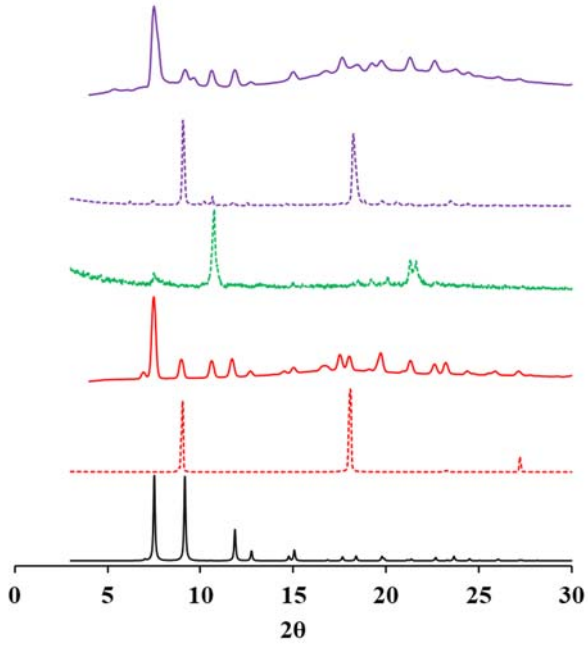

Figure 4.8 Calculated PXRD pattern of PPF-1(Ni) (black), "as-synthesised" PPF-1(Ni) recorded using Method 1 (red dotted line), "as-synthesised" PPF-1(Ni) recorded using Method 2 (red line), PPF-1(MnCl) recorded using Method 1 (green dotted line), "as synthesised" PPF-1(Mn/Ni) recorded using Method 1 (purple dotted line) and "as-synthesised" PPF-1(Mn/Ni) recorded using Method 2 (purple line).

4.3.3 Syntheses and structural description of PPF-5 type MOFs

The synthetic conditions for PPF-5 type structures were very similar to that described above, but now necessarily included bpy as a pillaring ligand. Crystals with square faces were obtained from each of the reaction mixtures and were analysed by single crystal X-ray diffraction.

Pillared single-metalloporphyrin PPF-5(Ni) is a known compound.[30] The X-ray structure determination performed here showed the structure consists of zinc paddlewheel SBUs that are bridged by bpy ligands in the axial positions via AA′ connections (Figure 4.9a). The paddlewheels are linked around their equatorial belts in a 2D layered fashion by the tetratopic porphyrins and as shown in Figure 4.9b, there are large pores of dimension 16.7 × 14.2 Å in the structure that run parallel to the *b*-axis. By virtue of this structures tetragonal space group, the same size pores also run parallel to the crystallographic *a*-axis. Thus, the metal centres in the metalloporphyrin linkers are highly accessible in PPF-5 materials.

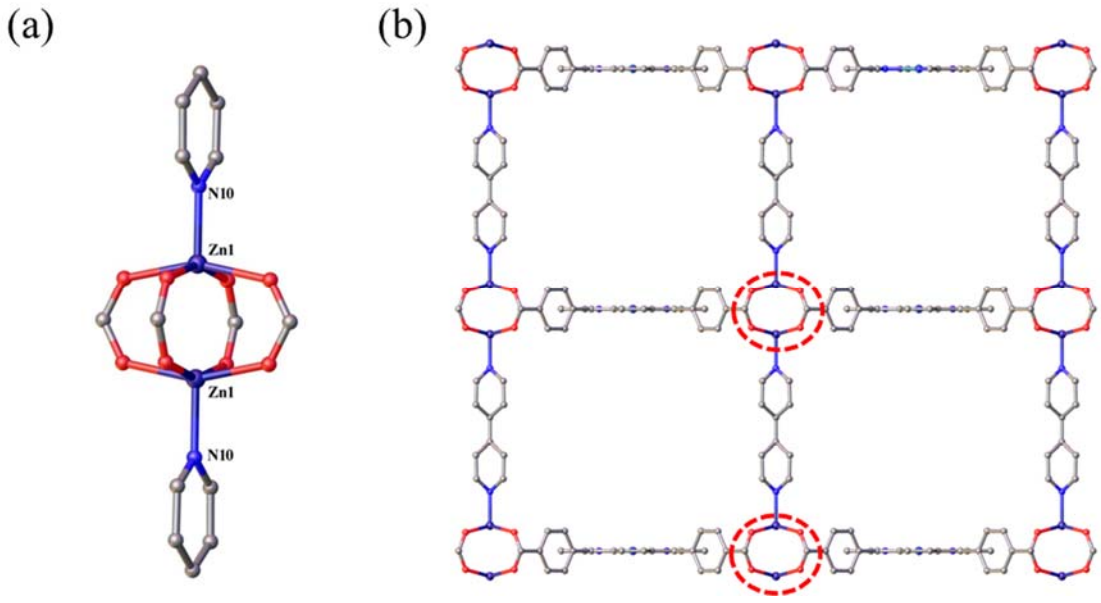

Figure 4.9 (a) Paddlewheel SBUs in zinc PPF-5-type MOFs and (b) representative view parallel to the *b*-axis of PPF-5 with paddlewheel-to-paddlewheel connections circled in red dashes.

PPF-5(Mn/Ni) was made via the standard procedure, starting with equimolar ratios of Ni(TCPP) and Mn(TCPP)Cl in the synthesis. The X-ray studies showed that the material crystallised in the same tetragonal space group as PPF-5(Ni) and with very similar unit cell constants. Thus, the structure is of the PPF-5 type with AA′ connections. This was a significant result as it meant that if Mn atoms were present in the material they would be accessible, and not coordinated by bpy. In most pillared 3D frameworks reported in the literature, there are no accessible metal centres due to coordination of the pillars to the metalloporphyrin. Electron density for a coordinating chloride to the metalloporphyrin metal site, which must be substitutionally occupied by Mn and Ni atoms, was found in the crystallographic analysis. Thus, the PPF-5(Ni/Mn) engineered here has accessible and potentially catalytically active manganese centres.

With this result, the synthesis of PPF-5(MnCl) was attempted using the conditions developed in this work. Choe reported that the reaction of Mn(TCPP)Cl, $Zn(NO_3)_2 \cdot 6H_2O$ and bpy in DMF/MeOH containing HNO_3 as a modulator at 80 °C for 24 hours gave the PPF-3 structure type.[36] The characteristic connection in PPF-3 is AB (metalloporphyrin-to-paddlewheel), which means there are no accessible metal centres as bpy pillars coordinate to all metals in the porphyrin linkers. The single crystal diffraction studies unambiguously identified the product of the reaction under the conditions developed in this work to be PPF-5. Therefore, in this study, a new member of the PPF series, PPF-5(Mn), was successfully engineered from PPF-3 to PPF-5 by manipulation of the reaction conditions. The primary change was a considerably shorter reaction time of 12 hours compared to 24 hours, suggesting PPF-5(Mn) could be a kinetic product.

The calculated and experimental PXRD patterns of PPF-5(Ni), PPF-5(MnCl) and PPF-5(Ni/Mn) recorded using Methods 1 and 2 are shown in Figure 4.10a–c. The traces obtained by Method 2 are very consistent with the calculated patterns in PPF-5(Ni), PPF-5(MnCl) and PPF-5(Ni/Mn), indicating that the samples are phase pure. Strong orientational effects were again observed when Method 1 was used, as major low angle peaks are missing at 2θ values of 5.30°, 7.48° and 9.78°.

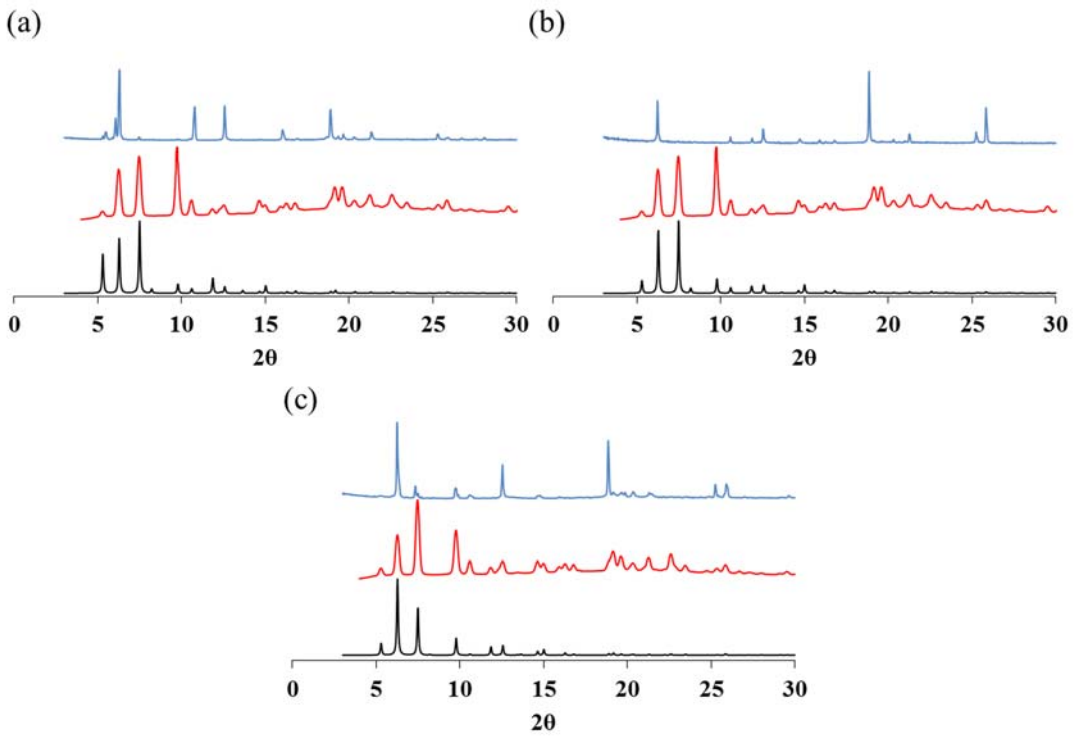

Figure 4.10 PXRD patterns for (a) PPF-5(Ni), (b) PPF-5(MnCl) and (c) PPF-5(Mn/Ni), calculated (black; bottom); Method 2 (red; centre) and Method 1(blue; top).

The asymmetric units of PPF-1(Ni), PPF-5(Ni), PPF-5(MnCl) and PPF-5(Mn/Ni) are presented in Appendix 2, Figure A2.1a–d. Crystallographic data of PPF-5(Ni) and PPF-5(Mn/Ni) are presented in Appendix 2, Table A2.2.

4.3.4 Crystal engineering of multi-metal Co/Ni PPFs

Choe reported that Co(TCPP) forms exclusively the PPF-3 structure type with AB (metalloporphyrin-to-paddlewheel) connections when reacted with bpy and with $Zn(NO_3)_2$ or $Co(NO_3)_2$. This is driven by the strong preference of cobalt ions in porphyrins to be six-coordinate.[36] The conditions of heating Co(TCPP), $Zn(NO_3)_2 \cdot 6H_2O$, bpy, and TFA in DMF at 85 °C for 12 hours were applied here and gave a good yield of crystalline product. Unfortunately, the crystal quality was not good enough for single crystal diffraction studies. PXRD was performed on this sample (*vide infra*) (Figure 4.11, red) and compared with a pattern calculated from the single crystal structure of PPF-3(Co) in the literature (Figure 4.11, black).[36] This unambiguously confirmed the match to the PPF-3 structure type. Like the other MOFs reported here,

strong orientational effects were observed when using a static flat plate in Bragg-Brentano geometry (Figure 4.11, blue). A representative view of the structure of PPF-3 is presented in Figure 4.12 with the metalloporphyrin-to-paddlewheel connection marked on the structure.

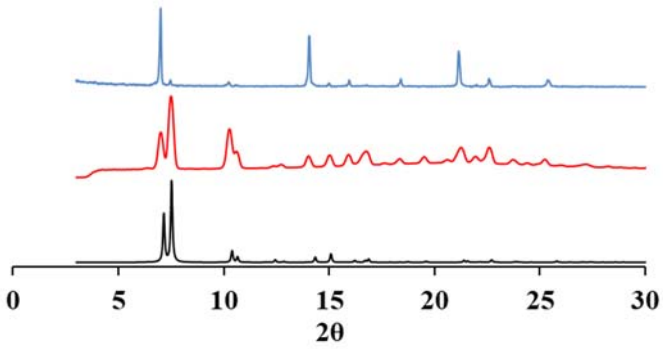

Figure 4.11 PXRD patterns for PPF-3(Co), calculated (black; bottom); Method 2 (red; centre) and Method 1 (blue; top).

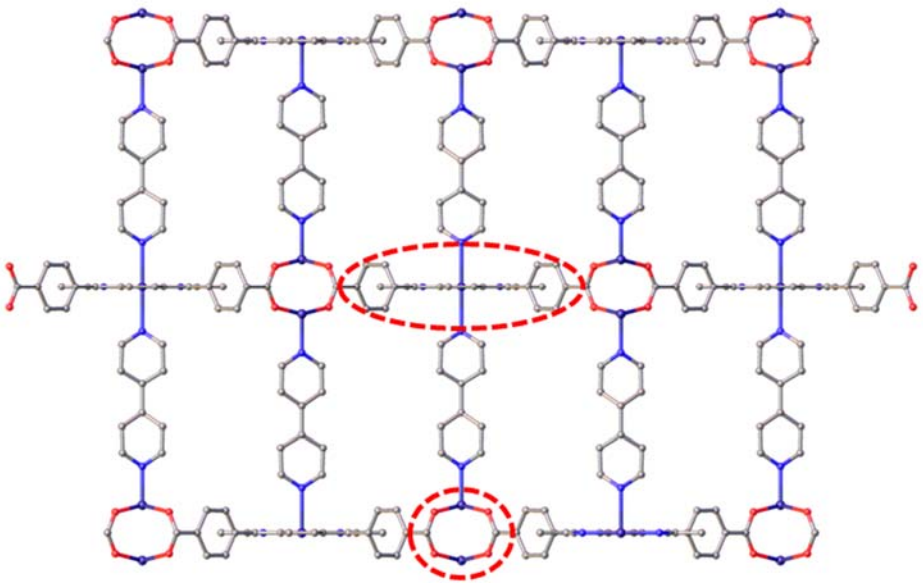

Figure 4.12 A representative view of the structure of PPF-3 along the *b*-axis. A metalloporphyrin-to-paddlewheel connection is circled in red dashes.

It was of considerable interest in this study to investigate the crystal engineering of multi-metal Ni/Co PPFs given that Co(TCPP) forms exclusively the PPF-3 network and Ni(TCPP) forms exclusively PPF-5. Could both Co(TCPP) and Ni(TCPP) be incorporated into a single lattice or would crystallisation occur as separate phases? A series of syntheses were therefore performed with varying mole fractions of Ni(TCPP) and Co(TCPP), as detailed in Table 4.2, under the standard conditions developed in this work.

Table 4.2 The syntheses of Ni/Co PPFs in terms of the ratio of the linkers

Structure	Ni(TCPP) (%)	Co(TCPP) (%)
PPF(0.75Ni/0.25Co)	0.75	0.25
PPF(0.50Ni/0.50Co)	0.50	0.50
PPF(0.25Ni/0.75Co)	0.25	0.75

The multi-metal Ni/Co PPFs were not suitable to study by single crystal X-ray diffraction and were first examined by PXRD. The experimental traces of these samples recorded using Method 2 and the experimental and calculated patterns of PPF-5(Ni), PPF-3(Co) are presented in Figure 4.13. Experimental patterns recorded using Method 1 are provided in Figure A2.2.

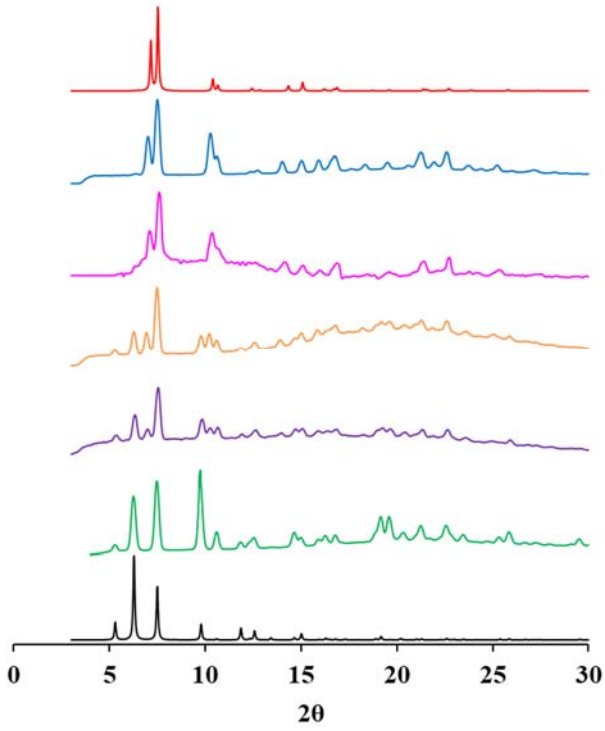

Figure 4.13 Calculated PXRD pattern for PPF-5 (black), experimental trace for PPF-5(Ni) (green), experimental trace for PPF(0.75Ni/0.25Co) (purple), experimental trace for PPF(0.50Ni/0.50Co) (orange), experimental trace for PPF(0.25Ni/0.75Co) (magenta), experimental trace for PPF-3(Co) (blue) and calculated pattern for PPF-3(Co) (red).

A key peak in the powder diffraction pattern of PPF-3(Co) is at 7.02° in 2θ. This peak first features when 25% of Co(TCPP) was introduced into the synthesis and grows in intensity as the feed ratio of Co(TCPP) increases to 50% and to 75%. Indeed, the powder trace of material obtained from a synthesis of equimolar proportions of Co(TCPP) and Ni(TCPP) is predominately PPF-3 in nature. Furthermore, only the presence of PPF-3 is evident in material from the synthesis of 75% Co(TCPP) and 25% Ni(TCPP).

The PXRD studies confirmed the presence of PPF-3 and PPF-5 in the multi-metal PPF samples. The metal contents in the bulk samples and individual crystals needed to be addressed and are discussed in sections 4.4 and 4.5 (*vide infra*).

4.3.5 Coordination environments of M(TCPP) linkers

The coordination environments of the metals in the porphyrins in the PPF-5(Ni), PPF-5(MnCl) and PPF-3(Co) structures are square-planar, square-pyramidal and octahedral, respectively, as shown in Figure 4.14a–c. While the axial position of Mn is occupied by Cl, the axial positions of Co are bonded to nitrogen atoms of bpy pillars. Thus, in PPF-5(Ni) and PPF-5(MnCl) the metal centres are accessible. In PPF-3(Co), the axial positions of the Co centres are occupied by bpy, and therefore there are no open metal sites.

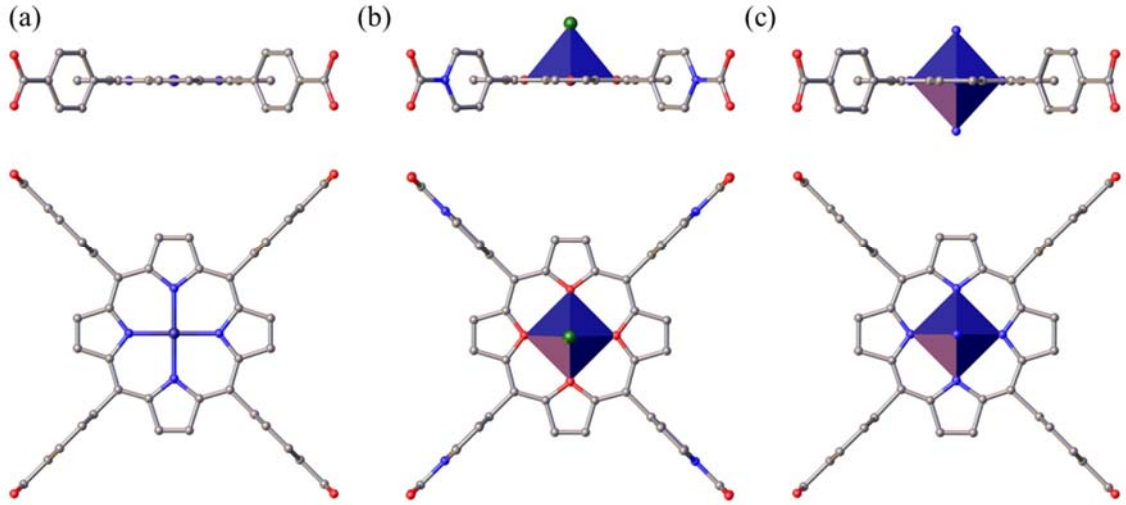

Figure 4.14 Coordination environments of the porphyrin metal centres in (a) PPF-5(Ni), (b) PPF-5(MnCl) and PPF-3(Co).

4.4 Analysis of metal compositions by Inductively Coupled Plasma Mass Spectrometry (ICP-MS)

ICP-MS analysis was performed to determine the metal compositions for the prepared PPFs. Sample preparation involved digestion of the samples in ultrapure 70% HNO_3 at 70 °C for 12 hours with stirring. The digested MOFs were then diluted with Milli Q water and 0.3 M HNO_3 prior to analysis.

The framework formula identified by Choe for PPF-1 and confirmed in this work consists of a paddle wheel node binding two terminal monodentate ligands (often water) and a metallated porphyrin to give the formula Zn_2(MTCPP)$(solv)_2$. In the case of PPF-5, the monodentate ligands are substituted by a bridging bpy ligand, resulting in a framework formula of Zn_2(MTCPP)(bpy). Therefore, for frameworks identified by single crystal and/or PXRD to have PPF-1 or PPF-5 structures, the values for Zn were set to 2.00 in the analysis of the ICP-MS results. This allows for the metals in the porphyrin to be assessed, particularly when mixtures of metalloporphyrins were used in framework synthesis. The results for all samples are presented in Table 4.3.

4.4.1 ICP-MS results of PPF-1 structures

As expected for a PPF-1 type MOF, the ICP-MS analysis gave the ratio of 2.00 : 1.04 for Zn : Ni in PPF-1(Ni), and confirmed this MOFs formulation as $Zn_2[Ni(TCPP)]_1$ (Table 4.3, entry 1). The metal content of PPF-1(MnCl) was in perfect agreement with the expected values for PPF-1 type materials with the ratio of 2.00 : 1.00 for Zn : Mn (Table 4.3, entry 2). In PPF-1(Mn/Ni) the Zn : Mn : Ni ratio was 2.00 : 0.44 : 0.56 and the MOF could be formulated as $Zn_2[Mn(TCPP)]_{0.44}[Ni(TCPP)]_{0.56}$. Notably, the Mn : Ni ratio is very different from the synthetic ratio (0.50 : 0.50), indicating there is considerable selectivity in favour of Ni(TCPP) being incorporated into this structure (Table 4.3, entry 3).

4.4.2 ICP-MS results of PPF-5 structures

The ratio of 2.00 : 1.05 for Zn : Ni was determined for PPF-5(Ni), in line with the expected formulation of $Zn_2[Ni(TCPP)]_1$ (Table 4.3, entry 4). The metal contents in

PPF-5(MnCl) agreed with expected values for PPF-5-type MOFs with ratio of 2.00 and 1.01 for Zn and Mn, respectively, and therefore, the MOF was formulated as $Zn_2[Mn(TCPP)Cl]_1$ (Table 4.3, entry 5). In PPF-5(Mn/Ni), the ratio of Zn : Mn : Ni was 2.00 : 0.40 : 0.45 and this would give the formulation of $Zn_2[Mn(TCPP)Cl]_{0.4}[Ni(TCPP)]_{0.45}$ (Table 4.3, entry 6). What is particularly interesting about this result is that the sum of the metallolinkers (0.85) is far less than that expected for a PPF-5 framework (1.00). Reasons for the lower ratio could be missing linkers and vacancy defects in this MOF.[39] The SC and PXRD of this material clearly support the PPF-5 structure type but these techniques, particularly PXRD, are not sensitive to this kind of lattice defect. The discrepancy is still, however, very large and could be further probed by obtaining the ratio of at least one metalloporphyrin component to bpy in this material. Another interesting point is the preference that is again observed for incorporation of Ni(TCPP) over Mn(TCPP)Cl (0.53 : 0.47, respectively). The Ni(TCPP) linker is incorporated into the framework preferentially over Mn(TCPP)Cl and given the very similar steric profiles of these molecules it is likely this occurs during crystal growth.[39]

4.4.3 ICP-MS results of PPF-3(Co) and PPF(Ni/Co) materials

The ratio determined by ICP-MS for PPF-3(Co) was 2.00 : 0.94 and confirmed the crystallographic ratio of $Zn_2[Co(TCPP)]_1$ (Table 4.3, entry 7). ICP-MS measurements made on the materials synthesised from mixtures of Co(TCPP) and Ni(TCPP) (Table 4.3, entries 8–10) showed there is a higher proportion of cobalt in the final materials than was provided in the synthetic ratio in every case. The magnitude of these changes was large, and is exemplified by the final ratio of 0.36 : 0.64 for the PPF starting from equimolar proportions of Ni(TCPP) and Co(TCPP), respectively. These results show Co(TCPP) is accepted into the framework preferentially over Ni(TCPP). This reinforces the results from PXRD where PPF-3, which is generated from Co(TCPP), is the dominant phase.

The other trend that emerges from the data is the drop in metalloporphyrin content upon greater proportion of Co(TCPP) in the final material. For example, in PPF(0.75Ni/0.25Co), where the dominant phase in PPF-5, the Zn : (Ni+Co) ratio is 2.00

: 0.98, as expected. In PPF(0.50Ni/0.50Co) and PPF(0.25Ni/0.75Co) the dominant phase is PPF-3 and the Zn : (Ni+Co) ratios drop to 2.00 : 0.81 and 2.00 : 0.84, respectively. These missing linkers are again suggestive of crystal defects in these frameworks. The formulations based on the ICP-MS ratios are shown in Table 4.3.

Table 4.3 Linker ratios as determined by ICP-MS and framework formulations of PPFs.

Structure	Metallolinker synthesis ratios			Linker ratios in MOF			Zn to metallolinker(s) ratios (mole%)	Framework formulation
	Mn	Ni	Co	Mn	Ni	Co		
PPF-1(Ni)		1.00					2.00 : 1.04	$Zn_{2.00}[Ni(TCPP)]_{1.04}$
PPF-1(MnCl)	1.00						2.00 : 1.00	$Zn_{2.00}[Mn(TCPP)Cl]$
PPF-1(Mn/Ni)	0.50	0.50		0.44	0.56		2.00 : 1.01	$Zn_{2.00}[Mn(TCPP)]_{0.44}[Ni(TCPP)]_{0.56}$
PPF-5(Ni)		1.00					2.00 : 1.05	$Zn_{2.00}[Ni(TCPP)]_{1.05}$
PPF-5(MnCl)	1.00						2.00 : 1.01	$Zn_{2.00}[Mn(TCPP)Cl]_{1.01}$
PPF-5(Mn/Ni)	0.50	0.50		0.47	0.53		2.00 : 0.85	$Zn_{2.00}[Mn(TCPP)]_{0.40}[Ni(TCPP)]_{0.45}$
PPF-3(Co)			1.00				2.00 : 0.94	$Zn_{2.00}[Co(TCPP)]_{0.94}$
PPF(0.75Ni/0.25Co)		0.75	0.25		0.69	0.31	2.00 : 0.98	$Zn_{2.00}[Ni(TCPP)]_{0.68}[Co(TCPP)]_{0.30}$
PPF(0.50Ni/0.50Co)		0.50	0.50		0.36	0.64	2.00 : 0.81	$Zn_{2.00}[Ni(TCPP)]_{0.39}[Co(TCPP)]_{0.42}$
PPF(0.25Ni/0.75Co)		0.25	0.75		0.19	0.81	2.00 : 0.84	$Zn_{2.00}[Ni(TCPP)]_{0.16}[Co(TCPP)]_{0.68}$

4.5 Scanning Electron Microscopy-Energy Dispersive X-ray Spectroscopy

The ICP-MS technique was used to give an accurate ratio of the metals in bulk samples of the prepared PPFs. Therefore, the PPFs were further characterised using SEM-EDS to determine the compositions and metal distributions within the faces and edges of individual crystals. All samples were solvent exchanged with dry CH_2Cl_2 and dried under vacuum before analysis.

It should be noted that EDS is not a reliable method for quantitative measurements of elements without rigorous standardisation. The EDS method relies on several assumptions related to beam-sample interactions that are affected by surface roughness, density, void fraction and uniformity, among many others. Its strength comes from being able to give good spatial elemental information and it is very useful in this capacity. Here, SEM-EDS analysis was used to confirm the success of the synthesis process by revealing the co-polymerisation of both metallolinkers in individual crystals. This provides evidence that there were not physical mixtures of crystals containing only one metallolinker.

High magnification images were used for close visual inspection of morphology, which can aid the identification of different crystal phases. Selected SEM images are shown in Figures 4.15, 4.16 and 4.17. The EDS was performed on selected spots on the surfaces and edges of the crystals. Representative elemental analyses of three spots were chosen (as indicated with arrows in the images), and summarised in the tables shown beneath the images for each sample.

4.5.1 SEM-EDS studies on PPF-1 structures

PPF-1(Ni) and PPF-1(MnCl) showed very similar crystal morphologies (Figure 4.15a and b). This is unsurprising given the isostructural crystal structures of these MOFs. Crystals of these materials grow as square blocks yet the crystals of PPF-1(Ni) form in considerably larger sizes (25–50 μm) than PPF-1(MnCl) (2–10 μm) under the same synthetic conditions. The SEM studies of PPF-1(Mn/Ni) revealed the formation of square blocks that grow to approximately 25–50 μm in size. Thus, the multi-metalloligand MOF matches more

closely in size the crystals of PPF-1(Ni) (Figure 4.15c). It was found that PPF-1(Mn/Ni) contained considerably more Ni(TCPP) and this has had the effect of growing larger crystals and is consistent with the hypothesis of a kinetic growth mechanism for preferential incorporation of Ni(TCPP).

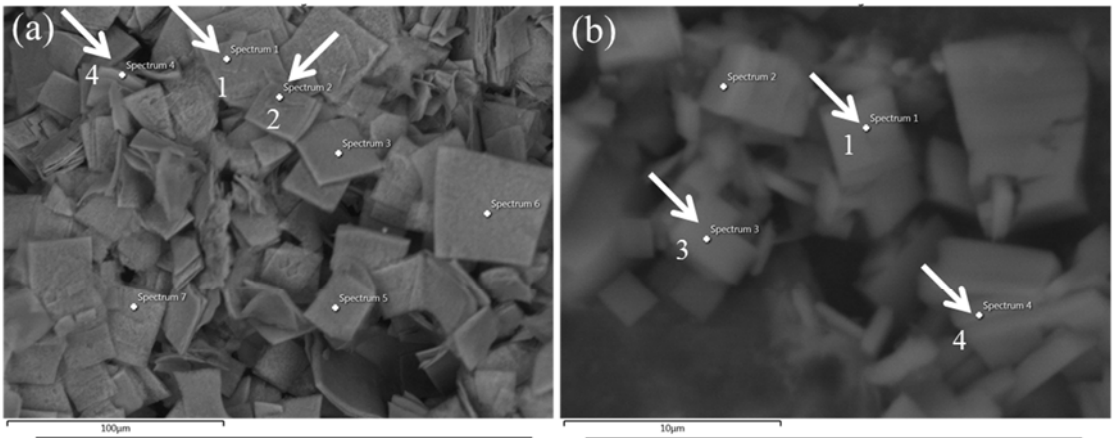

Spectrum Label	Spectrum 1 (wt%)	Spectrum 2 (wt%)	Spectrum 4 (wt%)
Ni	3.67	4.57	4.00
Zn	10.13	9.12	10.28

Spectrum Label	Spectrum 1 (wt%)	Spectrum 3 (wt%)	Spectrum 4 (wt%)
Mn	3.29	2.76	2.44
Zn	6.92	6.85	7.66

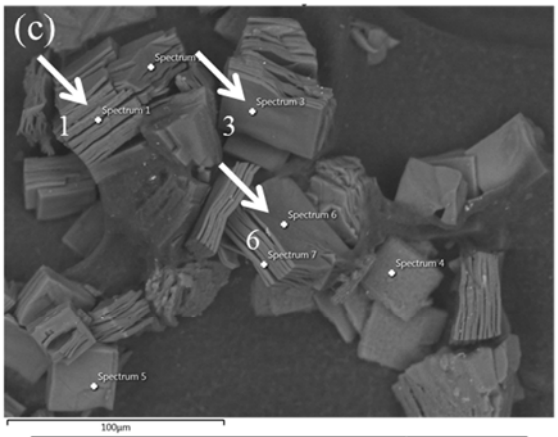

Spectrum Label	Spectrum 1 (wt%)	Spectrum 3 (wt%)	Spectrum 6 (wt%)
Mn	2.55	1.63	1.80
Ni	0.80	3.17	3.85
Zn	6.93	3.43	3.57

Figure 4.15 SEM images including EDS elemental analysis data for selected spots for (a) PPF-1(Ni), (b) PPF-1(MnCl) and (c) PPF-1(Mn/Ni). The elemental analyses of three spots are indicated with arrows.

PPF-1(Ni) showed a uniform distribution of Zn and Ni on crystal surfaces (Figure 4.15a spectra 1 and 2) and on edges (Figure 4.15a, spectrum 4). In PPF-1(MnCl), very similar

proportions of both Mn and Zn were observed in surfaces (Figure 4.15b, spectra 1 and 3) and with slightly more zinc found on crystal edges (Figure 4.15b, spectrum 4). EDS analysis of the surfaces and edges of the PPF-1(Mn/Ni) showed the presence of approximately twice the amount of Ni compared to Mn on the surfaces but Mn was far more abundant than Ni on the edges of the crystals. The ratio of Zn to (Mn+Ni) was lower on the surface (Figure 4.15c, spectra 3 and 6) compared to the edge (Figure 4.15c, spectrum 1).

4.5.2 SEM-EDS studies on PPF-5 structures

The SEM studies of PPF-5(Ni), PPF-5(Mn/Ni) and PPF-5(Mn) (Figure 4.16a–c) revealed very similarly shaped crystals. When viewed from edge on, the square sheets show a lamellar layering and this occurs when the crystals are dried. The crystals are quite uniform in size, in a range of 100–150 μm, for each of the samples.

As was expected, PPF-5(Ni) showed similar Zn : Ni ratios on surfaces and edges (Figure 4.16a). In PPF-5(MnCl), the edges showed a lower ratio of Zn compared to the surfaces (Figure 4.16b). PPF-5(Mn/Ni) crystals showed a consistent distribution of the metals on the crystal faces (Figure 4.16c, spectra 2 and 4), with the average of 0.57 : 0.43 of Mn : Ni, which reflects reasonably well the ratio determined using ICP-MS for the bulk material. This ratio changes somewhat at the lamellar edges of the crystals with a greater proportion of Mn and a lower proportion of Zn (Figure 4.16c, spectrum 6).

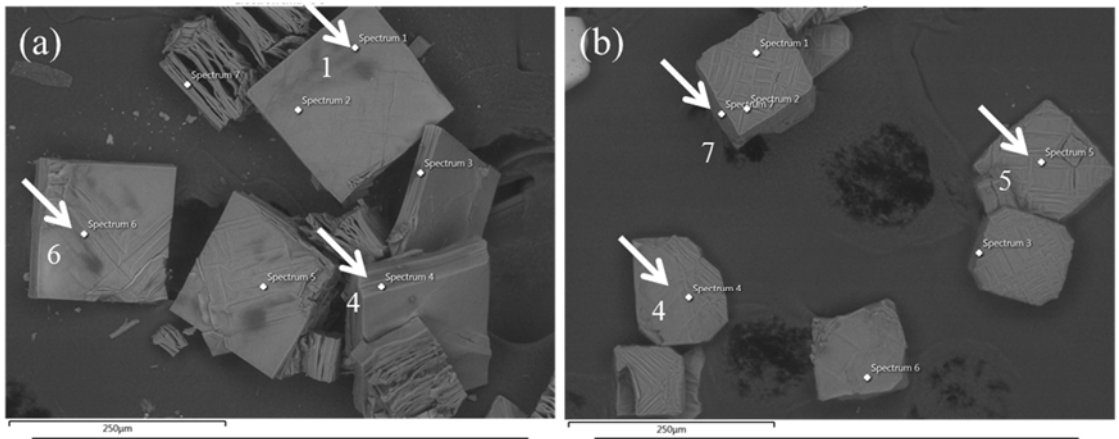

Spectrum Label	Spectrum 1 (wt%)	Spectrum 4 (wt%)	Spectrum 6 (wt%)
Ni	1.88	1.43	2.54
Zn	4.57	4.67	5.44

Spectrum Label	Spectrum 4 (wt%)	Spectrum 5 (wt%)	Spectrum 7 (wt%)
Mn	2.03	2.06	2.68
Zn	6.95	6.99	2.23

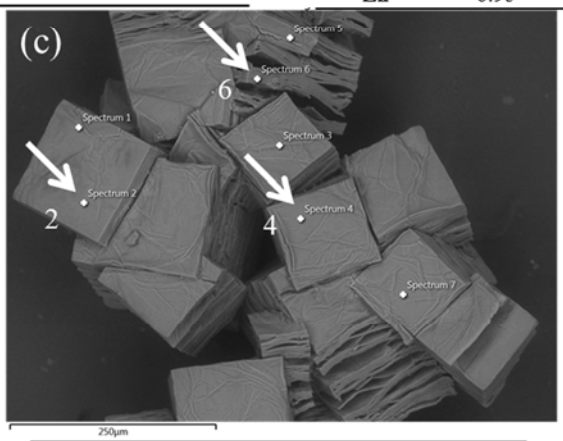

Spectrum Label	Spectrum 2 (wt%)	Spectrum 4 (wt%)	Spectrum 6 (wt%)
Mn	1.35	1.87	3.19
Ni	0.99	1.34	2.73
Zn	8.31	9.18	5.26

Figure 4.16 SEM images including EDS elemental analysis data for three selected spots for (a) PPF-5(Ni), (b) PPF-5(MnCl) and (c) PPF-5(Mn/Ni). The three spots for elemental analyses are indicated with arrows in SEM images.

The SEM images of PPF-5(Ni) and PPF-5(Mn/Ni) showed that they grew in the same morphology. Given that is more likely, in PPF-5(Mn/Ni), the PPF-5(Ni) crystals were formed first and then Mn(TCPP) linkers start to diffuse into the crystals from the surfaces and edges. This hypothesis is supported by EDS results as a higher ratio of Mn was observed at both surfaces and edges.

4.5.3 SEM-EDS studies on PPF-3 and PPF(Ni/Co) materials

Crystals of PPF-3(Co) formed as square and octahedral plates (Figure 4.17a). The latter presumably arising because of crystal growth rates. Compared to the PPF-1 and PPF-5 crystals, the PPF-3 crystals were different in morphology and much smaller in size, with a range of 10–20 μm observed. PPF-3(Co) showed a uniform distribution of Co and Zn at the edges and surfaces, as expected.

The SEM image of PPF(0.75Ni/0.25Co) showed the crystals have a square plate morphology and were approximately 20–30 μm in size (Figure 4.17b). The major phase of this material is PPF-5 and the smaller size of these crystals suggests that the 25% of Co(TCPP) present in the synthesis, retards crystal growth significantly. The EDS analysis at the crystal surfaces showed no Co was present (Figure 4.17b, spectra 2 and 3) and this element only becomes apparent on crystal edges (Figure 4.17b, spectrum 6). This EDS result was not in agreement with the ICP-MS data, as the bulk analysis confirmed the presence of higher proportions of Co than the synthesis feed ratio in all cases. The ratio of Zn : (Ni+Co) was found to have similar proportion on surfaces and edges.

PPF(0.50Ni/0.50Co) and PPF(0.25Ni/0.75Co) crystallised in square plate morphology with approximate sizes of 10–20 μm and 20–30 μm, respectively (Figure 4.17c–d). In both samples the presence of Ni and Co was confirmed by EDS, indicating the successful co-polymerisation of Ni(TCPP) and Co(TCPP) in individual crystals. These results were supported by ICP-MS in the bulk samples. In these materials, the distribution of Zn was very uniform at both surfaces and edges of the crystals.

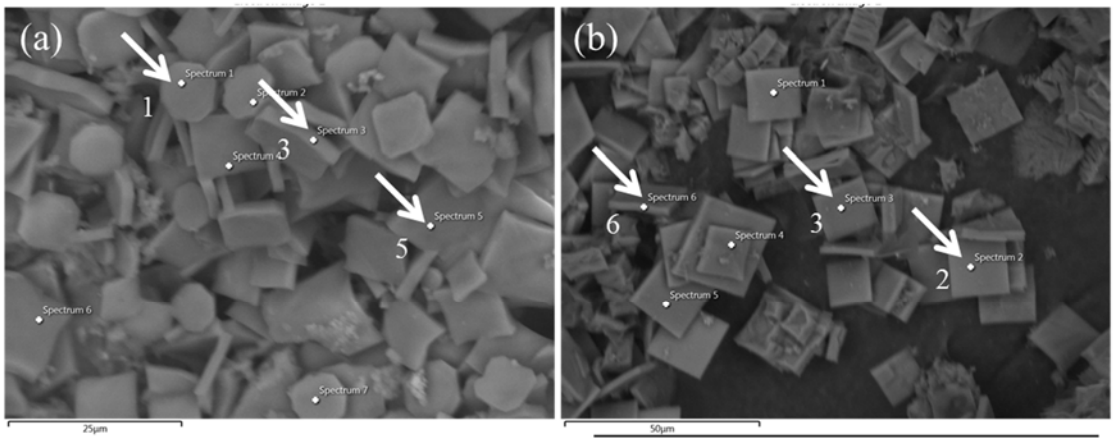

Spectrum Label	Spectrum 1 (wt%)	Spectrum 3 (wt%)	Spectrum 5 (wt%)
Co	2.07	2.36	3.32
Zn	7.91	8.22	6.77

Spectrum Label	Spectrum 2 (wt%)	Spectrum 3 (wt%)	Spectrum 6 (wt%)
Co	--	--	0.32
Ni	2.66	4.39	2.76
Zn	8.68	8.89	9.40

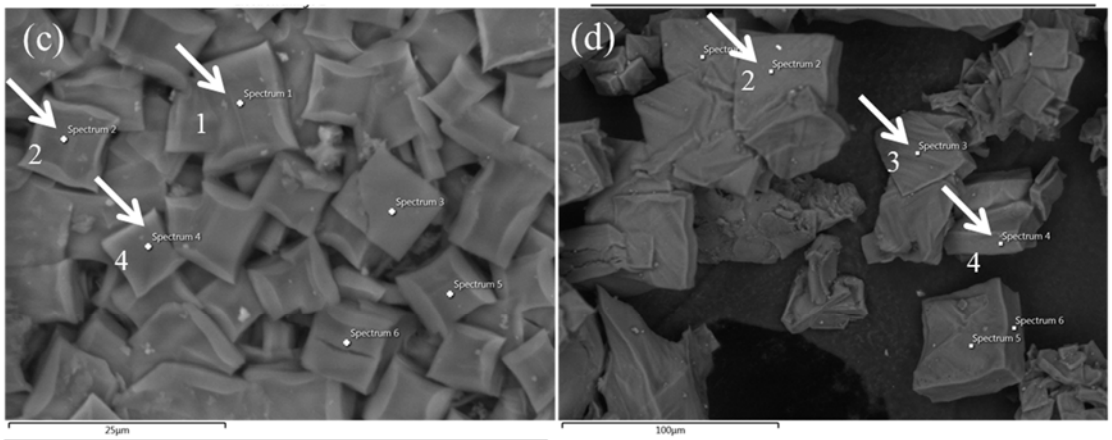

Spectrum Label	Spectrum 1 (wt%)	Spectrum 2 (wt%)	Spectrum 4 (wt%)
Co	2.07	2.47	2.41
Ni	0.93	1.16	1.08
Zn	8.66	8.92	8.83

Spectrum Label	Spectrum 2 (wt%)	Spectrum 3 (wt%)	Spectrum 4 (wt%)
Co	1.37	3.26	1.55
Ni	0.99	1.76	0.91
Zn	7.32	3.81	7.14

Figure 4.17 SEM images including EDS elemental analysis data for three selected spots for (a) PPF-3(Co), (b) PPF(0.75Ni/0.25Co), (c) PPF(0.50Ni/0.50Co) and (d) PPF(0.25Ni/0.75Co).

More SEM images of PPF-1(Ni), PPF-1(Mn), PPF-5(Ni), PPF-5(Mn/Ni), PPF-3(Co), PPF(0.75Ni/0.25Co), PPF(0.50Co/0.50Ni) and PPF(0.25Ni/0.75Co) are presented in Appendix 2, Figure A2.3.

4.6 ^{1}H NMR spectroscopic studies

In order to determine the ratio of bpy in the structures, ^{1}H NMR spectroscopy was employed on crystal samples that had been solvent exchanged with dry CH_2Cl_2, dried under vacuum, and then digested in *d*$_6$-DMSO containing DCl/D_2O. ^{1}H NMR spectra of bpy and the molecular complexes Ni(TCPP), Mn(TCPP)Cl and Co(TCPP) were recorded in *d*$_6$-DMSO for comparative purposes.[36]

The nickel atom in Ni(TCPP) is d^8 and in a square planar coordination environment. Thus, the Ni(TCPP) complex is diamagnetic and sharp signals for this complex can be obtained in ^{1}H NMR spectroscopy. On the other hand, Mn(TCPP)Cl and Co(TCPP) are highly paramagnetic with five and seven *d*-electrons in their square pyramidal and octahedral coordination environments, respectively. The ^{1}H NMR spectra of these complexes show no signals in high field NMR instruments. Therefore, in the ^{1}H NMR analysis, the signals for bpy and Ni(TCPP) were compared. ^{1}H NMR spectra recorded at 60 MHz on a benchtop NMR spectrometer over a spectral window of 400 ppm showed signals for all complexes, but was not satisfactory for accurate integration of signals.

4.6.1 ^{1}H NMR studies on PPF-1 and PPF-5 materials and molecular precursors

The chemical structures of bpy and Ni(TCPP) with their ^{1}H NMR chemical shifts are shown in Figure 4.18a and b. The ^{1}H NMR spectra of Ni(TCPP), bpy, PPF-1(Ni), digested PPF-1(Ni), digested PPF-5(Ni) and digested PPF-5(Mn/Ni) are shown in Figure 4.19a–e.

The ^{1}H NMR spectrum of digested PPF-1(Ni) is identical to Ni(TCPP), indicating the linker incorporated in the MOF is unchanged and there are no other signals. Figure 4.19d shows the NMR spectrum of digested PPF-5(Ni). The signals for Ni(TCPP) are identified by comparison to 4.19a but the signals for bpy (8.50 and 9.11 ppm) show a large downfield chemical shift. This is a result of protonation of bpy by DCl during the digestion procedure and this was confirmed by an independent NMR experiment. By integration of the signals at 8.50 ppm and 8.30 ppm the ratio is approximately 1.00 :

0.92 for bpy : Ni(TCPP) and together with the ICP-MS result confirms the expected formulation of $Zn_2[Ni(TCPP)]_1[bpy]_1$.

Analysis of the ^1H NMR spectrum of digested PPF-5(Mn/Ni) (Figure 4.19e) reveals that the bpy : Ni(TCPP) ratio is approximately 1.00 : 0.59. On the basis that Mn(TCPP)Cl does not contribute to the signals, the ratio of Ni(TCPP) : Mn(TCPP)Cl is therefore approximately 0.59 : 0.41, which is broad agreement with ICP-MS analysis of 0.53 : 0.47.

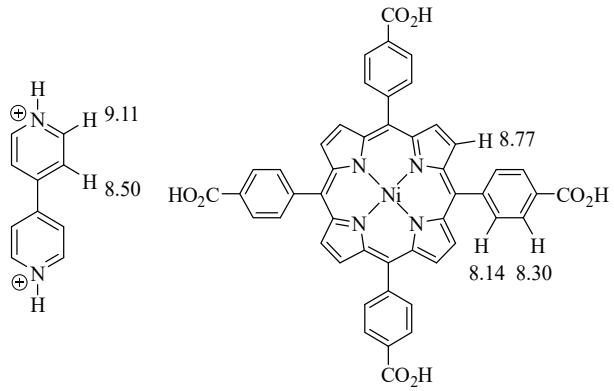

Figure 4.18 The chemical structures of (a) bpy and (b) Ni(TCPP) with their ^1H NMR chemical shifts.

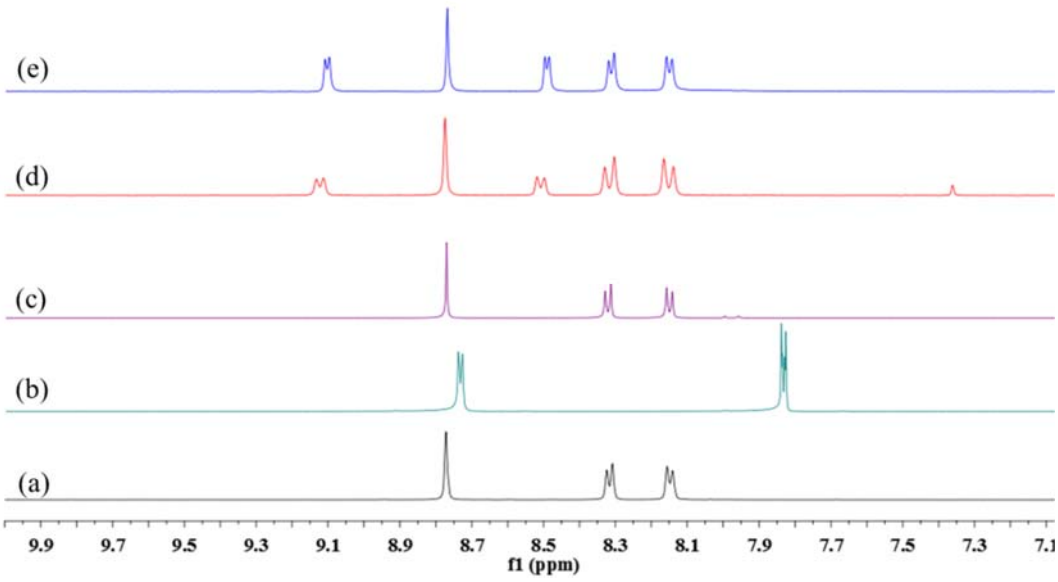

Figure 4.19 ^1H NMR spectra of the aromatic regions of (a) Ni(TCPP), (b) bpy, (c) digested PPF-1(Ni), (d) digested PPF-5(Ni) and (e) digested PPF-5(Mn/Ni).

4.6.2 ^{1}H NMR studies on PPF-3(Co) and mixed PPF(Ni/Co) materials

The PPF-3 structure type has a 2 : 1 ratio of bpy : M(TCPP), which was determined through crystallographic data.[36] As discussed above, the paramagnetic nature of Co(TCPP) did not allow for recording its ^{1}H NMR signals at high field. ^{1}H NMR spectroscopy of digested PPF-3(Co) did show the presence of bpy, with signals at 8.47 and 9.10 ppm. The aromatic ^{1}H NMR regions of PPF(0.75Ni/0.25Co), PPF(0.50Ni/0.50Co), PPF(0.25Ni/0.75Co) and, for comparative purposes, PPF-5(Ni), are shown in Figure 4.20a–d.

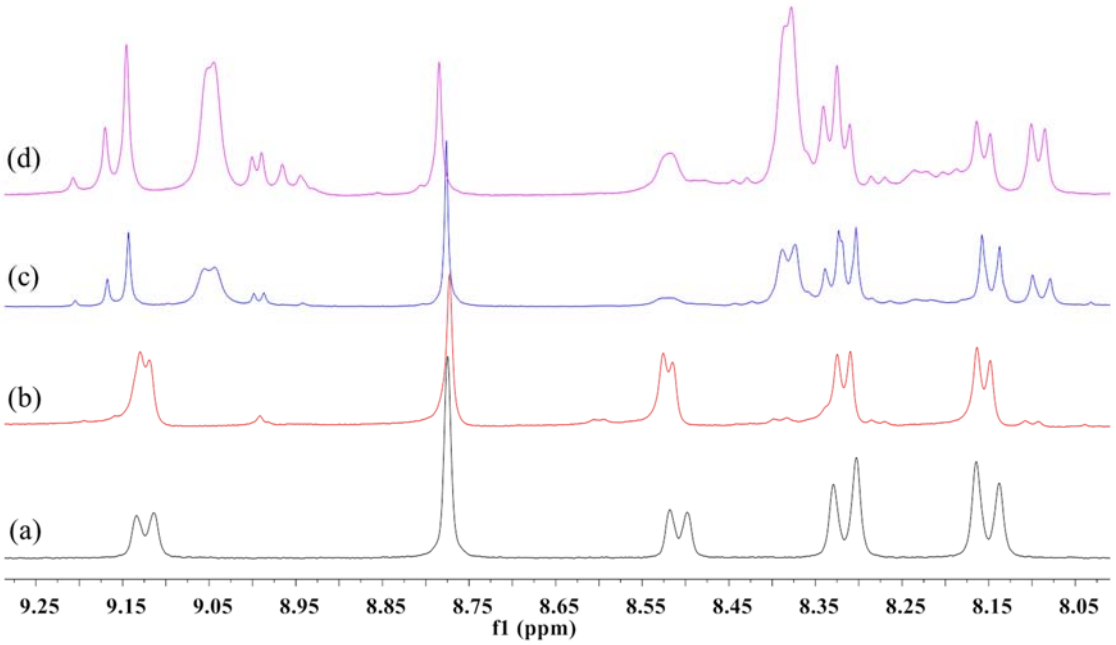

Figure 4.20 ^{1}H NMR spectra of (a) PPF-5(Ni), (b) digested PPF(0.75Ni/0.25Co), (c) digested PPF(0.50Ni/0.50Co) and (d) digested PPF(0.25Ni/0.75Co) after solvent exchange to dry CH_2Cl_2 and vacuum drying.

The ^{1}H NMR spectrum of PPF(0.75Ni/0.25Co) (Figure 4.20b) showed trace amounts of new material with signals at 8.08 ppm and 8.38 ppm in addition to bpy (8.50 ppm and 9.11 ppm) and Ni(TCPP) (8.15 ppm, 8.31 ppm and 8.77 ppm). The signal at 8.08 ppm has a coupling constant that matches signals in the *para*-substituted phenyl rings in TCPP, while the signal at 8.38 has a coupling constant close to that for bpy. The spectrum allowed the ratio of bpy : Ni(TCCP) of 1.00 : 0.56, respectively, to be estimated by peak integration of the signals at 8.50 ppm and 8.31 ppm. The intensity of

these signals increase in the spectra as the proportions of Co(TCPP) increase in the digests of PPF(0.50Ni/0.50Co) and PPF(0.25Ni/0.75Co) (Figure 4.20c and d). These spectra are broad and poorly resolved, most likely because of high proportions of paramagnetic Co^{2+} in the samples. The chemical shift for bpy also changes in 4.20c and d to 8.38 ppm and 9.05 ppm and this may be due to coordination to the cobalt metalloporphyrin centres. It was suspected that the new signals at 8.08 ppm, 8.34 ppm and 9.15 ppm could be a Co^{3+} metalloporphyrin, with oxidation occurring during the acid-based digestion of these materials in air. Complete oxidation of Co^{2+} to Co^{3+} by the addition of hydrogen peroxide to the MOF digests led to ^{1}H NMR spectra of worse quality.

With higher proportions of PPF-3, the proportion of bpy in the corresponding digest should also increase. The ratios of bpy to Ni(TCPP) were calculated by integration of the peaks at 8.15 ppm and 8.38 ppm, and showed the ratios of 1.00 : 0.38 and 1.00 : 0.17 for PPF(0.50Ni/0.50Co) and PPF(0.25Ni/0.75Co), respectively. The low quality of the spectra and the possible presence of Co^{2+} and Co^{3+} in the digests does not allow for comparison with ICP-MS data.

4.7 Structural evaluation of Ni/Co PPFs

Analysis of the ^{1}H NMR spectrum by peak integration of the signals at 8.50 ppm and 8.30 ppm of digested PPF(0.75Ni/0.25Co) reveals that the bpy : Ni(TCPP) ratio is approximately 1.00 : 0.56,. It has been already shown that this MOF is a mixture of the PPF-3 and PPF-5 structure types. As discussed earlier in this section, bpy coordinates between paddlewheel SBUs and Co(TCPP) metallolinkers in the PPF-3 structure, and consequently, compared to PPF-5 type MOFs the presence of more bpy in this structure. As discussed, the PPF-3(Co) structure type has a 2 : 1 ratio of bpy : Co(TCPP), which was identified through crystallographic data.

Taken together, the combined results from PXRD and SEM-EDS, and supported by ICP-MS and ^{1}H NMR spectroscopy, strongly support the presence of regions of PPF-3 and PPF-5 structures in the same lattice of individual crystals. Figure 4.21 is a suggested structure for the multi-metal Ni/Co PPFs. The presence of Co(TCPP) in the structures, leads to coordination of bpy to the Co(TCPP) centre and formation of heterogeneous AB stacking pattern within the framework.

Based on the suggested structure for multi-metal PPF(Ni/Co) MOFs, there would exist different coordination numbers for cobalt. As shown in Figure 4.21, there are paddlewheel-to-paddlewheel (AA′) and paddlewheel-to-porphyrin (AB) connections for Ni(TCPP) and Co(TCPP) linkers, respectively. As can be seen, other types of connections exist in this structure. Where Co(TCPP) and Ni(TCPP) are bridged within one framework, bpy may not be coordinated or just one bpy can be coordinated to the Co centres.

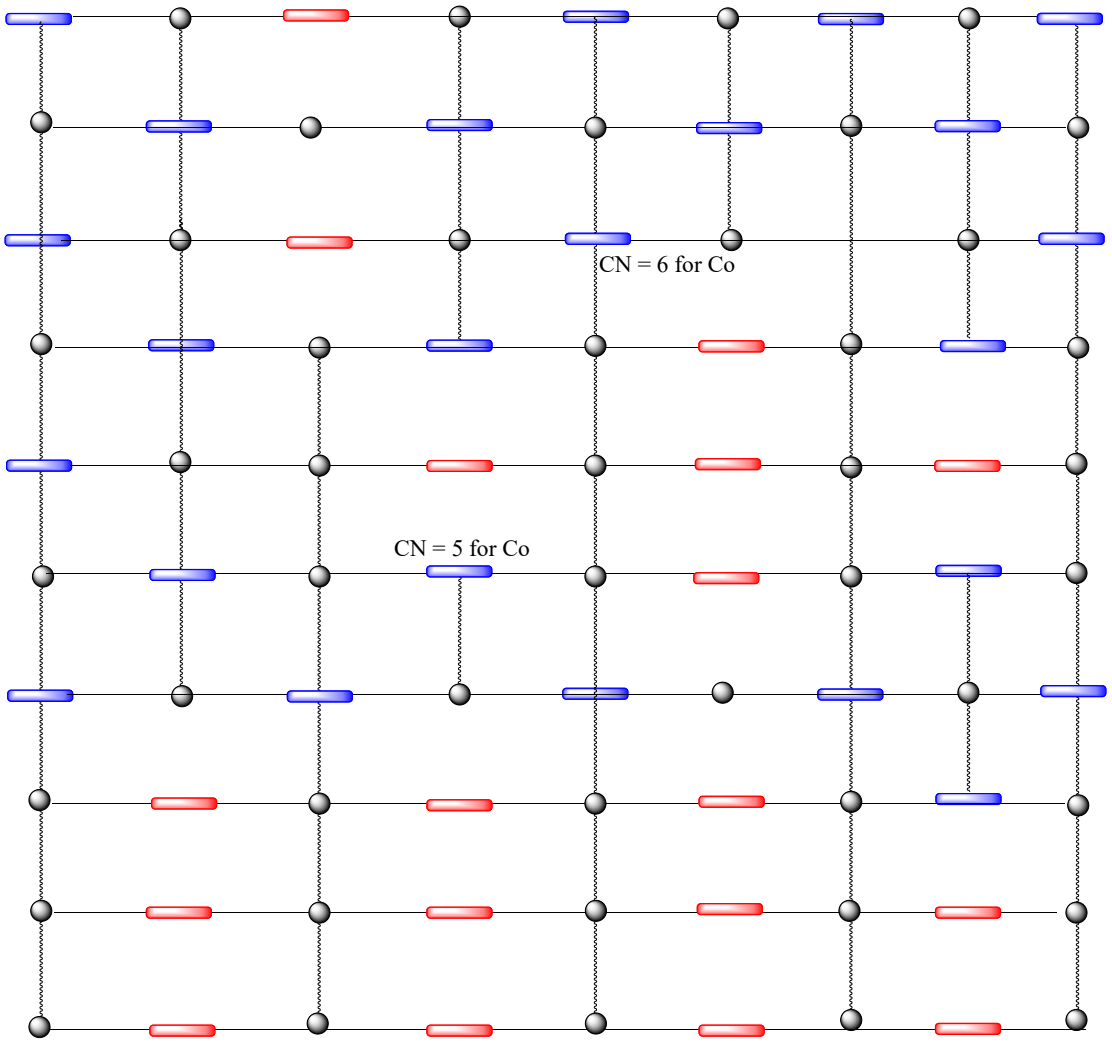

Figure 4.21 A suggested structure of multi-metal PPF(Ni/Co) materials with regions of PPF-5 and PPF-3 structures in a single lattice. Bpy pillars are represented by wavy lines, paddle wheels are presented by black rounds and Ni(TCPP) and Co(TCPP) linkers are in red and blue, respectively. CN stands for coordination number.

4.8 Catalytic activity of PPF-5(MnCl) and PPF-5(Mn/Ni)

PPF-5(MnCl) and PPF-5(Mn/Ni) were chosen to test their activity in the epoxidation of styrene.

A series of control experiments with Mn(TPPCO$_2$Me)Cl, Ni(TPPCO$_2$Me) and a 1 : 1 mixture of Mn(TPPCO$_2$Me)Cl : Ni(TPPCO$_2$Me) were performed under conditions similar to those described by the group of Wu[40] who used styrene as the substrate (1 eq.) and iodosylbenzene (PhIO)[41] as the terminal oxidant (1.5 eq.) and 5 mol% catalyst loading in acetonitrile or CH_2Cl_2 solutions at ambient temperature. The reactions carried out as part of this work, were monitored using GC-MS and full conversions to styrene epoxide were reached in 30 minutes for Mn(TPPCO$_2$Me)Cl and the 1 : 1 ratio of Mn(TPPCO$_2$Me)Cl : Ni(TPPCO$_2$Me) in CH_2Cl_2 solutions, but were incomplete in acetonitrile after 4 hours. No conversion to styrene epoxide was observed after 4 hours for Ni(TPPCO$_2$Me) in either solvent, confirming, as expected, this is inactive as an oxygen transfer catalyst.

The conditions developed for the homogeneous reactions in CH_2Cl_2 were used for PPF-5(Ni) and PPF-5(Mn/Ni) with 1,2,4,5-tetramethylbenzene (1 eq.) as an internal standard to enable conversion, selectivity and yield calculations. Aliquots were taken, filtered and diluted for GC-MS analysis at 0.16, 0.33, 0.5, 1, 1.5, 2, 4 and 24 hours. The kinetic traces are shown in Figure 4.22a and b and final results summarised in Table 4.4.

There is a very long induction period over the first two hours, with very little conversion to styrene epoxide observed in each reaction. Styrene epoxide formation then accelerates and 27% and 15% conversions are observed at the 4 hour mark and these rise to 77% and 72% at 24 hours for PPF-5(MnCl) and PPF-5(Mn/Ni), respectively. The slightly lower conversion of PPF-5(Mn/Ni) is likely related to the lower content of Mn in this material. Interestingly, significant proportions of 2-phenylacetaldehyde were detected in the reaction mixtures at 24 hours and this is a known conversion of styrene epoxide that is catalysed by Lewis acids.[42]

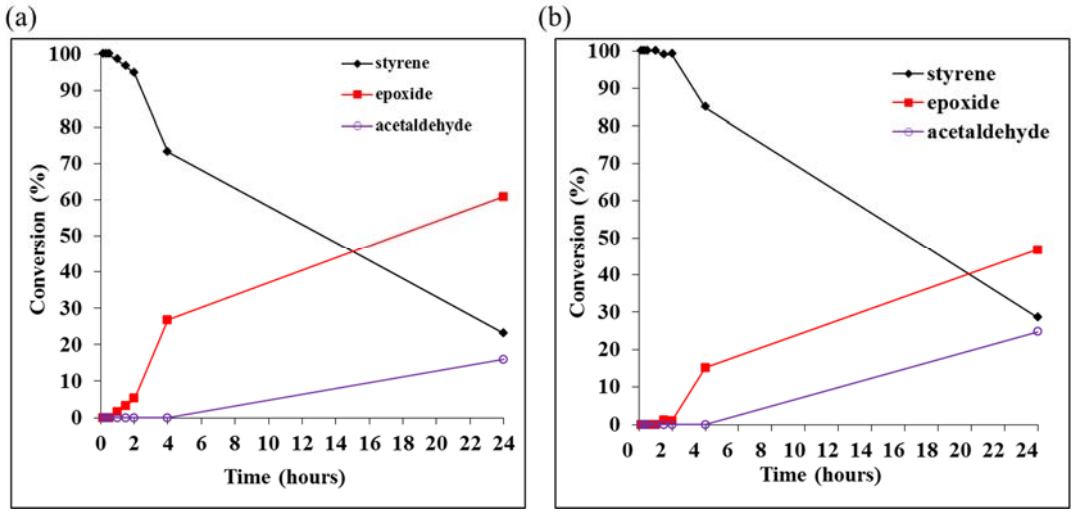

Figure 4.22 Kinetic traces of styrene epoxidation catalysed by (a) PPF-5(MnCl) and (b) PPF-5(Mn/Ni).

Table 4.4 The epoxidation of styrene catalysed by PPF-5(MnCl) and PPF-5(Mn/Ni).

Entry	Catalyst	Conversion (%)	Selectivity (%)	Yield (%)
1	PPF-5(MnCl)	77	79	56
2	PPF-5(Mn/Ni)	72	65	47

The heterogeneous catalysts were much slower compared to the homogeneous systems and also much slower than the results reported by Wu who reported > 99% conversion and 98% selectivity after 6 hours for a MOF with similar constituent units (Mn(TCPP)Cl linker, DPNI pillar and $Zn_2(CO_2)_4$ SBUs).[40] These results indicated that perhaps structural collapse occurred during the catalysis reaction, and led to low accessibility of the substrate to the catalytic centres. PXRD on solids recovered from these reactions (Appendix 2, Figure A2.5) showed very low intensities compared to as-synthesised MOFs, which indicated a high degree of framework collapse during the reactions and most probably the catalysis happened on the outer surface of the material, and not in the pores.

4.9 Crystal engineering of PCN-222(Mn/Ni) as a stable catalyst

Zhou and co-workers reported a family of Zr-porphyrin MOFs, which they termed Porous Coordination Networks 221–225 (PCNs 221–225), by the reaction of $ZrCl_4$ and M(TCPP) in the presence of benzoic , acetic or formic acid modulators.[10, 43, 24, 44] Figure 4.23 shows the structures and Table 4.5 gives some of the properties of the PCN-221–225 materials. The nature of the Zr-cluster, framework topology and therefore pore size(s) of these MOFs can be well controlled through the synthesis conditions, such as solvent, modulator, time, reaction temperature and metal to ligand ratio. In many cases, isoreticular frameworks were formed from differently metallated metalloporphyrin linkers. Thus, PCN-221–225 materials were identified as an appropriate series to apply the principles developed in this chapter to the construction of multi-metallolinker frameworks with catalytic potential.

Table 4.5 Properties of the PCN-221–225 frameworks.

MOF	PCN-221	PCN-222	PCN-223	PCN-224	PCN-225
BET surface area	~ 1500 – 1900 m^2g^{-1}	2200 m^2g^{-1}.	1600 m^2g^{-1}	2600 m^2g^{-1}	1902 m^2g^{-1}
Metallated linkers	M = No metal, Fe, Co, Cu	M = FeCl, MnCl, Co, Ni, Cu, Zn	M = FeCl	M = No metal, Ni, Co, Fe	M = no metal and Zn
Space group	*Pm̄3m*	*P*6/*mmm*	*P*6/*m*	*Im*$\bar{3}$*m*	*I*41/*amd*
Channel/pore system	Polyhedral cages with pore size of ~0.8 nm	1D hexagonal (3.2 nm) and triangular (1.3 nm) 1D channels	Triangular channels, 12 Å	Square channels, 1.9 nm	quadrangle shape, 0.8 × 1.5 nm^2
Stability test	---	boiling water and various concentrations of HCl	pH = 0 to pH = 10	pH = 0 to pH = 11	pH between 0 to 12 and boiling water

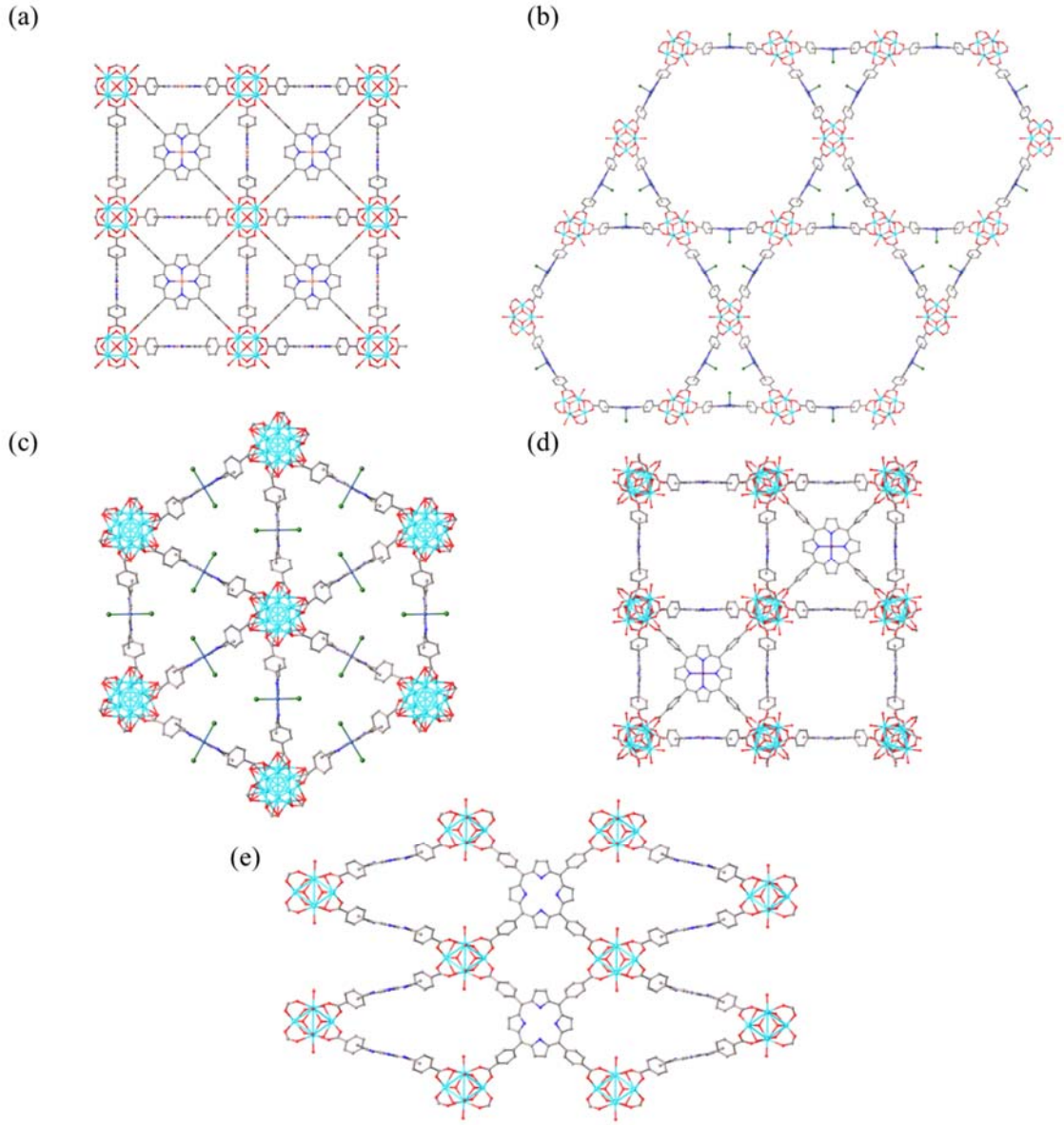

Figure 4.23 Structures of (a) PCN-221, (b) PCN-222, (c) PCN-223, (d) PCN-224 and (e) PCN-225.

While a PCN-221 framework was highly selective for ketone and alcohol products in the oxidation of cyclohexane[45] and PCN-223 proved to be an excellent catalyst in the hetero-Diels-Alder cycloaddition of aldehydes to dienes.[43] PCN-223(Fe) exhibited high H_2O/H_2O_2 selectivity when used as an electro-catalyst for the oxygen reduction reaction.[46] PCN-224 was active as a catalyst for the insertion of CO_2 to epoxides[24] and PCN-224(Fe) was tested for its photocatalytic ability in a gaseous isopropanol oxidation process.[47] It is PCN-222 that has garnered the most interest.

In PCN-222, each M(TCPP) is linked to four eight-connected Zr_6 clusters to form a 3D network with large hexagonal channels (~3.7 nm) and smaller triangular channels.[10] This MOF also showed good stability towards water, boiling water and various concentrations of HCl in organic solvents, as identified through PXRD and N_2 sorption measurements. This highly stabile and porous structure with large channels for fast diffusion of molecules and substrate-accessible metalloporphyrin sites, has tremendous potential as a catalyst. Indeed, the catalytic activity was tested as a peroxidase-like catalyst to oxidise a range of different substrates and it showed great activity.[10] The catalytic activity of PCN-222 was also investigated for the photo-oxidation of 2-chloroethyl ethyl sulfide to the sulfoxide and the sulfone.[48]

4.9.1 Syntheses of PCN-222 MOFs

This section presents the synthesis and characterisation of multi-metal PCN-222(Mn/Ni), which has not been reported in the literature. PCN-222(Ni) and PCN-222(Mn) were prepared for comparative purposes.

PCN-222(Ni) was synthesised as red needle-shaped crystals according to the established solvothermal conditions of heating Ni(TCPP), $ZrCl_4$ and benzoic acid in DEF solution at 120 °C for 48 hours, followed by raising the temperature to 130 °C for 24 hours. PCN-222(Mn) was synthesised similarly using Mn(TCPP)Cl, $ZrCl_4$ and benzoic acid in DMF at 120 °C for 48 hours. Olive green needle crystals of PCN-222(Mn/Ni) were grown in 56% yield by heating an equimolar mixture of Ni(TCPP) and Mn(TCPP)Cl with $ZrCl_4$ in DEF at 120 °C for 48 hours.

The "as-synthesised" MOFs were solvent exchanged to fresh dry DMF and treated with 8 M HCl in DMF at room temperature over 24 hours, according to the literature procedure.[10] The samples were solvent exchanged to dry acetone with several exchanges and vacuum dried immediately before further analysis. These samples were then used for PXRD, TGA, ICP-OES, SEM-EDS and gas sorption measurements and catalysis reactions.

4.9.2 Powder X-Ray Diffraction of PCN-222 MOFs

PXRD measurements were carried out to confirm the crystallinity and phase purity of each sample. This is particularly important given that PCNs 223–224 can be formed from the same molecular constituents. PXRD data were recorded for each "as-synthesised" MOF and again after the acid treatment. These patterns were then compared with the PXRD data from the literature for PCN-222(Mn) and PCN-222(Ni) and all are shown in Figure 4.24. PXRD data recorded on the materials after gas sorption and catalysis are plotted in Appendix 2, Figure A2.6. The patterns of as-synthesised PCN-222(Ni), PCN-222(Mn) and PCN-222(Mn/Ni) match the pattern from the literature with all peak positions matching well. However, significant differences in peaks intensities were observed compared with the simulated patterns. Excellent

matches in peaks positions and intensities were obtained after acid treatment for all samples, confirming this procedure gives improved crystallinity.

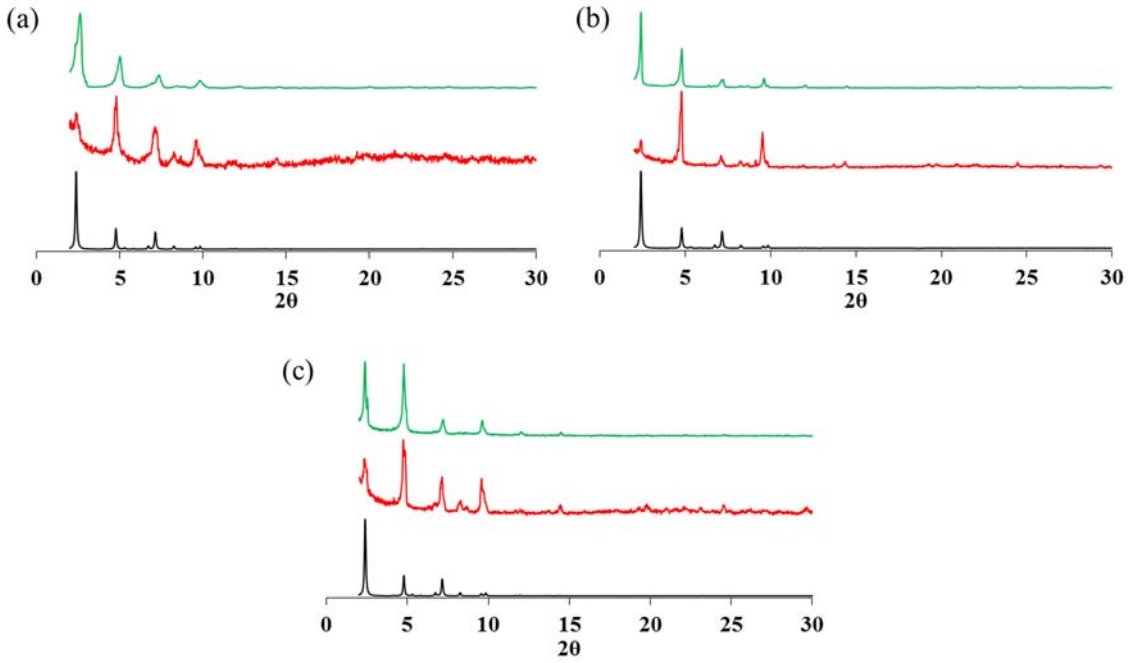

Figure 4.24 PXRD patterns for (a) PCN-222(Ni), (b) PCN-222(Mn) and (c) PCN-222(Mn/Ni); calculated PCN-222 from literature (black); 'as-synthesised' (red) and after acid treatment (green).

4.9.3 Inductively Coupled Plasma-Optical Emission Spectroscopy and Scanning Electron Microscopy-Energy Dispersive X-ray Spectroscopy studies analyses of PCN-222(Mn/Ni)

ICP-OES was performed to quantify the elemental ratio of Mn and Ni in a bulk sample of digested PCN-222(Mn/Ni). This revealed the ratio of 0.48 : 0.52 of Mn : Ni, respectively. This result indicated both metallolinkers were successfully crystallised and similarly to the multi-metal PPF-type MOFs explained earlier, a higher proportion of Ni(TCPP) linker was observed. It appears that the Ni(TCPP) linker is accepted into the framework with only a slight preference over Mn(TCPP)Cl for the PCN-222-type framework. Given that the ICP-OES is a bulk analysis technique, it did not answer the question if the metallolinkers are co-polymerised within each crystal.

The morphology and metal distribution of PCN-222(Mn/Ni) was investigated by SEM-EDS. Two images of crystals (50 μm scale bar) and EDS analysis of two of the selected spots (indicated with arrows on the images) are presented in Figure 4.25. The needle-shaped morphology is typical for this MOF, and the PCN-222(Mn/Ni) crystals produced here have an approximate size of 40 μm. The elemental analysis by EDS was performed on selected locations on the crystals to identify the distribution of the metallic elements. The selected spot in Figure 4.25a (spectrum 263) gave a Mn : Ni ratio of 1.34 : 1.57 (0.46 : 0.54) and the selected spot in Figure 4.25b (spectrum 268) the ratio of 1:06 : 1.03 (0.51 : 0.49), respectively. These results are very close to synthesis ratio of 0.50 : 0.50 and the results found by ICP-OES, indicating PCN-222(Mn/Ni) was successfully engineered by crystallisation of both linkers within the crystals. The EDS analyses of other spots are presented in Appendix 2, Figure A2.7.

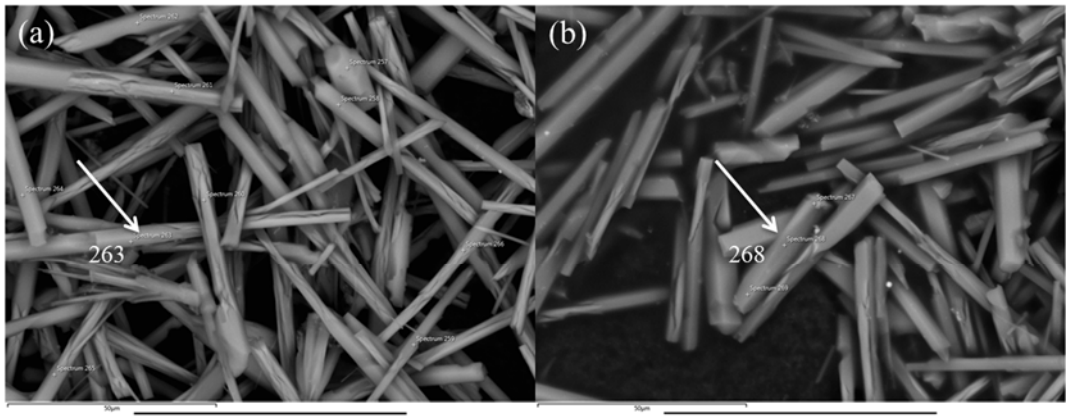

Spectrum Label	Spectrum 263 (wt%)
Mn	1.34
Ni	1.57

Spectrum Label	Spectrum 268 (wt%)
Mn	1.06
Ni	1.03

Figure 4.25 SEM images and EDS data of two different spots in the sample of PCN-222(Mn/Ni).

4.9.4 Activation and gas sorption studies

Acid-treated PCN-222(Ni), PCN-222(Mn/Ni) and PCN-222(MnCl) were activated by heating under dynamic vacuum at 60 °C for 1 hour and then at 120 °C for 16 hours. The samples were used immediately for gas sorption after bringing back to room temperature. TGA traces of the activated MOFs showed no mass losses, indicating perfect activation of the materials (Appendix 2, Section A2.2).

N_2 sorption measurements at 77 K were carried out to compare the porosity of the samples with those reported in the literature. The MOFs show Type IV isotherms, consistent with the mesoporosity of these materials. The obtained results are very consistent with the literature report for PCN-222 by Zhou and co-workers.[10] PCN-222(Ni) and PCN-222(Mn/Ni) showed the same N_2 uptake of 809 cm^3g^{-1} (Figure 4.26, purple and red, respectively). The Brunauer-Emmett-Teller (BET) surface areas calculated for PCN-222(Ni) and PCN-222(Mn/Ni) were 1962 m^2g^{-1} (Lit. 2283 m^2g^{-1})[10] and 2052 m^2g^{-1}, respectively. The PXRD pattern of PCN-222(Ni) recorded after gas sorption measurements showed an excellent match (Appendix 2, Figure A2.6a, blue), confirming crystallinity is retained after activation of the MOF. Although a high surface area was observed for PCN-222(Mn/Ni), PXRD data showed no crystallinity on the samples used for gas sorption analysis (Appendix 2, Figure A2.6c, blue). This suggests the crystals possibly collapsed before PXRD analysis during handling of the materials in air after gas sorption.

The activation of PCN-222(MnCl) was repeated multiple times, with the best N_2 uptake at 77 K of 531 cm^3g^{-1} and BET surface area of 1279 m^2g^{-1}, (Figure 4.26, black). This is considerably lower than the literature report for this material (2046 m^2g^{-1}).[10] The PXRD of the materials after activation showed very low crystallinity of the MOFs after gas sorption. Given the relatively low N_2 uptake at 77 K, but reasonable PXRD after acid treatment, it seems likely the PCN-222(MnCl) samples might have suffered some measure of collapse during activation (Appendix 2, Figure A2.6b, blue).

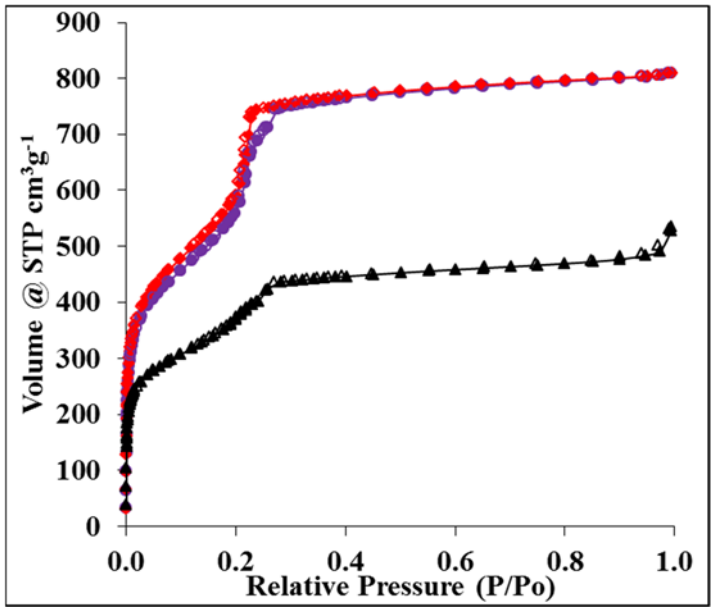

Figure 4.26 N_2 adsorption-desorption isotherms at 77 K for PCN-222(Ni) (purple), PCN-222(MnCl) (black) and PCN-222(Mn/Ni) (red). Closed and opened symbols indicate adsorption and desorption, respectively.

4.9.5 Catalytic activity of PCN-222(Mn) and PCN-222(Mn/Ni) in the epoxidation of styrene

The catalytic activity of PCN-222(Mn) and PCN-222(Mn/Ni) were examined in the epoxidation of styrene. The reaction conditions applied to the MOFs were established through control experiments with 5 mol% loadings of the molecular porphyrin complexes, Mn(TPPCO$_2$Me)Cl, Ni(TPPCO$_2$Me) and a 1:1 mixture of Mn(TPPCO$_2$Me)Cl : Ni(TPPCO$_2$Me), as explained in section 4.9. The epoxidation reactions were performed under different loadings of the MOF catalysts (0.5–5 mol%), styrene as the substrate (1 eq), PhIO as the terminal oxidant (1.5 eq.) and 1,2,4,5-tetramethylbenzene as an internal standard at a concentration of 0.1 M in CH_2Cl_2 solutions at room temperature. Aliquots were taken, filtered and diluted for GC-MS analysis at 0.5, 1, 1.5, 2 and 4 hours. The data are depicted graphically in Figure 4.27 and summarised in Table 4.6.

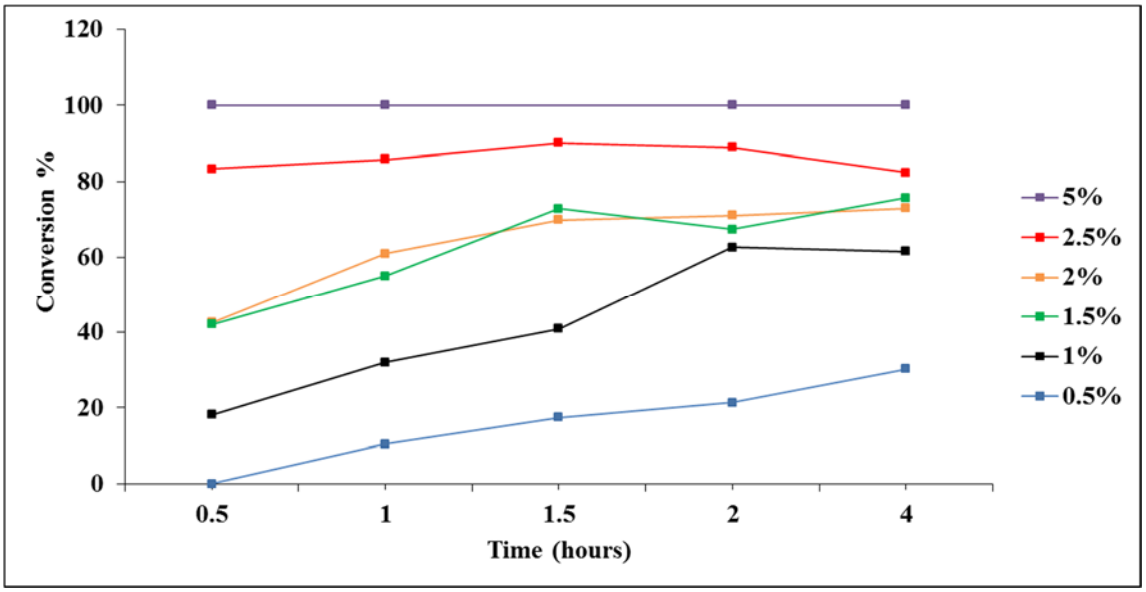

Figure 4.27 Kinetic traces of styrene epoxidation catalysed by PCN-222(Mn/Ni) at 5 mol% (purple), 2.5 mol% (red), 2 mol% (orange), 1.5 mol% (green), 1 mol% (black) and 0.5 mol% (blue) of catalyst loading.

Table 4.6 Conversion, selectivity and yield of styrene epoxide by various proportions of PCN-222(Mn/Ni), after 0.5 hour and 4 hour reaction times.

Entry	Catalyst loading	T = 0.5 hour			T = 4 hours		
		Conversion (%)	Selectivity (%)	Yield (%)	Conversion (%)	Selectivity (%)	Yield (%)
1	5%	100	100	100	100	100	100
2	2.5%	94	83	78	100	82	82
3	2%	55	78	43	94	78	73
4	1.5%	…	…	…	95	79	75
5	1%	…	…	…	69	89	61
6	0.5%	…	…	…	35	86	30

At 5 mol% loading of PCN-222(Mn/Ni), styrene was fully converted to styrene epoxide with 100% selectivity and yield after 0.5 hour (Table 4.6, entry 1). This result was also obtained after 4 hours of reaction time indicating that no secondary reaction occurred to produce any by-product. The data point at the 1.5 hour time mark was affected by accidental contamination and it therefore is not shown in the plot. PXRD showed very good crystallinity of the sample after 4 hours of reaction time, indicating the stability of the catalyst during the reaction (Appendix 2, Figure A2.6c, purple). The reaction with 2.5 mol% of catalyst showed conversion of styrene to styrene epoxide as the main product and the production of 2-phenylacetaldehyde as a by-product. The proportion of by-product was essentially constant during the transformation with 82% and 83% selectivity for styrene epoxide afforded after 0.5 hour and 4 hours of reaction time (Table 4.6, entry 2). With proportions of catalyst between 2–0.5% (Table 4.6, entries 3–6), significant proportions of 2-phenylacetaldehyde were formed together with the main reaction product, styrene epoxide. In these series of reactions with lower proportions of catalyst, GC-MS analysis revealed unreacted styrene after 4 hours reaction time. This result showed the conversion of the styrene depends strongly on the catalyst loading.

The reactions using 0.5–5 mol% catalyst loading were performed using the same batch of the crystals. Further batches of the PCN-222(Mn/Ni) MOFs were prepared using the

same synthesis and acid treatment procedures to repeat the catalysis reaction using 5 mol% catalyst loading. The best result was obtained with 98% conversion and 87% selectivity for styrene epoxide after 4 hours, with a trace amount of unreacted styrene and some 2-phenylacetaldehyde. Reproducibly producing high quality crystals was problematic; therefore, it was difficult to obtain the same conversion and selectivity for styrene epoxide using different batches of the catalysts.

The epoxidation reactions with 5 mol% of PCN-222(Mn) showed full conversion and selectivity of styrene to styrene epoxide after 0.5 hour and 4 hours (Appendix 2, Figure A2.10). The PXRD after catalytic reaction showed very good crystallinity for this MOF; indicating the framework remained stable during the catalysis reaction (Appendix 2, Figure A2.6b, purple).

In summary, a multi-metal PCN-222(Mn/Ni) was successfully engineered. This MOF showed high stability upon solvent removal and as a catalyst for the epoxidation of styrene. The presence of Ni as a Lewis acid within this MOF makes it a potential catalyst for tandem catalysis reaction. Some of this reactivity was seen in this study where large amounts of 2-phenylacetaldehyde were produced at low catalyst loadings of PCN-222(Mn/Ni). This tandem transformation of styrene to 2-phenylacetaldehyde catalysed by PCN-222(Mn/Ni) is presented in Scheme 4.2.

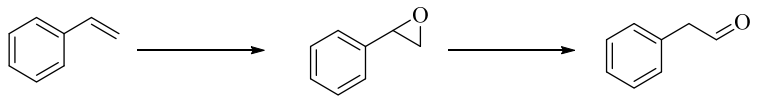

Scheme 4.2 Tandem transformation of styrene to 2-phenylacetaldehyde catalysed by PCN-222(Mn/Ni).

These results are comparable with a recently published paper by Hupp and co-workers. They demonstrated a ZnMnRPM-MOF containing Mn(MDPFP) (meso-5,15-dipyridyl-10,20-bis(pentafluorophenyl)-porphyrinatomangenese) and Zn(TCPP). The tandem catalysis was investigated on epoxidation of styrene followed by CO_2 insertion to styrene epoxide. The reaction was first performed using, 0.1 mol% of ZnMnRPM as the catalyst, styrene as the substrate and (*tert*-butylsulfonyl)-2-iodosylbenzene as the terminal oxidant, in CH_3CN solution at 60 °C for 40 hours. The reaction in the absence

of CO_2 yielded 20% of epoxide in addition to 28% of benzaldehyde and 2-phenylacetaldehyde as by-product. The tandem reaction was carried out in presence of CO_2, resulting in 60% of styrene carbonate product while no by-product formed. These results suggest both Mn and Zn are working together, with Mn for the epoxidation and Zn for the CO_2 insertion to produce styrene carbonate.[15]

4.10 Conclusion

The present study re-examined some members of the PPF family of porphyrin MOFs towards generating new, complex, trimetallic and 'defect engineered' members. Different synthetic conditions were developed here compared to the contributions by Choe and co-workers to the literature,[30, 35, 36, 37] and were largely responsible for some novel results. A new trimetallic member of the PPF-1 series was engineered starting from a 1 : 1 ratio of Ni(TCPP) and Mn(TCPP)Cl, with the final composition of this framework showing a distinct enhancement of nickel metalloporphyrin linker in the final product, $Zn_2[Mn(TCPP)]_{0.44}[Ni(TCPP)]_{0.56}$.

The bpy-pillared PPF-5 series was explored with nickel and manganese metalloporphyrins. The aim was to see if deliberate doping of Ni(TCPP) would be able to switch the structure from PPF-3[36] to PPF-5, which would then feature accessible and catalytically competent manganese metal centres. Using the new synthetic conditions developed here, the PPF-5(MnCl) structure formed without the need for doping. This was unexpected but was rationalised by the shorter reaction time. The synthesis by Choe was carried out for a much longer time and it is conceivable that the PPF-5 type structure forms first but converts to the PPF-3 type with more time in the presence of excess bpy ligand. A multi-metalloporphyrin PPF-5(Mn/Ni) framework was prepared from an equimolar starting mixture and a preference for Ni(TCPP) incorporation again observed in the final product, $Zn_2[Mn(TCPP)]_{0.4}[Ni(TCPP)]_{0.45}[bpy]$. PPF-5-type frameworks were not stable to solvent removal by the methods investigated here, and consequently, it was not possible to study surface area properties in these materials (Appendix 2, Section A2.1). Structural collapse was also encountered when attempting to use PPF-5(MnCl) and PPF-5(Mn/Ni) as catalysts for the epoxidation of styrene.

A series of multi-metal PPF(Ni/Co) were made through systematically varying mole fractions of the Co(TCPP) and Ni(TCPP) linkers in framework synthesis. The aim of the study was to discover if co-doping Ni(TCPP)/Co(TCPP) switches PPF-3 and PPF-5 structural types.[36] Through a combination of PXRD, ICP-MS, SEM-EDS and ^{1}H NMR spectroscopy, a picture emerged that Co(TCPP) incorporates preferentially over

Ni(TCPP) and that individual crystals contain regions of PPF-3 and PPF-5. Formulation of the frameworks revealed lower levels of metallolinkers than what should be expected and suggests these materials contain high amounts of defects. This, in turn, indicates that this strategy might be good for deliberate 'defect engineering' in MOFs.

Due to the low stability and activity of PPF-5(Mn/Ni) as a catalyst, a new trimetallic PCN-222(Mn/Ni) was successfully engineered. As found for the PPF-1(Mn/Ni) and PPF-5(Mn/Ni) examples, an enhancement of nickel metalloporphyrin linker in the final product was observed. PCN-222(Mn/Ni) was stable to solvent removal and highly porous, with a BET surface area comparable to PCN-222(Ni), and a very effective and stable catalyst in the epoxidation of styrene, with full conversion and selectivity when 5 mol% catalyst was used. 2-Phenylacetaldehyde was evident as a-product from a secondary reaction and is attributable to the presence of Ni(TCPP) in PCN-222(Mn/Ni). Thus, the strategy co-polymerising metalloporphyrin linkers has produced a bifunctional tandem catalyst capable of consecutive transformations.

4.11 Experimental

4.11.1 Synthesis of 5,10,15,20-tetrakis(4-methoxycarbonylphenyl)porphyrin-M (TPPCO$_2$Me)

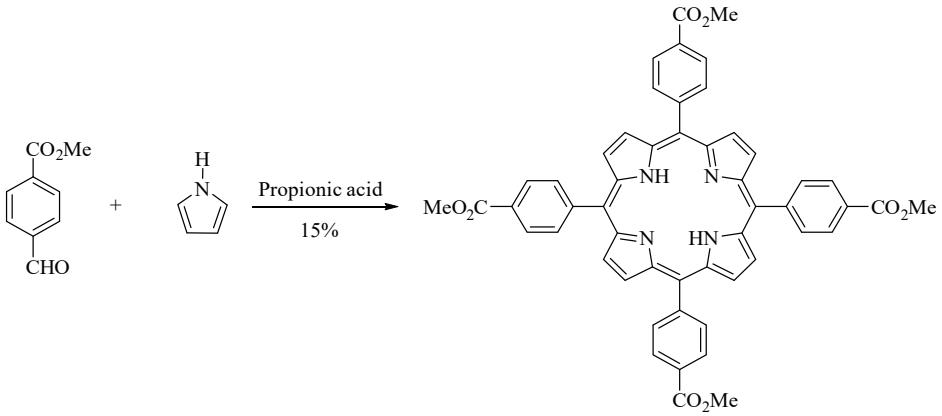

Scheme 4.3 The synthesis procedure of H_2TPPCO_2Me.

A mixture of methyl 4-formylbenzoate (16.4 g, 0.100 mol) and pyrrole (6.81 g, 0.100 mol) was dissolved in hot propionic acid (400 mL) and heated at 150 °C for 40 minutes. The reaction mixture was cooled down in an ice bath, and silica gel was added to the solution, and then the solvent was removed by rotary evaporation. The obtained solid, including the product and silica gel was taken up in hexane (50 mL) and filtered over a glass filter funnel. The crude product was purified by eluting from a silica gel plug using CH_2Cl_2 as the eluent. Most of the solvent was removed by rotary evaporation; and MeOH (40 mL) was added to precipitate the product. The product was collected over a glass filter funnel and air dried. Yield 3.20 g (15%). ^{1}H NMR δ_H ($CDCl_3$, 300 MHz): 4.11 (12 H, s), 8.28 (8 H, d, J = 8.16 Hz), 8.44 (8 H, d, J = 8.06 Hz), 8.82 (8 H, s).

4.11.2 Syntheses of the complexes

Three metalloporphyrin complexes of Ni(TCPP) Mn(TCPP)Cl and Co(TCPP) were synthesised based on a procedure reported by Zhou and co-workers with slight changes.[10] The complexes were made by heating a mixture of H_2TPPCO_2Me and corresponding metal salt ($NiCl_2{\cdot}6H_2O$, $MnCl_2{\cdot}4H_2O$ and $CoCl_2{\cdot}6H_2O$) in DMF and refluxed for 6 hours. As explained in section 4.3.1, a different purification procedure

was applied from Zhou group for the complexes. Each complex (ester form) the product was suspended in a small amount of MeOH and heated to boil. The solution was then cooled down to room temperature, and the product was then precipitated. The product was collected by filtration and air dried. The Ni(TPPCO$_2$Me), Mn(TPPCO$_2$Me)Cl and Co(TPPCO$_2$Me) were then hydrolysed using KOH (2 M) and in a mixture of MeOH/THF.

4.11.3 Syntheses of MOFs

4.11.3.1 *Synthesis of PPF-1(Ni)*

A mixture of Ni(TCPP) (17.25 mg, 0.02 mmol) and $Zn(NO_3)_2 \cdot 6H_2O$ (29.75 mg, 0.1 mmol) was added to dry DEF (2 mL) in a screw top 20 mL vial. TFA (2 μL) was added as a modulator and the reaction mixture was heated at 85 °C in an oven for 12 hours. The purple crystals that formed were washed and stored in fresh DEF. Yield 10.1 mg (52%). Found (ICP-MS): $Zn_2[Ni(TCPP)]_{1.04}$.

4.11.3.2 *Synthesis of PPF-1(MnCl)*

Mn(TCPP)Cl (17.88 mg, 0.02 mmol), $Zn(NO_3)_2 \cdot 6H_2O$ (29.75 mg, 0.10 mmol) and TFA (2 μL) were dissolved in dry DEF (2 mL) in a screw top 20 mL vial. Then, the reaction mixture was heated at 85 °C in an oven for 12 hours. Purple crystals were harvested, washed and stored in fresh DEF. Yield 9.2 mg (45%). Found (ICP-MS): $Zn_2[Mn(TCPP)Cl]_1$.

4.11.3.3 *Synthesis of PPF-1(Mn/Ni)*

Mn(TCPP)Cl (8.79 mg, 0.01 mmol) and Ni(TCPP) (8.47 mg, 0.01 mmol) were combined with $Zn(NO_3)_2 \cdot 6H_2O$ (29.75 mg, 0.1 mmol) in dry DEF (2 mL) in a screw top vial. TFA (2 μL) was added as a modulator and the reaction mixture was heated at 85 °C in an oven for 12 hours. The resulted purple cubic MOFs then were harvested and washed with dry DMF. Yield 8.9 mg (45%). Found (ICP-MS): $Zn_2[Mn(TCPP)]_{0.46}[Ni(TCPP)]_{0.55}$.

4.11.3.4 *Synthesis of PPF-5(Ni)*

Ni(TCPP) (17.25 mg, 0.02 mmol), $Zn(NO_3)_2 \cdot 6H_2O$ (29.75 mg, 0.1 mmol) and bpy (6.25 mg, 0.04 mmol) were dissolved in dry DMF (2 mL) in a screw top 20 mL vial. TFA (2 μL) then was added to the reaction mixture and was transferred to an oven at 85 °C for 12 hours. Purple cubic crystals were collected before washing with dry DMF. Yield 10.3 mg (46%). Found (ICP-MS and ^{1}H NMR): $Zn_2[Ni(TCPP)]_{1.05}[bpy]_{1.14}$.

4.11.3.5 *Synthesis of PPF-5(MnCl)*

Mn(TCPP)Cl (17.88 mg, 0.02 mmol) was combined with $Zn(NO_3)_2 \cdot 6H_2O$ (29.75 mg, 0.1 mmol) and bpy (6.25 mg, 0.04 mmol) in dry DMF (2 mL) in a screw top vial. TFA (2 μL) was added as a modulator and the reaction mixture was heated at 85 °C in an oven for 12 hours. The resulted purple cubic MOFs then were harvested and washed with dry DMF. Yield 11.6 mg (50%). Found (ICP-MS): $Zn_2[Mn(TCPP)Cl]_{1.01}[bpy]$.

4.11.3.6 *Synthesis of PPF-5(Mn/Ni)*

Mn(TCPP)Cl (8.79 mg, 0.01 mmol), Ni(TCPP) (8.47 mg, 0.01 mmol), $Zn(NO_3)_2 \cdot 6H_2O$ (29.75 mg, 0.1 mmol) and bpy (6.25 mg, 0.04 mmol) were dissolved in dry DMF (2 mL) in a screw top 20 mL vial. TFA (2 μL) then was added to the reaction mixture and was transferred to an oven at 85 °C for 12 hours. Purple cubic crystals were collected before washing with dry DMF. Yield 9.1 mg (41%) Found: (ICP-MS and ^{1}H NMR) $Zn_2[Mn(TCPP)]_{0.4}[Ni(TCPP)]_{0.45}[bpy]_{0.76}$.

4.11.3.7 *Synthesis of PPF-3(Co)*

Co(TCPP) (17.25 mg, 0.02 mmol), $Zn(NO_3)_2 \cdot 6H_2O$ (29.75 mg, 0.1 mmol) and bpy (6.25 mg, 0.04 mmol) were dissolved in dry DMF (2 mL) in a screw top 20 mL vial. TFA (2 μL) was added and the mixture was heated at 85 °C in an oven for 12 hours. Cubic purple crystals were collected and then washed with dry DMF several times. Yield 15.5 mg (59%). Found (ICP-MS): $Zn_2[Co(TCPP)]_{0.94}[bpy]_2$.

4.11.3.8 *Synthesis of PPF(0.75Ni/0.25Co)*

Ni(TCPP)Cl (12.93 mg, 0.015 mmol), Co(TCPP) (43.31 mg, 0.005 mmol), $Zn(NO_3)_2 \cdot 6H_2O$ (29.75 mg, 0.1 mmol) and bpy (6.25 mg, 0.04 mmol) were dissolved in dry DMF (2 mL) in a screw top 20 mL vial. TFA (2 μL) was added and the mixture was heated at 85 °C in an oven for 12 hours. Cubic purple crystals were collected and then washed with dry DMF several times. Yield 15.2 mg. Found (ICP-MS and ^{1}H NMR): $Zn_2[Ni(TCPP)]_{0.65}[Co(TCPP)]_{0.3}$ $[bpy]_{1.16}$.

4.11.3.9 *Synthesis of PPF(0.50Ni/0.50Co)*

Ni(TCPP) (86.25 mg, 0.01 mmol), Co(TCPP) (86.27 mg, 0.01 mmol), $Zn(NO_3)_2 \cdot 6H_2O$ (29.75 mg, 0.1 mmol) and bpy (6.25 mg, 0.04 mmol) were dissolved in dry DMF (2 mL) in a screw top 20 mL vial. TFA (2 μL) was added and the mixture was heated at 85 °C in an oven for 12 hours. Cubic purple crystals were collected and then washed with dry DMF several times. Yield 11.6 mg. Found (ICP-MS and ^{1}H NMR): $Zn_2[Ni(TCPP)]_{0.39}[Co(TCPP)]_{0.42}[bpy]_{1.03}$.

4.11.3.10 *Synthesis of PPF(0.25Ni/0.75Co)*

Ni(TCPP)Cl (43.12 mg, 0.005 mmol), Co(TCPP) (12.94 mg, 0.015 mmol), $Zn(NO_3)_2 \cdot 6H_2O$ (29.75 mg, 0.1 mmol) and bpy (6.25 mg, 0.04 mmol) were dissolved in dry DMF (2 mL) in a 20 mL vial. TFA (2 μL) was added and the mixture was heated at 85 °C in an oven for 12 hours. Cubic purple crystals were collected and then washed with dry DMF several times. Yield 18.9 mg. Found (ICP-MS and ^{1}H NMR): $Zn_2[Ni(TCPP)]_{0.16}[Co(TCPP)]_{0.68}[bpy]_{0.94}$.

4.11.3.11 *Synthesis of PCN-222 (Mn/Ni)*

Ni(TCPP) (24.6 mg, 0.029 mmol) and Mn(TCPP)Cl (25.5 mg, 0.029 mmol) were combined in DEF (4 mL) and added to $ZrCl_4$ (70 mg, 0.30 mmol) dissolved in DEF (4 mL). Following that, benzoic acid (2700 mg, 22 mmol) was added to the reaction solution. The reaction mixture was transferred to a screw top vial and heated at 120 °C for 48 hours. The crystals were collected by centrifuge, washed and stored in dry DMF before further treatments and solvent exchanges. Yield 37.7 mg (56%).

4.12 References

1. Jiang, W.; Yang, J.; Liu, Y.-Y.; Song, S.-Y.; Ma, J.-F., A stable porphyrin-based porous mog metal-organic framework as an efficient solvent-free catalyst for C-C bond formation. *Inorganic Chemistry* **2017,** *56* (5), 3036-3043.
2. Singha, S.; Maity, S. K.; Biswas, S.; Saha, R.; Kumar, S., A magnesium-based bifunctional MOF: Studies on proton conductivity, gas and water adsorption. *Inorganica Chimica Acta* **2016,** *453*, 321-329.
3. Ema, T.; Miyazaki, Y.; Shimonishi, J.; Maeda, C.; Hasegawa, J. Y., Bifunctional porphyrin catalysts for the synthesis of cyclic carbonates from epoxides and CO_2: Structural optimization and mechanistic study. *Journal of the American Chemical Society* **2014,** *136* (43), 15270-15279.
4. Liu, T. F.; Feng, D.; Chen, Y. P.; Zou, L.; Bosch, M.; Yuan, S.; Wei, Z.; Fordham, S.; Wang, K.; Zhou, H. C., Topology-guided design and syntheses of highly stable mesoporous porphyrinic zirconium metal-organic frameworks with high surface area. *Journal of the American Chemical Society* **2015,** *137* (1), 413-419.
5. Cui, H., A stable and porous iridium(III)-porphyrin metal-organic framework: Synthesis, structure and catalysis. *CrystEngComm* **2016,** *18* (12), 2203-2209.
6. Pereira, C. F.; Simões, M. M.; Tomé, J. P.; Almeida Paz, F. A., Porphyrin-based metal-organic frameworks as heterogeneous catalysts in oxidation reactions. *Molecules* **2016,** *21* (10).
7. Chino, M.; Leone, L.; Zambrano, G.; Pirro, F.; D'Alonzo, D.; Firpo, V.; Aref, D.; Lista, L.; Maglio, O.; Nastri, F.; Lombardi, A., Oxidation catalysis by iron and manganese porphyrins within enzyme-like cages. *Biopolymers* **2018**.
8. Chang, T.-H.; Kung, C.-W.; Chen, H.-W.; Huang, T.-Y.; Kao, S.-Y.; Lu, H.-C.; Lee, M.-H.; Boopathi, K. M.; Chu, C.-W.; Ho, K.-C., Planar heterojunction perovskite solar cells incorporating metal-organic framework nanocrystals. *Advanced Materials* **2015,** *27* (44), 7229-7235.
9. Wang, K.; Feng, D.; Liu, T. F.; Su, J.; Yuan, S.; Chen, Y. P.; Bosch, M.; Zou, X.; Zhou, H. C., A series of highly stable mesoporous metalloporphyrin Fe-MOFs. *Journal of the American Chemical Society* **2014,** *136* (40), 13983-13986.
10. Feng, D.; Gu, Z. Y.; Li, J. R.; Jiang, H. L.; Wei, Z.; Zhou, H. C., Zirconium-metalloporphyrin PCN-222: Mesoporous metal-organic frameworks with ultrahigh stability as biomimetic catalysts. *Angewandte Chemie - International Edition* **2012,** *51* (41), 10307-10310.
11. Li, J.; Ren, Y.; Qi, C.; Jiang, H., The first porphyrin-salen based chiral metal-organic framework for asymmetric cyanosilylation of aldehydes. *Chemical Communications* **2017,** *53* (58), 8223-8226.
12. Meng, S.; Zou, X.; Liu, C.; Ma, H.; Zhao, N.; Ren, H.; Jia, M.; Liu, J.; Zhu, G., Synthesis and catalytic properties of new metalloporphyrin-based porous organic framework materials with single and accessible sites. *ChemCatChem* **2016,** *8* (14), 2393-2400.
13. Kucheryavy, P., Spectroscopic interrogations of isostructural metalloporphyrin-based metal-organic frameworks with strongly and weakly coordinating guest molecules. *Journal of Coordination Chemistry 69* (11-13), 1780-1791.

14. Park, J.; Jiang, Q.; Feng, D.; Mao, L.; Zhou, H.-C., Size-controlled synthesis of porphyrinic metal-organic framework and functionalization for targeted photodynamic therapy. *Journal of the American Chemical Society* **2016,** *138* (10), 3518-3525.
15. Beyzavi, M. H.; Vermeulen, N. A.; Zhang, K.; So, M.; Kung, C. W.; Hupp, J. T.; Farha, O. K., Liquid-phase epitaxially grown metal-organic framework thin films for efficient tandem catalysis through site-isolation of catalytic centers. *ChemPlusChem* **2016,** *81* (8), 708-713.
16. Abrahams, B. F.; Hoskins, B. F.; Robson, R., A new type of infinite 3D polymeric network containing 4-connected, peripherally linked metalloporphyrin building blocks. *Journal of the American Chemical Society* **1991,** *113* (9), 3606-3607.
17. Fleischer, E. B.; Shachter, A. M., Coordination oligomers and a coordination polymer of zinc tetraarylporphyrins. *Inorganic Chemistry* **1991,** *30* (19), 3763-3769.
18. Johnson, J. A.; Lin, Q.; Wu, L. C.; Obaidi, N.; Olson, Z. L.; Reeson, T. C.; Chen, Y. S.; Zhang, J., A "pillar-free", highly porous metalloporphyrinic framework exhibiting eclipsed porphyrin arrays. *Chemical Communications* **2013,** *49* (27), 2828-2830.
19. Chaudhari, A. K.; Mukherjee, S.; Nagarkar, S. S.; Joarder, B.; Ghosh, S. K., Bi-porous metal-organic framework with hydrophilic and hydrophobic channels: selective gas sorption and reversible iodine uptake studies. *CrystEngComm* **2013,** *15* (45), 9465-9471.
20. Diskin-Posner, Y.; Patra, G. K.; Goldberg, I., Supramolecular assembly of metalloporphyrins in crystals by axial coordination through amine ligands. *Journal of the Chemical Society, Dalton Transactions* **2001,** (19), 2775-2782.
21. Nandi, G.; Goldberg, I., Fixation of CO_2 in bi-layered coordination networks of zinc tetra(4-carboxyphenyl)porphyrin with multi-component $[Pr_2Na_3(NO_3)(H_2O)_3]$ connectors. *Chemical Communications* **2014,** *50* (88), 13612-13615.
22. Beyzavi, M. H.; Vermeulen, N. A.; Howarth, A. J.; Tussupbayev, S.; League, A. B.; Schweitzer, N. M.; Gallagher, J. R.; Platero-Prats, A. E.; Hafezi, N.; Sarjeant, A. A.; Miller, J. T.; Chapman, K. W.; Stoddart, J. F.; Cramer, C. J.; Hupp, J. T.; Farha, O. K., A hafnium-based metal-organic framework as a nature-inspired tandem reaction catalyst. *Journal of the American Chemical Society* **2015,** *137* (42), 13624-13631.
23. Lin, Q.; Bu, X.; Kong, A.; Mao, C.; Zhao, X.; Bu, F.; Feng, P., New heterometallic zirconium metalloporphyrin frameworks and their heteroatom-activated high-surface-area carbon derivatives. *Journal of the American Chemical Society* **2015,** *137* (6), 2235-2238.
24. Feng, D.; Chung, W. C.; Wei, Z.; Gu, Z. Y.; Jiang, H. L.; Chen, Y. P.; Darensbourg, D. J.; Zhou, H. C., Construction of ultrastable porphyrin Zr metal-organic frameworks through linker elimination. *Journal of the American Chemical Society* **2013,** *135* (45), 17105-17110.
25. Zhuang, C.; Liu, J.; Dai, W.; Wu, Z.; Wang, Y.; Gao, S., Synthesis and applications in catalysis of porphyrinic metal-organic frameworks. *Progr. Chem.* **2014,** *26* (2-3), 277-292.
26. Ahrenholtz, S. R.; Epley, C. C.; Morris, A. J., Solvothermal preparation of an electrocatalytic metalloporphyrin MOF thin film and its redox hopping charge-transfer mechanism. *Journal of the American Chemical Society* **2014,** *136* (6), 2464-2472.
27. Brown, J. W.; Nguyen, Q. T.; Otto, T.; Jarenwattananon, N. N.; Glöggler, S.; Bouchard, L. S., Epoxidation of alkenes with molecular oxygen catalyzed by a

manganese porphyrin-based metal-organic framework. *Catalysis Communications* **2015,** *59*, 50-54.
28. Zou, C.; Zhang, T.; Xie, M. H.; Yan, L.; Kong, G. Q.; Yang, X. L.; Ma, A.; Wu, C. D., Four metalloporphyrinic frameworks as heterogeneous catalysts for selective oxidation and aldol reaction. *Inorganic Chemistry* **2013,** *52* (7), 3620-3626.
29. Gao, W.-Y.; Chrzanowski, M.; Ma, S., Metal-metalloporphyrin frameworks: a resurging class of functional materials. *Chemical Society Reviews* **2014,** *43* (16), 5841-5866.
30. Barron, P. M.; Son, H. T.; Hu, C.; Choe, W., Highly tunable heterometallic frameworks constructed from paddle-wheel units and metalloporphyrins. *Crystal Growth and Design* **2009,** *9* (4), 1960-1965.
31. Meng, L.; Cheng, Q.; Kim, C.; Gao, W. Y.; Wojtas, L.; Chen, Y. S.; Zaworotko, M. J.; Zhang, X. P.; Ma, S., Crystal engineering of a microporous, catalytically active fcu topology MOF using a custom-designed metalloporphyrin linker. *Angewandte Chemie - International Edition* **2012,** *51* (40), 10082-10085.
32. Barron, P. M.; Wray, C. A.; Hu, C.; Guo, Z.; Choe, W., A bioinspired synthetic approach for building metal-organic frameworks with accessible metal centers. *Inorganic Chemistry* **2010,** *49* (22), 10217-10219.
33. Farha, O. K.; Shultz, A. M.; Sarjeant, A. A.; Nguyen, S. T.; Hupp, J. T., Active-site-accessible, porphyrinic metal-organic framework materials. *Journal of the American Chemical Society* **2011,** *133* (15), 5652-5655.
34. Son, H. J.; Jin, S.; Patwardhan, S.; Wezenberg, S. J.; Jeong, N. C.; So, M.; Wilmer, C. E.; Sarjeant, A. A.; Schatz, G. C.; Snurr, R. Q.; Farha, O. K.; Wiederrecht, G. P.; Hupp, J. T., Light-harvesting and ultrafast energy migration in porphyrin-based metal-organic frameworks. *Journal of the American Chemical Society* **2013,** *135* (2), 862-869.
35. Choi, E.-Y.; Wray, C. A.; Hu, C.; Choe, W., Highly tunable metal-organic frameworks with open metal centers. *CrystEngComm* **2009,** *11* (4), 553-555.
36. Choi, E.-Y.; Barron, P. M.; Novotny, R. W.; Son, H.-T.; Hu, C.; Choe, W., Pillared porphyrin homologous series: Intergrowth in metal-organic frameworks. *Inorganic Chemistry* **2009,** *48* (2), 426-428.
37. Chung, H.; Barron, P. M.; Novotny, R. W.; Son, H. T.; Hu, C.; Choe, W., Structural variation in porphyrin pillared homologous series: Influence of distinct coordination centers for pillars on framework topology. *Crystal Growth and Design* **2009,** *9* (7), 3327-3332.
38. Olivo, G.; Lanzalunga, O.; DiStefano, S., Non-heme lmine-based iron complexes as catalysts for oxidative processes. *Advanced Synthesis & Catalysis* **2016,** *358* (6), 843-863.
39. Lee, S. J.; Doussot, C.; Baux, A.; Liu, L.; Jameson, G. B.; Richardson, C.; Pak, J. J.; Trousselet, F.; Coudert, F.-X.; Telfer, S. G., Multicomponent metal-organic frameworks as defect-tolerant materials. *Chemistry of Materials* **2016,** *28* (1), 368-375.
40. Xie, M. H.; Yang, X. L.; He, Y.; Zhang, J.; Chen, B.; Wu, C. D., Highly efficient C-H oxidative activation by a porous Mn(III)-porphyrin metal-organic framework under mild conditions. *Chemistry - A European Journal* **2013,** *19* (42), 14316-14321.
41. Lucas, H. J.; Kennedy, E. R.; Formo, M. W., Iodosobenzene. In *Organic Syntheses*, John Wiley & Sons, Inc.: 2003.

42. Chen, C.-X.; Zheng, S.-P.; Wei, Z.-W.; Cao, C.-C.; Wang, H.-P.; Wang, D.; Jiang, J.-J.; Fenske, D.; Su, C.-Y., A robust metal-organic framework combining open metal sites and polar groups for methane purification and co2/fluorocarbon capture. *Chemistry – A European Journal* **2017,** *23* (17), 4060-4064.
43. Feng, D.; Gu, Z. Y.; Chen, Y. P.; Park, J.; Wei, Z.; Sun, Y.; Bosch, M.; Yuan, S.; Zhou, H. C., A highly stable porphyrinic zirconium metal-organic framework with shp-a topology. *Journal of the American Chemical Society* **2014,** *136* (51), 17714-17717.
44. Morris, W.; Volosskiy, B.; Demir, S.; Gándara, F.; McGrier, P. L.; Furukawa, H.; Cascio, D.; Stoddart, J. F.; Yaghi, O. M., Synthesis, structure, and metalation of two new highly porous zirconium metal-organic frameworks. *Inorganic Chemistry* **2012,** *51* (12), 6443-6445.
45. Feng, D.; Jiang, H.-L.; Chen, Y.-P.; Gu, Z.-Y.; Wei, Z.; Zhou, H.-C., Metal-organic frameworks based on previously unknown Zr_8/Hf_8 cubic clusters. *Inorganic Chemistry* **2013,** *52* (21), 12661-12667.
46. Usov, P. M.; Huffman, B.; Epley, C. C.; Kessinger, M. C.; Zhu, J.; Maza, W. A.; Morris, A. J., Study of electrocatalytic properties of metal-organic framework PCN-223 for the oxygen reduction reaction. *ACS Applied Materials & Interfaces* **2017,** *9* (39), 33539-33543.
47. Shi, L.; Yang, L.; Zhang, H.; Chang, K.; Zhao, G.; Kako, T.; Ye, J., Implantation of iron(III) in porphyrinic metal-organic frameworks for highly improved photocatalytic performance. *Applied Catalysis B: Environmental* **2018,** *224*, 60-68.
48. Liu, Y.; Howarth, A. J.; Hupp, J. T.; Farha, O. K., Selective photooxidation of a mustard-gas simulant catalyzed by a porphyrinic metal-organic framework. *Angewandte Chemie - International Edition* **2015,** *54* (31), 9001-9005.

Chapter 5

Synthesis and Characterisation of Isostructural Amine-Functionalised Metal-Organic Frameworks

5 Introduction

In the last two decades, the design and synthesis of MOF structures containing functionalised organic linkers have been developed considerably due to a wide range of chemical and physical properties that the functionalised MOFs can display. The pore size and surface properties of a MOF can be tuned for targeted applications based on the functional group.[1, 2]

The synthesis of MOFs with the same topology yet containing specifically chosen chemical functionalities is a significant challenge. This challenge was identified by Yaghi and co-workers.[3] The authors indicated that in order to design desired structures with the same topology (i) the metal ions should have same propensity to assemble the framework, (ii) the same conditions would need to be applied for the MOFs syntheses. From a design perspective, an isoreticular series allows for structure-function relationships that would then allow rational design and tuning.

High surface area and porosity in MOFs make these materials great candidates for gas storage and separation applications. In addition to these sophisticated properties, functionalisation of the organic linker can increase the host-guest interaction, and therefore, improve the separation and selectivity in MOF materials. To date, functionalised MOFs with various tag groups such as amino,[4] alkylamino,[5] nitro,[6] halo[7] and hydroxyl,[8] etc. have been reported in the literature. Amine-functionalised MOFs have been considered due to a high affinity for gas molecules, such as CO_2. Moreover, amines provide a good platform for PSM, so that the properties of the MOF could be rationally tuned.[9, 10] Amine-functionalised MOFs can be prepared by a direct synthesis from an amine-functionalised ligand and by PSM to create amine-functionalised MOFs.

The amine-functionalised framework, MOF-46, consists of Zn^{2+} metal ions and 2-amino-1,4-benzenedicarboxylate (bdc-NH_2) bridging ligands, and was reported by Yaghi and co-workers in 2001.[11] IRMOF-3 is another amine-functionalised MOF with the same structure as MOF-5[12] (IRMOF-1) in which Zn_4O SBUs are bridged by bdc-NH_2 (Figure

5.1a).[3] This MOF was found to have high crystallinity and porosity, and the amine group was readily accessible within the pores to guest molecules.[3] In the time following, many researchers have been using amine tag groups to create novel MOF structures. Amine-functionalised MIL-101(Cr)-NH_2 was first reported by Ferey in 2012 (Figure 5.1b).[13] The CO_2 adsorption isotherms of this MOF showed a higher affinity compared to MIL-101(Cr), and this is due to the presence of the amine groups. Further investigation of this MOF showed it had high chemical stability, high surface area, pore volume and versatility of the amine group for PSM.[14] Since then, further amine-functionalised MILs were reported with different metal nodes such as MIL-101(Al)-NH_2,[15] NH_2-MIL-101(Fe)-NH_2[16] and MIL-68(In)-NH_2.[17]

Cohen and co-workers reported functionalised UiO-66 MOFs (Figure 5.1c) using bdc-X (X = -H, -NH_2, -NO_2, -OMe and -napthyl) and $ZrCl_4$ under solvothermal conditions. In the comparison of this isoreticular set of MOFs, the amine-functionalised material showed the highest adsorption loading for N_2, CO_2 and CH_4 compared to other functional groups. The MOF bearing this group also showed the best performance for CO_2/N_2 selectivity.[18, 19]

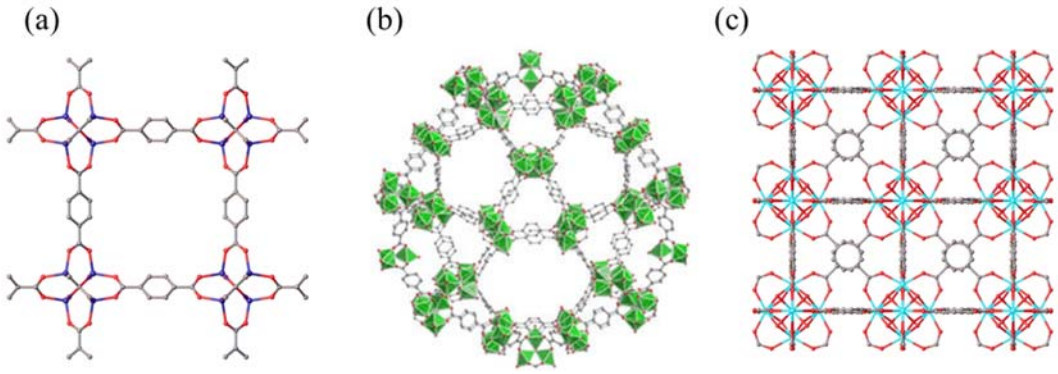

Figure 5.1 Important MOF structures in the literature, (a) MOF-5-NH_2[12], (b) MIL-101-NH_2[13] and (c) UiO-66-NH_2.[18]

To date, the amine-functionalised MOFs reported in the literature, are mostly designed in the aim of gas storage and separation applications. Moreover, there is no report regarding the systematic design of isoreticular amine-functionalised IRMOF-9/IRMOF-10 in the literature.

5.1 Outline and rationale

This chapter reports the syntheses and characterisation of four amine-functionalised biphenyl-4,4′-dicarboxylic acid (H_2bpdc) based linkers and their porous zinc MOFs. The purpose of the present work was to study the 'structural evolution' of the MOFs based on the nature of the pendant amine substituents. Thus, the impact of this functionality was investigated on the topology, pore dimensions and type of interpenetration of the frameworks. Surface area properties and CO_2 adsorption properties were examined in light of their amine functionalisation, and a new post-synthetic modification was studied.

5.2 Synthesis and Characterisation of amine-functionalised IRMOF

5.2.1 Ligand syntheses

In the present study, biphenyl-4,4′-dicarboxylic acid based organic linkers were chosen due to their ability to form isoreticular networks that would allow the effects of the functional groups to become evident. However, in some cases, MOFs based on biphenyl linkers typically interpenetrate (for pcu topology) which can lead to restricted access to functional groups. Four amine-functionalised linkers (Figure 5.2) were designed to investigate the impact of these functional groups on the topologies and properties of the resultant frameworks. The functional groups span a range of sizes from the small primary aromatic amine in H_2bpdc-NH_2 to the largest tertiary diallyl aromatic amine in H_2bpdc-N(allyl)$_2$. In between these two extremes lies the secondary allyl aromatic amine in the ligand, H_2bpdc-NHallyl. The chosen set of amines also spans a range of basicities. It is generally accepted that basicity of amines increases with increasing alkyl substitution.[20] On this basis, the primary aromatic amine in H_2bpdc-NH_2 is the least basic of the series and H_2bpdc-N(allyl)$_2$ and H_2bpdc-NMe_2 are likely the ligands with highest basicity. Based on substituent effects, the methyl group is a better σ-donor of electron density than the allyl group, and therefore it is expected that H_2bpdc-NMe_2 is the most basic of the ligands in the series. The ligand H_2bpdc-NH_2 is known[21] and has been used to construct MOFs.[22] These reports have considered gas sorption properties,[18] catalytic,[23, 24] and PSM.[25] There are a few reports in the literature to make H_2bpdc-NH_2 based MOFs such as UiO-67,[26] DUT-5.[27]

The linkers H_2bpdc-NHallyl, H_2bpdc-N(allyl)$_2$ have not been reported in the literature. Recently, H_2bpdc-NMe_2 was reported by the Hupp group who synthesised a Zr-MOF of UiO-67 topology with this ligand and used the MOF as a catalyst for nerve agent (soman) hydrolysis.[28]

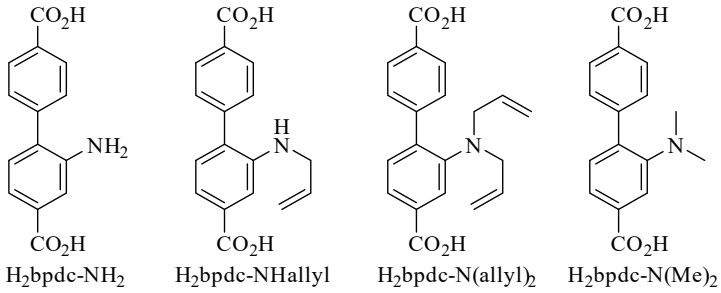

Figure 5.2 Chemical structures of the four amine-functionalised ligands investigated in this chapter.

5.2.1.1 *Synthesis of the common synthetic intermediate Me_2bpdc-NH_2 and hydrolysis to H_2bpdc-NH_2*

The synthesis of the ligands followed the routes shown in Schemes 5.1 and 5.2. Dimethyl [1,1'-biphenyl]-4,4'-dicarboxylate (Me_2bpdc) was used as the starting material to access the common intermediate Me_2bpdc-NH_2, which can be readily used as a platform for further functionalisation. On the one hand, Me_2bpdc-NH_2 can be hydrolysed to form H_2bpdc-NH_2 as one of the desired ligands; on the other hand, Me_2bpdc-NH_2 can be alkylated to generate Me_2bpdc-NH(allyl), Me_2bpdc-N(allyl)$_2$ and Me_2bpdc-NMe_2. These diester compounds could be hydrolysed to generate each of the ligands. To confirm the purity of the linkers, the products were characterised by ^{1}H and ^{13}C NMR spectroscopy and elemental analysis.

Me_2bpdc was nitrated under standard electrophilic conditions as reported in the literature.[6, 29] The product, Me_2bpdc-NO_2, was isolated in yields up to 98% yield, which is consistent with the yield reported in the literature (97%).[30]

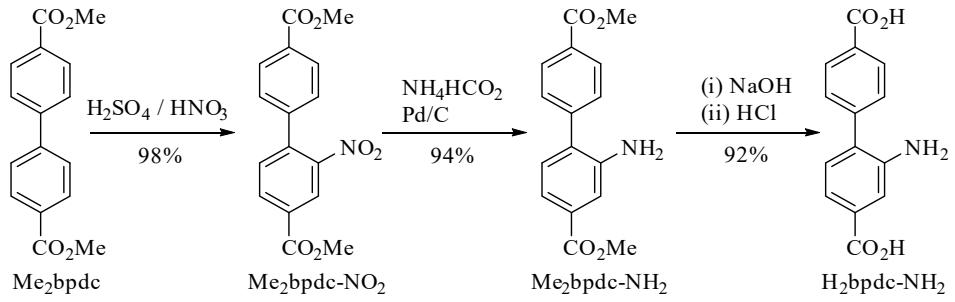

Scheme 5.1 The synthesis path of H_2bpdc-NH_2.

The second step of this sequence was reduction of the nitro group to the primary amine. There are several methods reported in the literature for this transformation, including Sn/HCl and Fe/AcOH.[22, 31] Here, this transformation was accomplished using ammonium formate with Pd/C as a catalyst in hot MeOH/THF solution. The crude product of this reaction was purified by column chromatography using chloroform as eluent to afford the product in a 94% yield. The purification was performed at this step to separate un-nitrated Me_2bpdc. The nitration reaction gives a mixture of Me_2bpdc and Me_2bpdc-NO_2 which are very close in R_f; thus, it is impossible to separate unreacted starting material after nitration. This is a comparable yield with yields previously published in the literature (higher than 94%).[30, 26, 27,] This convenient two-step sequence gave an efficient pathway to multigram amounts of Me_2bpdc-NH_2 for the synthesis of H_2bpdc-NHallyl and H_2bpdc-N(allyl)$_2$ and H_2bpdc-NMe_2.

Following hydrolysis using aqueous NaOH in MeOH/THF solution and aqueous acidic workup, H_2bpdc-NH_2 was obtained as a yellow powder in 92% yield.

5.2.1.2 *Synthesis of H_2bpdc-NHallyl*

Reaction of Me_2bpdc-NH_2 with allyl bromide in DMF in the presence of K_2CO_3 gives Me_2bpdc-NHallyl. Control over the stoichiometry, time and temperature of this reaction is crucially important in obtaining good yields. Reactions were conducted with an equimolar ratio of allyl bromide to Me_2bpdc-NH_2 as further allylation gives mixtures of Me_2bpdc-NHallyl and Me_2bpdc-N(allyl)$_2$, which are very close in R_f and not possible to

separate easily or in high yield by conventional flash chromatography on silica gel or by recrystallisation. The reaction was run so that the final mixture contained Me_2bpdc-NH_2 and Me_2bpdc-NHallyl which are easily separable by chromatography on silica gel. The temperature of 70 °C was found to give reasonable reactivity of Me_2bpdc-NH_2 without Me_2bpdc-NHallyl undergoing appreciable further allylation. Using this methodology Me_2bpdc-NHallyl could be isolated in 57% yield and the unreacted Me_2bpdc-NH_2 could be recovered and re-used. Hydrolysis of Me_2bpdc-NHallyl using aqueous NaOH in a solvent mixture of MeOH/THF followed by careful aqueous acidic workup precipitated H_2bpdc-NHallyl as a yellow powder that was collected by filtration in 97% yield (Scheme 5.2, Pathway A).

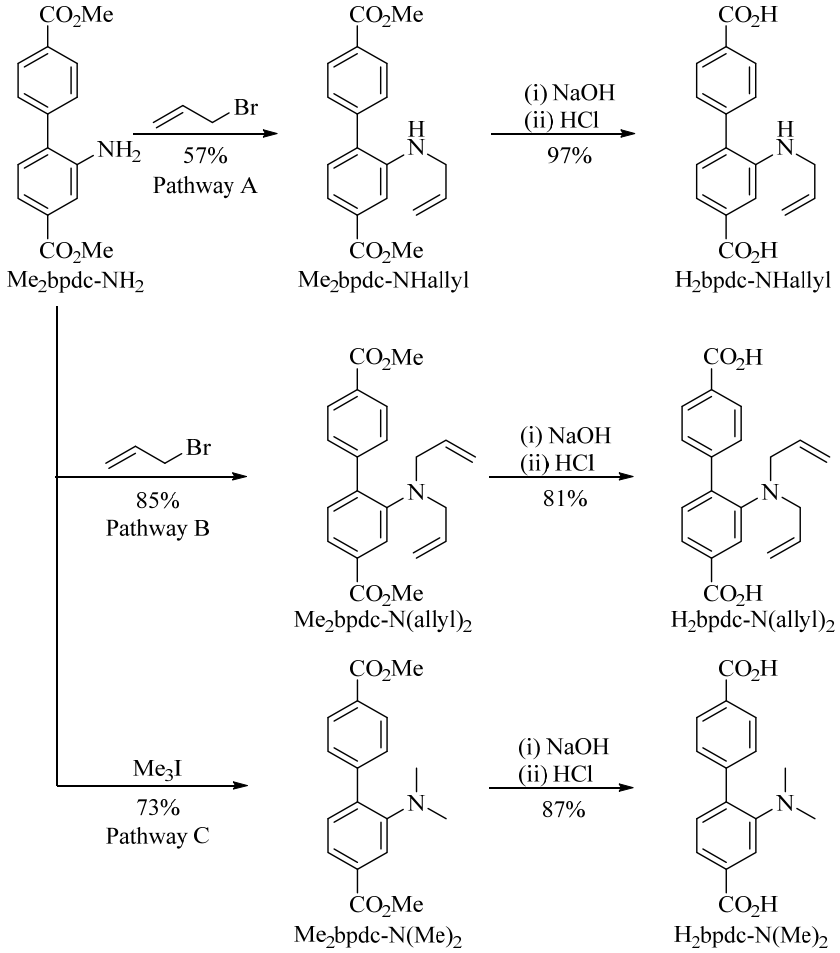

Scheme 5.2 The synthetic pathways to H_2bpdc-NHallyl, H_2bpdc-N(allyl)$_2$ and H_2bpdc-NMe_2.

5.2.1.3 *Synthesis of H_2bpdc-N(allyl)$_2$*

The synthesis of Me_2bpdc-N(allyl)$_2$ does not incur the same over-allylation problems as Me_2bpdc-NHallyl. The reaction was carried out with 3 equivalent of allyl bromide at 80 °C in DMF solution with powdered K_2CO_3 to neutralise the HBr by-product (Scheme 5.2, Pathway B). Even with the excess equivalents of allylating agent, formation of the quaternary salt, Me_2bpdc-N(allyl)$_3$Br, is not detected. This is presumably due to the allyl substituents sterically shielding the amine nitrogen from further alkylation. Under this set of conditions Me_2bpdc-N(allyl)$_2$ was obtained in 85% isolated yield. The standard aqueous NaOH hydrolysis was used and with careful acidification H_2bpdc-N(allyl)$_2$ was precipitated as a yellow powder and isolated in 81% yield by filtration.

5.2.1.4 *Synthesis of H_2bpdc-NMe_2*

A dialkylation approach using methyl iodide and $NaHCO_3$ as reagent and base, respectively, was used for the synthesis of Me_2bpdc-NMe_2 (Scheme 5.2, Pathway C). Due to the smaller size and greater reactivity of methyl iodide leading to the undesired formation of a quaternary amine salt, Me_2bpdc-NMe_3I, this procedure required greater control than the reaction to produce the diallyl amine in Me_2bpdc-N(allyl)$_2$. Under optimised conditions, the methylation reaction gave a good conversion and Me_2bpdc-NMe_2 could be isolated in a respectable yield of 73%. This was hydrolysed using aqueous NaOH in the MeOH/THF conditions at room temperature. It was particularly important to control the pH in the aqueous work up to obtain good precipitation of the product. However, with care, H_2bpdc-NMe_2 can be precipitated as a bright yellow coloured powder and collected by filtration in 87% isolated yield.

5.2.2 Syntheses and structure and refinements of amine-functionalised IRMOFs

The synthesis of IRMOF-NH_2, IRMOF-NHallyl, IRMOF-$N(allyl)_2$ and IRMOF-NMe_2 was conducted using established solvothermal reaction conditions, by heating $Zn(NO_3)_2 \cdot 6H_2O$ and the corresponding dicarboxylic acids in DMF at 100 °C for 24 hours.[32] Large crystals formed in each reaction and were stored under fresh DMF.

Single crystal X-ray crystallographic studies were performed on the amine-functionalised IRMOFs and the asymmetric units are plotted in Figure 5.3. Single crystal studies confirmed that IRMOF-NH_2, IRMOF-NHallyl and IRMOF-$N(allyl)_2$ crystallised in the tetragonal space group *P*-42$_1$*m*, and the structure of IRMOF-NMe_2 crystallises in the trigonal space group *R*-3. Crystal data and refinement details for amine-functionalised IRMOFs are presented in Appendix 3, Table A5.1.

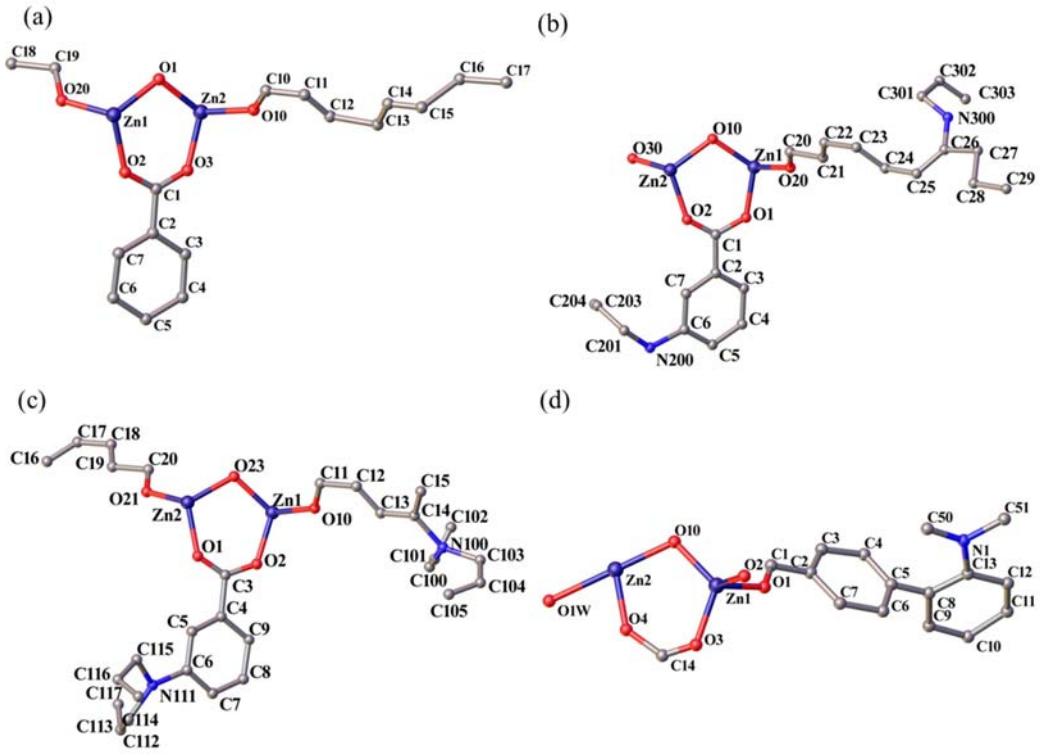

Figure 5.3 Asymmetric units of (a) IRMOF-NH_2, (b) IRMOF-NHallyl, (c) IRMOF-$N(allyl)_2$ and (d) IRMOF-NMe_2.

As shown in Figure 5.3a, the asymmetric unit of IRMOF-NH_2 consists of two Zn atoms (Zn1 and Zn2) and two half-ligands. Zn1 and Zn2 lie on mirror planes, and are bridged by one μ-oxido atom (O1) which itself is bisected by two orthogonal mirror planes, and two oxygen atoms (O2 and O3) from a carboxylate group of a half-ligand. Zn2 is coordinated to another carboxylate oxygen atom (O10) by another half-ligand. The atoms O10, C12, C13, C15, C16 and C17 lie along a mirror plane. The rest of the ligand (C10, C11, C14, C18 and C19) lies on the intersection of two mirror planes.

As shown in Figure 5.3b, the features in asymmetric unit of IRMOF-NHallyl are the same as IRMOF-NH_2. It contains two Zn atoms, two half linkers and one oxido-atom. Zn atoms lie on a mirror plane, and are bridged by one μ-oxo atom (O10) and two oxygen atoms of a half biphenyl consisting of an attached tag group (O1, O2, C1–C6, N200, C201-C204) with full occupancy. The asymmetric unit is completed by linking the Zn1 to a second half ligand containing a full tag group (O20, C20–C29, N300, C301–303), in which the atoms O20, C22–C23 and C26–C27 lie on the mirror plane.

The asymmetric unit of IRMOF-N(allyl)$_2$ (Figure 5.3c) consists of two Zn atoms (Zn1 and Zn2) and three half organic linkers, wherein Zn1 and Zn2 lie on mirror planes. The Zn atoms are connected by an oxido atom (O23) and two oxygen atoms of a half-ligand bearing a pendant group. The half-linker has full fixed occupancy (O1, O2, C3–C9), with the tag group (N111, C112–C117) lying on a mirror plane. Two half-phenyl rings are coordinated to Zn1 and Zn2, in which Zn1 is connected to a half-phenyl ring lying on a mirror plane (O10, C13- C15, N100, C100–C105). Zn2 is bridged by another half-phenyl ligand (O21, C16–C20).

Single crystal X-ray crystallography of IRMOF-NMe_2 (shown in Figure 5.3d) revealed the asymmetric unit of IRMOF-NMe_2 contains two Zn atoms (Zn1 and Zn2) and a bridging ligand with full occupancy connected to Zn1. Zn1 and Zn2 are bridged by one oxido atom (O10) and O3, O4 and C14 with full occupancy. Zn2 is linked to O1W which lies on mirror plane.

The positions of functional groups within the pores are important for the gas sorption properties. In amine-functionalised IRMOFs the tag groups could not be found in the crystallography, and they were implanted in the structure in chemically reasonable positions. This allows calculation of the surface area of the amine-functionalised IRMOFs with fixed positions of the linkers.

5.2.2.1 *Description of the SBUs in amine-functionalised IRMOFs*

The crystal structure studies indicated the SBUs of the IRMOF-NH_2, IRMOF-NHallyl and IRMOF-N(allyl)$_2$ were the same $Zn_4O(CO_2)_6$ clusters, as displayed in Figures 5.4a and b. The SBUs are built from four ZnO_4 tetrahedral units and six bridging carboxylates to give octahedral $Zn_4O(CO_2)_6$ clusters. The central oxygen is coordinated to four zinc atoms to form a Zn_4O tetrahedral sub-cluster, and the edge of each Zn is bridged by -CO_2 groups to form a $Zn_4O(CO_2)_6$ cluster. Similar structures containing $Zn_4O(CO_2)_6$ SBUs have been published previously in the literature.[7, 3] In IRMOF-NMe_2, the SBU is slightly different compared to IRMOF-NH_2, IRMOF-NHallyl and IRMOF-N(allyl)$_2$. This SBU consists of the same general arrangement as for the other MOFs but in addition there is one coordinated water molecule to a Zn atom. As it is shown in Figure 5.4c, one water molecule (O1W) is coordinated to Zn2 which results in the coordination number for Zn2 of five. The geometry of Zn2 is trigonal bipyramidal (Figure 5.4d); rather than the tetrahedral geometry seen for the other zinc atoms; thus, the SBU in this structure consisted of three tetrahedral ZnO_4 SBU-units and one trigonal bipyramidal ZnO_5 unit.

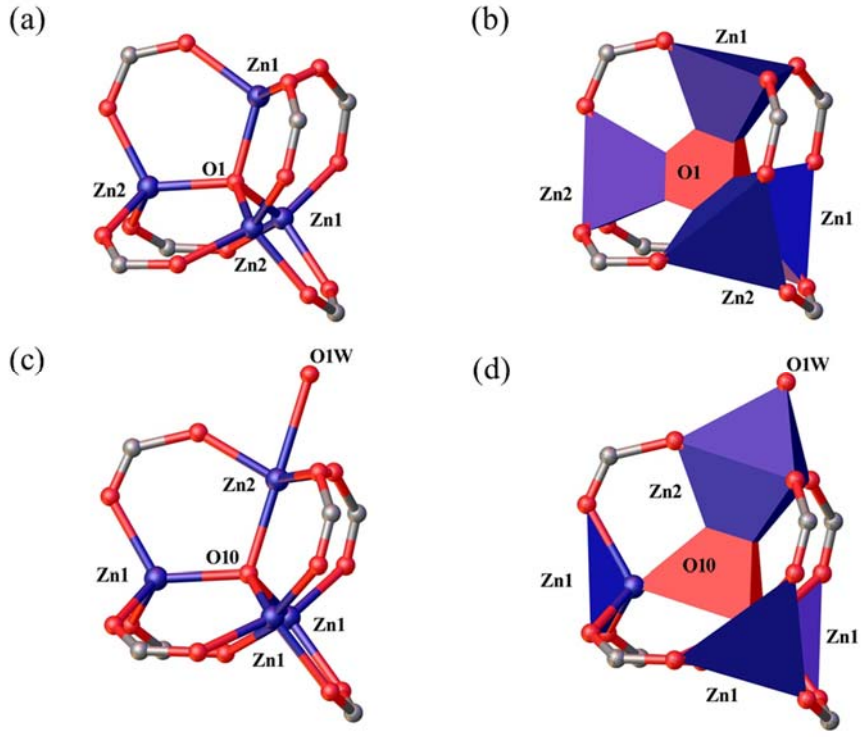

Figure 5.4 The $Zn_4O(CO_2)_6$ clusters of IRMOF-NH_2, IRMOF-NHallyl and IRMOF-N(allyl)$_2$ in (a) ball and stick representation and (b) polyhedral representation, and the $Zn_4O(CO_2)_6$ clusters of IRMOF-NMe_2 in (c) ball and stick representation and (d) polyhedral representation (Zn = blue, O = red and C = grey).

5.2.2.2 *Description of the three dimensional structures of amine-functionalised IRMOFs*

The octahedral SBUs lead to three dimensional cubic networks with Zn_4O units as the vertexes and organic linkers as the edges. Single crystal X-ray crystallography determined that structures of IRMOF-NH_2, IRMOF-NHallyl and IRMOF-NMe_2 are doubly interpenetrated and are therefore functionalised analogues of IRMOF-N(allyl)$_2$. The first crystal of IRMOF-N(allyl)$_2$ used for single crystal X-ray analysis was found to be non-interpenetrated and therefore a functionalised IRMOF-10 analogue. However, N_2 adsorption-desorption studies at 77 K (discussed in section 5.3.1) provided data that was consistent with IRMOF-9 being doubly interpenetrated. Furthermore, a thorough examination showed some crystals in the as-synthesised sample extinguished under cross polarisation, indicating these crystals belong to a cubic space group and that there existed

a mixture of phases in the sample. Cross polarisation is a common technique in single crystal diffraction to assess crystal quality by viewing the crystal while rotating polarising filters. For every crystal system except cubic, crystals extinguish the light. In this way, crystals belonging to cubic space groups are identified easily Thus, it seemed the sample contained a mixture of interpenetrated and non-interpenetrated framework crystals. Hence, it was assumed that a crystal of non-interpenetrated IRMOF-N(allyl)$_2$ was randomly selected to be analysed by SCXRD.

Biphenyl-4,4′-dicarboxylic acid ligands carrying bulky substituents are observed to form non-interpenetrated IRMOF-10 type structures. For example, Telfer and co-workers reported the synthesis of non-interpenetrated IRMOF-10 using bpdc-based ligands carrying various bulky substitutents such as N-Boc-proline, *tert*-butylcarbamate and nitrobenzyl groups. They indicated these chemical groups exhibit sufficient steric bulk to prevent interpenetration.[30, 31, 8]

Further single crystal analyses on IRMOF-N(allyl)$_2$ showed some crystals to be in the tetragonal space group *P*-421*m*. Powder X-ray diffraction studies (discussed in section 5.2.4) were not particularly helpful in distinguishing the proportions of the phases. In many interpenetrated IRMOF-9 phases, there is subtle peak splitting at ~5 and ~10 in 2θ that can be used for phase identification.[33] However, many of the large crystals that form under these synthetic conditions are intergrown and contain portions that show extinction as well as portion that do not show extinction under plane polarised light. This perhaps indicates the delicate balance between the interpenetration versus interpenetration in this system. A contributing factor to this situation might be the deallylation phenomenon that occurs for this MOF (discussed in section 5.2.5.1) which manifests in approximately 18% of the larger diallyl amine tag group being converted to the allyl amine group.

With as-synthesised IRMOF-N(allyl)$_2$ existing as a mixture of interpenetrated and non-interpenetrated phases yet the gas adsorption data more closely being consistent with the interpenetrated form, it suggested that IRMOF-N(allyl)$_2$ was undergoing an

autocatenation process from the as-synthesised sample into the activated form used for gas adsorption. This study is discussed in section 5.2.3.

A structure representative of IRMOF-NH_2, IRMOF-NHallyl and IRMOF-$N(allyl)_2$ is shown in Figure 5.5a and b and IRMOF-NMe_2 is shown in Figure 5.5c and d. As it can be seen, the MOFs show doubly interpenetrated networks; however, IRMOF-NH_2, IRMOF-NHallyl and IRMOF-$N(allyl)_2$ show a different type of interpenetration compared to IRMOF-NMe_2.

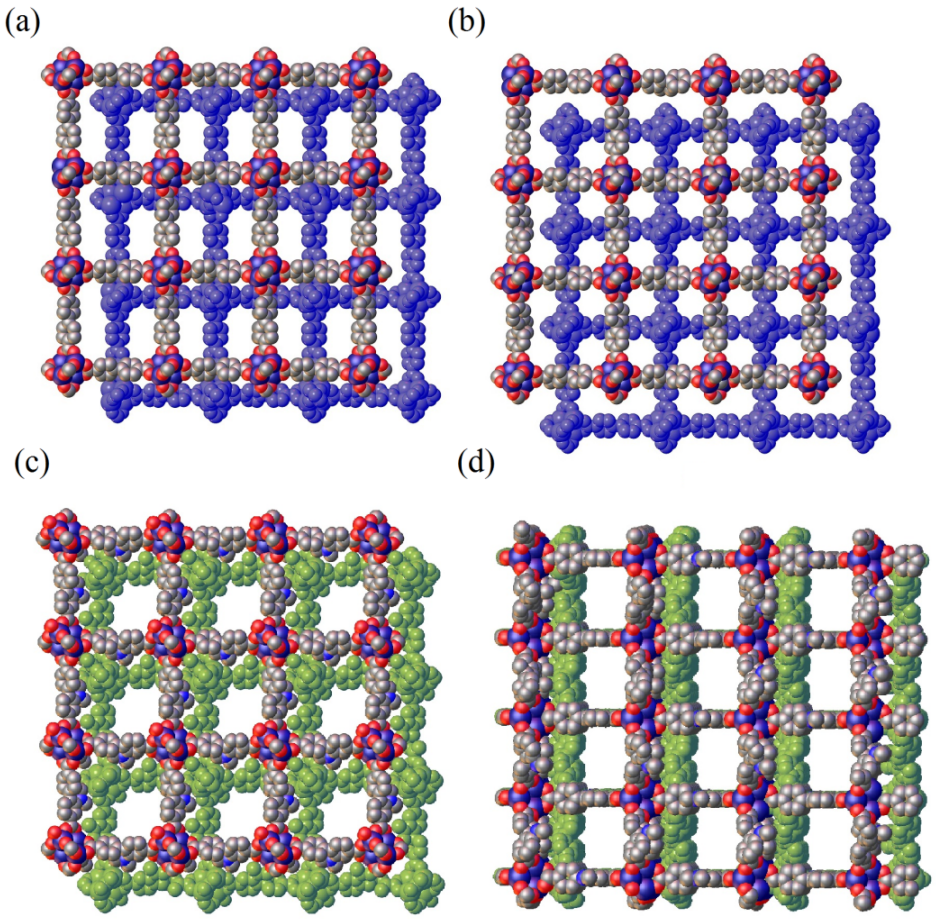

Figure 5.5 Representative views of the 3D structure of IRMOF-NH_2, IRMOF-NHallyl and IRMOF-$N(allyl)_2$ (a) along the *b*-axis and (b) along the *c*-axis and of IRMOF-NMe_2 (c) along the *b*-axis and (d) along the *c*-axis.

The type of interpenetration and pore size vary due to the nature and size of the functional groups. The types of interpenetrated structures of IRMOF-9 analogues can be classified according to three reported structural types in the literature (Figure 5.6). In Type I, the SBU of the second structure is located precisely in the centre of the first framework, and is equidistant from all other vertices.[34] Type II interpenetrated networks exhibit a second network node that lies equidistant from four vertices. Thus, the node can take any position from, but not including, the body centre towards a face-centred position in a cubic unit. It cannot exist in the face-centred position because of steric clashing with edges of the parent framework that are occupied by bridging ligands.[8] Within Type III interpenetrated frameworks, the node of the second framework resides nearest to only one of the nodes of the first framework. In principle, the nodal relationship in this type of interpenetration can take any position the Type I and Type II cannot take.

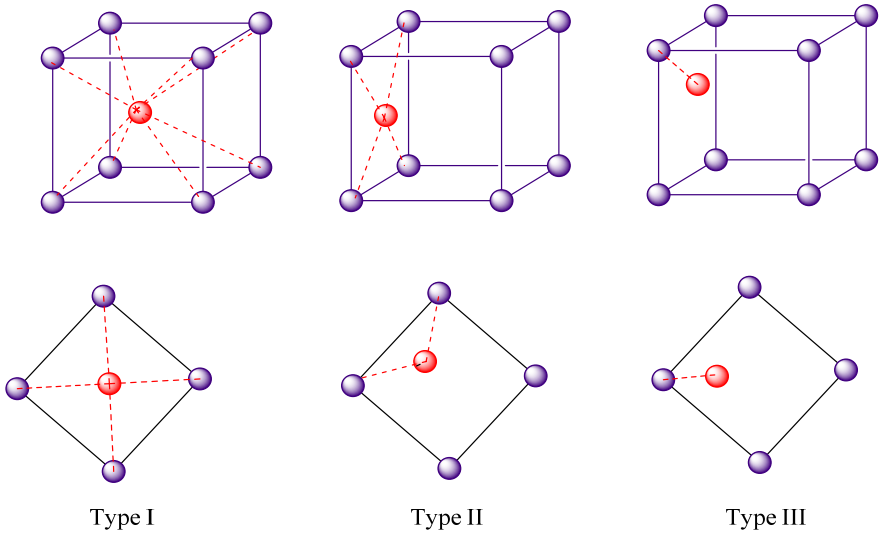

Figure 5.6 Types of interpenetration structures of IRMOF-9 analogues, Type I, Type II and Type III.

Perspective view of the 3D structures of amine-functionalised IRMOFs showed various types of interpenetration and pore sizes suggesting functionalisation of linker and the size of pendant group impact on position of the formation of the nodes of the second framework. The single crystal X-ray diffraction analysis showed IRMOF-NH_2, IRMOF-NHallyl and IRMOF-N(allyl)$_2$ have the nodes of the second framework equidistant from

four vertices, characteristic of Type II interpenetration. In IRMOF-NMe_2, the SBU in the second framework is closest to one of the nodes of the first cubic framework (Type III).

As suggested in the literature, there was observed a correlation between the size of the pendant attached groups, and the size of the pores.[7, 35] In IRMOF-NH_2 the smaller tag group has the larger pore diameter in 9.93 Å and 15.24 Å. Functionalisation of primary amine into secondary and tertiary amines resulted in a decrease in the pore sizes. The pore sizes were 9.69 Å and 14.72 Å in IRMOF-NHallyl and 9.46 Å and 13.25 Å in IRMOF-$N(allyl)_2$. IRMOF-NMe_2, with Type III interpenetration, showed pore sizes of 15.61 Å and 6.55 Å.

A representative view of pore size measurement for these MOFs is presented in Appendix 3, Figure A3.1.

5.2.3 A study of the autocatenation of IRMOF-N(allyl)$_2$

Telfer has suggested three methods for autocatenation processes: (i) a solvothermal process, (ii) desolvation of the crystals, and (iii) mechanical shearing. [34] Given the occurrence of the mixture of phases (potentially coupled with levels of partial interpenetration) encountered with IRMOF-N(allyl)$_2$, the aim of this investigation was converting non-interpenetrated to fully interpenetrated IRMOF-N(allyl)$_2$. Of the methods suggested by Telfer and co-workers, solvothermal heating and desolvation seemed most suited for the range of analysis techniques available.

5.2.3.1 *Solvothermal heating experiment of IRMOF-N(allyl)$_2$*

In this experiment, crystals of IRMOF-N(allyl)$_2$ were heated at 85 °C in DMF for 48 hours. Two crystals were chosen to be monitored by inspection under a microscope, shown in Figure 5.7. The sizes of the crystals were measured before doing the experiment and then afterward. The crystals numbered 1 and 2 showed size reductions of about 4.2% and 5.5%, respectively.

A solvothermal heating experiment was performed on ten more crystals and the crystals were analysed by SCXRD. This study showed that crystals extinguished under cross polarisation, and belonged to the interpenetrated phase. This result suggested this experiment delivered the mixture of frameworks to homogenous interpenetrated crystals.

Table 5.1 Solvothermal heating experiment of IRMOF-N(allyl)$_2$, and the sizes of the crystals before and after solvothermal heating experiment.

Entry	Before (mm)	After (mm)
Crystal 1	0.751 × 0.701	0.729 × 0.692 (4.2 %)
Crystal 2	0.823 × 0.771	0.806 × 0.744 (5.5 %)

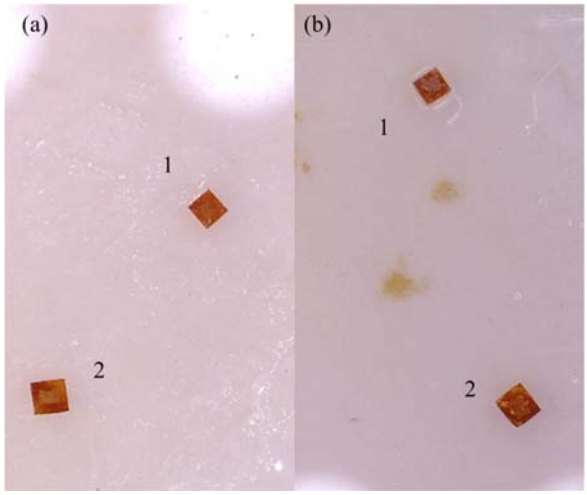

Figure 5.7 Crystals 1 and 2 of IRMOF-N(allyl)$_2$ (a) before and (b) after solvothermal heating experiment.

5.2.3.2 *Desolvation experiment of IRMOF-N(allyl)$_2$*

The desolvation experiment of IRMOF-N(allyl)$_2$ was performed on seven crystals over a period of 48 hours. In this time, the DMF molecules escape from the pores, and consequently a volume reduction occurs.[34] This experiment was monitored by optical microscopy, and the dimensions of the crystals were measured after after 1, 2, 3, 24 and 48 hours. Images of the IRMOF-N(allyl)$_2$ of the crystals and a view of crystal 9, after 1, 24 and 48 hours are presented in Figure 5.8a–g. The volume reductions of the crystals over the 48 hours are presented in Figure 5.9 and summarised in Table 5.2. Two crystals (number 3 and 6) were not good quality crystals; as they were seen to be damaged after magnifying to measure their sizes (Table 5.2, entries 3 and 6). The major size reduction occurred in the first one hour of the process. The crystals numbered 1, 2, 4, 5, 7 and 9 showed volume reductions of about 11% × 10% after one hour. The crystals also showed reduction in volume after 48 hours (18% × 22%). The results are comparable with the experiment reported by the Telfer group. They studied the autocatenation of non-interpenetrated α-MUF-9 to interpenetrated β-MUF-9, by desolvation over a period of 200 minutes. The experiment was monitored by SCXRD which showed full autocatenation occurring by 200 minutes. The optical microscopy showed reduction in volume of the crystals by around 25%.[36]

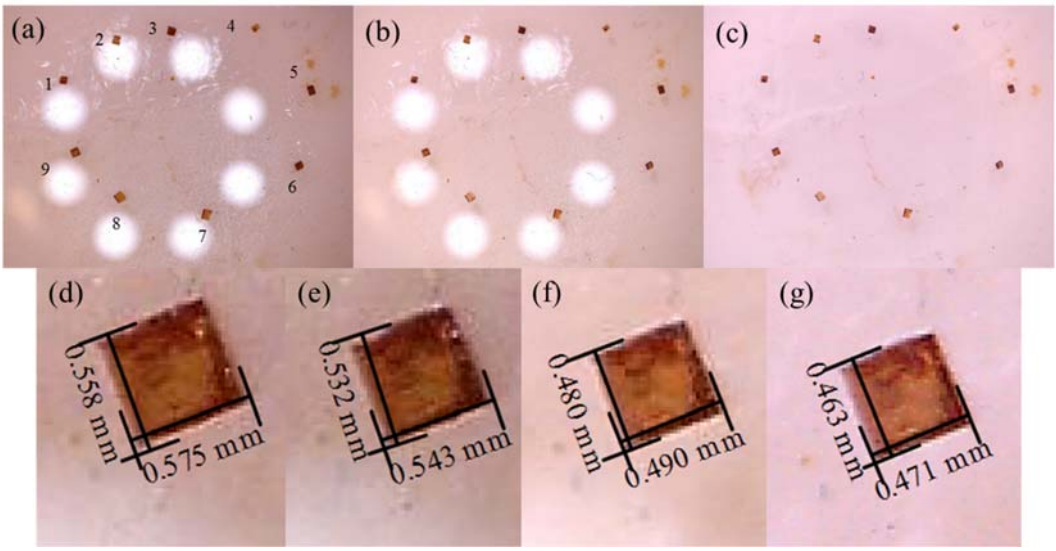

Figure 5.8 Images of IRMOF-N(allyl)$_2$ (a) at the start, (b) after 1 hour (c) after 48 hours, and views of crystal 9 with highest magnification (d) at the start, (e) after 1 hour, (f) after 24 hours and (g) after 48 hours of the desolvation experiment.

^{1}H NMR analysis performed on as-synthesised IRMOF-N(allyl)$_2$ crystals and after the autocatenation experiment. The sample preparation was carried out by filtration of the crystals and then air-drying for 5 minutes. The ^{1}H NMR spectrum confirmed the number of DMF molecules reduced from six to three molecules per unit cell after 48 hours.

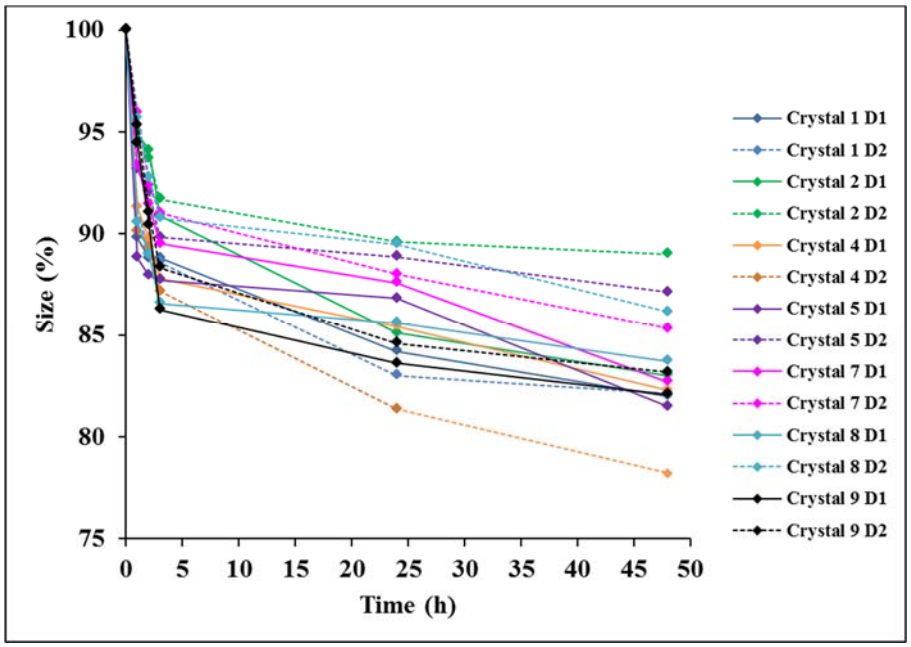

Figure 5.9 Desolvation experiment measurements of IRMOF-N(allyl)$_2$ crystala and the volume reductions of the crystals over 48 hours. D1 and D2 represent the dimensions for each crystal.

Table 5.2 Desolvation process experiment measurements of IRMOF-N(allyl)$_2$ at start, after 1, 24 and 48 hours of the experiment, in mm and percentage.

Entry	T = 0	T = 1 h (mm)	T = 24 h (mm)	T = 48 h (mm)
1	0.501 × 0.507 (100% × 100%)	0.450 × 0.463 (89.8% × 91.3%)	0.422 × 0.421 (84.2% × 83.0%)	0.411 × 0.416 (82.0% × 82.1%)
2	0.495 × 0.555 (100% × 100%)	0.470 × 0.527 (94.9% × 95.0%)	0.421 × 0.497 (85.1% × 89.6%)	0.411 × 0.494 (83.0% × 89.0%)
3	Not a good crystal	Not a good crystal	Not a good crystal	Not a good crystal
4	0.508 × 0.413 (100% × 100%)	0.464 × 0.372 (91.3% × 90.1%)	0.434 × 0.336 (85.4% × 81.4%)	0.418 × 0.323 (82.3% × 78.2%)
5	0.448 × 0.629 (100% × 100%)	0.398 × 0.586 (88.8% × 93.1%)	0.389 × 0.559 (86.8% × 88.9%)	0.365 × 0.548 (81.5% × 87.1%)
6	Not a good crystal	Not a good crystal	Not a good crystal	Not a good crystal
7	0.572 × 0.668 (100% × 100%)	0.534 × 0.641 (93.4% × 96.0%)	0.501 × 0.588 (87.6% × 88.0%)	0.473 × 0.570 (82.7% × 85.3%)
8	0.626 × 0.650 (100% × 100%)	0.567 × 0.622 (90.6% × 95.7)	0.536 × 0.582 (85.6% × 89.5%)	0.524 × 0.560 (83.7% × 86.2%)
9	0.575 × 0.558 (100% × 100%)	0.543 × 0.532 (94.4% × 95.3%)	0.490 × 0.480 (83.6% × 84.6%)	0.471 × 0.463 (81.9% × 83.0%)

5.2.4 Powder X-Ray Diffraction

Powder X-ray diffraction measurements were recorded to confirm the crystallinity and phase purity of the amine-functionalised IRMOFs. Figure 5.10 shows the data recorded for as-synthesised and activated MOFs, in addition to simulated PXRD patterns based upon the determined crystal structures.

Some differences in peak intensities of simulated patterns to recorded patterns arise from guest molecules within the MOF pores. The simulated patterns of the MOFs are calculated without solvent molecules within the pores.

As discussed in section 5.2.3.3, "as-synthesised" IRMOF-N(allyl)$_2$ is a mixture of two phases. Snurr and co-workers reported non-interpenetrated IRMOF-16-like compounds in a mixture with interpenetrated IRMOF-15 crystals. To prove their hypothesis, they used a combination of experimental and geometrical analysis such as TGA, PXRD and pore size analysis. They simulated PXRD patterns with 2-fold interpenetration, 2-fold interweaving, 3-fold interpenetration and 3-fold interweaving. The team discovered the PXRD peaks of non-interpenetrated and interpenetrated overlapped. Therefore, it was difficult to prove the purity of the phase based on PXRD alone.[37] In the present study, the experimental PXRD pattern of IRMOF-N(allyl)$_2$ was also similar with the simulated PXRD pattern of the interpenetrated MOF; thus, it was difficult to predict the phase purity of as-synthesised IRMOF-N(allyl)$_2$.

The peak positions of the activated IRMOFs match quite well in comparison with PXRD patterns of the as-synthesised and simulated patterns, implying that no conversion to another structure occurs upon activation of the IRMOFs.

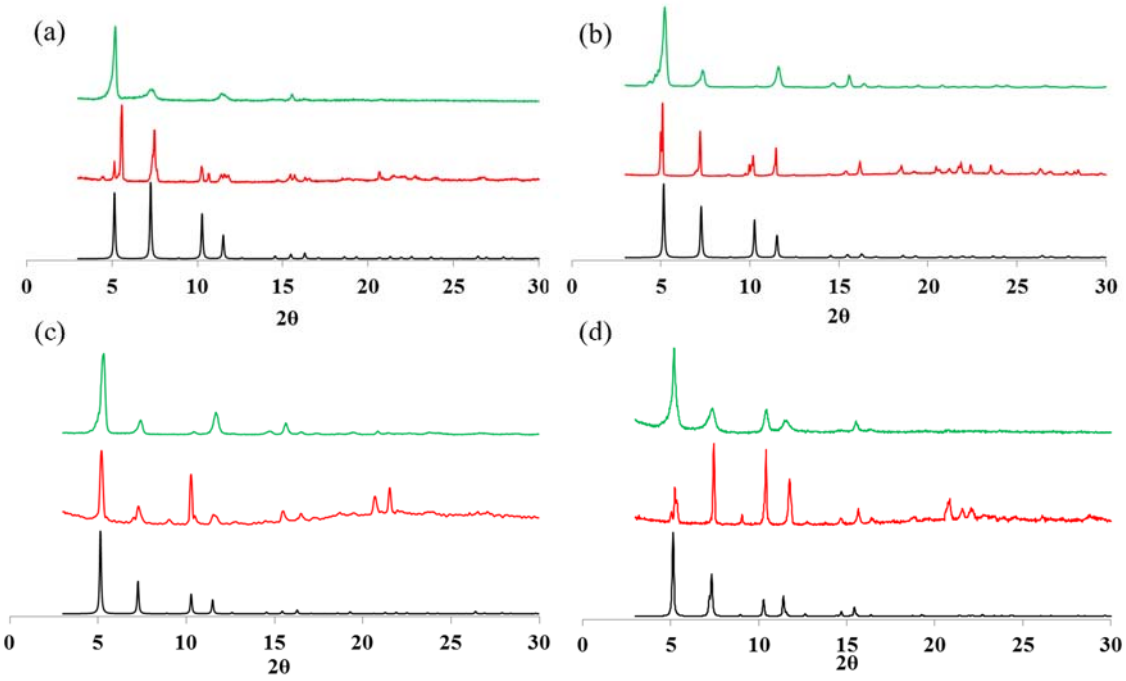

Figure 5.10 PXRD patterns for (a) IRMOF-NH_2, (b) IRMOF-NHallyl, (c) IRMOF-$N(allyl)_2$ and (d) IRMOF-NMe_2. Simulated (black; bottom); 'as-synthesised' (red; centre) 'activated' (green; top).

5.2.5 ^{1}H NMR spectroscopic studies of amine-functionalised IRMOFs

The amine-functionalised IRMOFs were solvent exchanged with CH_2Cl_2 and heated under vacuum to remove the volatiles before being) digested in a solution of DCl/D_2O in *d*$_6$-DMSO at room temperature and recording their ^{1}H NMR spectra. The corresponding linkers of the IRMOFs were dissolved in *d*$_6$-DMSO and their ^{1}H NMR spectra were recorded. The spectra of the IRMOFs and the corresponding linkers in the range of 4.75 to 8.5 ppm are plotted in Figure 5.11 and the full spectra are presented in Appendix 3, Figure A3.3.

The ^{1}H NMR spectra of IRMOF-NH_2 (Figure 5.11a) and IRMOF-NMe_2 (Figure 5.11d) are identical with the corresponding ligands. This shows that the ligands incorporated into these MOFs are unchanged. However, the spectra for IRMOF-NHallyl (Figure 5.11b) and IRMOF-N(allyl)$_2$ (Figure 5.11c) are not identical to the spectra of their respective ligands.

In the ^{1}H NMR spectrum of IRMOF-NHallyl, new peaks appeared in the aromatic region at 7.36 ppm, 7.42 ppm, 7.45 ppm, 7.49 ppm and 8.01 ppm. These are the peak positions of H_2bpdc-NH_2. The presence of the H_2bpdc-NH_2 linker in IRMOF-NHallyl suggested some H_2bpdc-NHallyl had been deallylated during the formation of the MOF. The ratio of H_2bpdc-NHallyl to H_2bpdc-NH_2 was approximately 81% : 19% by integration.

In the ^{1}H NMR spectrum of IRMOF-N(allyl)$_2$, additional peaks appeared in the aromatic region and alkenyl regions that corresponded to the presence of H_2bpdc-NHallyl. As before, this result suggested the deallylation reaction occurred in the formation of IRMOF-N(allyl)$_2$. From the integration of peaks at 5.60 ppm and 5.84 ppm, the ratio of 82 : 18 for H_2bpdc-N(allyl)$_2$ to H_2bpdc-NHallyl was determined.

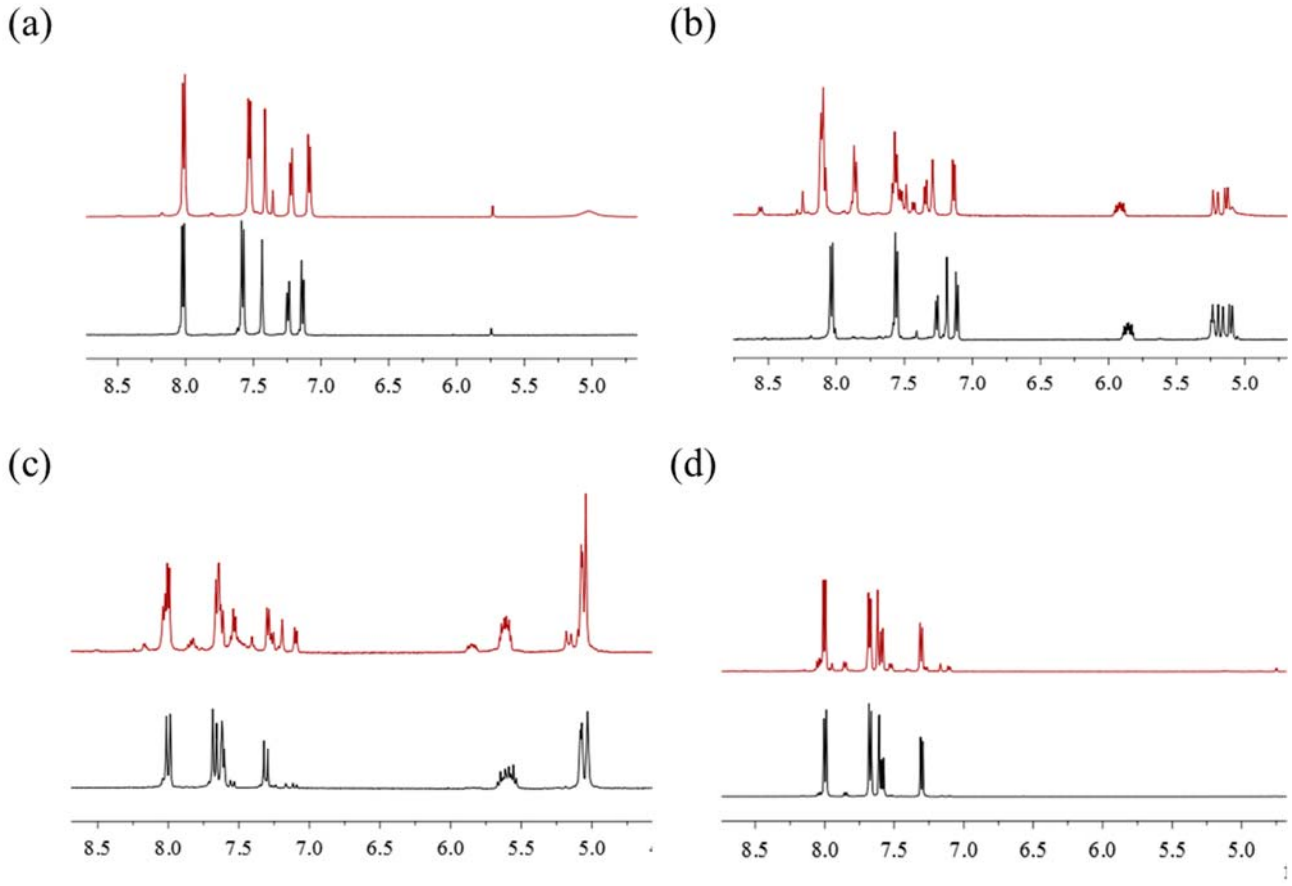

Figure 5.11 ^{1}H NMR spectra of (a) H_2bpdc-NH_2 (black) and digested IRMOF-NH_2 (red), (b) H_2bpdc-NHallyl (black) and digested IRMOF-NHallyl (red), (c) H_2bpdc-N(allyl)$_2$ (black) and digested IRMOF-N(allyl)$_2$ (red) and (d) H_2bpdc-NMe_2 (black) and digested IRMOF-NMe_2 (red) in the range of 4.75 to 8.5 ppm.

5.2.5.1 *C-N bond cleavage studies in IRMOF-NHallyl and IRMOF-N(allyl)$_2$*

Cleavage of the allyl groups led to a transformation of the secondary amine into a primary amine in IRMOF-NHallyl, and the conversion of a tertiary amine into a secondary amine in IRMOF-N(allyl)$_2$. As shown in Scheme 5.3, the final structures of IRMOF-NHallyl and IRMOF-N(allyl)$_2$ consist of mixed linkers. Cleavage of the allyl moieties was investigated with the aim of understanding under what conditions this reaction happened. Toward this goal, control experiments were carried out on the dimethyl ester forms of the ligands.

The control experiment emulated the conditions of MOF synthesis via a reaction between the corresponding diesters (Me$_2$bdc-NHallyl and Me$_2$bdc-N(allyl)$_2$) in the presence of $Zn(NO_3)_2 \cdot 6H_2O$ in DMF at 100 °C for 24 hours. The ^{1}H NMR studies after recovery of the esters showed no C-N cleavage. Thus, deallylation of the tertiary amine and secondary amines was considered to occur during framework formation or after incorporation of the linkers in the structures. This result suggested the presence of the dicarboxylic acid form of the linkers played an important role in the deallylation, and therefore, the deallylation phenomenon might be attributed to either the formation of a Zn intermediate[5] or the Zn_4O SBU in the framework. C-N bond cleavage was reported previously by Kim and co-worker in IRMOF and UiO-66, in which bdc-NMe$_2$ was demethylated to bdc-NHMe. The team demonstrated that approximately 80% and 63%, of the tertiary amine was converted to secondary amine in IRMOF and UiO-66, respectively.[5] In another example, Wang and co-workers reported full C-C σ-bond cleavage in 3-(2′,5′-dicarboxyphenyl)benzoic acid (H$_3$dbba) during synthesis of a zinc MOF. A possible mechanism was suggested, in which coordination of Zn^{2+} to carboxylic acid group and deprotonation of DMF produced an $[ZnH]^+$ intermediate. This is followed by an isomeration and an intramolecular nucleophilic attack which resulted C-C σ bond cleavage to generate the terephthalate and benzoate.[38]

With the aim of understanding the effect of temperature on C-N cleavage phenomenon, MOF syntheses were performed at a lower temperature of 80 °C for IRMOF-NHallyl and

IRMOF-N(allyl)$_2$ but for a longer time of 48 hours and the crystals were characterised by ^{1}H NMR spectroscopy and N_2 adsorption at 77 K.

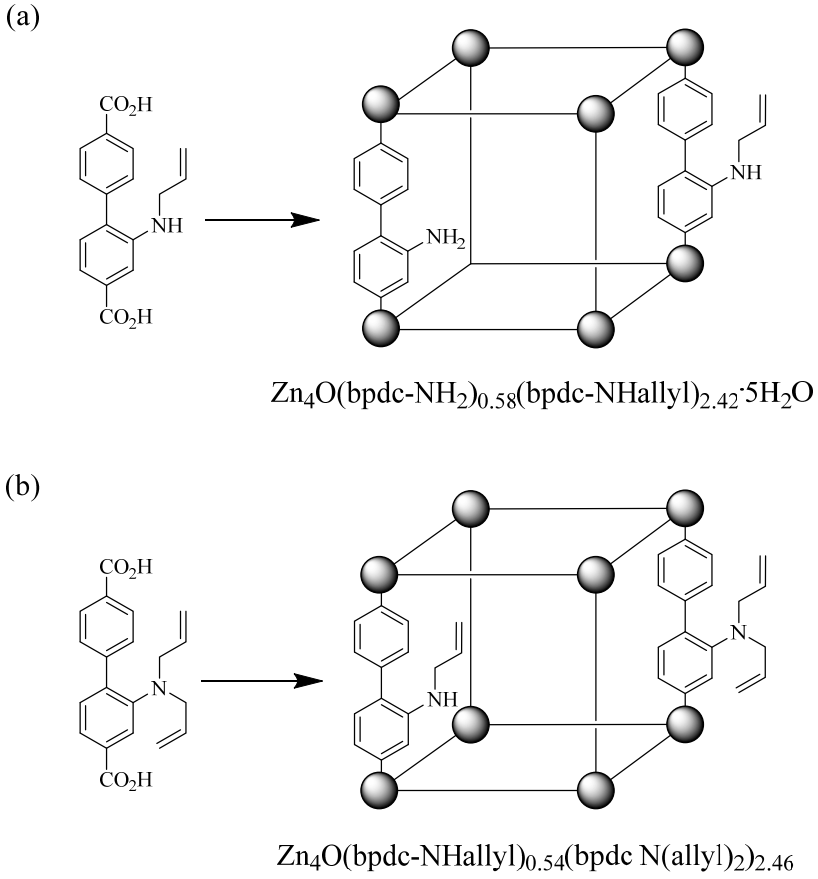

Scheme 5.3 Schematic structures with formulas of (a) IRMOF-NHallyl and (b) IRMOF-N(allyl)$_2$.

Deallylation was confirmed by the presence of the higher amount of primary amine in IRMOF-NHallyl and secondary amine in IRMOF-N(allyl)$_2$ in the ^{1}H NMR spectra after acid digestion of the MOFs. The ratio of the organic linkers was determined by ^{1}H NMR analysis and indicated more C-N cleavage occurred during the synthesis of the MOFs at 80 °C which might be explained by the longer reaction time (48 hours versus 24 hours). In these reactions, the crystals of IRMOF-NHallyl and IRMOF-N(allyl)$_2$ started nucleation after 24 hours; therefore, the reactions required a longer time than the original synthesis in order to obtain a satisfactory yield of crystals. Schematic structures and the formulas of IRMOF-NHallyl and IRMOF-N(allyl)$_2$ upon C-N cleavage are presented in

Scheme 5.3. The values of C-N cleavage in IRMOF-NHallyl and IRMOF-N(allyl)$_2$ at 80 °C and 100° C are presented in Table 5.3.

Table 5.3 The values of C-N cleavage determined by ^{1}H NMR integration in IRMOF-NHallyl and IRMOF-N(allyl)$_2$ at 80 °C and 100° C.

IRMOFs	Synthesis conditions	% of bpdc-N(allyl)$_2$	% of bpdc-NH(allyl)	% of bpdc-NH$_2$	Framework formula
IRMOF-NHallyl	100 °C, 24 h	-	81%	19%	$Zn_4O(bpdc\text{-}NH_2)_{0.58}(bpdc\text{-}NHallyl)_{2.42}$
IRMOF-NHallyl	80 °C, 48 h	-	66%	34%	$Zn_4O(bpdc\text{-}NH_2)_{1.2}(bpdc\text{-}NHallyl)_{1.8}$
IRMOF-N(allyl)$_2$	100 °C, 24 h	82%	18 %	-	$Zn_4O(bpdc\text{-}NHallyl)_{0.54}(bpdc\text{-}N(allyl)_2)_{2.46}$
IRMOF-N(allyl)$_2$	80 °C, 48 h	69%	31 %	-	$Zn_4O(bpdc\text{-}NHallyl)_{0.93}(bpdc\text{-}N(allyl)_2)_{2.07}$

5.2.6 Post-synthetic modification studies of IRMOF-N(allyl)$_2$ to IRMOF-NMe$_2$

The transformation of large diallyl amine groups into smaller dimethylamine substituents is an interesting prospect for the PSM of MOFs. The transformation would be valuable as it would reduce the size of the substituent and increase the basicity. This could be useful for increasing pore space, and potentially, host-guest binding properties.

To first test whether this type of reaction would be possible, a homogenous phase reaction was performed on Me$_2$bpdc-N(allyl)$_2$ using methyl iodide (MeI) as a reagent in DMF solvent (Scheme 5.4a). The aim of this experiment was to determine under what set of conditions this reaction would proceed. The synthesis conditions and results are summarised in Table 5.4.

In the first attempt, the reaction was performed using 10 equivalants of reagent in DMF at 50 ºC for 16 hours. The reaction was monitored by ^{1}H NMR spectroscopy, and showed no conversion of Me$_2$bpdc-N(allyl)$_2$ (Table 5.4, entry 1). In the next step, the temperature was raised to 70 °C (Table 5.4, entry 2), and the same result was obtained. The reaction was continued to 48 hours and to 72 hours (Table 5.4, entry 3 and 4), again the ^{1}H NMR spectroscopy showed only the presence of starting material.

Increasing the temperature to 90 °C for 16 hours (Table 5.4, entry 5) resulted in full conversion of Me$_2$bpdc-N(allyl)$_2$ to Me$_2$bpdc-NMe$_2$. The replacement of allyl by methyl was confirmed by ^{1}H NMR spectroscopy by peak appearing at 2.56 ppm corresponding to the amine methyl groups and the absence of allyl group signals at 5.12 ppm and 5.65 ppm (Figure 5.12a, red).

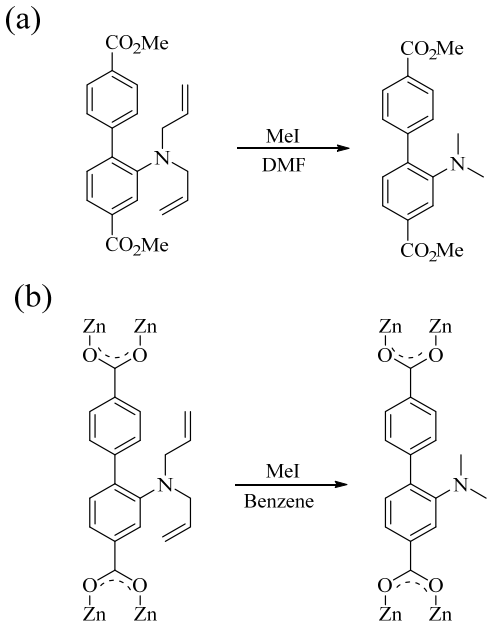

Scheme 5.4 (a) Homogenous reaction of conversion Me_2bpdc-N(allyl)$_2$ to Me_2bpdc-NMe_2 and (b) post-synthetic modification of IRMOF-N(allyl)$_2$ to IRMOF-NMe_2.

Table 5.4 Reaction conditions for conversion of Me_2bpdc-N(allyl)$_2$ to Me_2bpdc-NMe_2 and IRMOF-N(allyl)$_2$ to IRMOF-NMe_2.

	Entry	MeI, eq	Temperature, °C	Time, h	Solvent	Result
1	Me_2bpdc-N(allyl)$_2$	10	50	16	DMF	No conversion
2	Me_2bpdc-N(allyl)$_2$	10	70	16	DMF	No yield determined
3	Me_2bpdc-N(allyl)$_2$	10	70	48	DMF	No yield determined
4	Me_2bpdc-N(allyl)$_2$	10	70	72	DMF	No conversion
5	Me_2bpdc-N(allyl)$_2$	10	90	16	DMF	Full conversion
6	IRMOF-N(allyl)$_2$	10	90	2	DMF	MOF dissolved
7	IRMOF-N(allyl)$_2$	10	90	8	Benzene	No yield determined
8	IRMOF-N(allyl)$_2$	10	90	16	Benzene	No yield determined
9	IRMOF-N(allyl)$_2$	10	90	20	Benzene	No yield determined
10	IRMOF-N(allyl)$_2$	20	110	8	Benzene	No yield determined
11	IRMOF-N(allyl)$_2$	50	90	8	Benzene	No yield determined

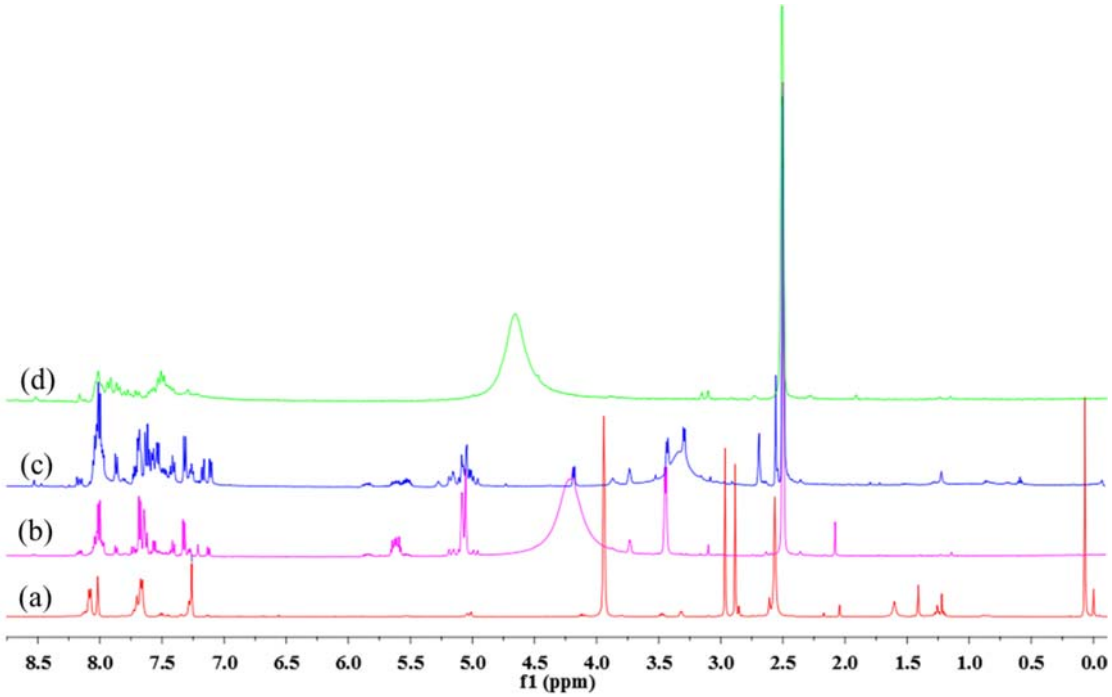

Figure 5.12 The ^{1}H NMR spectra of (a) Me_2bpdc-N(allyl)$_2$ to Me_2bpdc-NMe_2 (red), PSM on (b) IRMOF-N(allyl)$_2$ after 8 hours (magenta), (c) after 16 hours (blue) and (d) after 20 hours (green).

With the conditions established for the transformation of Me_2bpdc-N(allyl)$_2$ to Me_2bpdc-NMe_2, the focus was then to attempt this as a post-synthetic modification on IRMOF-N(allyl)$_2$ (Scheme 5.4b). The first solvent used for the PSM reaction was DMF, the solvent in which the reaction worked for the diester compound. Unfortunately, the crystals of IRMOF-N(allyl)$_2$ dissolved after 2 hours of reaction time in the DMF experiment (Table 5.4, entry 6). The reason for this is likely to be connected to hydriodic acid being produced. This could arise because of hydrolysis of methyl iodide to methanol and HI by the presence of water in the solvent and also as a result of alkylation of the secondary amines present in the structure of IRMOF-N(allyl)$_2$. This necessitated a change in solvent for the PSM reaction. The second solvent used for the PSM reaction was benzene. This was a less desirable choice because it has far less ability than a polar aprotic solvent to stabilise the formation of quaternary amines that are likely intermediates along the pathway of this transformation. Notwithstanding this, it was decided to examine some trial reactions. The reaction was monitored by ^{1}H NMR spectroscopy on digested MOF

samples after 8 (Figure 5.12b) and 16 hours (Figure 5.12c). No methylamine-type signals were seen in the 8 hour sample. The ^{1}H NMR spectrum of crystals digested after 16 hours did show a methylamine-type signal at 2.56 ppm, in addition to remaining -NHallyl and -N(allyl)$_2$ signals. Due to the messy appearance of the aromatic region, it was difficult to integrate and calculate ratios of the linkers in the 16 hour product. Continuing the reaction for 20 hours leads to complete consumption of the N(allyl)$_2$ group but did not confirm the presence of the dimethylamine group (Figure 5.12d). PXRD of the material after 16 hours confirmed the material was crystalline. These results suggest that although the methyl group can be introduced in the solution phase and that the MOF maintains crystallinity, this type of transformation is not easily applicable for the PSM of MOFs.

5.3 Gas sorption studies on amine-functionalised IRMOFs

5.3.1 MOF activation and N_2 sorption isotherms at 77 K

In order to perform gas sorption studies, the MOFs needed to be activated. Activations of IRMOF-NH_2, IRMOF-NHallyl and IRMOF-$N(allyl)_2$ were conducted by solvent exchange followed by freeze drying and heating under vacuum.[32] The as-synthesised samples were immersed in portions of dry CH_2Cl_2 over a period of 3 days to exchange DMF residing in the pores, and the CH_2Cl_2 was then exchanged for dry benzene similarly. The MOF samples in benzene were freeze dried for one hour and then heated under dynamic vacuum at 120 °C for 5 hours (Method 5.1). The samples were used immediately for gas sorption after bringing back to room temperature. The IRMOF-NH_2, -NHallyl and -$N(allyl)_2$ showed reversible Type I isotherm behaviour, which is typical of microporous materials (< 2 nm pore size). The N_2 isotherms for IRMOF-NH_2, IRMOF-NHallyl and IRMOF-$N(allyl)_2$ are shown in Figure 5.13. The surface areas were calculated using the BET equation, the use of which has seen some comment and validation in the literature.[39] IRMOF-NH_2, IRMOF-NHallyl and IRMOF-$N(allyl)_2$ showed accessible BET surface areas of 2245, 2095 and 1600 m^2g^{-1}, respectively (Table 5.5).

TGA traces of the activated MOFs showed no mass losses, indicating perfect activation of the materials (Appendix 3, Section A3.1). The PXRD pattern of the IRMOFs recorded after gas sorption measurements showed excellent matches to the as-synthesised (discussed in 5.2.4), confirming crystallinities are retained after activation of the IRMOF.

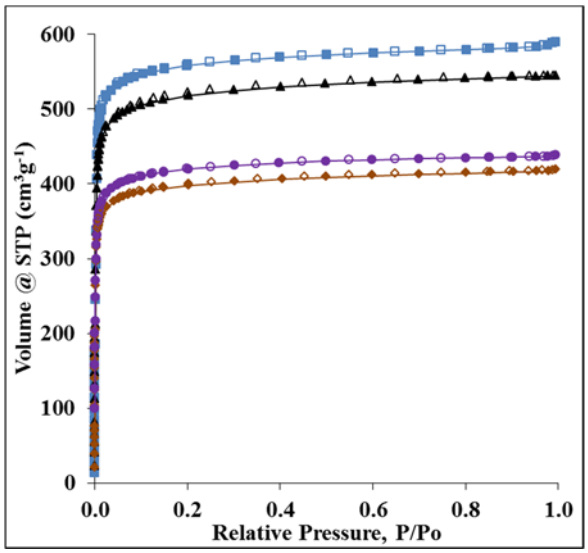

Figure 5.13 The N_2 sorption isotherms at temperature 77 K for IRMOF-NH_2 (blue), IRMOF-NHallyl (black), IRMOF-N(allyl)$_2$ (brown) and IRMOF-NMe_2 (purple). Closed and opened symbols indicate adsorption and desorption, respectively.

Table 5.5 Experimental and calculated BET surface area and total pore volume data from N_2 isotherms at 77 K and from CO_2 at 196 K.

Structure	Surface area from N_2 at 77 K (m^2g^{-1})	Calculated surface area (m^2g^{-1})	Total pore volume from N_2 at 77 K (cm^3g^{-1})	Total pore volume from CO_2 at 196 K (cm^3g^{-1})
IRMOF-NH_2	2245	2522	0.90	0.95
IRMOF-NHallyl	2095	1736	0.84	0.87
IRMOF-N(allyl)$_2$	1600	1050	0.64	0.67
IRMOF-NMe_2	1683	2177	0.67	0.66

The geometric surface areas for all the MOFs were calculated by a collaborator, Dr. Lujia Liu, from the corresponding single crystal structures using a method suggested by Duren[40] and are presented in Table 5.5. The geometrical BET surface areas are calculated from a model of a perfect single crystal of each MOF and it is reasonable to expect that the experimental samples are not perfect and any defects or imperfections will contribute to lower experimental surface areas than the geometric calculations. The experimental surface area of IRMOF-NH_2 is only slightly lower than that of the calculated surface area.

Nevertheless, the good congruence between experimental and theoretical values obtained here gives a good deal of confidence that this sample was well activated.

Seemingly counterintuitively, the experimentally determined surface areas of IRMOF-NHallyl and IRMOF-N(allyl)$_2$ were higher than the calculated surface areas. However, as discussed in section 5.2.5.1, both of these MOFs have a proportion of bridging ligands in their structures that have lost an allyl group. Consequently, these MOFs are composed of mixed linkers in the final structures. In IRMOF-NHallyl , there is 19% of primary amine as a result of deallylation of the allylamine functional group. Likewise, IRMOF-N(allyl)$_2$ contains 18% bpdc-NH(allyl) due to deallylation of bpdc-N(allyl)$_2$. In both cases the result is that a smaller substituent is generated and is part of the resultant frameworks. The geometric surface area calculations were performed on models of IRMOF-NHallyl and IRMOF-N(allyl)$_2$ that contain 100% of NH(allyl) and N(allyl)$_2$ groups, respectively. Therefore, the calculations were run on models with larger substituents in the pore space and the result of higher experimental surface areas can be explained as a result of the C-N cleavage reactions.

Adsorption measurements were recorded on IRMOF-NMe$_2$ which was activated via five methods. The N_2 adsorption measurements at 77 K are plotted in Figure 5.14a with a magnification of the data up to low P/P^o of 0.010 shown in Figure 5.14b for clarification. IRMOF-NMe$_2$ activated using the same procedure as IRMOF-NH$_2$, -NHallyl and -N(allyl)$_2$ (Table 5.6, Method 5.1). The BET surface area calculation indicated a surface area of 235 m^2g^{-1} (Figure 5.14a and b, turquoise). Method 5.2 involved heating the sample from CH_2Cl_2 under dynamic vacuum at 80 °C for 120 minutes followed by increasing the temperature to 120 °C for 300 minutes. The experimental result from this method yielded a small improvement in N_2 uptake (Figure 5.14a and b, magenta), with a surface area of 509 m^2g^{-1} being calculated. Another activation procedure was taken for IRMOF-NMe$_2$ by exchanging the DMF to dry acetone over a period of 3 days followed by $ScCO_2$ processing.[41, 42] The crystals were transferred directly from solution to a mesoporous capsule and placed in the critical point dryer, soaked in portions of liquid CO_2 (3 times, 15 min) to exchange residual solvent, then the temperature and pressure of the chamber

were raised to 40 °C and 100 bar, respectively, for a further of 8 hours before the CO_2 was vented off over a period of 18 hours. After degassing under vacuum at 40 °C for one hour (Method 5.3). A BET surface area of 330 m^2g^{-1} was determined.

$ScCO_2$ processing was used on samples solvent exchanged into dry benzene (Table 5.6 Methods 5.4 and 5.5). With a drying time under vacuum of 30 minutes at 40 °C, the accessible surface area rose to 1142 m^2g^{-1} (Figure 5.14a and b, red). Increasing the time under vacuum to 240 minutes further increased the accessible surface area to 1683 m^2g^{-1} (Figure 5.14a and b, purple). This is likely due to greater removal of residual solvent from the pores owing to the longer vacuum time. This method of activation by $ScCO_2$ through solvent exchange to dry CH_2Cl_2 and benzene has not been previously reported in the literature.

Table 5.6 Solvent exchange and activation procedures for IRMOF-NMe_2 with experimental surface areas data for each method.

Method	**Solvent exchange**	**Activation procedure**	**Heating protocol under dynamic vacuum**	**Surface area from N_2 at 77 K (m^2g^{-1})**
5.1	DMF → CH_2Cl_2 → benzene	Freeze drying	120 °C, 5 hours	235
5.2	DMF → CH_2Cl_2	Vacuum drying	80 °C, 2 hours, following by 120 °C, 5 hours	509
5.3	DMF → acetone	$ScCO_2$	40 °C, 1 hours	330
5.4	DMF → CH_2Cl_2 → benzene	$ScCO_2$	40 °C, 0.5 hours	1142
5.5	DMF → CH_2Cl_2 → benzene	$ScCO_2$	40 °C, 4 hours	1683

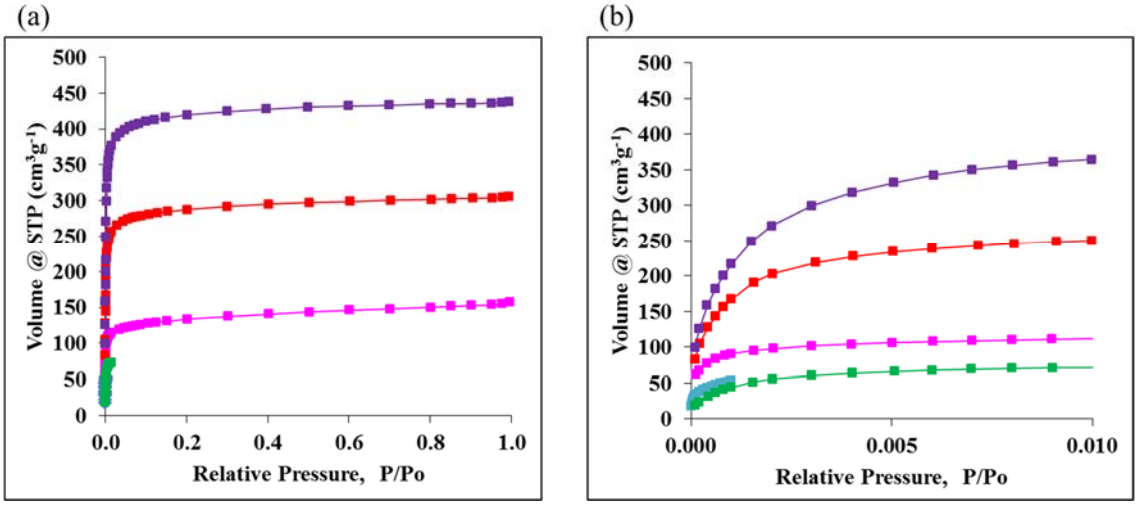

Figure 5.14 N_2 adsorption isotherms at 77 K for IRMOF-NMe_2 activated by Methods 5.1 (turquoise), 5.2 (magenta), 5.3 (green), 5.4 (red) and 5.5 (purple); (a) up to *P/Po* = 1.0 and (b) 0.010.

The N_2 sorption data pointed to a correlation between the size of the pendant group and the BET surface area. IRMOF-NH_2 showed the highest surface area of 2245 m^2g^{-1}, and contains the smallest functional group. The next highest surface area was IRMOF-NHallyl, where the addition of an allyl group led to a reduction in surface area to 2095 m^2g^{-1}. IRMOF-NMe_2 and IRMOF-N(allyl)$_2$ had surface areas of 1683 and 1600 m^2g^{-1}, respectively. As can be seen, BET surface areas were reduced by increasing the size of pendant groups attached. Similar results were previously published for functionalised IRMOF-9 types in the literature, in which larger functional groups resulted in lower surface areas.[35]

As explained in section 5.2.5.1, IRMOF-NHallyl and IRMOF-N(allyl)$_2$ were also synthesised at 80 °C to investigate the impact of temperature on the deallylation phenomenon, and the ^{1}H NMR spectroscopy studies showed more C-N bond cleavage in these MOFs at 80 °C than those synthesised at 100 °C. In IRMOF-NHallyl@80 C there exists 34% of primary amine ligand (*vs* 19% at 100 °C), and IRMOF-N(allyl)$_2$@80 contains 31% NHallyl linker (*vs* 18% at 100 °C). The N_2 sorption isotherms at 77 K were recorded on these samples synthesised at 80 °C to examine any changes in the surface areas. The N_2 isotherm profile of IRMOF-NHallyl@80 showed a very slightly lower N_2

uptake than the crystals grown at 100 °C. In IRMOF-N(allyl)$_2$@80 a higher N_2 uptake was observed in comparison with the crystals grown at 100 °C (Figure 5.15). The BET surface areas were calculated and are summarised in Table 5.7. Due to more deallylation occurring in IRMOF-NHallyl@80 and IRMOF-N(allyl)$_2$@80, higher surface areas were expected and this is the case for IRMOF-N(allyl)$_2$@80; however, the surface areas are essentially the same for the IRMOF-NHallyl samples.

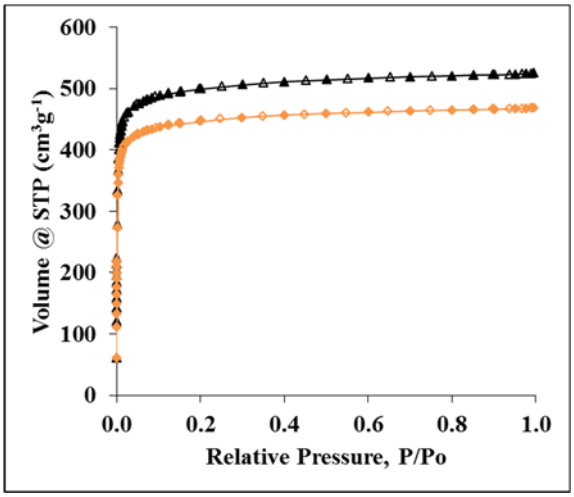

Figure 5.15 N_2 adsorption-desorption isotherms at 77 K for IRMOF-NHallyl@80 (black) and IRMOF-N(allyl)$_2$@80 (orange). Closed and opened symbols indicate adsorption and desorption, respectively.

Table 5.7 BET Surface areas of IRMOF-NHallyl and IRMOF-N(allyl)$_2$ synthesised at 80 °C and 100 °C

Structure	**Synthesis temperature (°C)**	**BET surface area from N_2 at 77 K(calc.) (m^2g^{-1})**
IRMOF-NHallyl	100	2095
IRMOF-NHallyl	80	2002
IRMOF-N(allyl)$_2$	100	1600
IRMOF-N(allyl)$_2$	80	1787

5.3.2 CO_2 adsorption properties of amine-functionalised IRMOFs

5.3.2.1 *CO_2 adsorption–desorption measurements at 196 K*

Adsorption-desorption isotherms of CO_2 at 196 K were measured in order to further investigate the porosity of the set of MOFs and are shown in Figure 5.16. The CO_2 adsorption isotherms at 196 K of each MOF show steep uptake at low pressure followed by even steeper uptake until saturation and then plateau. The shape of the isotherm is Type I and indicative of a high internal to external surface area. These results are consistent with rapid uptake into small pores and then a second period of uptake into larger pores. This was consistent with the results of Doonan who investigated other functionalised IRMOF-9 compounds.[35] Maximum uptakes of 505 cm^3g^{-1}, 465 cm^3g^{-1} and 354 cm^3g^{-1} at 519 Torr were found for IRMOF-NH_2, IRMOF-NHallyl and IRMOF-N(allyl)$_2$, and 351 cm^3g^{-1} at 483 Torr for IRMOF-NMe_2. These values are consistent with the results from N_2 measurements at 77 K where it was shown that IRMOF-NH_2 and IRMOF-NHallyl have higher surface areas and pore volumes compared to IRMOF-N(allyl)$_2$ and IRMOF-NMe_2. The total pore volumes from CO_2 at 196 K and N_2 at 77 K for the IRMOFs, are noted in Table 5.5.

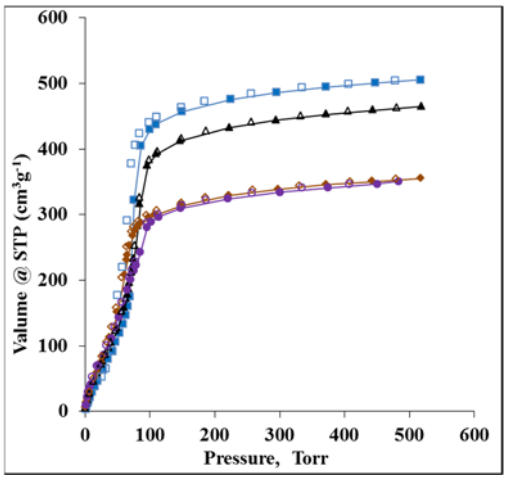

Figure 5.16 The CO_2 adsorption-desorption isotherms at 196 K for IRMOF-NH_2 (blue), IRMOF-NHallyl (black), IRMOF-N(allyl)$_2$ (brown) and IRMOF-NMe_2 (purple). Closed and opened symbols indicate adsorption and desorption, respectively.

5.3.2.2 *CO_2 and N_2 gas adsorption measurements between 273 K and 298 K*

CO_2 adsorption measurements for the IRMOFs were performed at 273 K, 283 K, 288 K, 293 K and 298 K. N_2 measurements were performed at 273 K and 298 K. The CO_2 and N_2 adsorption isotherms at 273 K and 298 K are shown in Figure 5.17 with the data for CO_2 adsorption at 283 K, 288 K, and 293 K in Appendix 3, Figure A3.4. The CO_2 uptake data are summarised in Table 5.8. IRMOF-NMe_2 showed the highest volumetric uptake of CO_2 with the values of 55 cm^3g^{-1} at 273 K and 31 cm^3g^{-1} at 298 K at 1 bar. IRMOF-NH_2 with the highest surface area from N_2 measurements at 77 K, displayed the lowest CO_2 uptake with the values of 41 cm^3g^{-1} at 273 K and 23 cm^3g^{-1} at 298 K. There are examples in the literature that porous materials with high surface areas and pore volumes show a low amount of CO_2 adsorption.[43, 44]

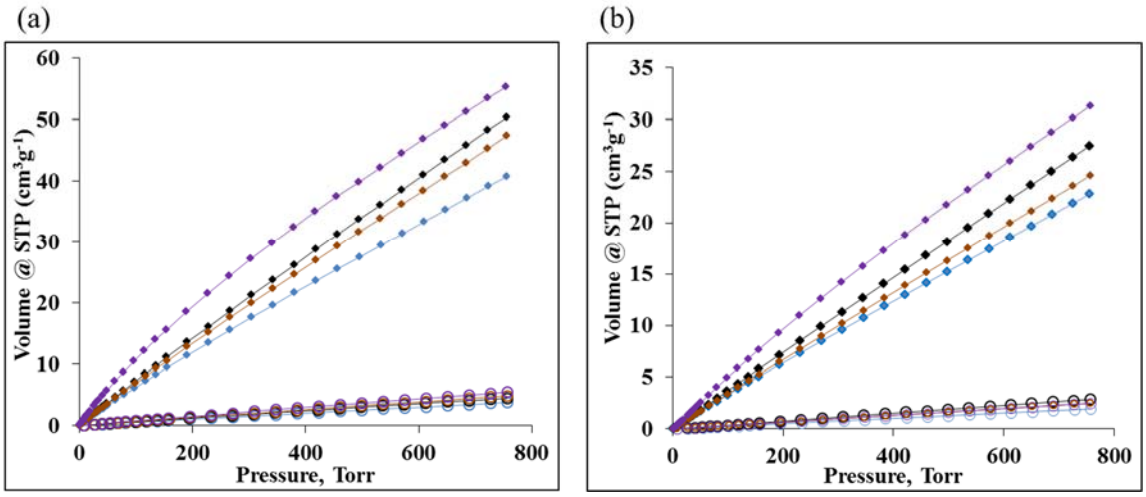

Figure 5.17 The CO_2 adsorption isotherms of CO_2 and N_2 at (a) 273 K and (b) 298 K for IRMOF-NH_2 (blue), IRMOF-NHallyl (black), IRMOF-N(allyl)$_2$ (brown) and IRMOF-NMe_2 (purple). Closed and opened symbols indicate CO_2 adsorption and N_2 adsorption, respectively.

Table 5.8 The CO_2 uptakes of IRMOFs at 273 K, 283 K, 288 K, 293 K and 298 K.

Structure	273 K	283 K	288 K	293 K	298 K
IRMOF-NH_2	41	33	28	25	23
IRMOF-NHallyl	50	38	N/R	27	31
IRMOF-N(allyl)$_2$	47	32	N/R	27	25
IRMOF-NMe_2	55	43	40	35	31

N/R = Not recorded

5.3.3 The heat of adsorption (HoA)

The heat of adsorption (HoA) is a key parameter which is used to gauge the strength of the interaction between the surface of a material and adsorbed gas molecules. Though there is no correlation between surface area and pore volume of a MOF and heat of adsorption,[44] it indicates how a molecule is favourable to a surface and functional groups in the porous MOF. A relatively higher HoA means the molecule is more favourable to the surface and adsorbed more strongly. Higher values of HoA also tend to correspond to selectivity of CO_2 over N_2 (and other gases such as CH_4). In general, the HoA value is often referred to the interaction between CO_2 and framework. The value for HoA less than 30 kJ mol^{-1} is regarded as relatively weak physisorption, values of 30–50 kJ mol^{-1} show strong physisorption, and above 50 kJ mol^{-1} exhibits a strong interaction nearing those seen for chemisorption.[45] Despite this, MOFs with high heats of adsorption (above 50 kJ mol^{-1}) are not necessarily suitable for gas separation, because of the energy cost required for desorption of the gas.[44] Incorporation of specific functional groups, such as primary amine, alkyl amine and arylamine, can result in strong interactions close to chemisorption with CO_2 molecules, and thus enhance the heat of adsorption to 60–100 kJ mol^{-1}.[46] Heat of adsorption can also be affected by other parameters such as accessibility of the functional groups and the size of pores. Heat of adsorption of MOFs can be calculated by CO_2 adsorption measurements using at least two temperatures, and by using the Clausius-Clapeyron equation, as explained in section 2.4.3.[44, 45] In this study, heats of adsorption

were calculated from CO_2 adsorption measurements at 273 K and 298 K. The heat of adsorption profiles are shown in Figure 5.18 and summarised in Table 5.9.

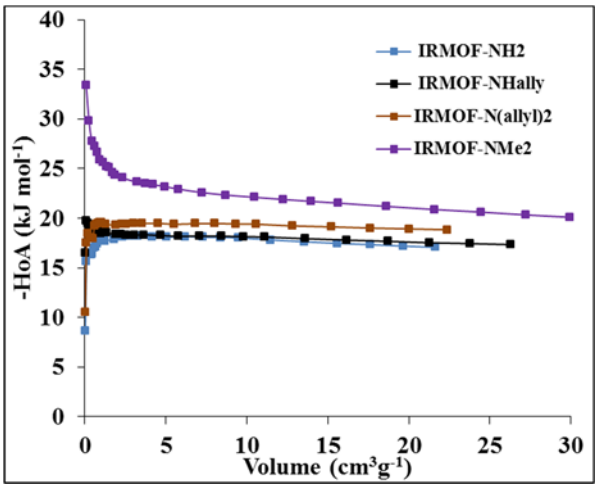

Figure 5.18 Isosteric heat of adsorption profiles for IRMOF-NH_2 (blue), IRMOF-NHallyl (black), IRMOF-N(allyl)$_2$ (brown) and IRMOF-NMe_2 (purple), calculated from data recorded at 273 K and 298 K.

As displayed in the graph, the heats of adsorptions were calculated using Quantachrome software, showed values between -17 to -21 kJ mol^{-1}. IRMOF-NMe_2 had the highest heat of adsorption with -21 kJ mol^{-1} and IRMOF-N(allyl)$_2$, IRMOF-NHallyl and IRMOF-NH_2 were calculated to have values of -19, -17.5 and -17 kJ mol^{-1}, respectively. As discussed above, the binding strength between amine tag groups and CO_2 affects the heat of adsorption. The values for the heats of adsorption indicated physisorption of CO_2 to the amine functional groups. Based on substituent effects, IRMOF-NMe_2 and IRMOF-N(allyl)$_2$ have the highest basicity, and IRMOF-NH_2 with the primary aromatic amine has the lowest basicity of the series (3° > 2° > 1°). As anticipated, based on their respective basicities, the first and second highest heats of adsorption were observed in IRMOF-NMe_2 and IRMOF-N(allyl)$_2$, with HoA values of -21 and -19 kJmol^{-1}, respectively. The HoA of IRMOF-NHallyl and IRMOF-NH_2 were both lower, as expected, due to the lower basicity of their secondary and primary amine functional groups. In addition, there was a correlation between the values of heat of adsorption and CO_2-functional group interactions. Sumby and co-workers suggested low values for the

heat of adsorption in functionalised IRMOF-9-type compounds can be attributed to the lack of accessibility of CO_2 to the pendant tag groups. They identified that the smaller pores were blocked with functional groups, negating effective interaction between CO_2 and these functional groups. Therefore, the major interaction occurs in the larger pores and leads to lower values for the heat of adsorption in these types of interpenetrated systems.[35]

5.3.4 Selectivity of CO_2 over N_2

MOFs as CO_2 adsorbents have to possess good adsorption capacity toward CO_2 and highly selectivity over N_2. This is related to polarity, quadrupole moment, and H-bonding of adsorbate and the surface properties, shape and size of adsorbent. Relatively, selective adsorption of CO_2 is due to the interaction between the higher quadrupole moment of CO_2 and polar functionalised bridging ligands. Selectivity of CO_2 over N_2 was calculated by The Ideal Adsorbed Solution Theory (IAST) of Myers and Prausnitz, as explained in section 2.4.3.[47]

Adsorption selectivity isotherm of CO_2 over N_2 was investigated at 273 K and 298 K which are presented in Figure 5.17a and b and summarised in Table 5.9. The selectivity calculations for the MOFs at 273 K and 298 K indicated IRMOF-NMe_2 had the highest selectivity of 14.6 and 15.1 at temperatures of 273 K and 298 K, respectively. However, there was no correlation between the values of selectivity and heats of adsorption in IRMOF-NH_2, IRMOF-NHallyl and IRMOF-$N(allyl)_2$. A reverse trend was observed at 273 K for these MOFs (IRMOF-NH_2 > IRMOF-NHallyl > IRMOF-$N(allyl)_2$). Surprisingly, IRMOF-$N(allyl)_2$ showed higher value of selectivity than IRMOF-NHallyl at 298 K.

Table 5.9 Selectivity of CO_2 over N_2 at 273 K and 298 K and HoA.

Structure	**273 K**	**298 K**	**HoA Calculated at 273 and 298 K (kJ mol^{-1})**
IRMOF-NH_2	12.5	12.7	17
IRMOF-NHallyl	12.1	9.8	17.5
IRMOF-N(allyl)$_2$	10.7	10.2	19
IRMOF-NMe_2	14.6	15.1	21

5.4 Conclusion

In this chapter, four porous MOF materials were successfully synthesised under solvothermal conditions from $Zn(NO_3)_2 \cdot 6H_2O$ and amine-functionalised biphenyl dicarboxylic acids. The MOFs were formulated as $[Zn_4O(bpdc\text{-}NH_2)_3]$ (IRMOF-NH_2), $[Zn_4O(bpdc\text{-}NH_2)_{0.58}(bpdc\text{-}NHallyl)_{2.42} \cdot 5H_2O]$ (IRMOF-NHallyl), $[Zn_4O(bpdc\text{-}NHallyl)_{0.54}(bpdc\text{-}N(allyl)_2)_{2.46}]$ (IRMOF-$N(allyl)_2$) and $[Zn_4O(bpdc\text{-}NMe_2)_3 \cdot 3H_2O]$ (IRMOF-NMe_2). The elemental analysis results of IRMOF-NHallyl and IRMOF-$N(allyl)_2$ are quite a long way off matching the expected elemental analysis values. However, it is not surprising for the MOFs. The structures were doubly interpenetrated cubic frameworks similar to the topology of IRMOF-9. The sample of as-synthesised IRMOF-$N(allyl)_2$ was a mixture of interpenetrated and non-interpenetrated frameworks. Consequently, a thermal annealing experiment was performed on the as-synthesised IRMOF-$N(allyl)_2$ crystals to convert them to a pure interpenetrated phase. In this work, the reported X-ray crystal structures were classified into three classes; Type I, Type II and Type III. Based on the classifications, IRMOF-NH_2, IRMOF-NHallyl and IRMOF-$N(allyl)_2$ were identified as Type II interpenetration and IRMOF-NMe_2 as Type III interpenetration.

^{1}H NMR studies of the digested MOFs indicated deallylation occurred during MOF synthesis by cleavage of C-N bonds in IRMOF-NHallyl and IRMOF-$N(allyl)_2$. The phenomenon of deallylation was investigated, and showed C-N cleavage is most likely to occur when the organic linker is incorporated or being incorporated in the frameworks.

The potential for structural modification on IRMOF-$N(allyl)_2$ to IRMOF-NMe_2 was investigated under different conditions. However, these attempts were unsuccessful.

Gas sorption measurements were carried out on the set of the compounds to evaluate the effect of functionalisation on the gas sorption properties. Activation methods developed in the Richardson group were applied to IRMOF-NH_2, IRMOF-NHallyl and IRMOF-$N(allyl)_2$ and were successful in giving well-activated MOFs. The activation procedure

of IRMOF-NMe_2 was a major challenge. This is likely due to the functional group being the best Brønsted base and therefore the strongest hydrogen bonder with water. Also the SBU of this MOF carries an additional water molecule as a ligand and removal of this might induce structural collapse. It is also notable that this MOF had a different mode of interpenetration compared with other MOFs in this study. In the activation procedure of IRMOF-NMe_2, the solvent from which the $ScCO_2$ processing was performed and time of vacuum heating were important factors to effectively activate this sample. N_2 isotherm measurements revealed that the MOFs were porous in which the surface area values correlate with the size of the functional groups. The experimental data was then compared to the calculated surface areas, and showed good matches for all four MOFs in light of the deallylation seen in IRMOF-NHallyl and IRMOF-$N(allyl)_2$.

5.5 Experimental

5.5.1 Ligand synthesis and characterisation

5.5.1.1 *Synthesis of 2-amino-[1,1'-biphenyl]-4,4'-dicarboxylic acid, H_2bpdc-NH_2*

H_2bpdc-NH_2 was obtained in three steps using dimethyl [1,1'-biphenyl]-4,4'-dicarboxylate (Me_2bpdc) as starting material.

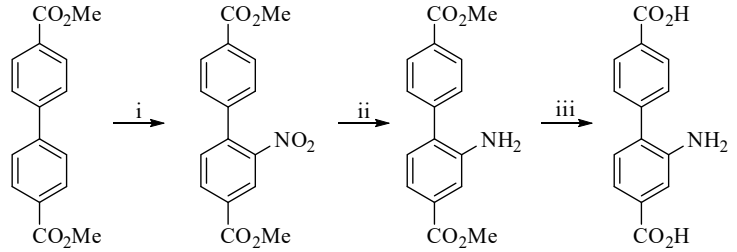

Scheme 5.5 (i) HNO_3, H_2SO_4, (ii) NH_4HCO_2, Pd/C, MeOH/THF and (iii) NaOH (aq), MeOH/THF.

5.5.1.2 *Synthesis of dimethyl 2-nitro-[1,1'-biphenyl]-4,4'-dicarboxylate, Me_2bpdc-NO_2*

Step (i) : Me_2bpdc-NO_2 (2.00 g, 7.40 mmol) was dissolved in concentrated H_2SO_4 (10 mL) with stirring and cooled down to 5 °C. A solution of 70% HNO_3 (482 µL, 7.40 mmol) in concentrated H_2SO_4 (3 mL) was added dropwise to the reaction mixture. The reaction temperature was kept at 5 °C and was stirred for 10 minutes. The reaction mixture was poured into an ice/water mixture (50 mL) with stirring. The precipitate was filtered, washed with water and dried at 70 °C. Yield 2.28 g (98%). ^{1}H NMR δ_H ($CDCl_3$, 500 MHz): 3.95 (3 H, s), 4.00 (3 H, s), 7.41 (2 H, d, J = 7.20 Hz), 7.55 (1 H, d, J = 7.96 Hz), 8.13 (2 H, d, J = 7.51 Hz), 8.30 (1 H, d, J = 7.96 Hz), 8.56 (1 H, s).

5.5.1.3 *Synthesis of 2-amino-[1,1'-biphenyl]-4, 4'-dicarboxylic acid, H_2bpdc-NH_2*

Step (ii) : Me_2bpdc-NO_2 (2.28 g, 7.23 mmol) dissolved in THF (64 mL) was added to a mixture of 10% Pd/C catalyst (0.25 g) in chilled MeOH (33 mL). Ammonium formate (2.05 g, 33 mmol) was added portion-wise and the mixture was heated at 60 °C for 2 hours. After cooling to RT, the Pd/C was removed by filtration and MeOH/THF were removed by rotary evaporation. The resulting precipitate as Me_2bpdc-NH_2 was extracted into ethyl acetate (100 mL) and washed with H_2O (3 × 100 mL), brine and dried over anhydrous Na_2SO_4 and the crude product was purified by passing through a plug of silica gel using chloroform as eluent. Yield 1.93 g (94%). ^{1}H NMR δ_H ($CDCl_3$, 500 MHz): 3.86 (2 H, s), 3.92 (3 H, s), 3.95 (3 H, s), 7.19 (1 H, d, J = 7.87 Hz), 7.45 (1 H, s), 7.49 (1 H, d, J = 7.86 Hz), 7.56 (2 H, d, J = 8.18 Hz) 8.14 (2 H, d, J = 8.17 Hz).

Step (iii) : 1 M NaOH (2.6 mL, 2.6 mmol) was added to Me_2bpdc-NH_2 (0.30 g, 1.05 mmol) dissolved in a mixture of MeOH/THF (1 : 1, 6 mL) and was stirred overnight at RT. The solvent mixture was removed by rotary evaporation and the residue was diluted with water, followed by acidification by 1 M HCl. The resulting precipitate was collected by filtration and air dried. Yield 0.25 g (92%). ^{1}H NMR δ_H (d_6-DMSO, 500 MHz): 7.14 (1 H, d, J = 7.89 Hz), 7.25 (1 H, d, J = 7.92 Hz), 7.44 (1 H, s), 7.59 (2 H, d, J = 8.1 Hz), 8.03 (2 H, d, J = 8.13 Hz), 12.74 (2 H, s). *m/z* (ESI) 256.00 ($[M - H]^-$; $[C_{14}H_{11}NO_4 - H]^-$ requires 256.21).

5.5.1.4 *Synthesis of 2-(allylamino)-[1,1'-biphenyl]-4,4'-dicarboxylic acid, H_2bpdc-NHallyl*

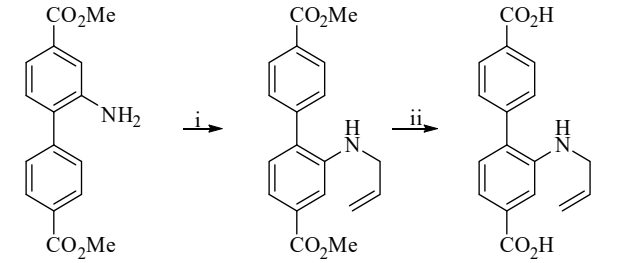

Me_2bpdc-NH_2 Me_2bpdc-NHallyl H_2bpdc-NHallyl

Scheme 5.6 (i) Allyl bromide, K_2CO_3, DMF (ii) NaOH (aq), MeOH/THF.

Step (i) : Allyl bromide (304 µl, 3.53 mmol) was added to a solution of Me_2bpdc-NH_2 (1.00 g, 3.50 mmol) and powdered K_2CO_3 (0.96 g, 6.95 mmol) in DMF (10 mL). The solution was heated to 70 °C and left to stir overnight. The reaction was cooled to RT and diluted with water (100 mL) and the precipitated solid was collected by filtration and washed with water. The crude product was purified on silica gel eluting with CH_2Cl_2 (R_f 0.93). Yield 0.65 g (57%). ^{1}H NMR δ_H ($CDCl_3$, 300 MHz): 3.80 (2 H, d, J = 5.15), 3.92 (3 H, s), 3.95 (3 H, s), 4.06 (1 H, s), 5.13 (2 H, m), 5.85 (1 H, m), 7.13 (1 H, d, J = 7.80 Hz), 7.35 (1 H, s), 7.44 (1 H, d, J = 7.80 Hz), 7.51 (2 H, d, J = 8.04 Hz), 8.13 (2 H, d, J = 8.03 Hz). ^{13}C NMR δ_C ($CDCl_3$, 75 MHz): 46.23, 52.14, 52.26, 111.63, 116.43, 118.44, 129.13, 129.38, 129.48, 130.00, 130.31, 130.56, 130.74, 130.81, 134.48, 143.37, 144.65, 166.72, 167.35.

Step (ii) : 1 M NaOH (2.7 mL, 2.7 mmol) was added to Me_2bpdc-NHallyl (0.35 g, 1.1 mmol) dissolved in MeOH/THF (1 : 1, 6 mL) and the mixture was stirred overnight at RT. The solvent mixture was removed by rotary evaporation and the residue was diluted with water followed by adding 1 M HCl to precipitate to the product. The yellow solid was separated by filtration, washed with water and air dried. Yield 0.310 g (97%). Found: C, 66.86; H, 4.72; N, 4.14. $C_{17}H_{15}NO_4 \cdot ½H_2O$ requires C, 66.66; H, 5.26; N, 4.57. ^{1}H NMR δ_H (d_6-DMSO, 500 MHz): 3.74 (2 H, s), 5.09 (2 H, m), 5.83 (1 H, m), 7.11 (1 H, d,

J = 7.77 Hz), 7.19 (1 H, s), 7.25 (1 H, d, *J* = 7.76 Hz), 7.55 (2 H, d, *J* = 8.08 Hz), 8.03 (2 H, d, *J* = 8.17 Hz), 12.88 (2 H, s). ^{13}C NMR δ_C (d_6-DMSO, 100 MHz): 45.68, 111.87, 115.73, 117.82, 129.55, 130.21, 130.37, 130.43, 130.58, 131.60, 136.14, 143.54, 145.43, 167.63, 168.15. *m/z* (ESI) 296.05 ($[M - H]^-$; $[C_{17}H_{15}NO_4 - H]^-$ requires 296.28).

5.5.1.5 *Synthesis of 2-(diallylamino)-[1,1'-biphenyl]-4, 4'-dicarboxylic acid, H_2bpdc-N (allyl)$_2$*

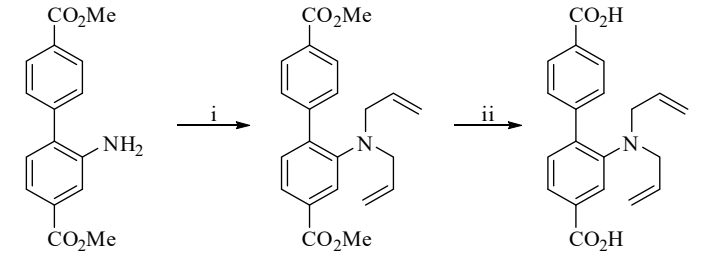

Me_2bpdc-NH_2 Me_2bpdc-N(allyl)$_2$ H_2bpdc-N(allyl)$_2$

Scheme 5.7 (i) Allyl bromide, K_2CO_3, DMF (ii) NaOH (aq), MeOH/THF.

Step (i) : Allyl bromide (265 µL, 3.0 mmol) and ground K_2CO_3 (0.289 g, 2.1 mmol) were added to Me_2bpdc-NH_2 (0.285 g, 1.0 mmol) dissolved in DMF (4 mL) and the mixture heated to 80 °C for 48 hours. After cooling to RT, the mixture was diluted with water (40 mL) and extracted with EtOAc (2 × 20 mL). The organic extracts were combined and washed with water (6 × 10 mL), brine (10 mL) and dried over Na_2SO_4. After filtering off the drying agent, the solvent was removed by rotary evaporation to yield a yellow oil. This was taken up in hot MeOH (2 mL) and the product crystallised on standing and was collected by filtration and air dried. Yield 0.300 g (85%). ^{1}H NMR δ_H ($CDCl_3$, 500 MHz): 3.80 (4 H, d, *J* = 5.15 Hz), 3.92 (3 H, s), 3.95 (3 H, s), 5.12 (4 H, m), 5.85 (2 H, m), 7.13 (1 H, d, *J* = 7.8 Hz), 7.15 (1 H, d, *J* = 1.56 Hz), 7.35 (1 H, d, *J* = 1.58 Hz), 7.43 (2 H, d, *J* = 8.04 Hz), 8.12 (2 H, d, *J* = 8.03 Hz). ^{13}C NMR δ_C ($CDCl_3$, 75 MHz) 46.23, 52.14, 52.26, 111.46, 116.44, 118.45, 129.13, 129.39, 129.49, 130.31, 130.57, 130.74, 130.84, 134.49, 143.37, 144.65, 166.73, 167.36.

Step (ii) : 1 M NaOH (4 mL, 4 mmol) was added to Me_2bpdc-N(allyl)$_2$ (0.40 g, 1.1 mmol) dissolved in MeOH/THF (1 : 1, 10 mL) and the mixture was left to stir at RT for 7 hours. The organic solvent was removed by rotary evaporation and the resulting solution was diluted with water. The clear solution was acidified to pH = 4 using 1 M HCl and the precipitated product was collected by filtration, washed with water and air dried. Yield 0.3 g (81%). Found: C, 68.05; H, 5.27; N, 3.98. $C_{20}H_{19}NO_4 \cdot 0.8H_2O$ requires C, 68.27; H, 5.96; N, 3.98. ^{1}H NMR δ_H (d_6-DMSO, 300 MHz): 3.41 (4 H, d, J = 6.07 Hz), 5.04 (4 H, m); 5.60 (2 H, m), 7.29 (1 H, d, J = 8.29 Hz), 7.61 (2 H, m), 7.67 (2 H, d, J = 8.38 Hz), 8.00 (2 H, d, J = 8.38 Hz). ^{13}C NMR δ_C (d_6-DMSO, 75 MHz): 54.62, 118.22, 122.27, 123.64, 128.94, 129.82, 130.89, 131.68, 134.59, 138.68, 144.91, 148.36, 167.48, 167.54. *m/z* (ESI) 336.10 ([M – H]$^-$; [$C_{20}H_{19}NO_4$ – H]$^-$ requires 336.34).

5.5.1.6 *Synthesis of 2-(dimethylamino)-[1,1'-biphenyl]-4,4'-dicarboxylic acid, H_2bpdc-NMe$_2$*

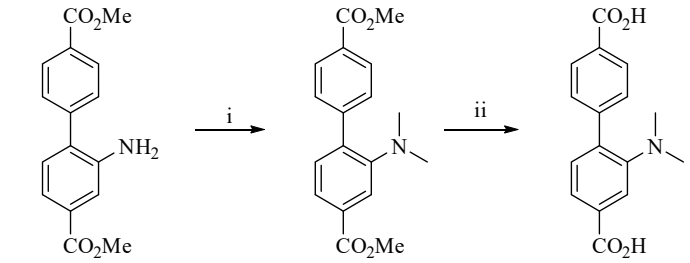

Me_2bpdc-NH_2 Me_2bpdc-NMe_2 H_2bpdc-NMe_2

Scheme 5.8 (i) MeI, DMF (ii) NaOH (aq), MeOH/THF.

Step (i) : Methyl iodide (175 µl, 2.81 mmol) was added to Me_2bpdc-NH_2 (0.300 g, 1.05 mmol) and $NaHCO_3$ (0.176 g, 2.09 mmol) in DMF (7 mL). The reaction mixture was sealed in an Ace Glass pressure tube and heated to 90 °C with stirring for 18 hours. The reaction was cooled down to RT and diluted with water (70 mL) and the product was collected by filtration. The pure yellow product was washed with water and air dried. Yield 0.238 g (73 %). ^{1}H NMR δ_H ($CDCl_3$, 300 MHz): 2.57 (6 H, s), 3.94 (3 H, s), 3.95

(3 H, s), 7.29 (1 H, d, overlap with $CDCl_3$), 7.66 (1 H, d, overlap), 7.69 (2 H, d, overlap), 8.07 (2 H, d, J = 8.28 Hz). ^{13}C NMR δ_C ($CDCl_3$, 75 MHz): 43.29, 52.11, 52.15, 118.77, 122.56, 127.22, 128.37, 128.75, 129.77, 130.18, 130.26, 131.52, 137.06, 144.31, 145.83, 151.34, 166.96, 167.10.

Step (ii) : 1 M NaOH (1.9 mL, 1.9 mmol) was added to Me_2bpdc-NMe_2 (0.238 g, 0.795 mmol) dissolved in MeOH/THF (1 : 1, 4 mL) and the mixture was stirred overnight at RT. After removing the organic solvents by rotary evaporation, the solution was diluted with water and acidified with 1 M HCl. The resulting solid was collected by filtration and washed with water. Yield 0.19 g (87%). Found: C, 66.59; H, 5.41; N, 4.87. $C_{16}H_{15}NO_4 \cdot ¼H_2O$ requires C, 66.32; H, 5.39; N, 4.83. ^1H NMR δ_H (d_6-DMSO, 500 MHz): 2.50 (6 H, S, overlapped with DMSO), 7.30 (1 H, d, J = 7.82 Hz), 7.57 (1 H, d, J = 7.84 Hz), 7.61 (1 H, s), 7.67 (2 H, d, J = 8.23 Hz), 7.99 (2 H, d, J = 8.22 Hz), 12.95 (2 H, s). ^{13}C NMR δ_C (d_6-DMSO, 125 MHz): 43.43, 118.73, 122.84, 128.67, 129.88, 130.7, 131.41, 132.02, 136.69, 145.50, 151.45, 167.58, 167.70. *m/z* (ESI) 284.00 ($[M - H]^-$; $[C_{16}H_{15}NO_4 - H]^-$ requires 284.27).

5.5.2 IRMOF syntheses

5.5.2.1 *Synthesis of IRMOF-NH_2*

H_2bpdc-NH_2 (0.100 g, 0.35 mmol) was combined with $Zn(NO_3)_2 \cdot 6H_2O$ (0.346 g, 1.16 mmol) in dry DMF (16 mL) in a 20 mL vial. The mixture was heated in a 100 °C oven for 24 hours. After cooling down at room temperature, cubic brown crystals were washed with dry DMF several times. Yield 69.8 mg (57%). Found: C, 48.17; H, 2.36; N, 3.62. $C_{42}H_{27}N_3O_{13}Zn_4$ | $[Zn_4O(C_{14}H_9N_3O_4)_3]$ | $[Zn_4O(bpdc\text{-}NH_2)_3]$ requires C, 48.35; H, 2.61; N, 4.03.

5.5.2.2 *Synthesis of IRMOF-NHallyl*

H_2bpdc-NHallyl (0.100 g, 0.34 mmol) and $Zn(NO_3)_2 \cdot 6H_2O$ (0.30 g, 1.0 mmol) were dissolved in dry DMF (16 mL) in a 20 mL vail and heated at 100 °C for 24 hours. Cubic dark brown crystals were collected and then washed with dry DMF several times. Yield 66.5 mg (47%). Found: C, 48.66; H, 2.43; N, 3.14. $C_{51}H_{49}N_3O_{18}Zn_4$ | $[Zn_4O(C_{17}H_{13}N_3O_4)_3 \cdot 5H_2O]$ | $[Zn_4O(bpdc\text{-}NH_2)_{0.58}(bpdc\text{-}N(allyl))_{2.42} \cdot 5H_2O]$ requires C, 48.87; H, 3.94; N, 3.35.

5.5.2.3 *Synthesis of IRMOF-N(allyl)$_2$*

H_2bpdc-N(allyl)$_2$ (0.100 g, 2.96 mmol) and $Zn(NO_3)_2 \cdot 6H_2O$ (0.264 g, 0.887 mmol) were combined in dry DMF (16 mL) in a 20 mL vail. The vial was transferred to an oven at 100 °C for 24 hours. The resulted brown crystals then were collected and washed with dry DMF. Yield 67.1 mg (53%). Found: C, 49.17; H, 2.76; N, 3.88. $C_{60}H_{51}N_3O_{13}Zn_4$ | $[Zn_4O(C_{20}H_{17}N_3O_4)_3]$ | $[Zn_4O(bpdc\text{-}N(allyl))_{0.54}(bpdc\text{-}N(allyl)_2)_{2.46}]$ requires C, 56.14; H, 4.00; N, 3.27.

5.5.2.4 *Synthesis of IRMOF-NMe_2*

H_2bpdc-N(Me)$_2$ (0.100 g, 0.35 mmol) and $Zn(NO_3)_2 \cdot 6H_2O$ (0.313 g, 1.05 mmol) were dissolved in dry DMF (16 mL) in a 20 mL vial. The vial was transferred to an oven at

100 °C for 24 hours. Shiny yellow crystals were collected before washing with dry DMF. Yield 69.5 mg (52%). Found: C, 48.99; H, 3.29; N, 4.04. $C_{48}H_{45}N_3O_{16}Zn_4$ | $[Zn_4O(C_{16}H_{13}N_3O_4)_3 \cdot 3H_2O]$ | $[Zn_4O(bpdc\text{-}N(Me)_2)_3 \cdot 3H_2O]$ requires C, 48.80; H, 3.84; N, 3.56

5.5.3 Post-synthetic modification studies of IRMOF-N(allyl)$_2$ to IRMOF-NMe$_2$

5.5.3.1 *Homogenous conversion of Me$_2$bpdc-N(allyl)$_2$ to Me$_2$bpdc-NMe$_2$*

MeI (62 µL, 1.0 mmol) was added to Me_2bpdc-N(allyl)$_2$ (36.5 mg, 0.1 mmol) in DMF (1 mL) in a screw top vial and was left to stir overnight at 90 °C. DMF was removed by rotary evaporation after cooling down the reaction mixture to RT. The resulted product was then extracted by ethyl acetate (20 mL) followed by washing with H_2O (3 × 30 mL), brine and dried over anhydrous Na_2SO_4. The oily dark brown product was collected after evaporation of the ethyl acetate by rotary evaporation. Yield 25.2 mg (80%).

5.5.3.2 *PSM of IRMOF-N(allyl)$_2$ to IRMOF-NMe$_2$*

Approximately (100 mg, 0.008 mmol) of IRMOF-N(allyl)$_2$ was placed in a screw top vial in benzene (1 ml) and methyl iodide (84.1 µL, 1.35 mmol, excess) was added. The reaction mixture was then left overnight at 90 °C without stirring. The crystals were collected by filtration.

5.6 References

1. Zhao, N.; Sun, F.; Li, P.; Mu, X.; Zhu, G., An amino-coordinated metal-organic framework for selective gas adsorption. *Inorganic Chemistry* **2017,** *56* (12), 6938-6942.
2. Dau, P. V.; Cohen, S. M., Cyclometalated metal-organic frameworks as stable and reusable heterogeneous catalysts for allylic N-alkylation of amines. *Chemical Communications* **2013,** *49* (55), 6128-6130.
3. Eddaoudi, M.; Kim, J.; Rosi, N.; Vodak, D.; Wachter, J.; O'Keeffe, M.; Yaghi, O. M., Systematic design of pore size and functionality in isoreticular MOFs and their application in methane storage. *Science* **2002,** *295* (5554), 469-472.
4. Wang, Z.; Tanabe, K. K.; Cohen, S. M., Accessing postsynthetic modification in a series of metal-organic frameworks and the influence of framework topology on reactivity. *Inorganic Chemistry* **2009,** *48* (1), 296-306.
5. Hahm, H.; Ha, H.; Kim, S.; Jung, B.; Park, M. H.; Kim, Y.; Heo, J.; Kim, M., Synthesis of secondary and tertiary amine-containing MOFs: C-N bond cleavage during MOF synthesis. *CrystEngComm* **2015,** *17* (30), 5644-5650.
6. Halis, S.; Reimer, N.; Klinkebiel, A.; Lüning, U.; Stock, N., Four new Al-based microporous metal-organic framework compounds with MIL-53-type structure containing functionalized extended linker molecules. *Microporous and Mesoporous Materials* **2015,** *216*, 13-19.
7. Meek, S. T.; Perry, J. J.; Teich-Mcgoldrick, S. L.; Greathouse, J. A.; Allendorf, M. D., Complete series of monohalogenated isoreticular metal-organic frameworks: Synthesis and the importance of activation method. *Crystal Growth and Design* **2011,** *11* (10), 4309-4312.
8. Deshpande, R. K.; Waterhouse, G. I. N.; Jameson, G. B.; Telfer, S. G., Photolabile protecting groups in metal-organic frameworks: Preventing interpenetration and masking functional groups. *Chemical Communications* **2012,** *48* (10), 1574-1576.
9. Ingleson, M. J.; Perez Barrio, J.; Guilbaud, J. B.; Khimyak, Y. Z.; Rosseinsky, M. J., Framework functionalisation triggers metal complex binding. *Chemical Communications* **2008,** (23), 2680-2682.
10. Costa, J. S.; Gamez, P.; Black, C. A.; Roubeau, O.; Teat, S. J.; Reedijk, J., Chemical modification of a bridging ligand inside a metal-organic framework while maintaining the 3D structure. *European Journal of Inorganic Chemistry* **2008,** (10), 1551-1554.
11. Braun, M. E.; Steffek, C. D.; Kim, J.; Rasmussen, P. G.; Yaghi, O. M., 1,4-Benzenedicarboxylate derivatives as links in the design of paddle-wheel units and metal-organic frameworks. *Chemical Communications* **2001,** (24), 2532-2533.
12. Li, H.; Eddaoudi, M.; O'Keeffe, M.; Yaghi, O. M., Design and synthesis of an exceptionally stable and highly porous metal-organic framework. *Nature* **1999,** *402* (6759), 276-279.
13. Lin, Y.; Kong, C.; Chen, L., Direct synthesis of amine-functionalized MIL-101(Cr) nanoparticles and application for CO_2 capture. *RSC Advances* **2012,** *2* (16), 6417-6419.

14. Jiang, D.; Keenan, L. L.; Burrows, A. D.; Edler, K. J., Synthesis and post-synthetic modification of MIL-101(Cr)-NH_2 via a tandem diazotisation process. *Chemical Communications* **2012,** *48* (99), 12053-12055.
15. Serra-Crespo, P.; Ramos-Fernandez, E. V.; Gascon, J.; Kapteijn, F., Synthesis and characterization of an amino functionalized MIL-101(Al): Separation and catalytic properties. *Chemistry of Materials* **2011,** *23* (10), 2565-2572.
16. Hartmann, M.; Fischer, M., Amino-functionalized basic catalysts with MIL-101 structure. *Microporous and Mesoporous Materials* **2012,** *164*, 38-43.
17. Savonnet, M.; Bazer-Bachi, D.; Bats, N.; Perez-Pellitero, J.; Jeanneau, E.; Lecocq, V.; Pinel, C.; Farrusseng, D., Generic postfunctionalization route from amino-derived metal-organic frameworks. *Journal of the American Chemical Society* **2010,** *132* (13), 4518-4519.
18. Cmarik, G. E.; Kim, M.; Cohen, S. M.; Walton, K. S., Tuning the adsorption properties of UiO-66 via ligand functionalization. *Langmuir* **2012,** *28* (44), 15606-15613.
19. Cavka, J. H.; Jakobsen, S.; Olsbye, U.; Guillou, N.; Lamberti, C.; Bordiga, S.; Lillerud, K. P., A new zirconium inorganic building brick forming metal-organic frameworks with exceptional stability. *Journal of the American Chemical Society* **2008,** *130* (42), 13850-13851.
20. Cerofolini, G. F.; Re, N., Studies in the Acid-Base theory. The base strength of amines. *Chemical Physics Letters* **2001,** *339* (5–6), 375-379.
21. Ol'khovik, V. K.; Vasilevskii, V. A.; Galinovskii, N. A., Synthesis of new polyconjugated compounds based on 9,10-diphenylphenanthrene. *Russian Journal of Organic Chemistry* **2010,** *46* (8), 1167-1172.
22. Liu, C.; Li, T.; Rosi, N. L., Strain-promoted "click" modification of a mesoporous metal-organic framework. *Journal of the American Chemical Society* **2012,** *134* (46), 18886-18888.
23. Chen, C. X.; Wei, Z.; Jiang, J. J.; Fan, Y. Z.; Zheng, S. P.; Cao, C. C.; Li, Y. H.; Fenske, D.; Su, C. Y., Precise modulation of the breathing behavior and pore surface in Zr-MOFS by reversible post-synthetic variable-spacer installation to fine-tune the expansion magnitude and sorption properties. *Angewandte Chemie - International Edition* **2016,** *55* (34), 9932-9936.
24. Sun, R.; Liu, B.; Li, B. G.; Jie, S., Palladium(II)@zirconium-based mixed-linker metal-organic frameworks as highly efficient and recyclable catalysts for Suzuki and Heck cross-coupling reactions. *ChemCatChem* **2016,** *8* (20), 3261-3271.
25. Halls, J. E.; Hernán-Gómez, A.; Burrows, A. D.; Marken, F., Metal-organic frameworks post-synthetically modified with ferrocenyl groups: Framework effects on redox processes and surface conduction. *Dalton Transactions* **2012,** *41* (5), 1475-1480.
26. Kaposi, M.; Cokoja, M.; Hutterer, C. H.; Hauser, S. A.; Kaposi, T.; Klappenberger, F.; Pothig, A.; Barth, J. V.; Herrmann, W. A.; Kuhn, F. E., Immobilisation of a molecular epoxidation catalyst on UiO-66 and -67: the effect of pore size on catalyst activity and recycling. *Dalton Transactions* **2015,** *44* (36), 15976-15983.
27. Gotthardt, M. A.; Grosjean, S.; Brunner, T. S.; Kotzel, J.; Gänzler, A. M.; Wolf, S.; Bräse, S.; Kleist, W., Synthesis and post-synthetic modification of amine-, alkyne-,

azide- and nitro-functionalized metal-organic frameworks based on DUT-5. *Dalton Transactions* **2015,** *44* (38), 16802-16809.
28. Peterson, G. W.; Moon, S. Y.; Wagner, G. W.; Hall, M. G.; Decoste, J. B.; Hupp, J. T.; Farha, O. K., Tailoring the pore size and functionality of UiO-type metal-organic frameworks for optimal nerve agent destruction. *Inorganic Chemistry* **2015,** *54* (20), 9684-9686.
29. Kutzscher, C.; Hoffmann, H. C.; Krause, S.; Stoeck, U.; Senkovska, I.; Brunner, E.; Kaskel, S., Proline functionalization of the mesoporous metal-organic framework DUT-32. *Inorganic Chemistry* **2015,** *54* (3), 1003-1009.
30. Lun, D. J.; Waterhouse, G. I. N.; Telfer, S. G., A general thermolabile protecting group strategy for organocatalytic metal-organic frameworks. *Journal of the American Chemical Society* **2011,** *133* (15), 5806-5809.
31. Deshpande, R. K.; Minnaar, J. L.; Telfer, S. G., Thermolabile groups in metal-organic frameworks: Suppression of network interpenetration, post-synthetic cavity expansion, and protection of reactive functional groups. *Angewandte Chemie - International Edition* **2010,** *49* (27), 4598-4602.
32. Bryant, M. R.; Richardson, C., Thermally-promoted post-synthetic Pummerer chemistry in a sulfoxide-functionalized metal-organic framework. *CrystEngComm* **2015,** *17* (46), 8858-8863.
33. Rankine, D.; Avellaneda, A.; Hill, M. R.; Doonan, C. J.; Sumby, C. J., Control of framework interpenetration for in situ modified hydroxyl functionalised IRMOFs. *Chemical Communications* **2012,** *48* (83), 10328-10330.
34. Ferguson, A.; Liu, L.; Tapperwijn, S. J.; Perl, D.; Coudert, F. X.; Van Cleuvenbergen, S.; Verbiest, T.; Van Der Veen, M. A.; Telfer, S. G., Controlled partial interpenetration in metal-organic frameworks. *Nature Chemistry* **2016,** *8* (3), 250-257.
35. Babarao, R.; Coghlan, C. J.; Rankine, D.; Bloch, W. M.; Gransbury, G. K.; Sato, H.; Kitagawa, S.; Sumby, C. J.; Hill, M. R.; Doonan, C. J., Does functionalisation enhance CO_2 uptake in interpenetrated MOFs? An examination of the IRMOF-9 series. *Chemical Communications* **2014,** *50* (24), 3238-3241.
36. Ferguson, A.; Liu, L.; Tapperwijn, S. J.; Perl, D.; Coudert, F.-X.; Van Cleuvenbergen, S.; Verbiest, T.; van der Veen, M. A.; Telfer, S. G., Controlled partial interpenetration in metal–organic frameworks. *Nat Chem* **2016,** *8* (3), 250-257.
37. Bae, Y. S.; Dubbeldam, D.; Nelson, A.; Walton, K. S.; Hupp, J. T.; Snurr, R. Q., Strategies for characterization of large-pore metal-organic frameworks by combined experimental and computational methods. *Chemistry of Materials* **2009,** *21* (20), 4768-4777.
38. Liu, B.; Zhou, H.-F.; Guan, Z.-H.; Hou, L.; Cui, B.; Wang, Y.-Y., Cleavage of a C-C' bond between two phenyl groups under mild conditions during the construction of Zn(II) organic frameworks. *Green Chemistry* **2016,** *18* (20), 5418-5422.
39. Rouquerol, J.; Llewellyn, P.; Rouquerol, F., Is the BET equation applicable to microporous adsorbents? In *Studies in Surface Science and Catalysis*, 2006; Vol. 160, pp 49-56.

40. Düren, T.; Millange, F.; Férey, G.; Walton, K. S.; Snurr, R. Q., Calculating geometric surface areas as a characterization tool for metal-organic frameworks. *Journal of Physical Chemistry C* **2007,** *111* (42), 15350-15356.
41. Prasad, T. K.; Suh, M. P., Control of interpenetration and gas-sorption properties of metal-organic frameworks by a simple change in ligand design. *Chemistry - A European Journal* **2012,** *18* (28), 8673-8680.
42. Song, X.; Kim, T. K.; Kim, H.; Kim, D.; Jeong, S.; Moon, H. R.; Lah, M. S., Post-synthetic modifications of framework metal ions in isostructural metal-organic frameworks: Core-shell heterostructures via selective transmetalations. *Chemistry of Materials* **2012,** *24* (15), 3065-3073.
43. Liu, J.; Thallapally, P. K.; McGrail, B. P.; Brown, D. R.; Liu, J., Progress in adsorption-based CO_2 capture by metal-organic frameworks. *Chemical Society Reviews* **2012,** *41* (6), 2308-2322.
44. Khutia, A.; Janiak, C., Programming MIL-101Cr for selective and enhanced CO_2 adsorption at low pressure by postsynthetic amine functionalization. *Dalton Transactions* **2014,** *43* (3), 1338-1347.
45. Das, A.; D'Alessandro, D. M., Tuning the functional sites in metal-organic frameworks to modulate CO_2 heats of adsorption. *CrystEngComm* **2015,** *17* (4), 706-718.
46. Demessence, A.; D'Alessandro, D. M.; Foo, M. L.; Long, J. R., Strong CO_2 binding in a water-stable, triazolate-bridged metal-organic framework functionalized with ethylenediamine. *Journal of the American Chemical Society* **2009,** *131* (25), 8784-8786.
47. Myers, A. L.; Prausnitz, J. M., Thermodynamics of mixed-gas adsorption. *AIChE Journal* **1965,** *11* (1), 121-127.

Chapter 6

Structural Studies of Strontium Coordination Networks

6 Introduction

The logical design and construction of MOFs is increasing not only due to their applications such as gas storage and separation,[1] heterogeneous asymmetric catalysts,[2] chemical sensing,[3] luminescence,[4, 5] and magnetism,[6] but also because of their fascinating structures and topologies.[7] However, it is currently impossible to predict the structure and topology of MOFs created by solvothermal means (or other means) as the synthetic conditions, such as reaction time, metal-to-ligand molar ratios, pH, concentration and solvent system, have enormous effects. In addition to the type of metal and the shape and number of binding groups on the organic linker.[8]

Most studies for coordination networks have focused on transition metal[9] and rare-earth metal ions,[6] while alkaline earth metal ions have been paid less attention.[10, 11] One reason for this may be the perceived difficulty in controlling the coordination properties of alkaline earth metal ions due to their large ionic radii, which give rise to a wide range of coordination numbers and geometries. Mg^{2+} has the smallest radii and is typically 6 coordinate octahedral,[7] Ca^{2+} is larger and accommodates coordination numbers up to 9,[12] while Sr^{2+} and Ba^{2+} possess large ionic radii, and have coordination numbers between 6 and 10.[13, 14]

Multicarboxylate organic linkers have been widely used to make coordination networks with transition metal ions, rare-earth ions and alkaline-earth metal ions due to the strong bonding interaction between the metal ions and oxygen atoms.[15] Rigid aryl carboxylate organic linkers have been widely used to grow porous MOF crystals, and the rigid natures of these ligands have simplified and aided crystal engineering.[16, 10] By comparison, flexible carboxylate linkers are more susceptible to forming dense structures. As explained earlier in 1.1.1, the nature of binding to carboxylates is different for transition metal ions compared to alkaline-earth ions. [17]

Alkaline earth metals in coordination networks, and particularly porous MOFs, offer several advantages; (i) many alkaline earth-carboxylate networks exhibit high thermal stability,[18] which is most likely because of the relatively high charge density and ionic

nature of the metal-to-ligand bonds, (ii) low atomic weight of early alkaline earth metals could confer gravimetric advantages for gas storage applications,[19] (iii) networks containing closed shell alkaline earth metal ions have applications stemming from excitation-emission properties, particularly in electronic systems such as fluorescence probes, lasers, photo- and electro-luminescence,[20, 21] and (iv) alkaline earth metals are cheap and relatively nontoxic.

6.1 Carboxylate coordination modes for alkaline-earth metal ions

Carboxylate linkers adopt a wide range of coordination modes in alkaline-earth coordination networks. The Schröder group reported the synthesis and characterisation of Mg, Ca, Sr and Ba coordination networks with a range of dicarboxylic acids (Figure 6.1) and investigated the effects of the metal cation size and carboxylate linkers on the network structures.[7] Single crystal X-ray diffraction studies showed many of the structures had channels, but were nonporous, as the channels were filled by solvents coordinated to the SBUs of the network structures. Additionally, it was indicated that increasing metallic ionic radii led to increasing coordination numbers (six for Mg^{2+}; eight for Sr^{2+} and Ba^{2+}). However, Ca^{2+} showed coordination numbers of six, seven and eight with different linkers and solvents. Schröder observed four carboxylate coordination modes as depicted in Figure 6.1a–d; bridging (μ_2-(η^1 : η^1)) (named as binding mode **a**); chelating (η^2) (named as binding mode **b**); chelating and bridging with one oxygen atom (μ_2-(η^2 : η^1)) (named as binding mode **c**); and bridging and chelating with two oxygen atoms (μ_3-(η^1 : η^2 : η^1)) (named as binding mode **d**).

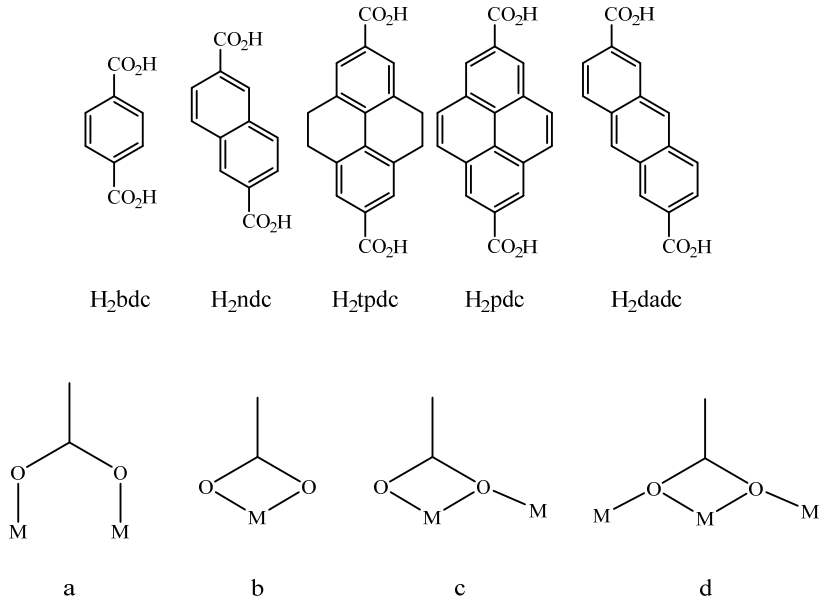

Figure 6.1 Structures of the dicarboxylic acids used to make alkaline-earth coordination networks by Schroder. Carboxylate coordination modes, (a) bridging, (b) chelating, (c) chelating and bridging with one oxygen atom, and (d) bridging and chelating with two oxygen atoms, as described by Schroder and co-workers.[7]

Several research groups have investigated 2,5-thiophenedicarboxylic acid (H_2tdc) as an organic linker to generate Sr coordination networks. Parise and co-workers reported a nonporous framework Sr(tdc)(DMF) [tdc = thiophene-2,5-dicarboxylate] grown under solvothermal reaction conditions.[22] The SBU is a 1D chain of edge- and face-shared strontium polyhedra bridged by tdc^{2-} to form a 3D framework with the rhombus-shaped pores that run parallel to the crystallographic *a*-axis filled by coordinating DMF (Figure 6.2). The photoluminescence properties of this material showed exceptional emission broadness attributed to delocalization of the lone electron pair within the thiophene ring.

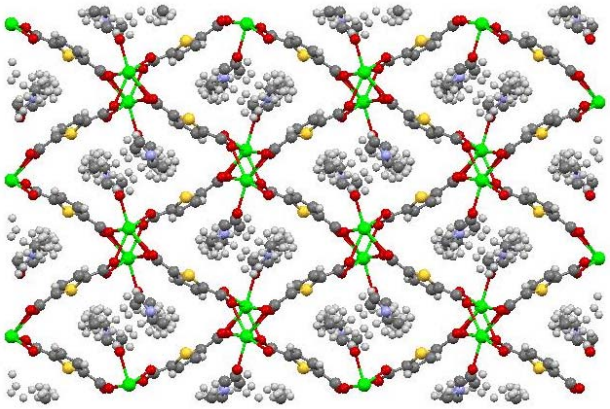

Figure 6.2 A view of the extended structure of Sr(tdc)(DMF) along the crystallographic *a*-axis.[22]

Ren and co-workers applied a different synthesis procedure using H_2tdc to grow crystals formulated as Sr(tdc)(DMF).[23] In this structure, the Sr centre is an eight coordination moiety, consisting of seven oxygen atoms from carboxylates and one coordinated DMF to create a distorted hendecahedron network. The connectivity between Sr centres and tdc^{2-} resulted in an uncommon I^1O^2 type 3D framework.[24]

Cheetham and co-workers used 9-fluorenone-2,7-dicarboxylic acid (H_2fdc) and a hydrothermal synthesis procedure to grow crystals of a nonporous coordination polymer, formulated as $Sr(fdc)(H_2O)_5 \cdot 2H_2O$.[16] The network formed through edge-sharing of SrO_8 polyhedra to create 1D chains, which are connected by bridging carboxylate groups to create a nonporous 3D framework. The photoluminescence properties of the coordination polymer were investigated and the results indicated that it was the first example of a framework with luminescent properties based on ligand with valuable emission broadness for solid state lighting.

6.2 Outline and rationale

Sr-carboxylate MOFs are worth researching due to the fact that there are only a few examples reported in the literature to date. Many of the Sr-carboxylate structures reported in the literature up to now are nonporous.[14, 16, 22] This chapter presents the synthesis and characterisation of six Sr-based materials of nitro and amine functionalised biphenyl-4,4′-dicarboxylic acid (H_2bpdc) linkers. The focus here was assembling Sr coordination networks, which are less studied, compared to the *d*-block, with novel topologies and their structural evaluation based on the number, size and shape of substituents, carboxylate binding modes, and Sr coordination environments. Selected networks were also studied by gas sorption and for their photoluminescence properties.

6.3 Synthesis and characterisation of Sr coordination networks

6.3.1 Ligand syntheses

Six functionalised dicarboxylic acid based linkers, H_2bpdc-NO_2, H_2bpdc-$(NO_2)_2$, H_2bc, H_2bpdc-NH_2, H_2bpdc-NMe_2 and H_2bpdc-$(NH_2)_2$ were used to construct Sr coordination networks. These linkers have been used to construct MOFs with various metal ions; however, to date, they have not been reported in Sr coordination networks.

Literature procedures were applied to prepare H_2bpdc-NO_2, H_2bpdc-$(NO_2)_2$,[25] H_2bc,[26] H_2bpdc-NH_2[27] and H_2bpdc-$(NH_2)_2$. The syntheses of H_2bpdc-NH_2 and H_2bpdc-NMe_2 were discussed in 5.2.1.1 and 5.2.1.4, respectively. The structures of the nitro- and amine-functionalised ligands are presented in Figure 6.3.

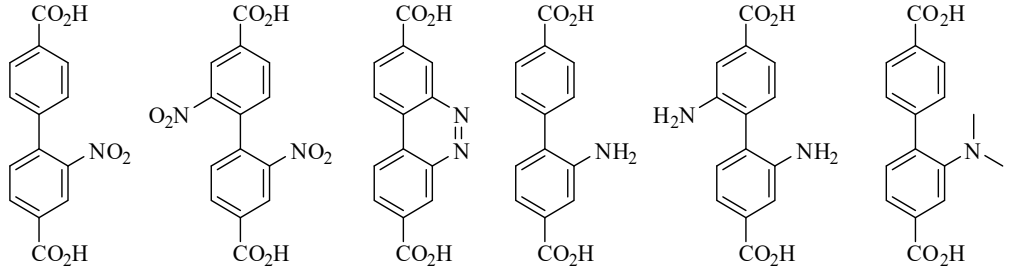

Figure 6.3 The structures of the nitro and amine functionalised ligands investigated in this chapter.

The linker H_2bpdc-NO_2 has been incorporated in lanthanide MOFs that were investigated for their luminescent and magnetic properties.[6] The synthesis of Al(OH)bpdc-NO_2 (DUT-5) is also reported using this linker.[28, 29] The linker H_2bpdc-$(NO_2)_2$ was used in a number of copper based MOFs. Zhu and co-workers reported [Cu_3(bpdc-$(NO_2)_2)_2(\mu_3$-$OH)_2(\mu_2$-$H_2O)$]·2DMA and investigated CO_2 adsorption selectivity, the stability of this MOF in the presence of water, and guest induced single-crystal-to-single-crystal transformations.[30] The group of Gao prepared three Cu-MOFs using H_2bpdc-$(NO_2)_2$ under different synthesis conditions and investigated the diversity in topology of the resultant frameworks.[31] In two other reports the linker was used in conjunction with dipyridyl derivatives and the MOFs were structurally characterized by single crystal X-ray

diffraction.[32, 33] Telfer and co-workers demonstrated the synthesis of a series multi-component MOFs using three different divergent carboxylate linkers, including H_2bc, to generate isostructural MOFs.[26]

There are no reports of H_2bpdc-$(NH_2)_2$ being used in the direct synthesis of MOFs. In two different papers, the group of Su report the synthesis of flexible Zr-bpdc-$(CF_3)_2$-based MOFs and the post-synthetic installation of a number of linkers, including H_2bpdc-$(NH_2)_2$.[34, 35]

As explained in 5.2.1.2, nitration of Me_2bpdc under standard electrophilic conditions yields Me_2bpdc-NO_2 along with a trace amount of unreacted material that is impossible to separate by chromatography or crystallisation. Therefore, Me_2bpdc-NO_2 was synthesised via a Suzuki coupling reaction using ethyl 4-iodo-3-nitrobenzoate and 4-carboxyphenylboronic acid as starting materials with aqueous Na_2CO_3 and Pd(dppf)Cl_2 as base and catalyst, respectively, in degassed DMF at 90 °C. Following esterification (conc. H_2SO_4 in MeOH,) and hydrolysis (aq. NaOH in THF/MeOH), H_2bpdc-NO_2 was isolated as a pure white powder in 77% yield over the two steps.

The synthesis of H_2bpdc-$(NO_2)_2$ was without complication. Me_2bpdc was dinitrated in concentrated H_2SO_4 and 70% HNO_3 in 86% yield (Lit. 70%)[25] and aqueous NaOH hydrolysis in THF/MeOH solution gave H_2bpdc-$(NO_2)_2$ as a white powder in a 89% yield after acidification (Scheme 6.1). H_2bc was prepared as a yellow powder in three steps from Me_2bpdc-$(NO_2)_2$ by nitro group reduction using Pd/C and ammonium formate in THF/MeOH (84%), oxidative amine dimerization using 30% aqueous H_2O_2 in acetic acid (73%; Lit. 49%) and hydrolysis employing aqueous NaOH in THF/MeOH with aqueous acidic work up (95%). This sequence gave good conversions with no further purification required (Scheme 6.1). Me_2bpdc-$(NH_2)_2$, generated as an intermediate in H_2bc synthesis, was hydrolysed using aqueous NaOH in THF/MeOH solution and H_2bpdc-$(NH_2)_2$ was isolated as a yellow powder in 87% yield following aqueous acidic workup (Scheme 6.1).

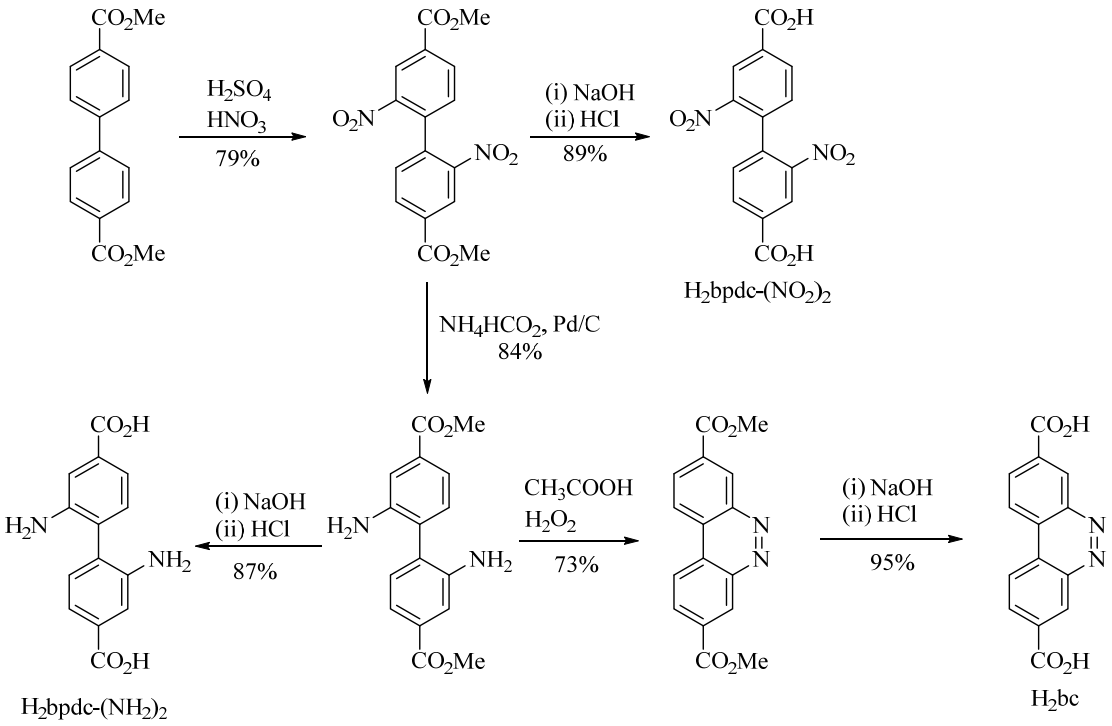

Scheme 6.1 The synthetic pathways to $H_2bpdc\text{-}(NO_2)_2$, H_2bc and $H_2bpdc\text{-}(NH_2)_2$.

6.3.2 Single crystal X-ray diffraction studies

6.3.2.1 *Synthesis and structural description of [$Sr_2(bpdc\text{-}NO_2)_2(H_2O)_2$]*

Needle crystals were obtained by heating an equimolar mixture of H_2bpdc-NO_2 and $Sr(NO_3)_2$ at 130 °C in DMF containing 5% water. Single crystal X-ray diffraction studies showed the structure crystallises in the space group *Ima*2. The asymmetric unit consists of two Sr atoms, four half ligands and two coordinated water molecules (Figure 6.4) allowing the framework to be formulated as [$Sr_2(bpdc\text{-}NO_2)_2(H_2O)_2$]. It should be noted that the crystal structure indicated that only water was the coordinated solvent; however, ^{1}H NMR spectroscopy of a digested sample of this MOF and also elemental analysis showed there existed half of a DMF molecule per asymmetric unit.

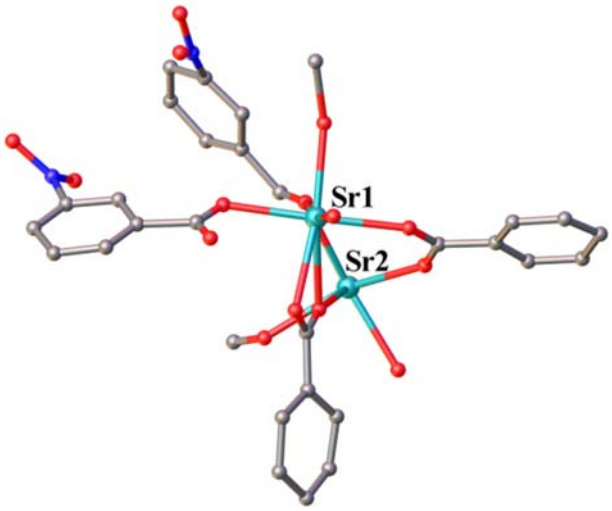

Figure 6.4 The asymmetric unit of [$Sr_2(bpdc\text{-}NO_2)_2(H_2O)_2$]. Hydrogen atoms are not shown for clarity.

Three carboxylate binding modes observed in the structure are represented schematically in Figure 6.5a–c. In coordination modes **a** and **b**, two oxygen atoms of one carboxylate linker chelate one Sr atom and bridge two Sr atoms (μ_3-($\eta^1 : \eta^2 : \eta^1$)), respectively. In binding mode **c**, the carboxylate oxygens bridge two Sr atoms with each binding in a monodentate fashion (μ_2-($\eta^1 : \eta^1$). These binding modes are seen in the literature for Sr-based MOFs.[14, 22]

The coordination environments of Sr1 and Sr2 are shown in Figure 6.5d and e, respectively. Sr1 is seven-coordinate (SrO_7) with four oxygen atoms in an equatorial plane (O10, O13, O30 and O31), and it may be considered as being in a distorted octahedral geometry if the chelating carboxylate (O1 and O2, binding mode **a**) is considered as a single vertex point. O10 and O13 come from bridging carboxylate groups in binding mode **c** and O30 and O31 are bound via binding mode **b.** The last oxygen is provided by coordinated water (O70W).

Sr2 is a SrO_8 centre with two oxygen atoms of binding mode **a** (O30 and O31), two of binding mode **b** (O1 and O2), two with binding mode **c** (O11 and O12) and two terminal water molecules (O40W and O50W). The eight coordinated Sr2 centre is more likely a distorted pentagonal bipyramid if the chelating carboxylate (O30 and O31) is again considered a single vertex point, with five oxygen atoms in an equatorial plane (O1, O2, O11, O12 and O50W).

Infinite 1D chain SBUs alternating the crystallographically distinct Sr centres run parallel to the crystallographic *b*-axis (Figure 6.5f). The chains are generated by edge-shared polyhedra from two oxygen atoms (O1-O30 and O2-O31).

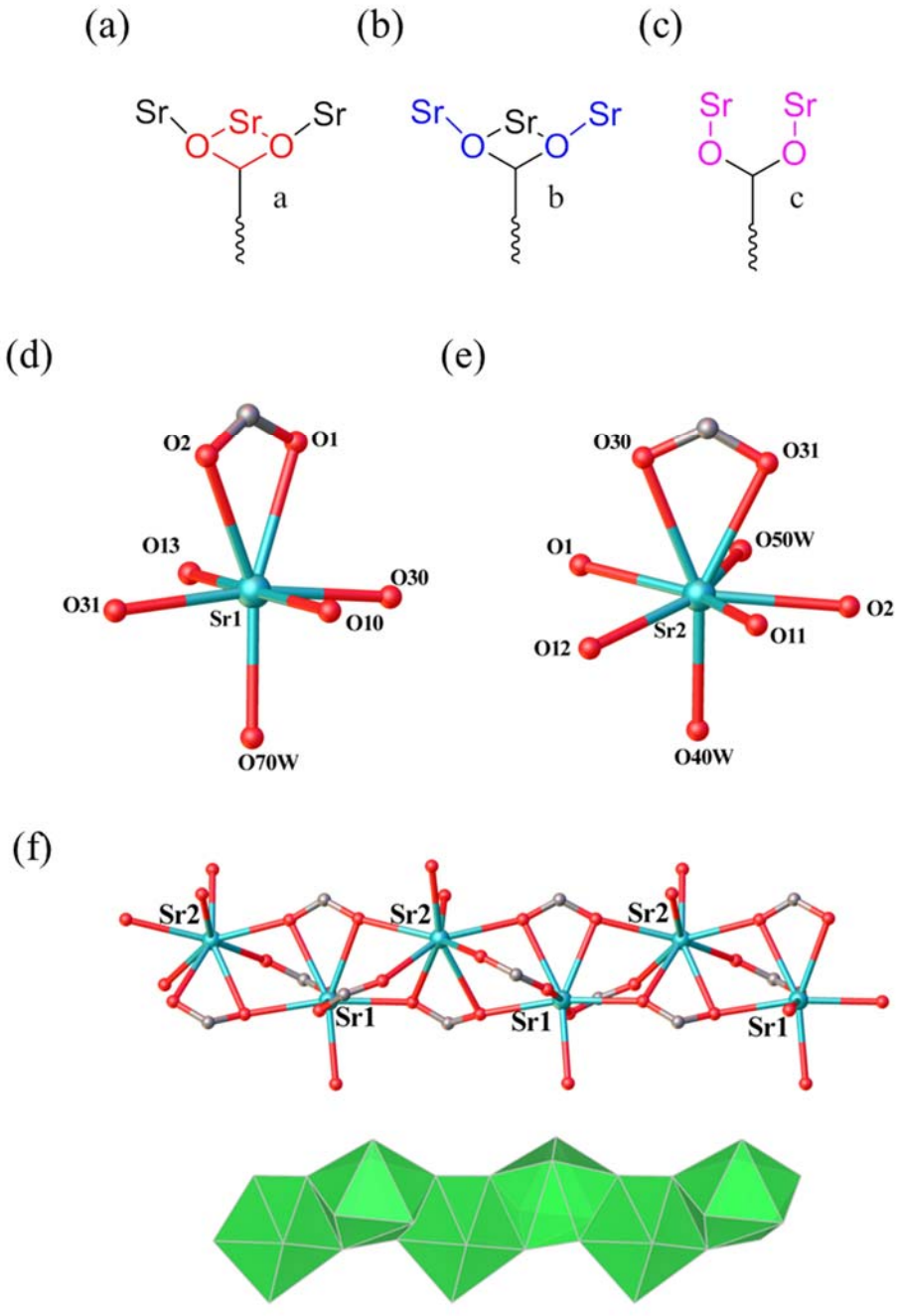

Figure 6.5 Coordination modes of the carboxylates in the structure of $[Sr_2(bpdc\text{-}NO_2)_2(H_2O)_2]$ (a) chelating, (b) chelating and bridging, (c) bridging, and the coordination environments of (d) Sr1 with seven oxygen atoms from five carboxylates and one water molecule (O70W), (e) Sr2 with eight oxygen atoms from five carboxylates and two water molecules (O40W and O50W) and (f) views of the infinite 1D chain SBU along the crystallographic *b*-axis in ball and stick and polyhedral representations, respectively. Hydrogen atoms are not shown for clarity.

The bonding arrangements of bpdc-NO_2^{2-} ligands are shown in Figure 6.6a and b. The bpdc-NO_2^{2-} linker shown in Figure 6.6a has a μ^3-($\eta^1 : \eta^2 : \eta^1$) binding mode at each end and thus binds six Sr centres. The linker has a dihedral angle of 22.2° and the nitro tag groups could not be found in the crystallographic analysis. The other bpdc-NO_2^{2-} linker bridges Sr centres of each chain with $\mu^2(\eta^1 : \eta^1)$ binding modes and hence binds four Sr atoms. The biphenyl rings of this linker have a larger dihedral angle of 54.2° and the nitro group was located in the crystallographic analysis. The extended framework of [Sr_2(bpdc-NO_2)$_2$(H_2O)$_2$] is a porous 3D structure. The edge-sharing polyhedral chains are connected by bpdc-NO_2^{2-} linkers to form the MOF. There exists two shapes of pores that run parallel to the *c*-axis in this structure; large square-shaped pores are ca. 18.4 Å and smaller triangle shaped pores of ca. 10.5 Å (Figure 6.6c).

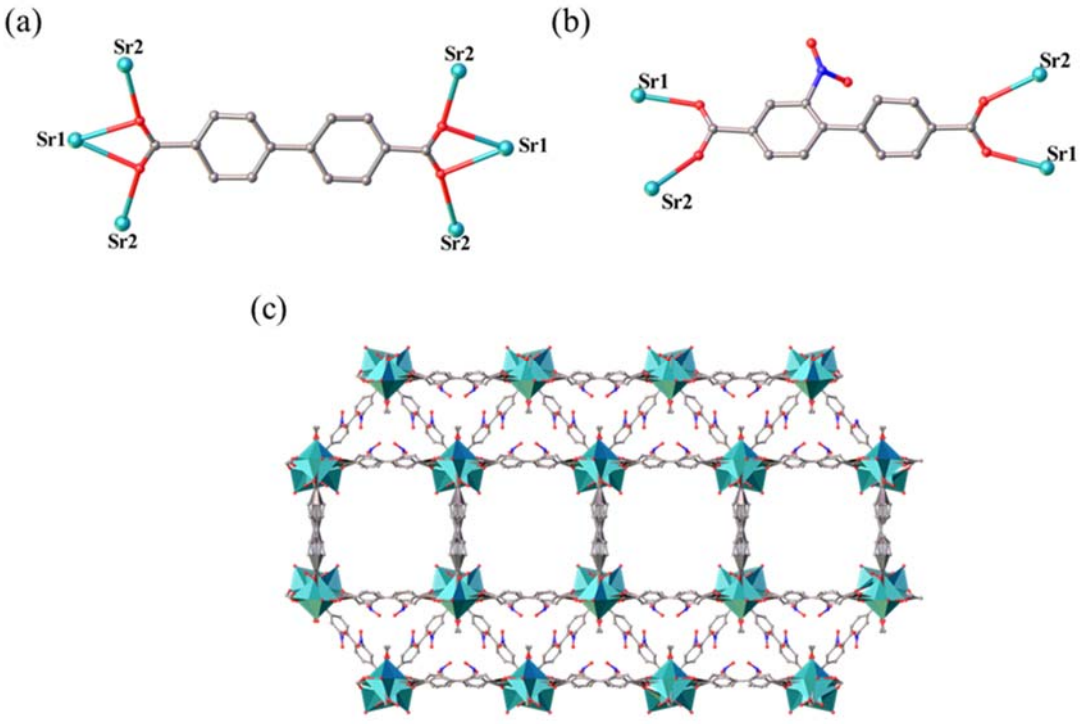

Figure 6.6 (a) and (b) Coordination modes of the bpdc-NO_2^{2-} ligands and (c) view of the extended structure of [Sr_2(bpdc-NO_2)$_2$(H_2O)$_2$] parallel to the crystallographic *c*-axis. Hydrogen atoms are not shown for clarity.

6.3.2.2 *Synthesis and structural description of [$Sr_4(bpdc\text{-}(NO_2)_2)_4 \cdot 2DMF \cdot 4H_2O$]*

Brown needle-like crystals suitable for single crystal analysis formed under the same conditions as [$Sr_2(bpdc\text{-}NO_2)_2(H_2O)_2$] in 52% yield. Single crystal X-ray diffraction studies showed the structure crystallises in the monoclinic space group *C*c. As displayed in Figure 6.7, the asymmetric unit contains four Sr atoms, two complete ligands, four half-ligands, two coordinated DMF and four coordinated water molecules. The SCXRD study also showed the presence of two DMF molecules within the pores.

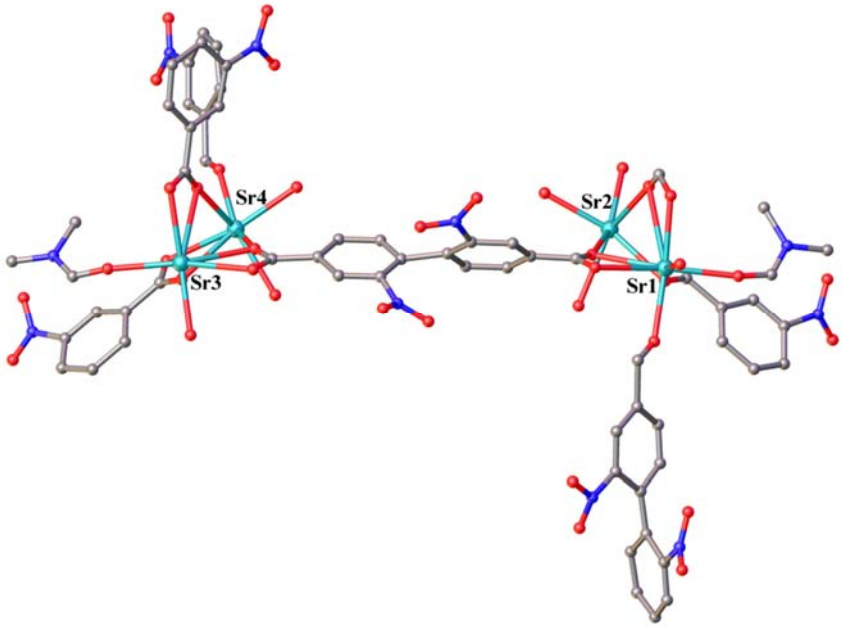

Figure 6.7 A view along the crystallographic *c*-axis of the asymmetric unit of [$Sr_4(bpdc\text{-}(NO_2)_2)_4 \cdot 2DMF \cdot 4H_2O$]. Hydrogen atoms are not shown for clarity.

In the crystal structure, Sr1 and Sr3 are seven-coordinated (SrO_7) with distorted octahedral geometry (Figure 6.8a and b) and Sr2 and Sr4 are eight-coordinated (SrO_8) in distorted pentagonal pyramidal geometry (Figure 6.8c and d). The Sr centres in this framework adopt similar geometries as [$Sr_2(bpdc\text{-}NO_2)_2(H_2O)_2$] and the same binding modes of **a**, **b** and **c** (Figure 6.5a–c). However, the coordinated water in Sr1 in [$Sr_2(bpdc\text{-}NO_2)_2(H_2O)_2$] is replaced by DMF in Sr1 in

$[Sr_4(bpdc\text{-}(NO_2)_2)_4 \cdot 2DMF \cdot 4H_2O]$. Sr-O bond lengths are in the range 2.47–2.77 Å and matched well with previously published results.[22]

The crystal structure of this framework shows two similar infinite chain SBUs with alternating types of Sr centres running parallel to the *c*-axis (Figure 6.8e). Sr1 and Sr2 are linked by oxygen atoms of the bpdc-$(NO_2)_2^{2-}$ linkers in one chain and Sr3 and Sr4 in the second chain. As displayed in Figure 6.8f, the chains are connected by bpdc-$(NO_2)_2^{2-}$ in much the same way as $[Sr_2(bpdc\text{-}NO_2)_2(H_2O)_2]$, to generate the framework.

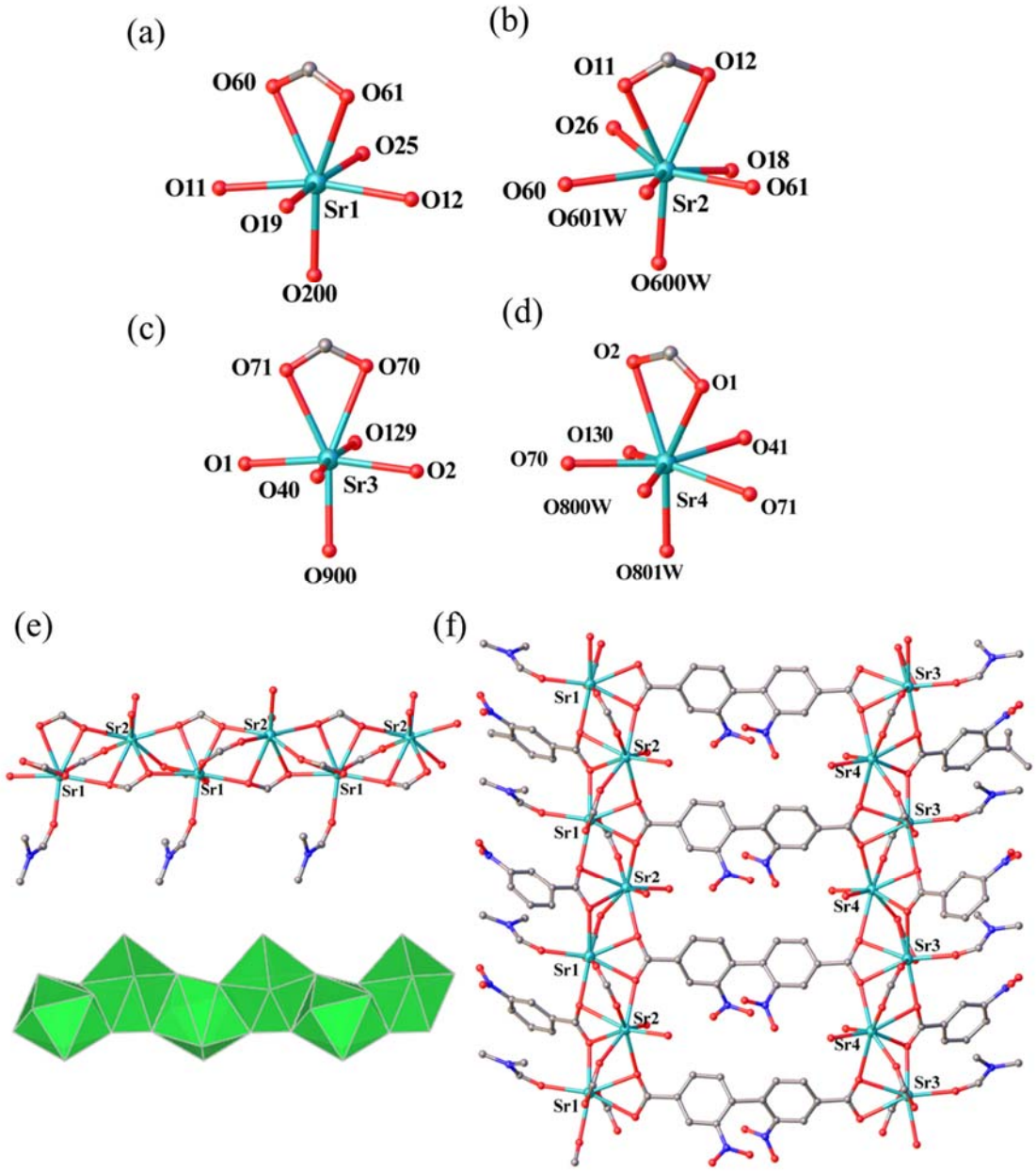

Figure 6.8 The coordination environments of the Sr centres in $[Sr_4(bpdc\text{-}(NO_2)_2)_4 \cdot 2DMF \cdot 4H_2O]$, (a) Sr1, (b) Sr2, (c) Sr3, (d) Sr4, and (e) 1D infinite chain SBU from Sr1 and Sr2 in ball and stick and polyhedral representations and (f) a view of interconnection of two chains to form the framework along the crystallographic *b*-axis. Hydrogen atoms are not shown for clarity.

The coordination arrangements of bpdc-$(NO_2)_2^{2-}$ in the *b*-axis and *c*-axis are presented in Figure 6.9a and b, respectively. The phenyl rings of the bpdc-$(NO_2)_2^{2-}$ linkers are arranged with a large dihedral angle of 49.7° along the *b*-axis. In the *c*-axis, the tag groups are located in the linkers, and the phenyl rings are distorted with an even larger dihedral angle of 83.3°. X-ray crystallography showed $[Sr_4(bpdc\text{-}(NO_2)_2)_4 \cdot 2DMF \cdot 4H_2O]$ (Figure 6.9c) is isotopological with $[Sr_2(bpdc\text{-}NO_2)_2(H_2O)_2]$ (Figure 6.6c) with the same types of triangular and larger square pores.

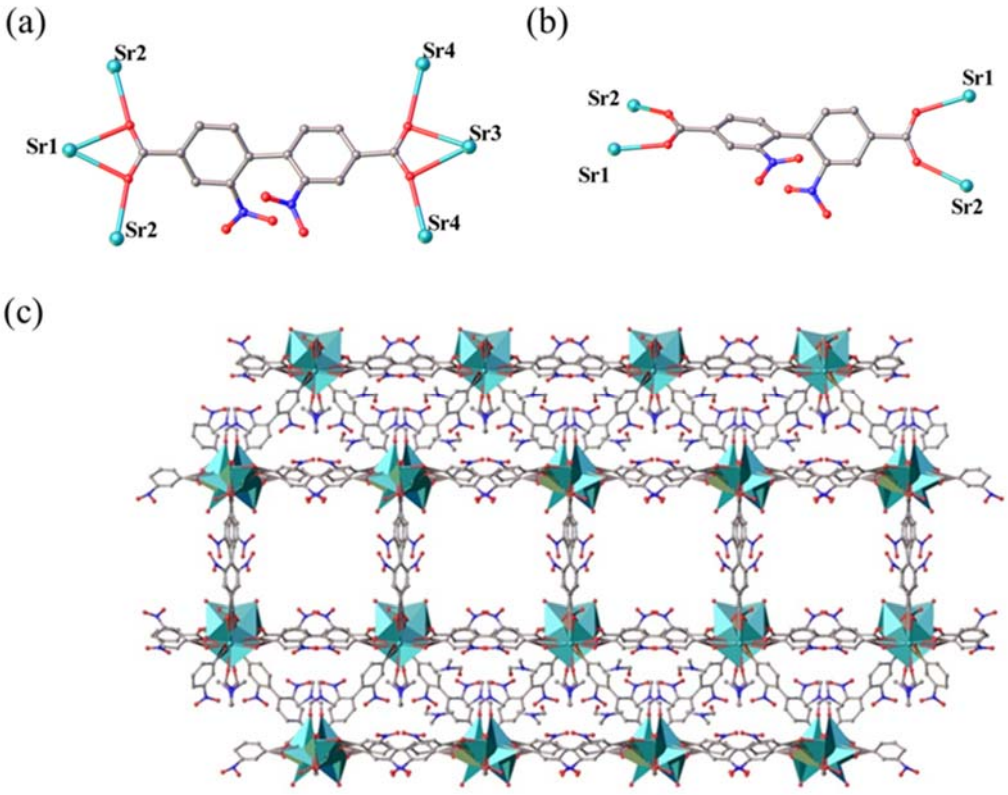

Figure 6.9 Coordination modes of bpdc-NO_2^{2-} linkers along the crystallographic (a) *b*-axis and (b) *c*-axis, and (c) a view along the crystallographic *c*-axis of $[Sr_4(bpdc\text{-}(NO_2)_2)_4 \cdot 2DMF \cdot 4H_2O]$. Hydrogen atoms are not shown for clarity.

6.3.3 Studies of the synthetic conditions of $Sr(NO_3)_2$ with $H_2bpdc\text{-}(NO_2)_2$

A number of conditions were explored for crystal growth with $H_2bpdc\text{-}(NO_2)_2$ and $Sr(NO_3)_2$. This was done to see if the coordinating DMF ligands in $[Sr_4(bpdc\text{-}(NO_2)_2)_4 \cdot 2DMF \cdot 4H_2O]$ could be replaced by water. Thus, syntheses were carried out by varying the water content and reaction temperature, as shown in Table 6.1.

Table 6.1 The synthesis conditions investigated with $H_2bpdc\text{-}(NO_2)_2$ and $Sr(NO_3)_2$.

Entry	Water content (%)	Temperature (°C)	Time (h)	Formulation
1	8	130	16	$[Sr_4(bpdc\text{-}(NO_2)_2)_4 \cdot 2DMF \cdot 4H_2O]$
2	16	130	16	$[Sr_4(bpdc\text{-}(NO_2)_2)_4 \cdot 2DMF \cdot 4H_2O]$
3	24	130	16	No crystal formation
4	32	130	16	No crystal formation
5	24	130	72	No crystal formation
6	32	130	72	No crystal formation
7	24	150	96	$Srbc_{0.51}(bc\text{-}NO)_{0.49}$
8	32	150	96	$Srbc_{0.76}(bc\text{-}NO)_{0.24}$
9	40	150	96	Srbc

In the first set of experiments, the water content was increased to 8%, 16%, 24% and 32% while the time and temperature were held constant (16 h at 130 °C) (Table 6.1, entries 1–4). The reaction mixtures with 8% and 16% water resulted in crystal growth while those with 24% and 32% did not, even after 72 h (Table 6.1, entries 5–6). Digestion in *d*$_6$-DMSO and DCl and subsequent ^{1}H NMR analysis revealed the crystals from entries 1 and 2 contained the same ratio of DMF to $H_2bpdc\text{-}(NO_2)_2$ as digested $[Sr_4(bpdc\text{-}(NO_2)_2)_4 \cdot 2DMF \cdot 4H_2O]$ (Figure 6.11 a and b). The chemical structure of $H_2bpdc\text{-}(NO_2)_2$ annotated with ^{1}H NMR chemical shifts is shown in Figure 6.10a.

Crystals formed by 96 hours in syntheses at 150 °C with 24%, 32% and 40% water content (Table 6.1, entries 7–9). To our surprise, the ^{1}H NMR studies indicated a ligand transformation in which H_2bpdc-$(NO_2)_2$ was converted to benzo[*c*]cinnoline-3,8-dicarboxylic acid (H_2bc) via cinnoline N-oxide (bcNO) as an intermediate. The chemical structures of H_2bc and bcNO annotated with ^{1}H NMR chemical shifts are shown in Figure 6.10b and c.

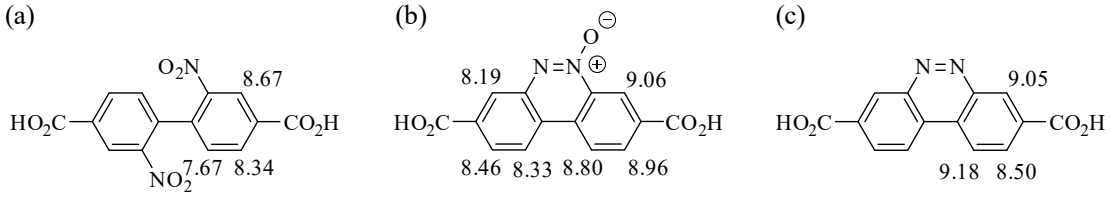

Figure 6.10 The chemical structures with ^{1}H NMR chemical shifts in ppm of (a) H_2bpdc-$(NO_2)_2$, (b) bcNO and (c) H_2bc.

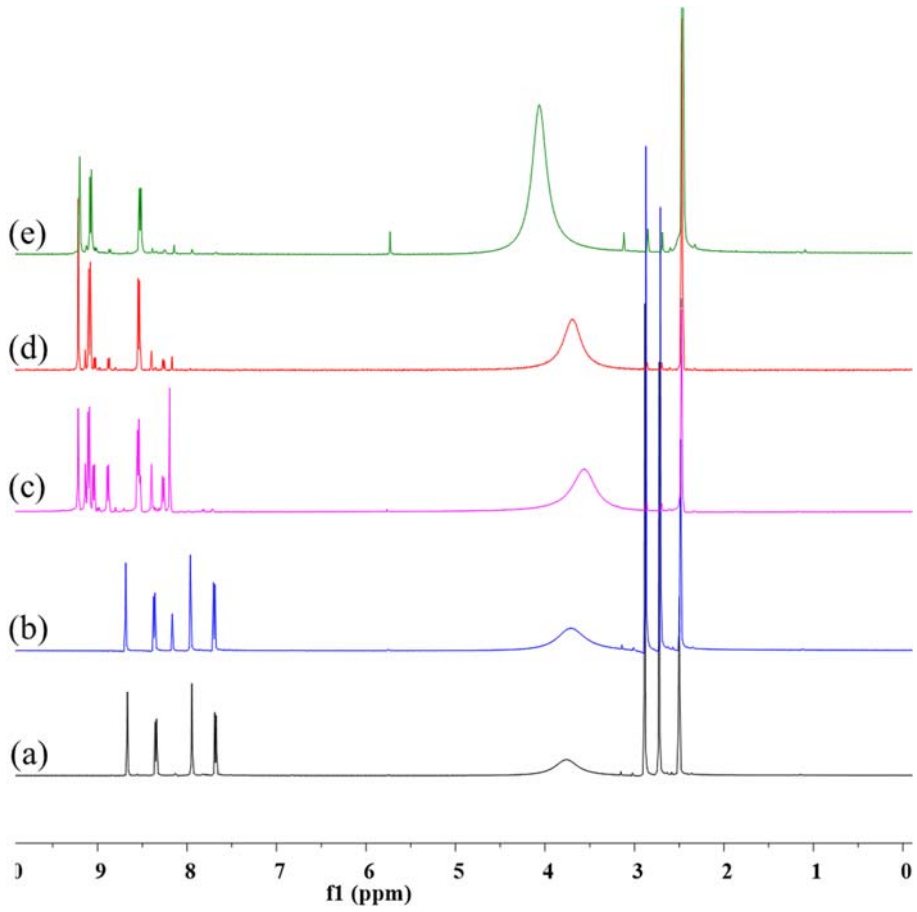

Figure 6.11 ^{1}H NMR spectra of digests of crystals grown at water content (a) 8% (black), (b) 16% (blue), (c) 24% (magenta), (d) 32% (red) and (e) 40% (green).

Crystals containing bc^{2-} and $bcNO^{2-}$ in the ratio of 0.51 to 0.49 were formed in solutions at 150 °C with 24% water content. The conversion to H_2bc was confirmed by peaks appearing in the ^1H NMR spectrum at 8.50 ppm, 9.05 ppm and 9.18 ppm for this known compound[26] (Figure 6.11c) and 8.19 ppm, 8.33 ppm, 8.46 ppm, 8.80 ppm, 9.06 ppm and 9.19 ppm for H_2bcNO. Increasing the water content to 32% resulted in a bc^{2-} to $bcNO^{2-}$ ratio of 0.76 to 0.24 in the framework (Figure 6.11d). A full conversion to bc^{2-} was observed with 40% water content in the solvent (Figure 6.11e). The ^1H NMR results allowed the composition of the networks to be formulated (Table 6.1) and were supported by ESI-MS in all cases with signals at *m/z* 283 for $HbcNO^-$ and *m/z* 267 for Hbc^-. This conversion is a known reaction of 2,2'-dinitrobiphenyls, and a mechanism has been proposed in the literature.[36] In light of this result, H_2bc was prepared by an independent route[26] for incorporation into a framework.

6.3.3.1 *Synthesis and structural description of [Sr(bc)(H₂O)₂]*

Needle crystals were grown by heating an equimolar mixture of H_2bc and $Sr(NO_3)_2$ at 100 °C in DMF containing 24% water. Single crystal X-ray diffraction studies indicated that the structure crystallises in the monoclinic *C*c space group. As shown in Figure 6.12a, the asymmetric unit contains one Sr atom, one bc^{2-} ligand and two coordinated water molecules to give a formula of $[Sr(bc)(H_2O)_2]$.

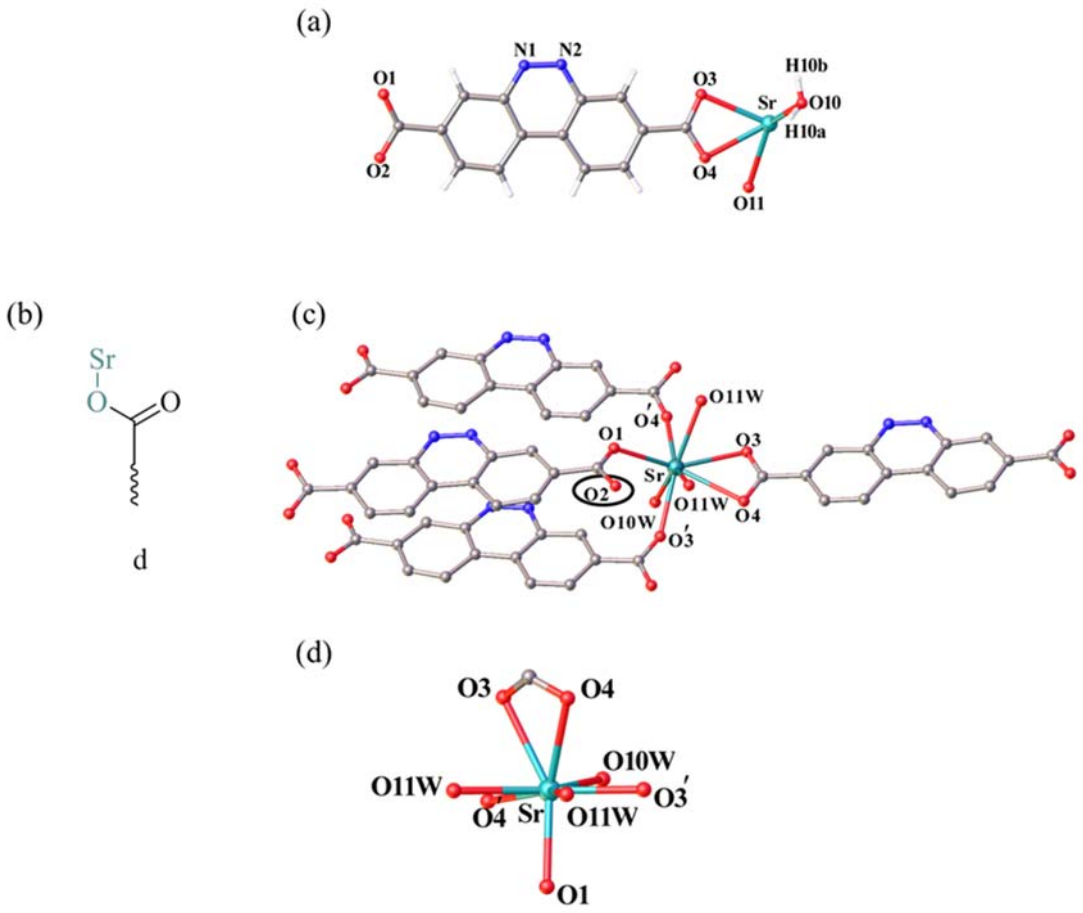

Figure 6.12 (a) A perspective view of the asymmetric unit of $[Sr(bc)(H_2O)_2]$, (b) binding mode **d** in $[Sr(bc)(H_2O)_2]$, (c) a view of the Sr coordination environment with the non-coordinating carboxylate oxygen atom circled in black and (d) a view of the Sr coordination environment showing the distorted pentagonal bipyamidal geometry. Hydrogen atoms are not shown for clarity for clarity in (c) and (d).

There exist three carboxylate coordination modes to the Sr centre; coordination modes of **a** and **b** as observed in $[Sr_2(bpdc\text{-}NO_2)_2(H_2O)_2]$ and $[Sr_4(bpdc\text{-}(NO_2)_2)_4\cdot 2DMF\cdot 4H_2O]$ (section 6.1.2.1) and a new binding mode where a single carboxylate oxygen binds (denoted binding mode **d**), as shown in Figure 6.12b. This binding mode was reported previously for Sr-carboxylate materials.[16] The Sr coordination environment is SrO_8 and distorted pentagonal bipyramidal in geometry from five carboxylate oxygen atoms belonging to four linkers, and three oxygen atoms from one terminal (O10W) and two bridging water molecules (O11W) (Figure 6.12c and d). The SrO_8 unit has O3 and O4 in binding mode **a**, O3′ and O4′ in binding mode **b**, and O1 in binding mode **d**. Bond lengths of Sr-O were in the range of 2.48–2.72 Å, and these values are consistent with previously published Sr-based MOFs.[14] The SrO_8 units assemble into 1D infinite chain SBUs by face-sharing of four oxygen atoms (O3, O4 and O11W) as shown in ball and stick and polyhedral styles in Figure 6.13.

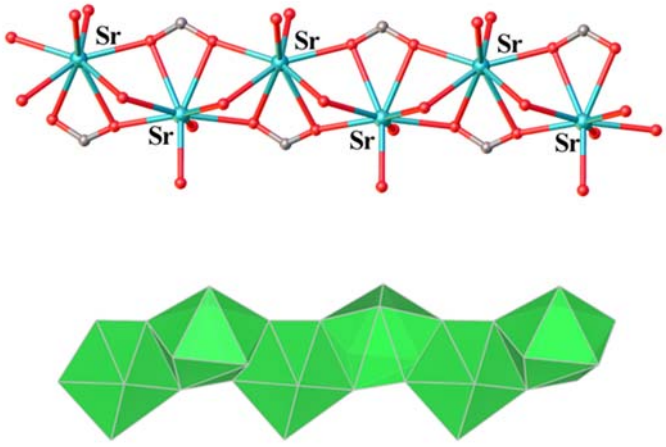

Figure 6.13 1D chain of $[Sr(bc)(H_2O)_2]$ in ball and stick style and polyhedral representation. Hydrogen atoms are not shown for clarity.

The bc^{2-} linker coordinates three Sr centres at one end and only binds to one Sr at the other end (Figure 6.14a). Figure 6.14b shows the extended structure of $[Sr(bc)(H_2O)_2]$. The polymeric SBU chains are connected by planar bc^{2-} into a dense 3D network. In this structure, the hydrogens of the bound water molecules (H10a and H10b) participate in hydrogen bonds with bridging water molecules

(O11W) and the oxygen of the unbound carboxylate groups (O2) (Figure 6.14c), with 2.11 Å and 1.94 Å hydrogen bonding distances, respectively. The 3D structure is thus stabilised through π-π stacking interactions of planar bc^{2-} linkers, and extensive hydrogen bonding (Figure 6.14d).

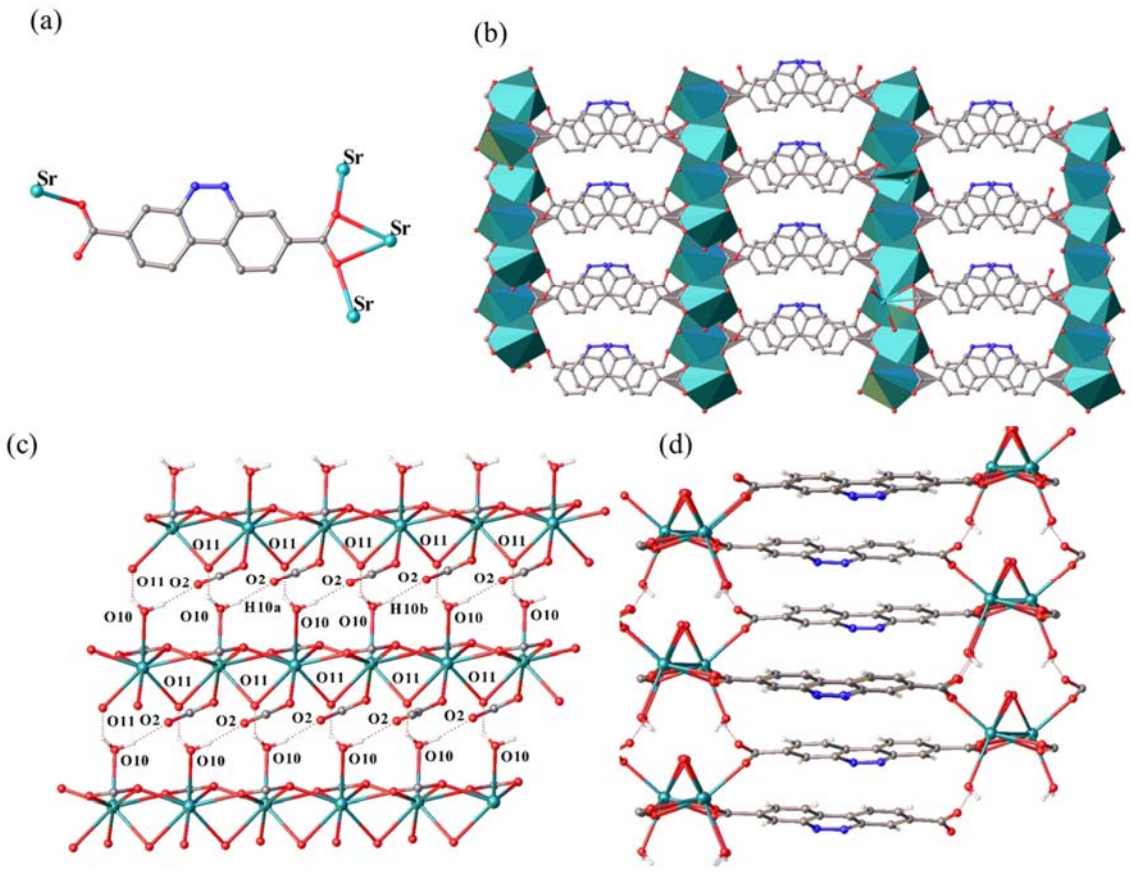

Figure 6.14 (a) The coordination modes of bc^{2-} linkers, (b) a view of the 3D structure of $[Sr(bc)(H_2O)_2]$ parallel to the crystallographic *c*-axis, (c) a view of the hydrogen bonding between H10a and H10b and O11 and O2 parallel to the crystallographic *b*-axis and (d) a view of π-π stacking interactions of bc^{2-} along the crystallographic *a*-axis. Hydrogen atoms are not shown for clarity in (a) and (b).

6.3.3.1 *Synthesis and structural description of [$Sr_3(bpdc\text{-}NH_2)_3(DMF)_2$]*

Needle crystals were prepared in a very high yield of 86% from a reaction between H_2bpdc-NH_2 and $Sr(NO_3)_2$ at 130 °C in a mixture of DMF containing 5% water. Single crystal X-ray diffraction studies revealed that the asymmetric unit of this structure contains one and a half Sr cations, one complete and one half-ligand, and one DMF molecule in the triclinic space group *P*-1 (Figure 6.15a).

Sr1 is seven coordinate (SrO_7) but may be considered as a distorted octahedral geometry if the chelating carboxylate (O19 and O20) with binding mode **a** is considered as a single vertex point (Figure 6.15b). The remaining sites are occupied by two oxygen atoms (O1 and O2) via binding mode **b** and two oxygen atoms (O30 and O31) coordinated via binding mode **c** and the coordination sphere is completed by binding a DMF molecule. Sr2 crystallises on an inversion centre and is eight coordinate (SrO_8) with distorted square prismatic geometry (Figure 6.15c). O1 and O2 coordinate in binding mode **a** and O19 and O20 coordinate via binding mode **b**.

The SBU of this structure consists of three Sr centres with the crystallographically distinct Sr cations connected by bridging carboxylates (Figure 6.15d). These atoms alternate to generate an infinite chain in the *b*-axis with edge-shared polyhedra (Figure 6.15e).

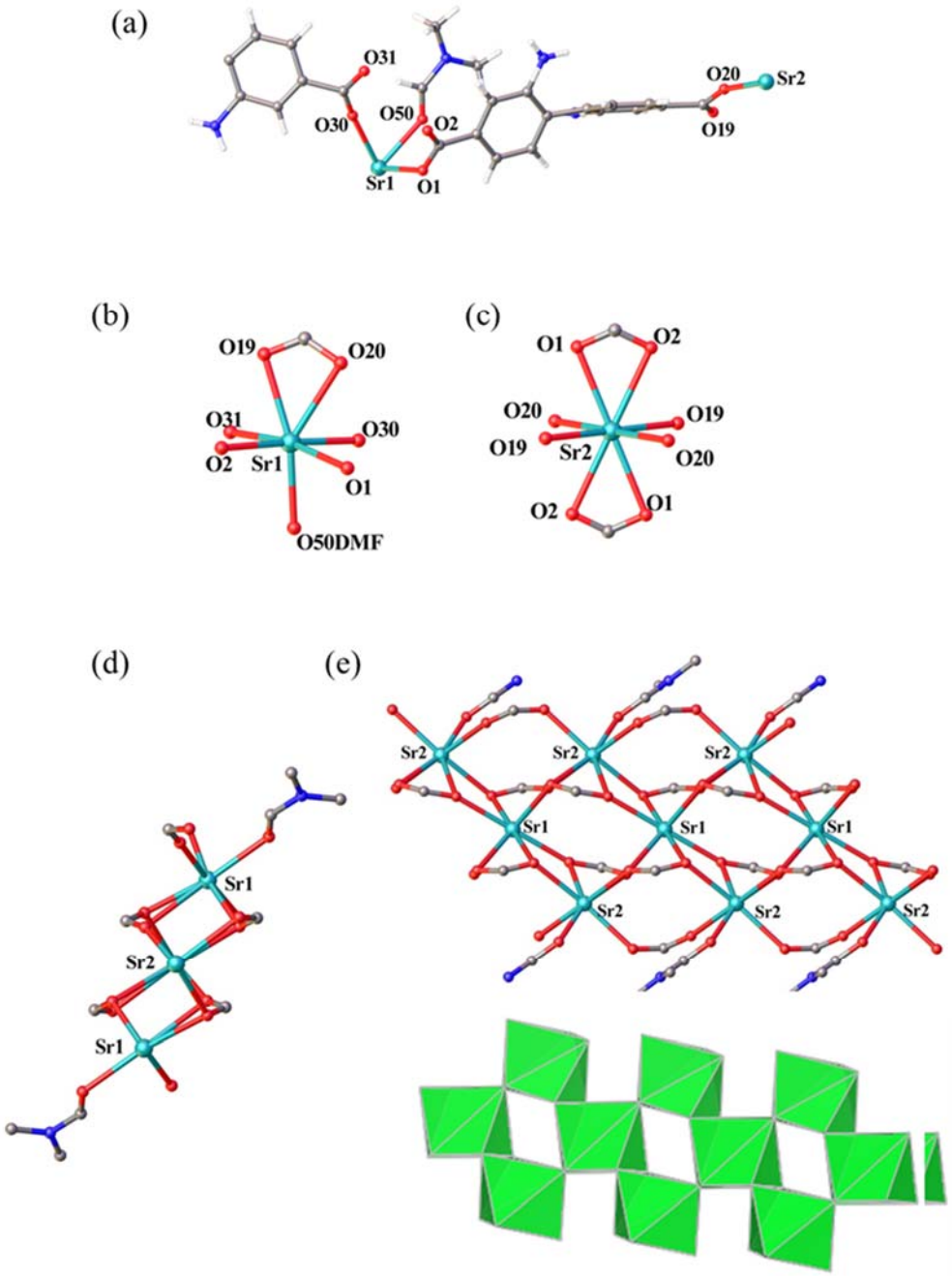

Figure 6.15 (a) A view of the asymmetric unit of $[Sr_3(bpdc\text{-}NH_2)_3(DMF)_2]$, perspective views of the coordination environments of (b) Sr1, (c) Sr2, (d) part of the infinite 1D chain SBU, as viewed along the crystallographic *a*-axis and (e) views parallel to the crystallographic *b*-axis of part of the 1D infinite chain SBU in ball and stick and polyhedral styles. Hydrogen atoms are not shown for clarity for clarity in (d) and (e).

As shown in Figure 6.16a and b, one linker coordinates six Sr atoms utilising bridging and chelating modes with a dihedral angle of 57.2° while another linker bridges four Sr atoms with the phenyl groups dihedral angle equal to zero. It should be noted that the amine tag groups could not be found in the crystallographic analysis and were placed in the ligand structure in chemically reasonable positions. The polymeric SBUs are connected by bpdc-NH_2^{2-} linkers into a non-porous 3D framework. Rhomboidal channels run out along the crystallographic *a*-axis but are filled by the DMF coordinated to Sr1 atoms of the network (Figure 6.16c).

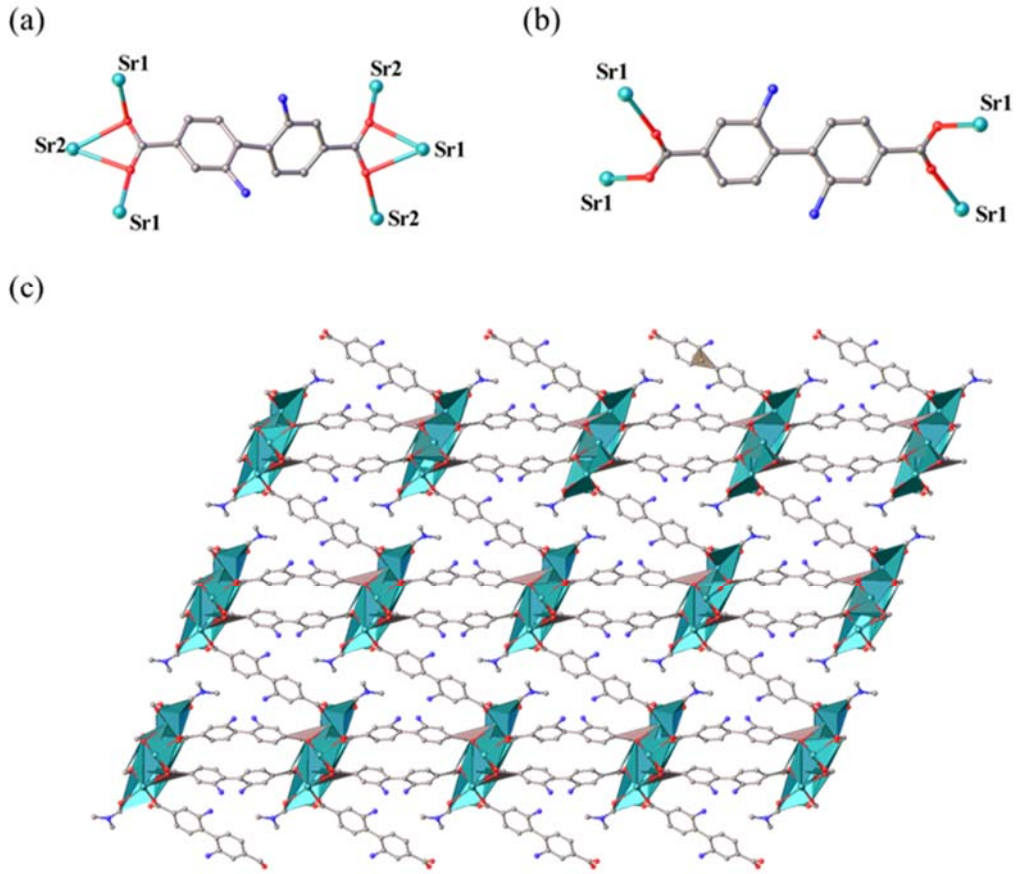

Figure 6.16 (a) and (b) Coordination modes of bpdc$(NH_2)^{2-}$and (c) a view parallel to the crystallographic *a*-axis of part of the 3D structure of $[Sr_3(bpdc\text{-}NH_2)_3(DMF)_2]$. Hydrogen atoms are not shown for clarity.

6.3.3.1 *Synthesis and structural description of [Sr_4(bpdc-$(NH_2)_2)_4(H_2O)_3$]*

Needle brown crystals were grown via a solvothermal reaction between H_2bpdc-$(NH_2)_2$ and $Sr(NO_3)_2$ by heating at 100 °C in a solvent system of DMF containing 5% water. Single crystal X-ray diffraction studies showed the structure crystallises in the triclinic space group *P*-1 with four Sr centres, four completed ligands and three bound water molecules in the asymmetric unit (Figure 6.17), to give this structure a formulation of [Sr_4(bpdc-$(NH_2)_2)_4(H_2O)_3$].

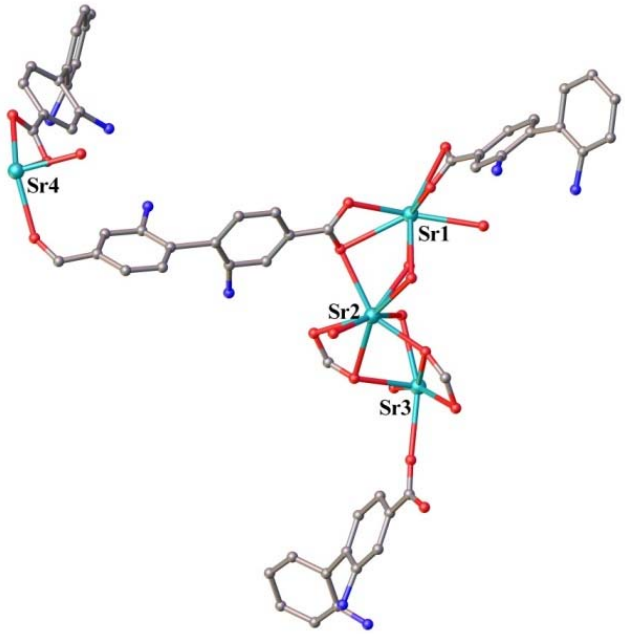

Figure 6.17 A perspective view of the asymmetric unit of [Sr_4(bpdc-$(NH_2)_2)_4(H_2O)_3$]. Hydrogen atoms are not shown for clarity.

There exist four carboxylate coordination modes in [Sr_4(bpdc-$(NH_2)_2)_4(H_2O)_3$]; coordination modes of **a** and **b** as observed in all structures described above. In this structure, a further binding mode was observed where a carboxylate chelates one Sr centre (μ_2-(η^1 : η^2) (Figure 6.18a purple bonds, denoted as binding mode **e**) and bridges to a second Sr centre (Figure 6.18b orange bond, denoted as binding mode **f**). This binding mode is known in the literature.[7] Sr1 is a seven-coordinate distorted capped octahedron from five bpdc-$(NH_2)_2^{2-}$ linkers and one bridging aqua ligand (Figure

6.18c). Sr2 and Sr4 are eight-coordinate in distorted pentagonal bipyramidal geometries albeit with different carboxylate coordination modes (Figure 6.18d and 6.18f, respectively). The Sr3 atom is nine-coordinate with different carboxylate binding modes.

The Sr atoms are arranged in a 1D infinite helical chain SBU, decorated with bridging carboxylates, as shown in Figures 6.18g. The connection of Sr polyhedra in this structure is considerably more complicated compared to the other materials reported in this study. The polyhedra are connected by three face-sharing relationships and one edge-sharing relationship between the Sr centres. The connection of Sr1 and Sr2 is by face-sharing O48, O88 and O68. Sr2 and Sr3 are linked by face-sharing of O3, O49 and O102 and Sr3 and Sr4 face-share O70, O52 and O19. The connection between Sr1 and Sr4 is by edge-sharing O30 and O71.

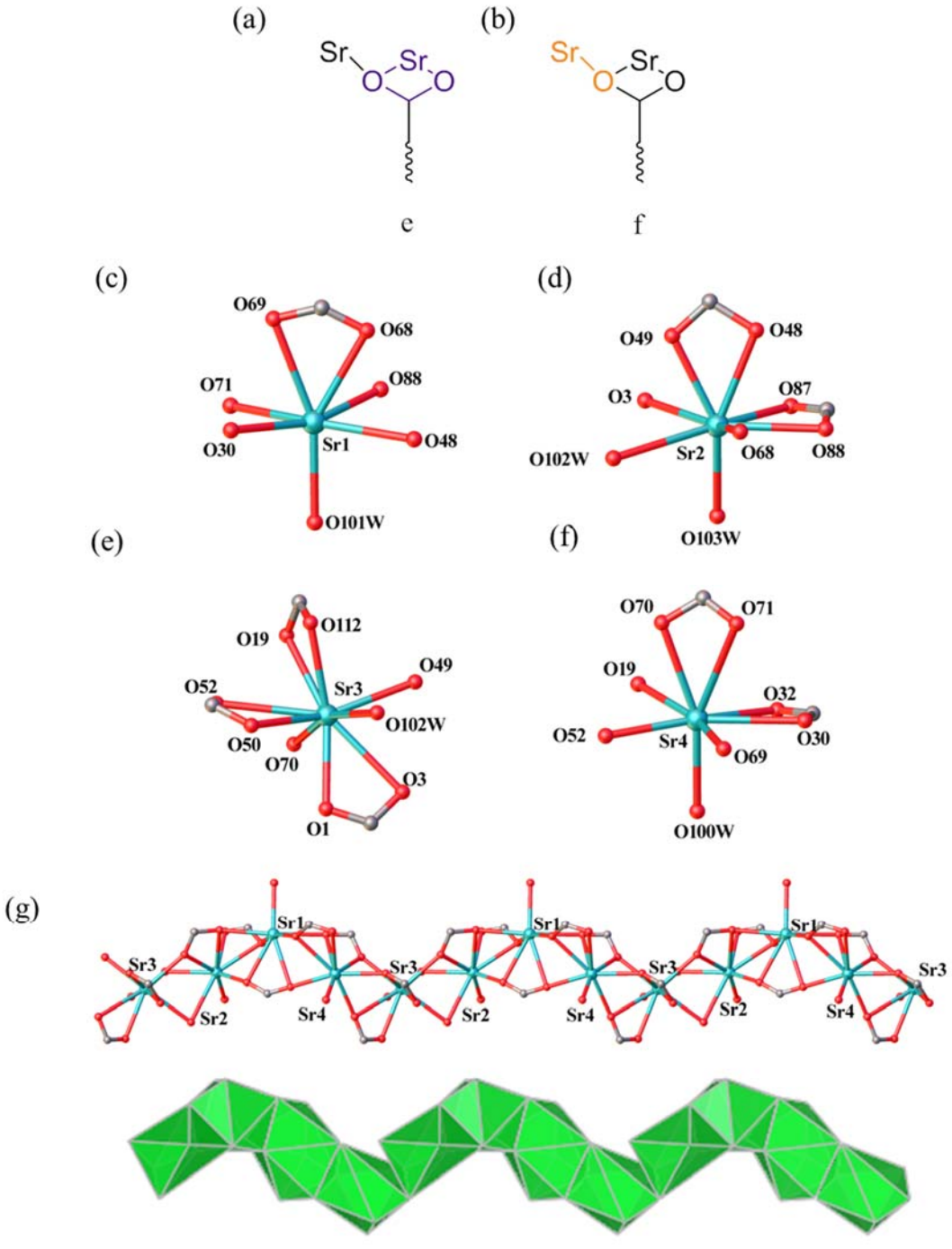

Figure 6.18 Binding modes (a) **e** and (b) **f** observed in the structure of $[Sr_4(bpdc\text{-}(NH_2)_2)_4(H_2O)_3]$, coordination environments in Sr atoms in (c) Sr1, (d) Sr2, (e) Sr3, (f) Sr4 and (g) the 1D infinite helical chain in ball and stick and polyhedral styles, views along the crystallographic *b*-axis.

As displayed in Figure 6.19a, along the *c*-axis, bpdc-$(NH_2)_2^{2-}$ is chelated and bridged between two Sr atoms on each side. In the *b*-axis (Figure 6.19b), there are two different coordination modes at the ends of the linker, the bpdc-$(NH_2)_2^{2-}$ linker is chelated between three Sr centres of the chain. In the other side, the carboxylate group is bridged between two Sr centres. The bpdc-$(NH_2)_2^{2-}$ linkers show 81.9° and 59.1° dihedral angles along the *c*- and *b*-axes, respectively. Linkage of the helical chains by bpdc-$(NH_2)_2^{2-}$generates a 3D framework with large rhombic shaped pores of size 22 Å (atom-centre-to-atom-centre) and smaller triangular-shaped pores of size 12 Å running parallel to the *a*-axis (Figure 6.19c).

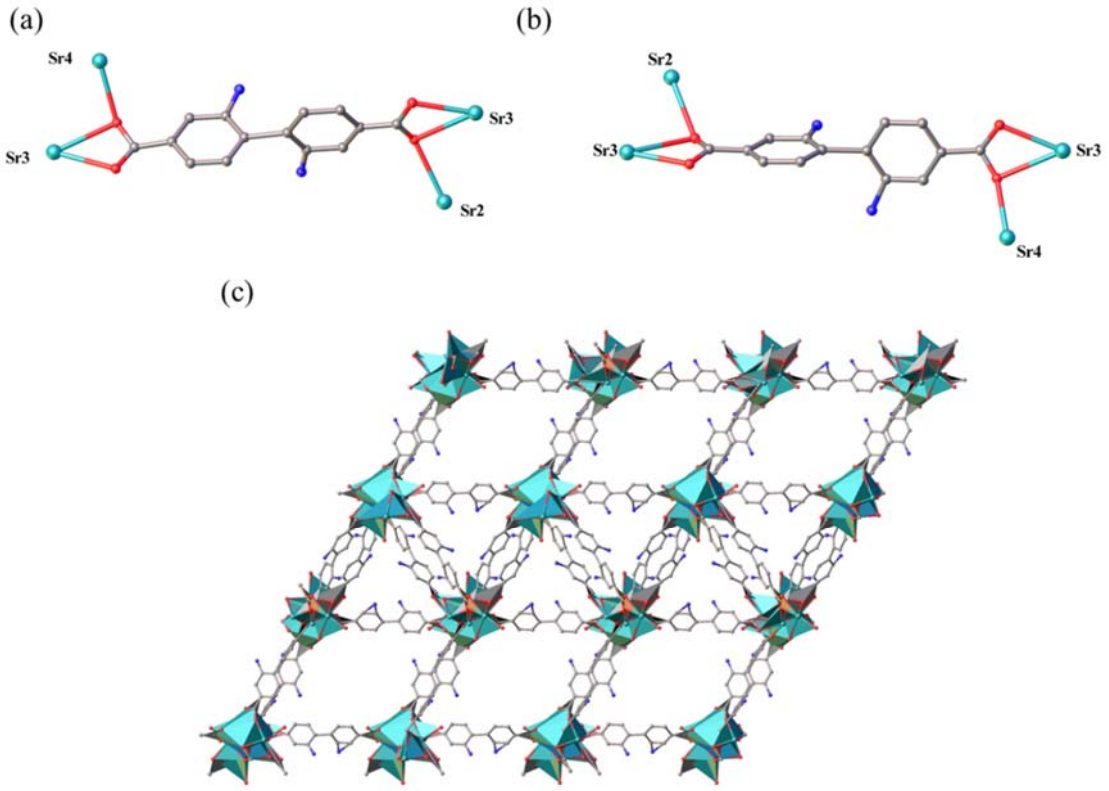

Figure 6.19 (a) and (b) Coordination modes of bpdc-$(NH_2)_2^{2-}$, (c) part of the extended structure of $[Sr_4(bpdc\text{-}(NH_2)_2)_4(H_2O)_3]$ as viewed parallel to the crystallographic *a*-axis. Hydrogen atoms are not shown for clarity.

6.3.3.2 *Synthesis and structural description of [Sr(bpdc-NMe$_2$)(H$_2$O)]*

Yellow needle crystals were obtained through a solvothermal reaction between H$_2$bpdc-NMe$_2$ and Sr(NO$_2$)$_2$ in a mixture of DMF containing 5% water at 130 °C. Single crystal X-ray diffraction studies revealed that the crystals belong to the trigonal space group *P*3$_1$. As displayed in Figure 6.20a, the asymmetric unit consists of one Sr atom, one bpdc-NMe$_2^{2-}$ ligand and one coordinated water molecule. The dimethylamine groups were located in the crystallographic analysis. There is an intraligand hydrogen bond between one of the biphenyl hydrogen atoms (H7) and the nitrogen of the dimethyl amine group.

As shown in Figure 6.20b, the Sr centre is eight-coordinate SrO$_8$ and bonded to seven carboxylate oxygen atoms from five bpdc-NMe$_2^{2-}$, via a chelating binding mode **a** (O18 and O19), two bridging oxygen atoms in binding mode **b** (O18 and O19), two oxygen atoms binding in mode **e** (O2' and O3), one oxygen binding in mode **f** (O2') and one water molecule (O30W). This arrangement is similar to [Sr$_2$(bpdc-NO$_2$)$_2$(H$_2$O)$_2$], [Sr$_4$(bpdc-(NO$_2$)$_2$)$_4$·2DMF·4H$_2$O], [Sr(bc)(H$_2$O)$_2$] and [Sr$_4$(bpdc-(NH$_2$)$_2$)$_4$(H$_2$O)$_3$] coordination networks, where the eight-coordinated Sr centres adopt the distorted pentagonal bipyramidal geometry.

The coordination between the Sr^{2+} ions and carboxylate groups of bpdc-NMe$_2^{2-}$ produces an infinite helical 1D rod SBU. The Sr centres are linked through three oxygen atoms by face-sharing of O2, O18 and O19, which are similar to the face-sharing polyhedra of [Sr$_4$(bpdc-(NH$_2$)$_2$)$_4$(H$_2$O)$_3$]. The view is along the *b*-axis, as ball and stick and polyhedra styles are presented in Figure 6.20c.

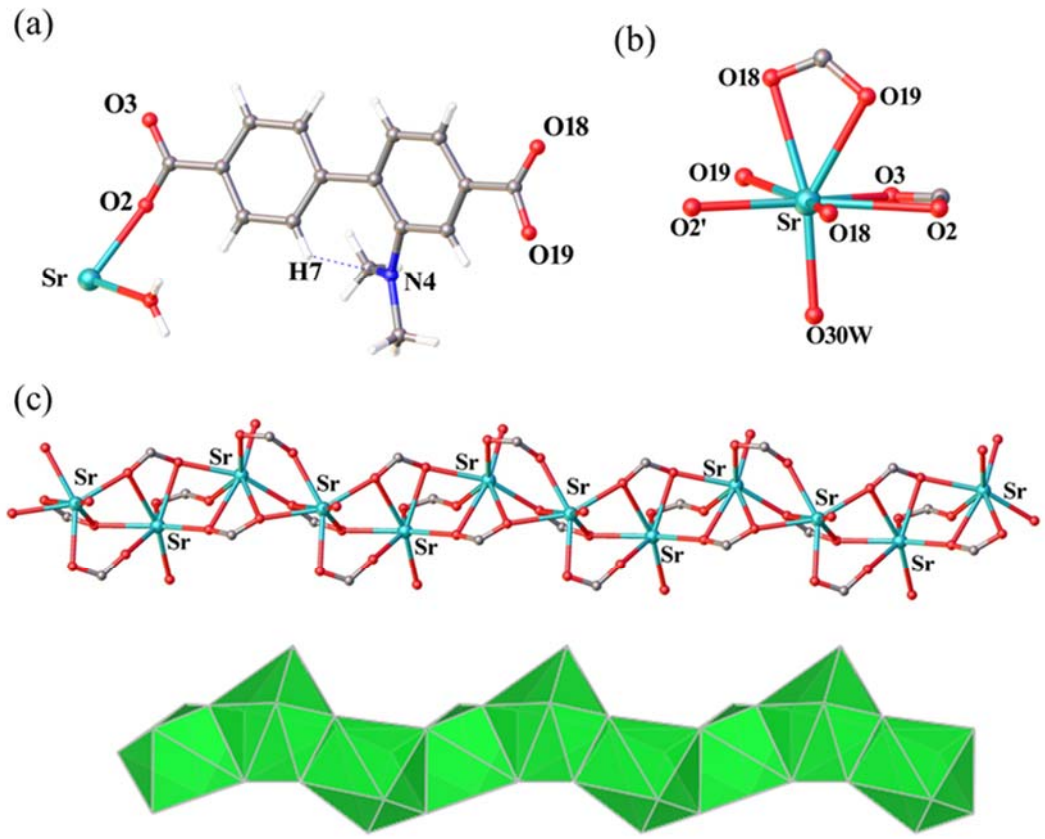

Figure 6.20 (a) A perspective view of the asymmetric unit of [Sr(bpdc-NMe_2)(H_2O)], (b) distorted pentagonal bipyramid geometry of SrO_8; five oxygen atoms are in equatorial plane (O2, O2', O3, O18 and O19), two oxygens in axial positions O18 and O30W) and one oxygen atom (O19) between axial and equatorial positions and (c) views of the helical SBU along the *b*-axis in ball and stick and polyhedral styles, respectively. Hydrogen atoms are not shown for clarity in (b) and (c).

As displayed in Figure 6.21a, bpdc-NMe_2^{2-} binds three Sr centres via **a** and **b** type modes at one end and to two Sr centres by and **e** and **f** type modes at the other. Figure 6.21b shows the framework contains two triangular shaped pores, where the larger pore is 14 Å and smaller pore is 10 Å (as measured atom-centre-to-atom-centre).

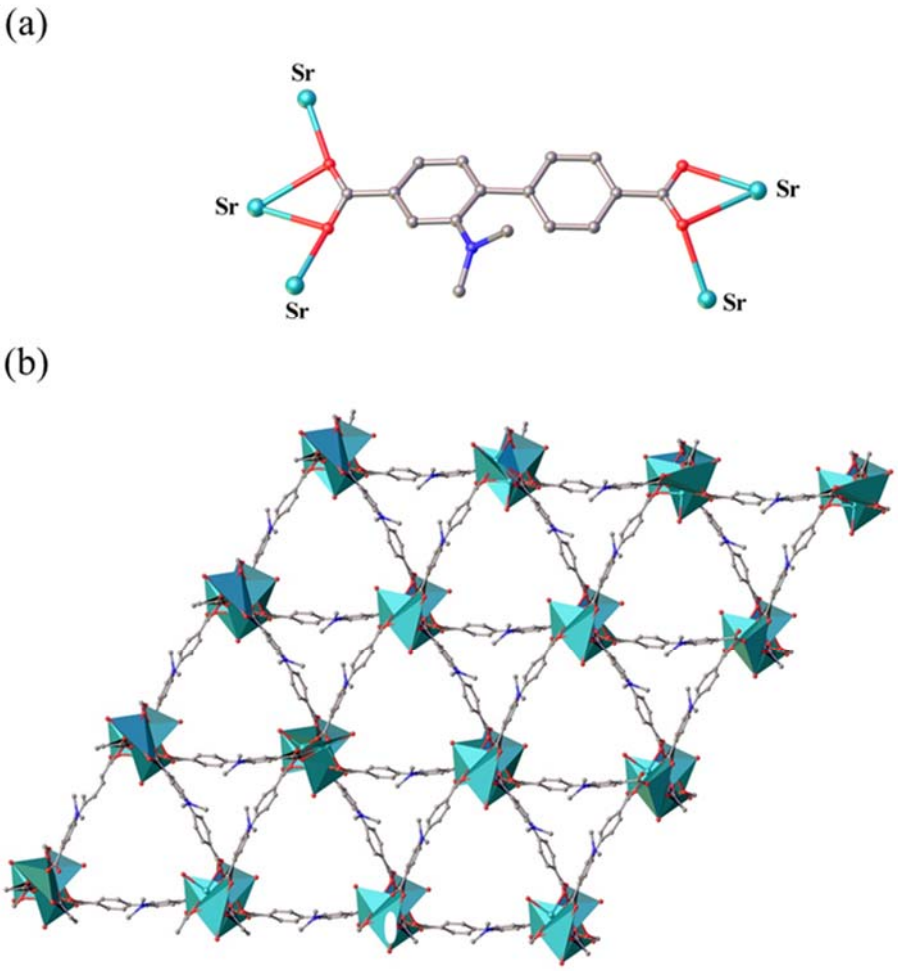

Figure 6.21 (a) Coordination modes of bpdc-NMe_2^{2-} that connects chains along the crystallographic *a*-axis and (b) part of the extended structure of [Sr(bpdc-NMe_2)(H_2O)] as viewed along the crystallographic *c*-axis. Hydrogen atoms are not shown for clarity.

6.3.1 Comments on the strontium coordination networks

The coordination numbers and modes of strontium centres in the coordination networks are summarised in Table 6.2. The coordination numbers of 7 and 8 are the most commonly observed in these coordination networks and the highest coordination number was 9, and was only observed in $[Sr_4(bpdc\text{-}(NH_2)_2)_4(H_2O)_3]$. Six binding modes of **a**, **b**, **c**, **d**, **e** and **f** were identified, and within this set the interdependent binding modes **a** and **b** are the most frequently repeated. In contrast, the binding modes of **e** and **f** were only observed in $[Sr_4(bpdc\text{-}(NH_2)_2)_4(H_2O)_3]$ and $[Sr(bpdc\text{-}NMe_2)(H_2O)]$. The **a**/**b** binding mode is a particularly efficient mode to satisfy the high coordination numbers required for the large strontium atom at the same time as forming charge-neutral frameworks. Notable is that the ligands with two functional groups in their organic linkers showed higher numbers of crystallographically distinct Sr centres in their asymmetric units, which might be related to the torsional angles adopted around the biphenyl bonds. In general, the ligands carrying larger substituent groups resulted in coordination networks with larger channels and potential porosity. The presence of water was crucial to the crystallisation of the networks and most contain this as a ligand to strontium, mostly in a terminal fashion. In $[Sr_4(bpdc\text{-}(NO_2)_2)_4 \cdot 2DMF \cdot 4H_2O]$ and $[Sr_3(bpdc\text{-}NH_2)_3(DMF)_2]$ coordinated DMF molecules were observed in their crystal structures.

Crystal data and structures refinement for Sr-based coordination networks are presented in Appendix 4, Table A4.1.

Table 6.2 Coordination numbers and modes of strontium centres in the coordination networks.

Structure		CN	a	b	c	d	e	f	DMF	Terminal H_2O	Bridging H_2O
$[Sr_2(bpdc\text{-}NO_2)_2(H_2O)_2]$	Sr1	7	1	2	2					1	
	Sr2	8	1	2	2					2	
$[Sr_4(bpdc\text{-}(NO_2)_2)_4 \cdot 2DMF \cdot 4H_2O]$	Sr1	7	1	2	2				1		
	Sr2	8	1	2	2					2	
	Sr3	7	1	2	2				1		
	Sr4	8	1	2	2					2	
$[Sr(bc)(H_2O)_2]$	Sr	8	1	2		1				1	2
$[Sr_3(bpdc\text{-}NH_2)_3(DMF)_2]$	Sr1	7	1	2	2				1		
	Sr2	8	2	4							
$[Sr_4(bpdc\text{-}(NH_2)_2)_4(H_2O)_3]$	Sr1	7	1	2				2		1	
	Sr2	8	1	1			1	1		1	1
	Sr3	9		2			3				1
	Sr4	8	1	1			1	2		1	
$[Sr(bpdc\text{-}NMe_2)(H_2O)]$	Sr	8	1	2			1	1		1	

6.3.1 Gas sorption studies

As porous Sr-based coordination networks are less reported in the literature, their activation is still quite challenging. Several solvent exchange and drying procedures were trialled on networks containing solvent-filled voids in order to be able to measure their porosity by gas adsorption techniques.

In order to find the best activation method for each coordination network, and consequently, achieve the highest gas sorption uptake, various solvent exchange and activation procedures were performed on the coordination networks. The crystals were then studied in CO_2 adsorption at 273 K. The CO_2 adsorption measurements at 273 K are plotted in Appendix 4, Figure A4.4.

6.3.1.1 *Solvent exchange, activation procedures, and gas adsorption studies of $[Sr_2(bpdc\text{-}NO_2)_2(H_2O)_2]$ and $[Sr_4(bpdc\text{-}(NO_2)_2)_4\cdot 2DMF\cdot 4H_2O]$*

Four solvent exchange methods were examined for $[Sr_2(bpdc\text{-}NO_2)_2(H_2O)_2]$ and $[Sr_4(bpdc\text{-}(NO_2)_2)_4\cdot 2DMF\cdot 4H_2O]$ and were assayed by PXRD to assess crystallinity and ^1H NMR analysis (Appendix, Figures A4.1a and b and A4.5a and b) to assess solvent removal: (i) dry CH_2Cl_2 over two weeks at room temperature, (ii) as for (i) with additional heating for 6 hours in refluxing dry CH_2Cl_2, replacing with fresh dry CH_2Cl_2 three times, (iii) exchange to dry acetone at room temperature, and (iv) exchange with wet acetone at room temperature (Appendix, Table A4.2, entries 1–4). PXRD patterns of the as-synthesised and activated coordination networks are presented in Appendix 4, Section A4.1. TGA traces of the as-synthesised and activated coordination networks are presented in Appendix 4, Figure A4.3.

^1H NMR spectra (Figure A4.5) showed bpdc-NO_2^{2-} and bpdc-$(NO_2)_2^{2-}$ are incorporated into the MOFs unchanged and that exchange protocols with CH_2Cl_2 were ineffective at removing all DMF. Given the vacuum drying process and the ^1H NMR ratios, it is likely that the remaining DMF is bound at the Sr nodes. This was expected in $[Sr_4(bpdc\text{-}(NO_2)_2)_4\cdot 2DMF\cdot 4H_2O]$ where the single crystal structure shows DMF is bound. Solvent exchange in dry acetone successfully removed all DMF but signals for acetone were

now observed in ratios that were consistent with these being coordinated to Sr. ^{1}H NMR spectra recorded after solvent exchange with wet acetone showed no signals for DMF or acetone and it was thought that water was now coordinating to the Sr atoms. This was deemed very desirable as water is the smallest of the ligands, and therefore would open up the most space in these structures.

$ScCO_2$ and freeze drying were applied as gentle methods to remove solvents from the pores of the networks and notes on the exact methods are given in Table A4.2 in the appendix. Large mass losses from samples exchanged in $ScCO_2$ upon further drying under dynamic vacuum prior to gas adsorption measurements suggested ineffective solvent removal in the $ScCO_2$ process for both $[Sr_2(bpdc\text{-}(NO_2)_2(H_2O)_2]$ and $[Sr_4(bpdc\text{-}(NO_2)_2)_4\cdot 2DMF\cdot 4H_2O]$. Furthermore, the very low uptakes of CO_2 at 273 K and 298 K suggested that the structures of both MOFs had collapsed upon full activation. This was confirmed by the powder diffraction patterns of the crystals after gas sorption studies (Appendix 4, Figure A4.1a).

Similarly poor results were found from freeze drying before vacuum drying (Appendix, Table A4.2, entries 1–3). However, in $[Sr_4(bpdc\text{-}(NO_2)_2)_4\cdot 2DMF\cdot 4H_2O]$, the activation procedure using Method 6.4 resulted in a very large improvement in CO_2 uptake. The CO_2 sorption measurements on activated $[Sr_4(bpdc\text{-}(NO_2)_2)_4\cdot 2DMF\cdot 4H_2O]$ took unusually long and while volumetric uptakes of 21.5 cm^3g^{-1} at 273 K and 17.5 cm^3g^{-1} at 298 K were achieved, the isotherms showed large hysteresis (Figure 6.22a). The shapes of the isotherms and the hysteresis suggests a strong interaction of CO_2 with the surface.[37] A plot of the heat of adsorption versus uptake was calculated from data at 273 K and 298 K using Quantachrome ASiQwin software (interpolation method) as a first appreciation of the strength of the adsorbate-adsorbent interaction and the plot is shown in the appendix to this chapter (Appendix 4, Figure A4.6). The plot shows that the data is not handled well by the interpolation method at low uptakes and therefore may be giving a skewed picture of the adsorbate-adsorbent interaction. For what it is worth, the plot shows a rapidly decreasing heat of adsorption which could indicate a heterogeneous surface of this activated material, in which there are few, but energetically favoured, sites that saturated first with CO_2.[38, 39, 40] No other calculation methods were pursued as

it was felt that the experimental data were not reliable due to the poor crystallinity of the samples after gas sorption measurements (Appendix 4, Figure A4.1b). This was also speculated to have been the cause of the very long data collection time with the material surface being quite heterogeneous.

6.3.1.2 *Solvent exchange, activation procedures, and gas adsorption studies of $[Sr_4(bpdc\text{-}NH_2)_2)_4(H_2O)_3]$ and $[Sr(bpdc\text{-}NMe_2)(H_2O)]$*

The same methods of solvent exchange and analysis were applied to $[Sr_4(bpdc\text{-}NH_2)_2)_4(H_2O)_3]$ and $[Sr(bpdc\text{-}NMe_2)(H_2O)]$ and are noted in Table A4.2 in the appendix to this chapter. Solvent exchange methods using dry CH_2Cl_2 at room temperature or at reflux and subsequent vacuum drying were not effective at removing all DMF from $[Sr_4(bpdc\text{-}NH_2)_2)_4(H_2O)_3]$ or $[Sr(bpdc\text{-}NMe_2)(H_2O)]$ as ^1H NMR analysis revealed a ratio of 2 : 1 of $H_2bpdc\text{-}(NH_2)_2$ to DMF and a ratio of 1 : 0.7 of $H_2bpdc\text{-}NMe_2$ to DMF, respectively. For digestions of $[Sr_4(bpdc\text{-}NH_2)_2)_4(H_2O)_3]$, the spectra needed to be compared to acidified solutions of the free $H_2bpdc\text{-}(NH_2)_2$ ligand in *d*$_6$-DMSO to account for changes in chemical shift upon protonation by DCl. ^1H NMR spectra in *d*$_6$-DMSO of $H_2bpdc\text{-}(NH_2)_2$, $H_2bpdc\text{-}(NH_2)_2$ with DCl/D_2O and digested $[Sr_4(bpdc\text{-}NH_2)_2)_4(H_2O)_3]$ are shown in Appendix 4, Figure A4.6c.

CO_2 adsorption at 273 K on activated $[Sr_4(bpdc\text{-}(NH_2)_2)_4(H_2O)_3]$ (Table A4.2, entry 5; cyclohexane/freeze drying/dynamic vacuum) showed an uptake of 11.6 cm^3g^{-1} at 760 Torr. There appears to be a gate-opening phenomenon in the adsorption leg of the isotherm starting around 450 Torr and 4.5 cm^3g^{-1} with clear hysteretic behaviour (Figure 6.22b). The uptake was below that expected based on the channel sizes evident in the single crystal structure, and PXRD of samples after this activation method showed limited crystallinity (Appendix Figure A4.2b). Curiously, there is no evidence of a gate opening process and the hysteresis is less pronounced at 298 K. It may be that the framework needs to accommodate sufficient CO_2 to open the channels and this is not met at 298 K where only 3.7 cm^3g^{-1} is taken up at 760 Torr. There was no N_2 uptake at 298 K and this is in line with the smaller kinetic diameter of CO_2 (3.30 Å *vs* 3.64 Å) and the stronger interactions it has with surfaces because of its higher quadrupole moment. There was also no uptake of N_2 at 77 K.

Activation of [Sr(bpdc-NMe_2)(H_2O)] by Methods 6 and 7 (Appendix 4, Table A4.2, entry 6; benzene/freeze drying/dynamic vacuum and Table A4.2, entry 7; CH_2Cl_2/dynamic vacuum) gave highly porous samples, taking up 23.3 cm^3g^{-1} and 26.2 cm^3g^{-1} of CO_2 at 760 Torr and 273 K. PXRD measurements on these activated samples showed very good crystallinity (Appendix 4, Figure A4.2c). ^1H NMR analysis showed that approximately 0.75 DMF molecules remained in these materials per formula unit (Appendix 4, Figure A4.6d) and this was supported by elemental analysis. Considering the presence of DMF and the heavy mass of strontium, the results of the gas uptake are very good. Other activation methods (Appendix 4, Table A4.2, entry 4 and entry 8) were successful at completely removing DMF but resulted in lower CO_2 uptakes and poorer crystallinity. CO_2 isotherms recorded at 273 K and 298 K are shown in Figure 6.22c and the CO_2 uptake data for all complexes is summarised in Table 6.3.

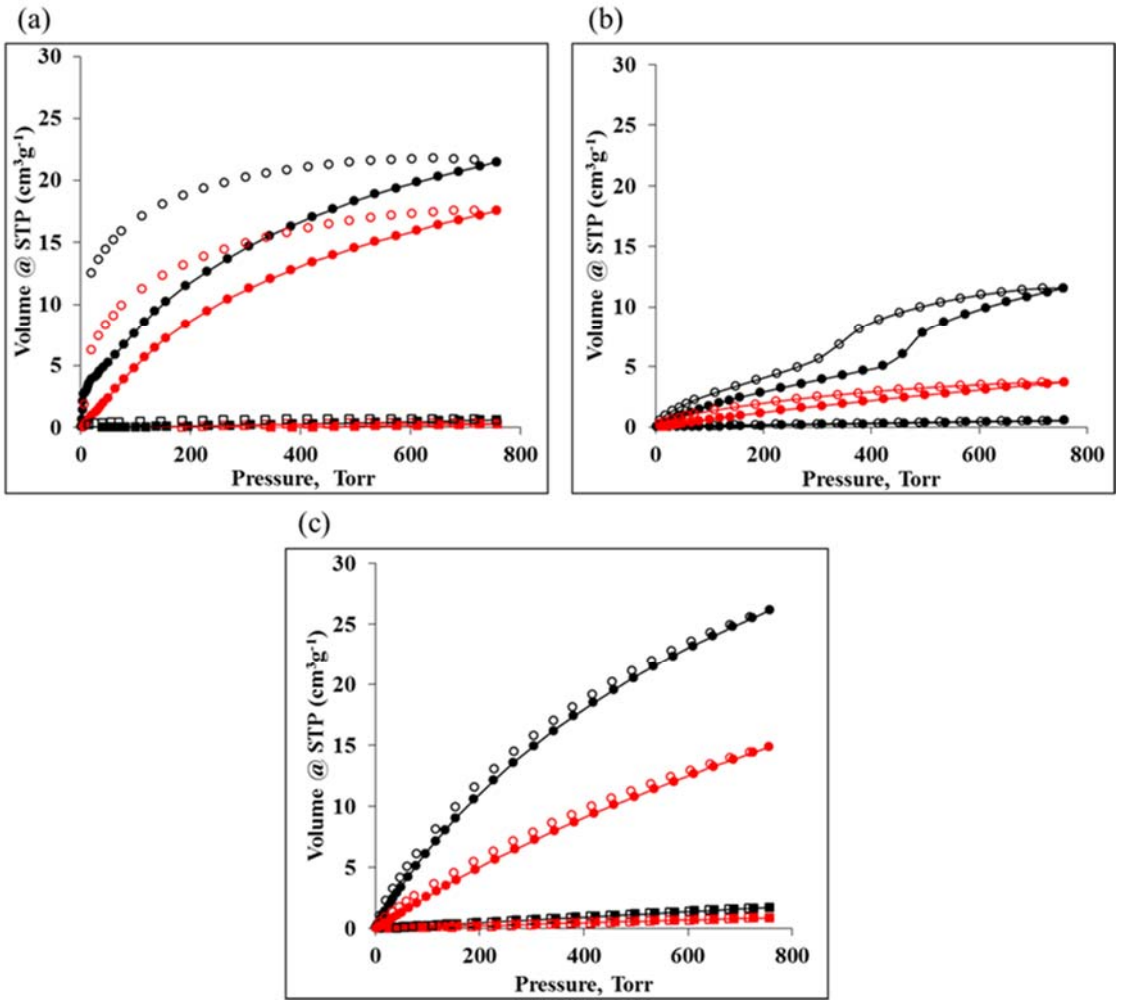

Figure 6.22 Adsorption-desorption isotherms of CO_2 and N_2 at 273 K (black) and 298 K (red) in (a) $[Sr_4(bpdc\text{-}(NO_2)_2)_4 \cdot 2DMF \cdot 4H_2O]$, (b) $[Sr_4(bpdc\text{-}NH_2)_2)_4(H_2O)_3]$ and (c) $[Sr(bpdc\text{-}NMe_2)(H_2O)]$. Closed and opened circles indicate adsorption and desorption of CO_2, respectively. Closed and opened squares indicate adsorption and desorption of N_2, respectively.

Table 6.3 The CO_2 adsorption data of $[Sr_4(bpdc\text{-}(NO_2)_2)_4 \cdot 2DMF \cdot 4H_2O]$, $[Sr_4(bpdc\text{-}NH_2)_2)_4(H_2O)_3]$ and $[Sr(bpdc\text{-}NMe_2)(H_2O)]$ at 273 K, 288 K and 298 K.

Structure	273 K	288 K	298 K
$[Sr_4(bpdc\text{-}(NO_2)_2)_4 \cdot 2DMF \cdot 4H_2O]$	21.5	19.7	17.5
$[Sr_4(bpdc\text{-}NH_2)_2)_4(H_2O)_3]$	11.6	6.4	3.7
$[Sr(bpdc\text{-}NMe_2)(H_2O)]$	26.2	18.3	14.8

A heat of adsorption plot was calculated for [Sr(bpdc-NMe_2)(H_2O)] by the interpolation method in the ASiQwin software and is shown in Figure 6.23. The plot reaches approximately -36 $kJmol^{-1}$ near zero loading of CO_2 and decreases gradually to around -25 $kJmol^{-1}$. This is only a moderate heat of adsorption compared to some alkyl amine functionalised MOFs but compares well with other aryl amine functionalised MOFs in the literature.[41, 42] For example, the heat of adsorption reported for IRMOF-3 is 19.2 $kJmol^{-1}$ as this material is functionally similar to [Sr(bpdc-NMe_2)(H_2O)].[43] One reason for the relatively modest performance is the internal hydrogen bond involving the amine nitrogen. The result of this being the amine lone pair is not available to interact with CO_2. It is also worth pointing out that this is an aryl amine and is far less basic than alkyl amines on which notably high heat of adsorption values have been found in some MOFs.[44]

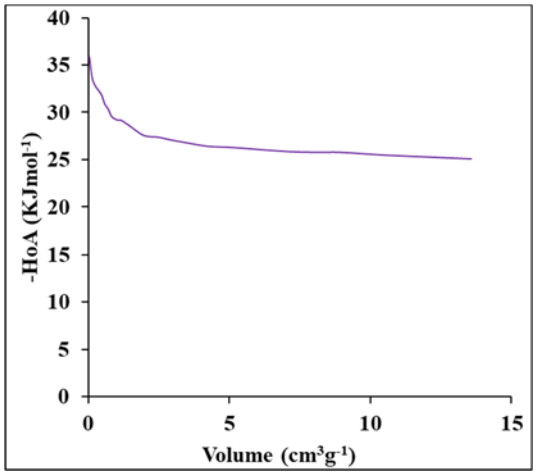

Figure 6.23 Isosteric heat of adsorption profiles for [Sr(bpdc-NMe_2)(H_2O)] calculated from data recorded at 273 K and 298 K.

CO_2 isotherms were measured at 196 K on [Sr_4(bpdc-NH_2)$_2$)$_4$(H_2O)$_3$] and [Sr(bpdc-NMe_2)(H_2O)] for further investigation into their porosity (Figure 6.34). The isotherms show Type I behaviour with uptakes of approximately 25 cm^3g^{-1} and 78 cm^3g^{-1} with corresponding surface areas of 90 m^2g^{-1} and 287 m^2g^{-1}, as calculated using (BET) theory, for [Sr_4(bpdc-NH_2)$_2$)$_4$(H_2O)$_3$] and [Sr(bpdc-NMe_2)(H_2O)], respectively. These uptakes are not able given these coordination networks show no uptake of N_2 at 77 K.

The result for $[Sr_4(bpdc\text{-}NH_2)_2)_4(H_2O)_3]$ reflects the poor crystallinity of the material, as previously noted. In contrast, the result of $[Sr(bpdc\text{-}NMe_2)(H_2O)]$ is very good. Geometric calculation of the surface area, as was used in chapter 5, was not done as the position of the DMF that remains in the structure is not known, and it was thought that this would be critical in the calculation providing useful information.

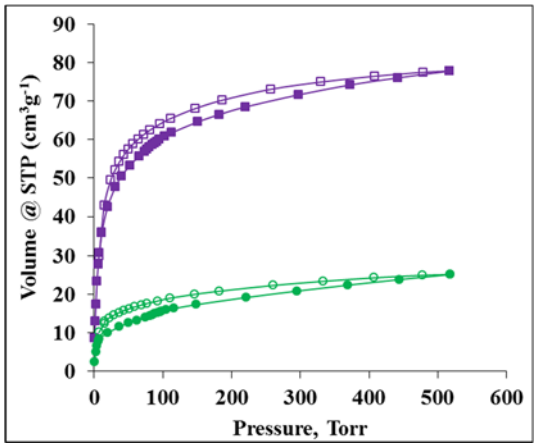

Figure 6.24 The CO_2 isotherms at 196 K for $[Sr_4(bpdc\text{-}NH_2)_2)_4(H_2O)_3]$ (green) and $[Sr(bpdc\text{-}NMe_2)(H_2O)]$ (purple). Filled and empty symbols indicate adsorption and desorption, respectively.

6.3.2 Photoluminescence studies

The luminescence properties of $[Sr_2(bpdc\text{-}NO_2)_2(H_2O)_2]$, $[Sr_4(bpdc\text{-}(NO_2)_2)_4 \cdot 2DMF \cdot 4H_2O]$ and $[Srbc(H_2O)]$ and their corresponding organic linkers were investigated in the solid state. Emission spectra, recorded on thin layers of powdered samples between 330–600 nm with the excitation wavelength of 310 nm, are shown in Figure 6.25.

$H_2bpdc\text{-}NO_2$ shows broad emission peaks centred at 351 nm and 460 nm and incorporation of the linker in $[Sr_2(bpdc\text{-}NO_2)_2(H_2O)_2]$ leads to small red shifts to 357 and 464 nm and a reduction in the luminescence. These are very small red shifts and can be explained by only small changes to the HOMO and LUMO energy levels from the neutral ligand to the coordinated organic linker. There are no noticeable changes in emission between $H_2bpdc\text{-}(NO_2)_2$ and its corresponding MOF. Both show two broad emission peaks located at 367 nm and 505 nm with no significant difference in intensity.

The emission curve of H_2bc shows peaks at 374 nm and 524 nm with greater intensity compared to $H_2bpdc\text{-}NO_2$ and $H_2bpdc\text{-}(NO_2)_2$. These photoluminescence properties are likely to arise from a $\pi \rightarrow \pi^*$ electronic transition in the planar H_2bc structure, and consequently, to the strong emission observed.[45, 46] It is even possible that this photoluminescence is via a ligand-to-ligand-charge transfer in the solid state. $[Srbc(H_2O)]$ has even more intense emission, with a new shoulder appearing at 486 nm in the spectrum. The π-π stacking arrangement between bc^{2-} linkers in the structure is postulated to give rise to a more efficient pathway for interligand excitation and emission. Taking this into account, the strong π-π interaction between the bc^{2-} linkers in the layers possibly reduces the transition energy of the $\pi \rightarrow \pi^*$, and consequently, increases the photoluminescence.[46]

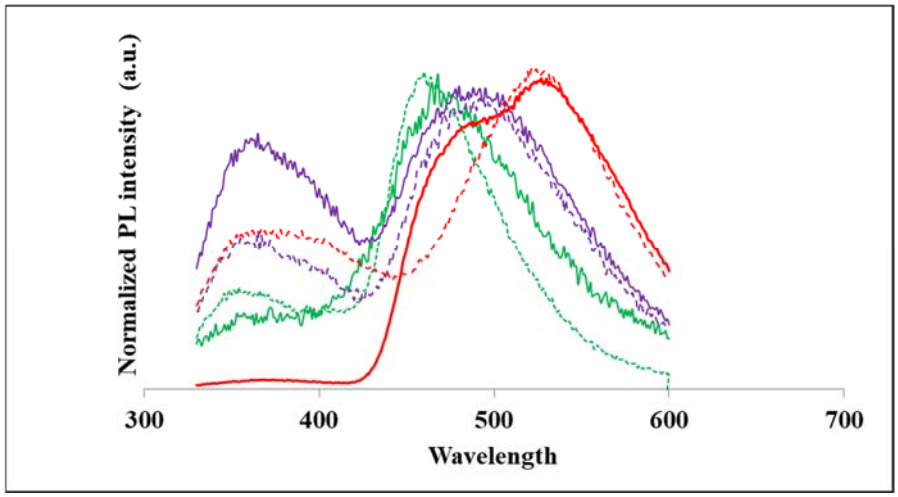

Figure 6.25 Photoluminescence spectra of $[Sr_2(bpdc\text{-}NO_2)_2(H_2O)_2]$ and $H_2bpdc\text{-}NO_2$ (green), $[Sr_4(bpdc\text{-}(NO_2)_2)_4 \cdot 2DMF \cdot 4H_2O]$ and $H_2bpdc\text{-}(NO_2)_2$ (purple) and $[Sr(bc)(H_2O)]$ and H_2bc (red). Solid lines represent the Sr coordination networks and dotted lines the organic linkers.

6.4 Conclusion

In this chapter, six strontium coordination networks were successfully synthesised under solvothermal conditions from $Sr(NO_3)_2$ and nitro- and amine-functionalised linear biphenyl dicarboxylic acids in DMF containing water. Water was found to play a crucial in promoting good crystallisation. The structures of the materials were determined by single crystal X-ray diffraction. Ligands carrying small substituents, such as H_2bpdc-NH_2, or no substituent, as in the case of H_2bc, were found to give non-porous structures whereas functionalisation with larger substituents resulted in more open structures. In the case of the 2-nitro and 2,2'-dinitro tag groups, this resulted in two isostructural porous frameworks with large pores. The coordination networks [Sr_4(bpdc-$(NH_2)_2)_4(H_2O)_3$] and [Sr(bpdc-NMe_2) (H_2O)] also showed very large pores. Unfortunately, not all of the porous networks were sufficiently well activated to allow exploration of their surface areas by gas adsorption techniques and this is an area for further work. Nevertheless, these large-pore frameworks are seemingly stable to a range of solvents and contain exchangeable monodentate aqua or DMF ligands, which make them attractive candidates as heterogeneous Lewis acid catalysts for various organic transformations.

6.5 Experimental

6.5.1 Ligand synthesis and characterisation

6.5.1.1 *Synthesis of 2-nitro-[1,1'-biphenyl]-4,4'-dicarboxylic acid, H_2bpdc-NO_2*

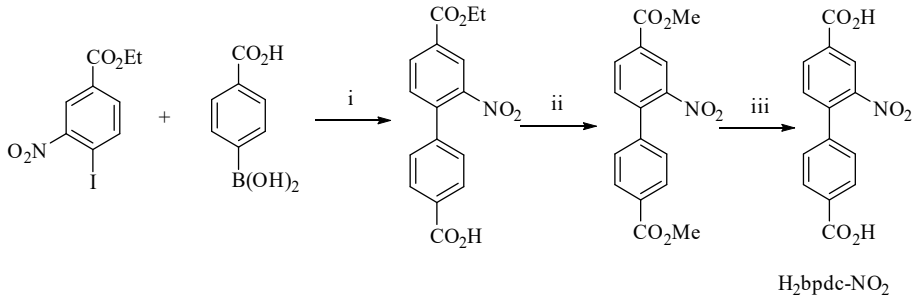

Scheme 6.1 (i) $PdCl_2dppf{\cdot}CH_2Cl_2$, degassed DMF, Na_2CO_3, N_2 (ii) MeOH, H_2SO_4, (iii) NaOH (aq), MeOH/THF.

Step (i) : Ethyl 4-iodo-3-nitrobenzoate (1.00 g, 3.05 mmol), 4-carboxyphenylboronic acid (0.620 g, 3.74 mmol) and $PdCl_2dppf{\cdot}CH_2Cl_2$ (0.063 g) were dissolved in degassed DMF (7 mL). The reaction mixture was purged with N_2 before adding degassed 2 M Na_2CO_3 (3 mL). The mixture was heated at 90 °C for 3 hours with stirring under an atmosphere of N_2. The solution was cooled to RT, and 1 M NaOH was added (3.35 mL, 3.35 mmol) and left to stir for 3 hours. The reaction mixture was diluted with water (7 mL) and filtered over Celite. The filtrate was acidified by adding concentrated HCl to precipitate EtHbpdc-NO_2. The solid was collected by filtration, washed with H_2O and air dried.

Step (ii) : EtHbpdc-NO_2 was converted to Me_2bpdc-NO_2 in MeOH (20 mL) in the presence of concentrated H_2SO_4 (3 drops) and the mixture was heated under reflux for 16 hours. After cooling to RT, the mixture was diluted with water (100 mL) and extracted with EtOAc (3 × 30 mL). The organic extracts were combined and washed with water (3 × 40 mL), brine (40 mL) and dried over Na_2SO_4. After filtering off the drying agent, the solvent was removed by rotary evaporation to yield a yellow solid (1.26 g).

Step (iii) : $Me_2bpdc\text{-}NO_2$ (0.44 g, 1.4 mmol) was dissolved in THF/MeOH (1 : 1, 8 mL) and 1 M NaOH (3.48 mL, 3.48 mmol) was added and the mixture stirred overnight at RT. The solvent mixture was removed by rotary evaporation and the residue was diluted by water (10 mL) followed by acidification by 1 M HCl. The resulting white solid was collected by filtration and air dried. Yield 0.377 g (77%). ^{1}H NMR δ_H (d_6-DMSO, 300 MHz) 7.51 (2 H, d, J = 8.18 Hz), 7.72 (1 H, d, J = 7.98 Hz), 8.01 (2 H, d, J = 8.14 Hz, 8.27 (1 H, d, J = 8.01 Hz), 8.46 (1 H, S). *m/z* (ESI) 286.1 ($[M - H]^-$; $[C_{14}H_{19}NO_6 - H]^-$ requires 286.2).

6.5.1.2 *Synthesis of 2,2'-dinitro-[1,1'-biphenyl]-4,4'-dicarboxylic acid, $H_2bpdc\text{-}(NO_2)_2$*

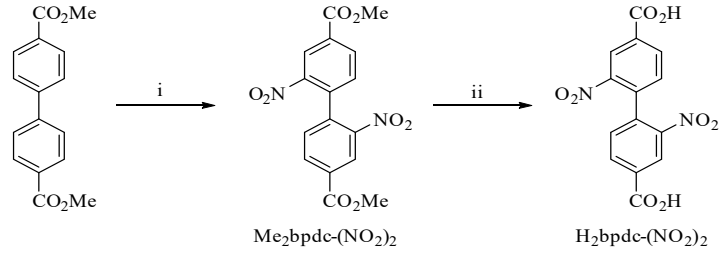

Figure 6.26 (i) HNO_3, H_2SO_4 (ii) NaOH (aq), MeOH/THF.

Step (i) : Me_2bpdc (2.00 g, 7.40 mmol) was added to concentrated H_2SO_4 (10 mL) and the mixture was stirred for one hour at RT. A solution of 70% HNO_3 (964 µl, 14.8 mmol) in concentrated H_2SO_4 (3 mL) was added portion-wise to the reaction mixture and left to stir at RT for 2 hours. The solution was then poured into an ice/water mixture (50 mL) under stirring. The resulting precipitate was collected by filtration and air dried. The white solid product was dissolved in MeOH (5 mL) at 70 °C, then cooled down to RT, filtered off and air dried. Yield: 2.29 g (86%). ^{1}H NMR ($CDCl_3$, 500 MHz) 7.39 (2 H, d, J = 7.92 Hz), 8.36 (2 H, dd, J = 0.95, 9.6 Hz), 8.90 (2 H, s).

Step (ii) : 1 M NaOH (3.5 mL, 3.5 mmol) was added to $Me_2bpdc\text{-}(NO_2)_2$ (0.50 g, 1.39 mmol) dissolved in MeOH/THF (3 : 3, 6 mL), and the mixture was stirred overnight at RT. The solvent mixture was removed by rotary evaporation and the solution was acidified with aqueous 1 M HCl to precipitate to the product. The yellow solid was separated via vacuum filtration, washed with water and air dried. Yield: 0.412 g (89%).

^{1}H NMR δ_H (d_6-DMSO, 500 MHz) 7.67 (2 H, d, J = 7.94 Hz), 8.34 (2 H, dd, J = 1.58, 1.52 Hz), 8.66 (2 H, d, J = 1.33 Hz). *m/z* (ESI) 331.1 ([M – H]$^-$; [$C_{14}H_8N_2O_8$ – H]$^-$ requires 331.2).

6.5.1.3 *Synthesis of benzo[c]cinnoline-3,8-dicarboxylic acid, H_2bc*

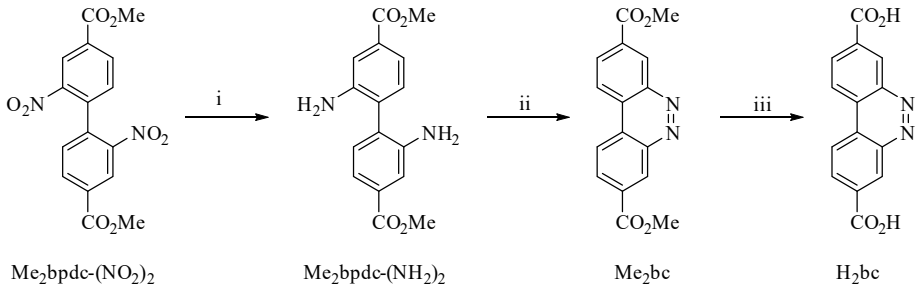

Me_2bpdc-$(NO_2)_2$ Me_2bpdc-$(NH_2)_2$ Me_2bc H_2bc

Scheme 6.2 (i) HNO_3, H_2SO_4, (ii) NH_4HCO_2, Pd/C, MeOH/THF, (iii) H_2O_2, acetic acid, (iv) NaOH (aq), MeOH/THF.

Step (i) : Me_2bpdc-$(NO_2)_2$ (2.2 g, 6.1 mmol) dissolved in THF (64 mL) was added to a mixture of 10% Pd/C catalyst (0.25 g) in chilled MeOH (33 mL). Ammonium formate (3.46 g, 55 mmol) was added portion-wise, and the reaction mixture was heated at 60 °C for 4 h. After cooling the reaction mixture to RT, the Pd/C was removed by filtration and MeOH and THF were removed by rotary evaporation to afford the crude product as Me_2bpdc-$(NH_2)_2$. Yield 1.54 g (84%). ^{1}H NMR δ_H ($CDCl_3$, 500 MHz) 3.48 (4 H, s, amine groups), 3.92 (6 H, s), 7.17 (2 H, dd, J = 7.78 Hz), 7.47 (2 H, s), 7.49 (2 H, d, J = 7.88 Hz).

Step (ii) : Me_2bpdc-$(NH_2)_2$ (1.07 g, 3.56 mmol) was dissolved in acetic acid (2.85 mL), and 30% aqueous H_2O_2 (2.85 mL) was added dropwise to the solution. The reaction mixture was left to stir at RT for 18 hours. The solution was then diluted with water (100 mL) and the crude product was collected by filtration and washed with a mixture of H_2O : EtOH (1 : 1, 4 mL). The crude product then was dissolved in $CHCl_3$ and ethyl acetate (80 : 20) and passed through a plug of silica gel. The solvent was removed by rotary evaporation to yield a yellow solid. Yield 0.77 g (73%) ^{1}H NMR δ_H ($CDCl_3$, 500 MHz) 4.08 (6 H, s), 8.57 (2 H, d, J = 8.45 Hz), 8.68 (2 H, d, J = 8.55 Hz), 9.47 (2 H, s).

Step (iii) : 1 M NaOH (2 mL, 2 mmol) was added to Me_2bc (0.20 g, 0.67 mmol) dissolved in THF/MeOH (1 : 1; 10 mL, 2 mL), and the mixture was heated under reflux for 6 hours. After removing the organic solvents by rotary evaporation, the solution was diluted with water and acidified with 1 M HCl. The product was then collected by filtration, washed with water and air dried. Yield 0.172 g (95%). ^{1}H NMR δ_H (d_6-DMSO, 500 MHz) 8.52 (2 H, d, J = 8.52 Hz), 9.06 (2 H, d, J = 8.58 Hz), 9.20 (2 H, d, J = 1.01 Hz). *m/z* (ESI) 267.1 ($[M - H]^-$; $[C_{14}H_8N_2O_4 - H]^-$ requires 267.2).

6.5.1.4 *Synthesis of 2,2'-diamino-[1,1'-biphenyl]-4,4'-dicarboxylic acid, $H_2bpdc\text{-}(NH_2)_2$*

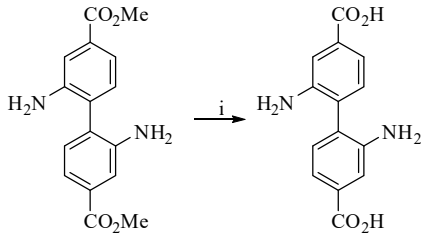

$Me_2bpdc\text{-}(NH_2)_2$ $H_2bpdc\text{-}(NH_2)_2$

Scheme 6.3 (i) NaOH (aq), MeOH/THF

Step (i) : $Me_2bpdc\text{-}(NH_2)_2$ was synthesised according to the procedure provided in section 7.3.1.3 (ii).

Step (ii) : 1 M NaOH (17.6 mL, 17.6 mmol) was added to $Me_2bpdc\text{-}(NH_2)_2$ (2.1 g, 7.0 mmol), dissolved in THF/MeOH (1 : 1, 20 mL) and stirred overnight at RT. The solvent mixture was removed by rotary evaporation and the residue was diluted with water followed by acidification by 1 M HCl. The resulting precipitate was collected by filtration and air dried. Yield 1.75 g (91%). ^{1}H NMR δ_H (d_6-DMSO, 500 MHz) 4.92 (4 H, s, amine groups), 7.05 (2 H, dd, J = 7.84 Hz), 7.22 (2 H, dd, J = 9.5 Hz), 7.43 (2 H, d, J = 1.62 Hz). *m/z* (ESI) 271.2 ($[M - H]^-$; $[C_{14}H_{12}N_2O_4 - H]^-$ requires 271.2).

6.5.2 Sr coordination network syntheses

6.5.2.1 *Synthesis of [$Sr_2(bpdc\text{-}NO_2)_2(H_2O)_2$]*

H_2bpdc-NO_2 (31.1 mg, 0.108 mmol) was combined with $Sr(NO_3)_2$ (25.1 mg, 0.119 mmol) in dry DMF (6 mL) and H_2O (0.3 mL) in a screw top vial and heated at 130 °C in an oven for 16 hours. After cooling down at RT, needle yellow crystals were washed with dry DMF several times. Yield 29.3 mg (55%). Found: C, 40.38; H, 3.13; N, 4.20. $C_{14}H_7NO_6Sr\cdot 3H_2O\cdot ½DMF$ requires C, 40.18; H, 3.59; N, 4.53.

6.5.2.2 *Synthesis of [$Sr_4(bpdc\text{-}(NO_2)_2)_4\cdot 2DMF\cdot 4H_2O$]*

H_2bpdc-$(NO_2)_2$ (35.8 mg, 0.108 mmol) and $Sr(NO_3)_2$ (25.14 mg, 0.1188 mmol) were dissolved in dry DMF (6 mL) and H_2O (0.3 mL) in a screw top vial. The vial was transferred to an oven at 130 °C for 16 hours. The resultant brown needle crystals were collected and washed with dry DMF. Yield 24.6 mg (52%). Found: C, 37.99; H, 2.98; N, 7.23. $C_{14}H_6N_2O_8Sr\cdot 2H_2O\cdot ½DMF$ requires C, 37.95; H, 2.78; N, 7.14.

6.5.2.3 *Synthesis of [Srbc$(H_2O)_2$]*

H_2bc (28.96 mg, 0.108 mmol) and $Sr(NO_3)_2$ (25.14 mg, 0.1188 mmol) were dissolved in a mixture of dry DMF (4.8 mL) and water (1.5 mL) in a screw top vial. The vial was transferred to oven at 100 °C for 16 hours. Needle brown crystals were collected by filtration and washed with dry DMF. Yield 14.7 mg (35%). Found: C, 43.22; H, 2.57; N, 7.14. $C_{14}H_6O_4N_2Sr\cdot 2H_2O$ requires C, 43.14; H, 2.59; N, 7.18.

6.5.2.4 *Synthesis of [$Sr_6(bpdc\text{-}NH_2)_6(DMF)_4\cdot(H_2O)$]*

H_2bpdc-NH_2 (27.7 mg, 0.108 mmol) and $Sr(NO_3)_2$ (25.14 mg, 0.1188 mmol) were dissolved in dry DMF (6 mL) and H_2O (0.3 mL) in a screw top vial. The reaction mixture was heated at 130 °C for 16 hours. The needle brown crystals were collected by filtration and washed with fresh dry DMF. Yield 31.7 mg (86%). C, 48.60%, H, 3.41%, N, 5.84%.$C_{64}H_{54}NO_{24}Sr_6\cdot H_2O\cdot 4DMF$ requires C, 48.68%, H, 3.58%, N, 5.92%.

6.5.2.5 *Synthesis of [$Sr_4(bpdc\text{-}(NH_2)_2)_4(H_2O)_3$]*

H_2bpdc-$(NH_2)_2$ (117.6 mg, 0.4320 mmol) and $Sr(NO_3)_2$ (100.56 mg, 0.47520 mmol) were dissolved in dry DMF (24 mL) and H_2O (1.2 mL) in a screw top vial. The reaction solution was transferred to oven and the temperature was kept at 100 °C for four days. Pale yellow needle crystals were harvested and washed with fresh dry DMF. Yield 86 mg (49%). Found: C, 46.56; H, 3.82; N, 8.40. $C_{56}H_{40}N_8O_{16}Sr_4 \cdot 3H_2O \cdot 2DMF$ requires C, 45.62; H, 3.71; N, 8.59.

6.5.2.6 *Synthesis of [Sr(bpdc-NMe_2)(H_2O)]*

H_2bpdc-NMe_2 (30.8 mg, 0.108 mmol) and $Sr(NO_3)_2$ (25.1 mg, 0.119 mmol) were combined in dry DMF (6 mL) and H_2O (0.3 mL) in a screw top vial. The vial was transferred to oven at 130 °C for 16 hours. The needle yellow crystals were washed and stored in fresh dry DMF. Yield 26.3 mg (52%). Found: C, 46.64, H, 4.32, N, 5.06. $C_{16}H_{13}NO_4Sr \cdot 2.5H_2O \cdot 0.75DMF$ requires C, 46.56, H, 4.98, N, 5.21.

6.6 References

1. Lee, D. W.; Jo, V.; Ok, K. M., $Sr_2[C_6H_3(CO_2)_3(NO_3)]\cdot DMF$: One-dimensional nano-channel in a new non-centrosymmetric strontium-organic framework with high thermal stability. *Crystal Growth and Design* **2011,** *11* (7), 2698-2701.
2. Saha, D.; Maity, T.; Koner, S., Metal-organic frameworks based on alkaline earth metals-hydrothermal synthesis, X-ray structures, gas adsorption, and heterogeneously catalyzed hydrogenation reactions. *European Journal of Inorganic Chemistry* **2015,** *2015* (6), 1053-1064.
3. Li, S.; Lu, L.; Zhu, M.; Yuan, C.; Feng, S., A bifunctional chemosensor for detection of volatile ketone or hexavalent chromate anions in aqueous solution based on a Cd(II) metal-organic framework. *Sensors and Actuators, B: Chemical* **2018,** *258*, 970-980.
4. Douvali, A.; Papaefstathiou, G. S.; Gullo, M. P.; Barbieri, A.; Tsipis, A. C.; Malliakas, C. D.; Kanatzidis, M. G.; Papadas, I.; Armatas, G. S.; Hatzidimitriou, A. G.; Lazarides, T.; Manos, M. J., Alkaline earth metal ion/dihydroxy-terephthalate MOFs: structural diversity and unusual luminescent properties. *Inorganic Chemistry* **2015,** *54* (12), 5813-5826.
5. Lo, S. H.; Liu, H. K.; Zhan, J. X.; Lin, W. C.; Kao, C. C.; Lin, C. H.; Zima, V., Assembly of a water-insoluble strontium metal-organic framework with luminescent properties. *Inorganic Chemistry Communications* **2011,** *14* (10), 1602-1605.
6. Guo, L.-R.; Tang, X.-L.; Ju, Z.-H.; Zhang, K.-M.; Jiang, H.-E.; Liu, W.-S., Lanthanide metal-organic frameworks constructed by asymmetric 2-nitrobiphenyl-4,4'-dicarboxylate ligand: syntheses, structures, luminescence and magnetic investigations. *CrystEngComm* **2013,** *15* (44), 9020-9031.
7. Williams, C. A.; Blake, A. J.; Wilson, C.; Hubberstey, P.; Schröder, M., Novel metal-organic frameworks derived from group (II) metal cations and aryldicarboxylate anionic ligands. *Crystal Growth and Design* **2008,** *8* (3), 911-922.
8. Zhang, X.; Huang, Y. Y.; Zhang, M. J.; Zhang, J.; Yao, Y. G., A series of Ca(II) or Ba(II) inorganic-organic hybrid frameworks based on aromatic polycarboxylate ligands with the inorganic M-O-M (M = Ca, Ba) connectivity from 1D to 3D. *Crystal Growth and Design* **2012,** *12* (6), 3231-3238.
9. Zhang, N.; Sun, Y. J.; Yang, H.; Zhang, J. Y.; Gao, E. Q., Solvothermal synthesis, structures, and magnetic properties of Ni(II) compounds directed by *N,N'*-bridging auxiliary ligands. *Inorganica Chimica Acta* **2015,** *428*, 37-43.
10. Zhou, X.; Chen, Q.; Li, L.; Yang, T.; Wang, J.; Huang, W., Three alkaline earth metal-organic frameworks based on fluorene-containing carboxylates: syntheses, structures and properties. *Science China Chemistry* **2017,** *60* (1), 115-121.
11. Chen, S.; Shuai, Q.; Gao, S., Two three-dimensional metal-organic frameworks constructed from alkaline earth metal cations (Sr and Ba) and 5-nitroisophthalic acid-synthesis, charaterization, and thermochemistry. *Zeitschrift für anorganische und allgemeine Chemie* **2008,** *634* (9), 1591-1596.
12. Wang, P.; Wu, G.; Wang, X., A novel binodal (4,9)-connected 3D calcium coordination polymer: Synthesis, characterization, thermal stability and luminescent properties. *Journal of Inorganic and Organometallic Polymers and Materials* **2012,** *22* (6), 1377-1383.

13. Wen, L. L.; Wang, F. M.; Leng, X. K.; Wang, M. M.; Meng, Q. J.; Zhu, H. Z., Synthesis and structures of two Ba(II) metal-organic frameworks based on pyridine-2,6-dicarboxylic acid N-Oxide. *Journal of Inorganic and Organometallic Polymers and Materials* **2010,** *20* (2), 313-319.
14. Wang, P.; Wu, G.; Yuan, J.; Wang, X., Syntheses, crystal structures, thermal stabilities and luminescent properties of two pillared layered alkaline-earth coordination polymers. *Journal of Inorganic and Organometallic Polymers and Materials* **2013,** *23* (5), 1153-1158.
15. Foo, M. L.; Horike, S.; Duan, J.; Chen, W.; Kitagawa, S., Tuning the dimensionality of inorganic connectivity in barium coordination polymers via biphenyl carboxylic acid ligands. *Crystal Growth and Design* **2013,** *13* (7), 2965-2972.
16. Furman, J. D.; Warner, A. Y.; Teat, S. J.; Mikhailovsky, A. A.; Cheetham, A. K., Tunable, ligand-based emission from inorganic-organic frameworks: A new approach to phosphors for solid state lighting and other applications. *Chemistry of Materials* **2010,** *22* (7), 2255-2260.
17. Yang, L.-M.; Vajeeston, P.; Ravindran, P.; Fjellvag, H.; Tilset, M., Revisiting isoreticular MOFs of alkaline earth metals: a comprehensive study on phase stability, electronic structure, chemical bonding, and optical properties of A-IRMOF-1 (A = Be, Mg, Ca, Sr, Ba). *Physical Chemistry Chemical Physics* **2011,** *13* (21), 10191-10203.
18. Du, S.; Ji, C.; Xin, X.; Zhuang, M.; Yu, X.; Lu, J.; Lu, Y.; Sun, D., Syntheses, structures and characteristics of four alkaline-earth metal-organic frameworks (MOFs) based on benzene-1,2,4,5-tetracarboxylic acid and its derivative ligand. *Journal of Molecular Structure* **2017,** *1130*, 565-572.
19. Singha, S.; Maity, S. K.; Biswas, S.; Saha, R.; Kumar, S., A magnesium-based bifunctional MOF: Studies on proton conductivity, gas and water adsorption. *Inorganica Chimica Acta* **2016,** *453*, 321-329.
20. Fard, Z. H.; Kalinovskyy, Y.; Spasyuk, D. M.; Blight, B. A.; Shimizu, G. K. H., Alkaline-earth phosphonate MOFs with reversible hydration-dependent fluorescence. *Chemical Communications* **2016,** *52* (87), 12865-12868.
21. Usman, M.; Mendiratta, S.; Batjargal, S.; Haider, G.; Hayashi, M.; Rao Gade, N.; Chen, J. W.; Chen, Y. F.; Lu, K. L., Semiconductor behavior of a three-dimensional strontium-based metal-organic framework. *ACS Applied Materials and Interfaces* **2015,** *7* (41), 22767-22774.
22. Chen, X.; Plonka, A. M.; Banerjee, D.; Parise, J. B., Synthesis, structures and photoluminescence properties of a series of alkaline earth metal-based coordination networks synthesized using thiophene-based linkers. *Crystal Growth and Design* **2013,** *13* (1), 326-332.
23. Chen, Q.; Guo, P.-C.; Zhao, S.-P.; Liu, J.-L.; Ren, X.-M., A rhombus channel metal-organic framework comprised of Sr^{2+} and thiophene-2,5-dicarboxylic acid exhibiting novel dielectric bistability. *CrystEngComm* **2013,** *15* (6), 1264-1270.
24. Cheetham, A. K.; Rao, C. N. R.; Feller, R. K., Structural diversity and chemical trends in hybrid inorganic-organic framework materials. *Chemical Communications* **2006,** (46), 4780-4795.
25. Dau, P. V.; Cohen, S. M., The influence of nitro groups on the topology and gas sorption property of extended Zn(II)-paddlewheel MOFs. *CrystEngComm* **2013,** *15* (45), 9304-9307.

26. Liu, L.; Konstas, K.; Hill, M. R.; Telfer, S. G., Programmed pore architectures in modular quaternary metal-organic frameworks. *Journal of the American Chemical Society* **2013,** *135* (47), 17731-17734.
27. Lun, D. J.; Waterhouse, G. I. N.; Telfer, S. G., A general thermolabile protecting group strategy for organocatalytic metal-organic frameworks. *Journal of the American Chemical Society* **2011,** *133* (15), 5806-5809.
28. Gotthardt, M. A.; Grosjean, S.; Brunner, T. S.; Kotzel, J.; Ganzler, A. M.; Wolf, S.; Brase, S.; Kleist, W., Synthesis and post-synthetic modification of amine-, alkyne-, azide- and nitro-functionalized metal-organic frameworks based on DUT-5. *Dalton Transactions* **2015,** *44* (38), 16802-16809.
29. Halis, S.; Reimer, N.; Klinkebiel, A.; Lüning, U.; Stock, N., Four new Al-based microporous metal-organic framework compounds with MIL-53-type structure containing functionalized extended linker molecules. *Microporous and Mesoporous Materials* **2015,** *216*, 13-19.
30. Qin, T.; Gong, J.; Ma, J.; Wang, X.; Wang, Y.; Xu, Y.; Shen, X.; Zhu, D., A 3D MOF showing unprecedented solvent-induced single-crystal-to-single-crystal transformation and excellent CO_2 adsorption selectivity at room temperature. *Chemical Communications* **2014,** *50* (100), 15886-15889.
31. Zhang, N.; Zhang, J.-Y.; Jia, Q.-X.; Deng, W.; Gao, E.-Q., Solvent-controlled structural diversity observed in three Cu(II) MOFs with a 2,2'-dinitro-biphenyl-4,4'-dicarboxylate ligand: synthesis, structures and magnetism. *RSC Advances* **2015,** *5* (87), 70772-70780.
32. Li, B.; Li, G.; Liu, D.; Peng, Y.; Zhou, X.; Hua, J.; Shi, Z.; Feng, S., Coordination polymers constructed by 1,3-bi(4-pyridyl)propane with four different conformations and 2,2'-dinitro-4,4'-biphenyldicarboxylate ligands: the effects of metal ions. *CrystEngComm* **2011,** *13* (5), 1291-1298.
33. Chen, L.-Z.; Pan, Q.-J.; Cao, X.-X.; Wang, F.-M., Crystal structure, magnetism, and dielectric properties based on the axially chiral ligand 2,2'-dinitro-4,4'-biphenyldicarboxylic acid. *CrystEngComm* **2016,** *18* (11), 1944-1952.
34. Chen, C. X.; Wei, Z.; Jiang, J. J.; Fan, Y. Z.; Zheng, S. P.; Cao, C. C.; Li, Y. H.; Fenske, D.; Su, C. Y., Precise modulation of the breathing behavior and pore surface in Zr-MOFS by reversible post-synthetic variable-spacer installation to fine-tune the expansion magnitude and sorption properties. *Angewandte Chemie - International Edition* **2016,** *55* (34), 9932-9936.
35. Chen, C.-X.; Wei, Z.-W.; Jiang, J.-J.; Zheng, S.-P.; Wang, H.-P.; Qiu, Q.-F.; Cao, C.-C.; Fenske, D.; Su, C.-Y., Dynamic spacer installation for multirole metal-organic frameworks: A new direction toward multifunctional MOFs achieving ultrahigh methane storage working capacity. *Journal of the American Chemical Society* **2017,** *139* (17), 6034-6037.
36. Bjørsvik, H. R.; González, R. R.; Liguori, L., Investigations of a novel process to the framework of benzo[c]cinnoline. *Journal of Organic Chemistry* **2004,** *69* (22), 7720-7727.
37. Kanoo, P.; Gurunatha, K. L.; Maji, T. K., Versatile functionalities in MOFs assembled from the same building units: interplay of structural flexibility, rigidity and regularity. *Journal of Materials Chemistry* **2010,** *20* (7), 1322-1331.

38. Karra, J. R.; Walton, K. S., Effect of open metal sites on adsorption of polar and nonpolar molecules in metal-organic framework Cu-BTC. *Langmuir* **2008,** *24* (16), 8620-8626.
39. Zhao, Y.; Liu, X.; Han, Y., Microporous carbonaceous adsorbents for CO_2 separation via selective adsorption. *RSC Advances* **2015,** *5* (38), 30310-30330.
40. Saha, D.; Fieback, T. M.; Tom, B., Characteristics of methane adsorption in micro-mesoporous carbons at low and ultra-high pressure. *Energy Technology* **2016,** *4* (11), 1392-1400.
41. Das, A.; Choucair, M.; Southon, P. D.; Mason, J. A.; Zhao, M.; Kepert, C. J.; Harris, A. T.; D'Alessandro, D. M., Application of the piperazine-grafted CuBTTri metal-organic framework in postcombustion carbon dioxide capture. *Microporous and Mesoporous Materials* **2013,** *174*, 74-80.
42. McDonald, T. M.; Lee, W. R.; Mason, J. A.; Wiers, B. M.; Hong, C. S.; Long, J. R., Capture of carbon dioxide from air and flue gas in the alkylamine-appended metal-organic framework mmen-Mg_2(dobpdc). *Journal of the American Chemical Society* **2012,** *134* (16), 7056-7065.
43. Farrusseng, D.; Daniel, C.; Gaudillère, C.; Ravon, U.; Schuurman, Y.; Mirodatos, C.; Dubbeldam, D.; Frost, H.; Snurr, R. Q., Heats of adsorption for seven gases in three metal-organic frameworks: systematic comparison of experiment and simulation. *Langmuir* **2009,** *25* (13), 7383-7388.
44. Liu, X.; Li, H.; Zhang, Y.; Xu, B.; Sigen, A.; Xia, H.; Mu, Y., Enhanced carbon dioxide uptake by metalloporphyrin-based microporous covalent triazine framework. *Polym. Chem.* **2013,** *4* (8), 2445-2448.
45. Yuan, Y.; Tian, M.; Yin, Q.; Feng, F., Synthesis, crystal structure and spectroscopic properties of a novel tricyclic cinnoline derivative. *Dyes and Pigments* **2017,** *141*, 363-365.
46. Wang, X. W.; Chen, J. Z.; Liu, J. H., Photoluminescent Zn(II) metal-organic frameworks built from tetrazole ligand: 2D four-connected regular honeycomb (4363)-net. *Crystal Growth and Design* **2007,** *7* (7), 1227-1229.

Chapter 7

Summary and Future Work

7 Summary and Future work

This work described in thesis is essentially divided into two sections. Chapter 3 and Chapter 4 focused on the rational design and crystal engineering of multi-metallolinker MOFs by co-polymerisation, while the work in Chapter 5 and Chapter 6 focused on synthesis and characterisation of Zn- and Sr-based materials using functionalised biphenyl dicarboxylate linkers.

In Chapter 3, a racemic salen ligand, *rac*-1,2-cyclohexanediamino-*N,N'*-bis(5-carboxysalicylidene) (H_4cdacs), metallated with Cu, VO, Fe and Mn *in situ* and by pre-metallated procedures, was used to grow metallosalen MOFs. In general, the pre-metallated route was superior and produced a vanadium coordination polymer {Zn[VO(cdacs)$_2$(DMF)$_2$]} and an iron MOF with salen units linked by bridging oxido bonds, {$Zn_7(OH)_4$[Fe(cdacs)-μ-oxido-Fe(cdacs)]$_3$} and featuring large 1D ca. 28 Å hexagonal channels. It would be valuable to investigate the activation and gas sorption properties of $Zn_7(OH)_4$[Fe(cdacs)-μ-oxido-Fe(cdacs)]$_3$ and investigate it as a catalyst for epoxidation, oxidation and sulfoxidation reactions. Firstly, synthesising this MOF in a pure form must be accomplished. The synthesis of a multi-metal vanadium-zinc network was not successful and perhaps indicates limitations for co-polymerisation of salen metallolinkers within one structure.

The work presented in Chapter 4 demonstrated the rational design and pore surface engineering of multi-metalloporphyrin frameworks. Ni(TCPP) and Mn(TCPP)Cl metallolinkers were chosen to see if co-polymerisation would induce PPF-5 type frameworks with accessible metal centres. Interestingly, with the new synthesis conditions developed in this work, both linkers formed PPF-5 type frameworks with bpy connecting the 2D porphyrin-paddlewheel layers. A multi-metal PPF-5(Mn/Ni) was formed using an equimolar feed ratio of Ni(TCPP) and Mn(TCPP)Cl linkers. SEM-EDS was used to confirm incorporation of both linkers within one structure and ICP-MS showed preferential incorporation of Ni(TCPP) over Mn(TCPP)Cl.

A series of MOFs with systematically varied composition of Ni(TCPP) and Co(TCPP) were made and investigated by PXRD, ICP-MS, SEM-EDS and ^{1}H NMR spectroscopy to identify the final structures of the materials. Through these examinations, a mixture

of PPF-5 and PPF-3 topologies was identified in each crystal. The formulation of the frameworks indicated the preferential incorporation of Co(TCPP) over Ni(TCPP).

The successful activation of PPF-type MOFs is still a big challenge. The lack of stability and permanent porosity arise from large open pores, and these MOFs are unable to survive guest (solvent) molecule removal. Structural collapse also occurred upon using PPF-type MOFs in catalytic reactions and might be concluded that PPF-type MOFs are not stable, and therefore, unsuitable as catalysts.

Due to the problems encountered with the PPF-5 structures, a multi-metal PCN-222(Mn/Ni) was successfully engineered, and used a catalyst for the epoxidation of styrene. Full conversion, selectivity and yield were observed when 5 mol% catalyst was used and lower catalyst loadings lead to formation of 2-phenylacetaldehyde as a by-product. The MOF showed very good crystallinity after the reaction, indicating very stable as catalyst. Due to the presence of nickel in the framework, this MOF would be worthy for future investigations as a tandem catalyst for two consecutive transformations.

In Chapter 5, four amine-functionalised linkers were successfully synthesised, characterised and used to prepare four porous Zn-MOFs. The MOFs were formulated based on SCXRD, elemental analysis and ^{1}H NMR spectroscopy as doubly interpenetrated $Zn_4O(bpdc\text{-}NH_2)_3$, $Zn_4O(bpdc\text{-}NH_2)_{0.58}(bpdc\text{-}NHallyl)_{2.42}\cdot 5H_2O$, $Zn_4O(bpdc\text{-}NHallyl)_{0.54}(bpdc\text{-}N(allyl)_2)_{2.46}$ and $Zn_4O(bpdc\text{-}NMe_2)_3\cdot 3H_2O$. The multivariate nature of these MOFs was a result of a C-N bond cleavage reaction during synthesis. This type of reaction seems to have some generality for secondary and tertiary amines[1] and is something that now needs to be considered in designing and synthesising coordination networks with ligands containing these groups. The apparent surface areas of the MOFs showed a correlation with the size of the pendant tag group; IRMOF-NH_2 with the smallest pendant group showed the highest surface area and IRMOF-$N(allyl)_2$ with the largest tag group showed the lowest surface area. The heat of adsorption values showed a correlation with basicity; IRMOF-NMe_2 and IRMOF-$N(allyl)_2$ with the highest basicity exhibited the highest heat of adsorption values in the series.

In Chapter 6, six nitro- and amine-functionalised ligands were synthesised and used for the solvothermal preparation of Sr-based materials. Due to the high electron affinity of Sr atom to oxygen ligands, especially for water molecules, the reactions were carried out in the presence of H_2O as a co-solvent. The structures of the resultant materials were studied based on the number of substituents and their size and shape, binding modes and Sr coordination environments. It was found that the number and the size of the substituent tag groups played a crucial role to form open structures. Nitro, dinitro, diamino and dimethylamino tag groups resulted in porous frameworks while amino and benzo[*c*]cinnoline resulted in non-porous frameworks. Analysis of the binding modes showed the complementary modes **a** and **b** are the most common. The synthesis and study of more Sr dicarboxylate networks would allow for exploration of more topologies, binding modes and coordination environments of Sr centres in these materials, and would likely be a fruitful area for future work.

The activation of the porous networks was quite challenging, and therefore, the surface properties of the open materials were not studied deeply. It would be worthy to further investigate the activation of these materials look at their gas sorption properties. Another interesting feature of these materials was the exchangeable nature of coordinated water or DMF on the strontium metal centres. This is a feature that makes these MOFs attractive to investigate as heterogeneous Lewis acid catalysts for organic transformations, such as Mannich, Michael, Aldol and 1,4-addition reactions.

In summary, this thesis covered the crystal engineering, synthesis and structural determination of multivariate coordination networks of salen and porphyrin metallolinkers and an isoreticular series of zinc MOFs. A number of factors were identified that are unique to the crystal engineering of these systems. This thesis also provided an account of initial explorations into the potentially rich area of strontium biphenyl dicarboxylate network structures.

7.1 References

1. Hahm, H.; Ha, H.; Kim, S.; Jung, B.; Park, M. H.; Kim, Y.; Heo, J.; Kim, M., Synthesis of secondary and tertiary amine-containing MOFs: C-N bond cleavage during MOF synthesis. *CrystEngComm* **2015,** *17* (30), 5644-5650.

Appendices

Appendix 1

C = Crystal, P = Precipitation, X= No reaction occurred, G = Gel, D = Decomposition

Table A1.1 A summary of the *in situ* reactions performed in different solvent systems at 65 °C.

		Temperature	**Solvent system and product type**											
		65 °C		**DMF**			**DMA**			**NMP**			**DEF**	
Entry	**Metal acetate salt**	**Metal acetate : $Zn(NO_3)_2 \cdot 6H_2O$ ratio**	DMF	DMF/EtOH	DMF/MeOH	DMF/H_2O	DMA	DMA/EtOH	NMP	NMP/EtOH	NMP/MeOH	NMP/H_2O	DEF	DEF/ EtOH
1	Cu	1 : 1	C	P	P	P	P	P	P	P	X	P	P	P
2	Cu	1 : 2	P	P	P	P	P	P	P	P	X	P	P	P
3	Cu	1 : 3	P	P	P	P	P	P	P	P	X	P	P	P
4	Ni	1 : 1	C	P	P	P	P	P	P	P	X	P	P	P
5	Ni	1 : 2	P	P	P	P	P	P	P	P	X	P	P	P
6	Ni	1 : 3	P	P	P	P	P	P	P	P	X	P	P	P
7	Zn	1 : 1	X	X	G	P	G	G	G	G	X	X	P	P
8	Zn	1 : 2	X	X	G	P	G	G	G	G	X	X	P	P
9	Zn	1 : 3	X	X	G	P	G	G	G	G	X	X	P	P

Table A1.2 A summary of the *in situ* reactions performed in different solvent systems at 80 °C.

Temperature **80 °C**			**Solvent system and product type**									
			DMF				**DMA**			**NMP**		
Entry	**Metal acetate salt**	**Metal acetate : $Zn(NO_3)_2 \cdot 6H_2O$ ratio**	DMF	DMF/EtOH	DMF/MeOH	DMF/H_2O	DMA	DMA/EtOH	NMP	NMP/EtOH	NMP/MeOH	NMP/H_2O
1	Cu	1 : 1	C	P	C	D	C	X	X	X	C	P
2	Cu	1 : 2	C	P	C	D	X	X	X	X	C	P
3	Cu	1 : 3	C	P	P	D	X	X	X	X	C	P
4	Ni	1 : 1	P	P	P	P	P	P	X	P	X	P
5	Ni	1 : 2	P	P	P	P	P	P	X	P	X	P
6	Ni	1 : 3	P	P	C	P	P	P	P	P	X	P
7	Zn	1 : 1	G	G	X	P	X	X	G	G	X	X
8	Zn	1 : 2	G	G	X	P	X	X	G	G	X	X
9	Zn	1 : 3	G	G	X	P	G	G	G	G	X	X

Table A1.3 A summary of the *in situ* reactions performed in different solvent systems at 100 °C.

Temperature			**Solvent system and product type**									
100 °C												
			DMF				**DMA**			**NMP**		
Entry	**Metal acetate salt**	**Metal acetate : $Zn(NO_3)_2 \cdot 6H_2O$ ratio**	DMF	DMF/EtOH	DMF/MeOH	DMF/H_2O	DMA	DMA/EtOH	NMP	NMP/EtOH	NMP/MeOH	NMP/H_2O
1	Cu	1 : 1	X	C	C	P	D	C	D	C	X	P
2	Cu	1 : 2	D	D	P	P	D	C	D	X	X	P
3	Cu	1 : 3	D	D	C	P	D	D	D	X	X	P
4	Ni	1 : 1	P	P	P	P	D	D	D	D	P	P
5	Ni	1 : 2	P	P	P	P	D	D	D	D	P	P
6	Ni	1 : 3	P	P	P	P	D	D	D	D	D	P
7	Zn	1 : 1	X	X	G	P	D	D	D	D	X	P
8	Zn	1 : 2	D	X	G	P	D	D	D	D	X	P
9	Zn	1 : 3	D	X	G	P	D	D	D	D	X	P

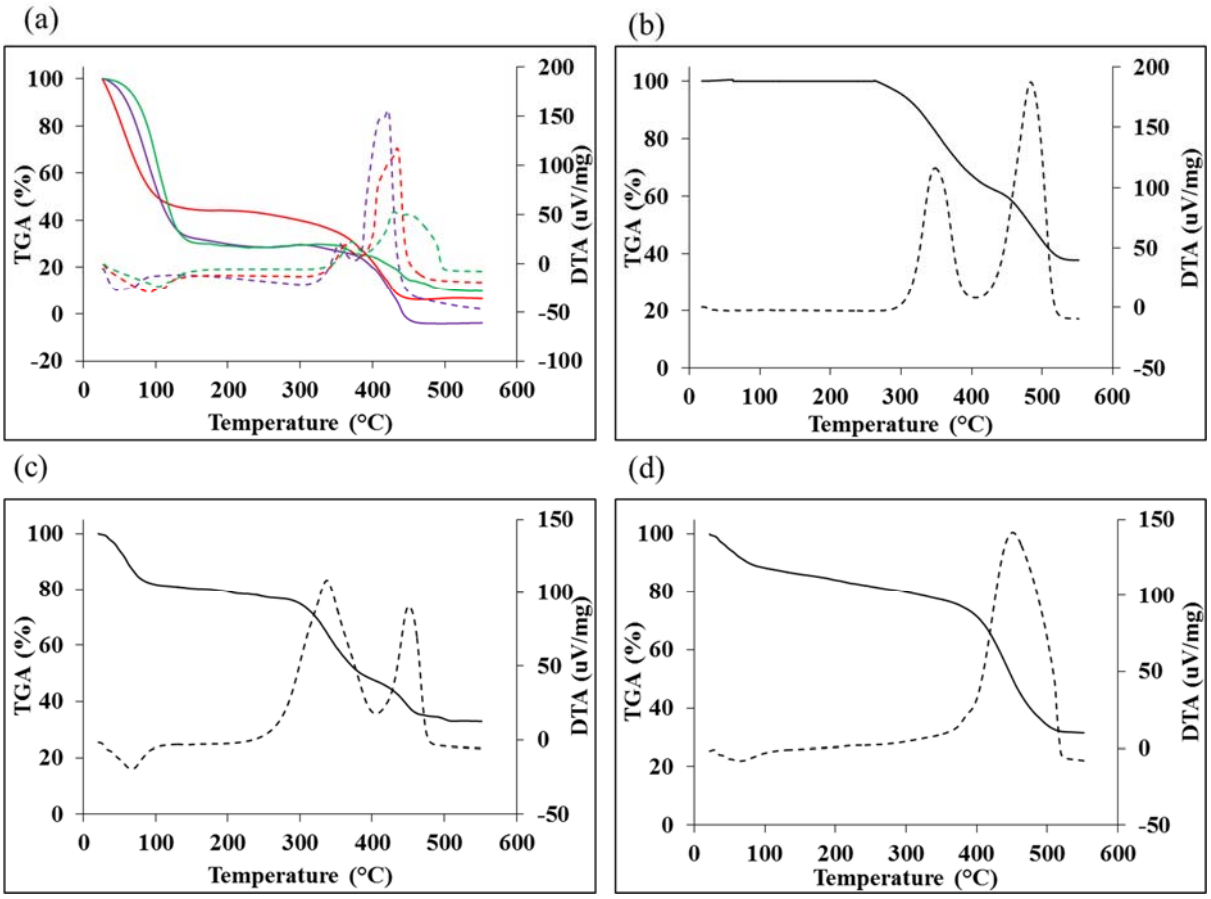

Figure A1.1 TGA-DTA traces for as-synthesised (a) cdacs-CP-1 (red), cdacs-CP-2 (purple) and cdacs-CP-3 (green) (b) $Zn[VO(cdacs)_2(DMF)_2]$, (c) $Zn_7(OH)_4(Fe(cdacs)\text{-}\mu\text{-oxido-}Fe(cdacs)]_3$ and (d) $Zn_4O[Mn(cdacs)Cl]_2 \cdot 6DMF \cdot 5H_2O$. Solid lines represent the TGA trace; the dotted lines represent the DTA trace.

Appendix 2

Table A2.1 The PPF structures reported by Choe and co-workers.

Structure	Linker	Metal node	Topology	Pillar	Stacking pattern
PPF-1	Zn(TCPP)	Zn	sql	N/A	Layer
PPF-1	Co(TCPP)	Co	sql	N/A	Layer
PPF-3	Co(TCPP)	Co	pcu-b	bpy	AB
PPF-3	Mn(TCPP)	Zn	pcu-b	bpy	AB
PPF-3	Mn(TCPP)	Co	pcu-b	bpy	AB
PPF-3	Fe(TCPP)	Zn	pcu-b	bpy	AB
PPF-3	Fe(TCPP)	Co	pcu-b	bpy	AB
PPF-4	Zn(TCPP)	Zn	fsx	bpy	ABBA
PPF-5	Pd(TCPP)	Co	fsc	bpy	AA
PPF-5	Pt(TCPP)	Co	fsc	bpy	AA
PPF-5	Ni(TCPP)	Zn	fsc	bpy	AA
PPF-5	VO(TCPP)	Zn	fsc	bpy	AA
PPF-11	Zn(TCPP)	Zn	fsc	Dmbpy	AA
PPF-11	Co(TCPP)	Co	fsc	Dmbpy	AA
PPF-11	Mn(TCPP)	Zn	fsc	Dmbpy	AA
PPF-11	Fe(TCPP)	Zn	fsc	Dmbpy	AA
PPF-18	Zn(TCPP)	Zn	Bilayer	DPNI	AB bilayer
PPF-19	Zn(TCPP)	Zn	fsc	DPNI	AA interpenetration
PPF-20	Zn(TCPP)	Zn	fsx	DPNI	ABBA
PPF-21	Zn(TCPP)	Zn	Bilayer	DPT	AB bilayer
PPF-22	Zn(TCPP)	Zn	fsx	DPT	ABBA
PPF-27	Zn(TCPP)	Zn	Bilayer	DPNI	AB bilayer

*NP stands for No Pillar

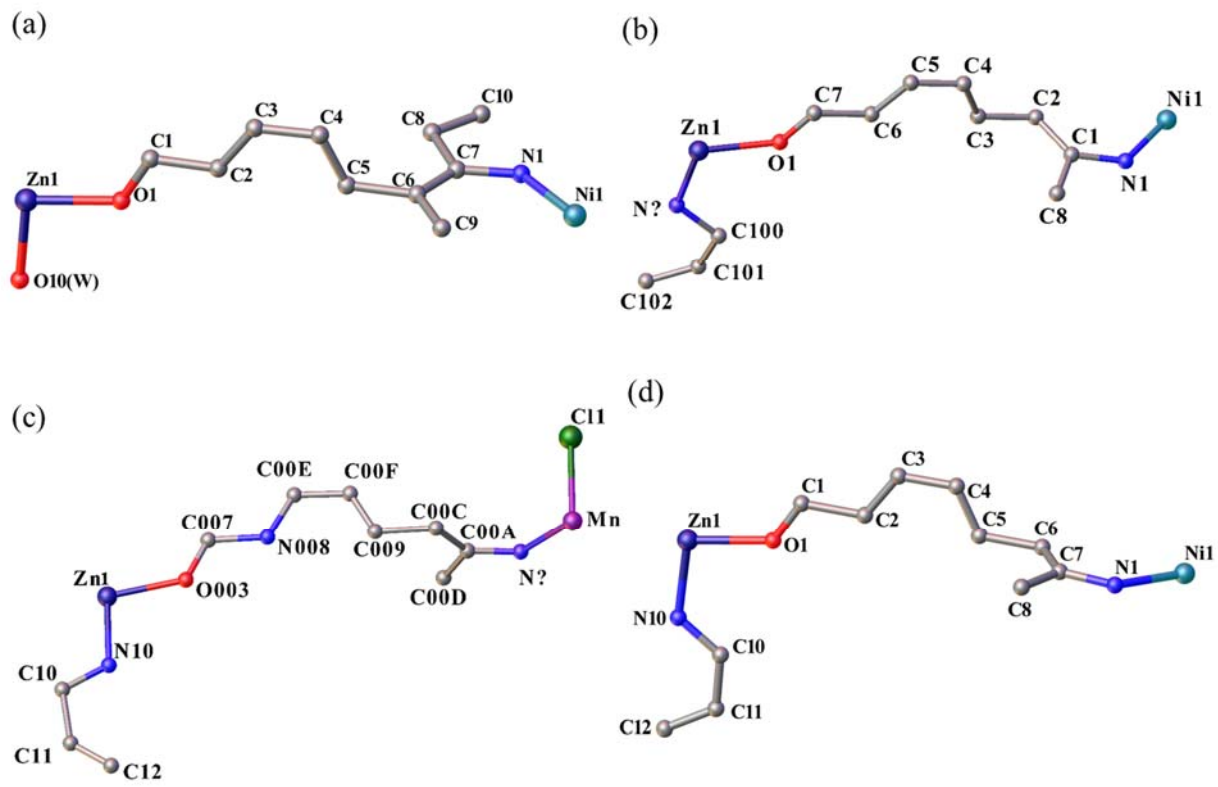

Figure A2.1 Contents of the asymmetric units of (a) PPF-1(Ni), (b) PPF-5(Ni), (c) PPF-5(MnCl) and (d) PPF-5(Mn/Ni).

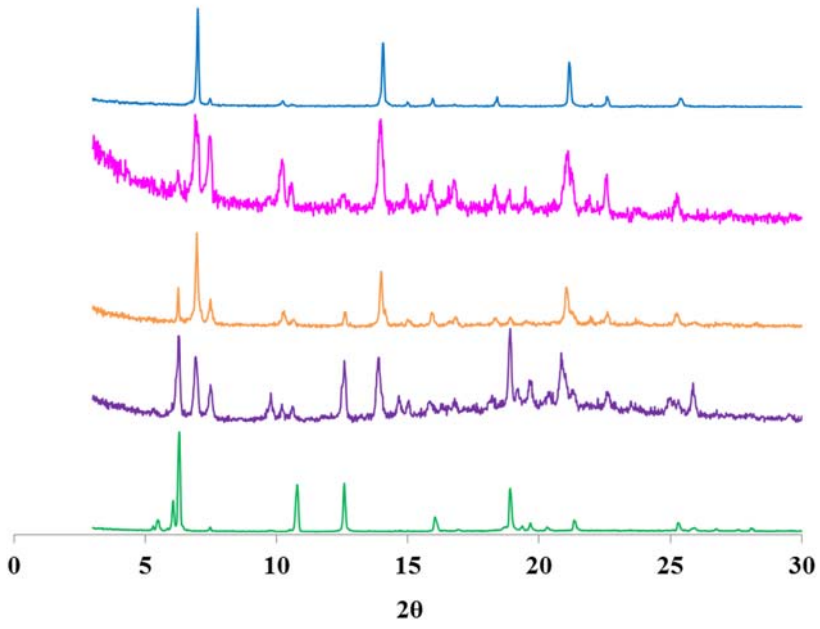

Figure A2.2 Experimental PXRD patterns recorded by Method 1 for PPF-5(Ni) (green), PPF(0.75Ni/0.25Co) (purple), PPF(0.50Ni/0.50Co) (orange), PPF(0.25Ni/0.75Co) (magenta) and PPF-3(Co) (blue).

Table A2.2 Crystallographic data of PPF-5(Ni) and PPF-5(Mn/Ni).

Identification code	PPF-1(Ni)	PPF-5(Ni)	PPF-5(Mn)	PPF-5(MnNi)
Empirical formula	$C_{48}H_{28}N_4NiO_{10}Zn_2$	$C_{58}H_{32}N_6NiO_8Zn_2$	$C_{58}H_{32}ClMnN_6O_8Zn_2$	$C_{58}H_{32}Cl_{0.5}Mn_{0.5}N_6Ni_{0.5}O_8Zn_2$
Formula weight	1010.19	1130.34	1162.02	1146.18
Temperature/K	292	292.15	292.15	293
Crystal system	tetragonal	tetragonal	tetragonal	tetragonal
Space group	I4/mmm	P4/mmm	P4/mmm	P4/mmm
a/Å	16.624(17)	16.6590(8)	16.6875(2)	16.6751(4)
b/Å	16.624(17)	16.6590(8)	16.6875(2)	16.6751(4)
c/Å	19.284(16)	14.0609(10)	14.0791(10)	14.0727(10)
α/°	90	90	90	90
β/°	90	90	90	90
γ/°	90	90	90	90
Volume/Å^3	5329(12)	3902.2(5)	3920.6(3)	3913.0(3)
Z	2	1	1	1
ρ_{calc}g/cm^3	0.63	0.481	0.492	0.486
μ/mm^{-1}	0.953	0.667	1.33	0.999
F(000)	1024	574	588	581
Crystal size/mm^3	0.15 × 0.15 × 0.1	0.3 × 0.25 × 0.2	0.25 × 0.25 × 0.15	0.4 × 0.4 × 0.2

Radiation	CuKα (λ = 1.54178)	CuKα (λ = 1.54178)	CuKα (λ = 1.54178)	CuKα (λ = 1.54178)
2Θ range for data collection/°	14.066 to 117.814	13.45 to 144.11	13.428 to 144.114	13.436 to 144.136
Index ranges	-18 ≤ h ≤ 18, -12 ≤ k ≤ 18, -21 ≤ l ≤ 17	-19 ≤ h ≤ 12, -20 ≤ k ≤ 20, -17 ≤ l ≤ 17	-19 ≤ h ≤ 18, -20 ≤ k ≤ 17, -10 ≤ l ≤ 16	-19 ≤ h ≤ 20, -19 ≤ k ≤ 19, -17 ≤ l ≤ 11
Reflections collected	9247	26227	21326	21261
Independent reflections	1115 [R_{int} = 0.1174, R_{sigma} = 0.0960]	2217 [R_{int} = 0.0553, R_{sigma} = 0.0403]	2221 [R_{int} = 0.0288, R_{sigma} = 0.0165]	2240 [R_{int} = 0.0282, R_{sigma} = 0.0165]
Data/restraints/parameters	1115/0/59	2217/0/74	2221/0/77	2240/0/77
Goodness-of-fit on F^2	1.217	1.448	1.668	1.501
Final R indexes [I>=2σ (I)]	R_1 = 0.1216, wR_2 = 0.3241	R_1 = 0.0974, wR_2 = 0.3090	R_1 = 0.1064, wR_2 = 0.3237	R_1 = 0.0858, wR_2 = 0.2945
Final R indexes [all data]	R_1 = 0.1884, wR_2 = 0.3850	R_1 = 0.1149, wR_2 = 0.3416	R_1 = 0.1128, wR_2 = 0.3540	R_1 = 0.0935, wR_2 = 0.3247
Largest diff. peak/hole / e $Å^{-3}$	0.80/-0.39	0.61/-0.80	2.52/-1.71	0.65/-0.99

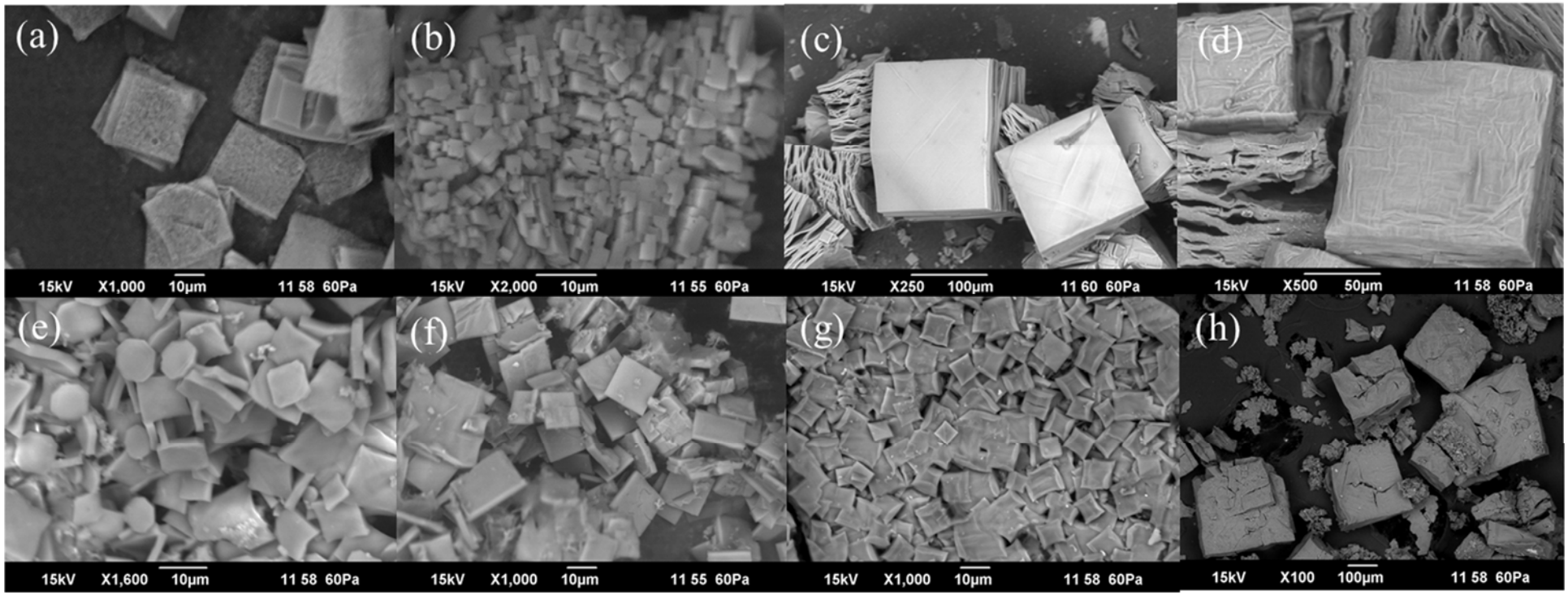

Figure A2.3 SEM images of (a) PPF-1(Ni), (b) PPF-1(MnCl), (c) PPF-5(Ni), (d) PPF-5(Mn/Ni), (e) PPF-3(Co), (f) PPF(0.75Ni/0.25Co), (g) PPF(0.50Co/0.50Ni) and (h) PPF(0.25Ni/0.75Co).

.

A2.1 Gas sorption studies on PPF-5(Ni)

The N_2 adsorption-desorption measurements at 77 K were carried out on PPF-5(Ni), activated by four methods. In the first activation procedure, the higher boiling point DMF was exchanged to dry CH_2Cl_2, over a period of 3 days. The crystals were transferred to the instrument station and held under dynamic vacuum at 30 °C for 60 minutes (Table A2.3, entry 1, Method 4.1). In the second activation method, the same solvent exchange procedure as Method 4.1 was performed on PPF-5(Ni) crystals. Then, the crystals were transferred to the critical point dryer before vacuuming at 30 °C for 120 minutes (Table A2.3, entry 2, Method 4.2). The third method involved soaking PPF-5(Ni) crystals in portions of dry CH_2Cl_2 over a period of 3 days followed by exchanging to dry benzene over 3 days. The crystals were then exchanged with liquid CO_2 in the critical point dryer. The crystals were quickly placed in a sealed tube, taken to the degas station and kept under vacuum at 30 °C for 120 minutes (Table A2.3, entry 3, Method 4.3). The final attempt involved the same solvent exchange as Method 4.3. Then, the MOF samples in benzene were freeze dried followed by heating under vacuum at 120 °C for 300 minutes (Table A2.3, entry 4, Method 4.4). The experimental sorption measurements yielded no gas uptake for Methods 4.1–4.3. The highest uptake was obtained after activation of the crystals by Method 4.4 with a surface area of 60 m^2g^{-1}. The gas sorption isotherm is shown in FigureA2.4. These results suggested crystal collapse occurred during the activation of the crystals. Choe and co-workers studied gas sorption measurements on a 2D PPF-1 material, which was among 27 materials reported. Their failure was because they were unable to survive the guest molecules removal, and consequently, structural collapses of these materials occurred, as reported in the related thesis published for these materials.

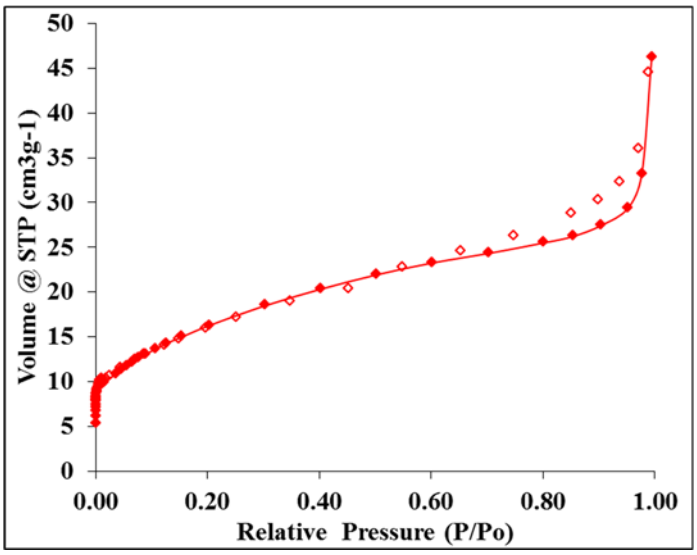

Figure A2.4 N_2 sorption measurement at 77 K for PPF-5(Ni), activated by method 4.4

Table A2.3 Solvent exchange and activation procedures on PPF-5(Ni) and N_2 adsorption result at 77 K

Entry	Method	Solvent exchange	Activation procedure	Heating protocol under dynamic vacuum	Surface area from N_2 at 77 K (m^2g^{-1})
1	4.1	DMF → CH_2Cl_2	Vacuum drying	30 °C, 2 hours	failed
2	4.2	DMF → CH_2Cl_2	$ScCO_2$	30 °C, 2 hours	failed
3	4.3	DMF → CH_2Cl_2 → benzene	$ScCO_2$	30 °C, 2 hours	failed
4	4.4	DMF → CH_2Cl_2 → benzene	Freeze drying	120 °C, 5 hours	60

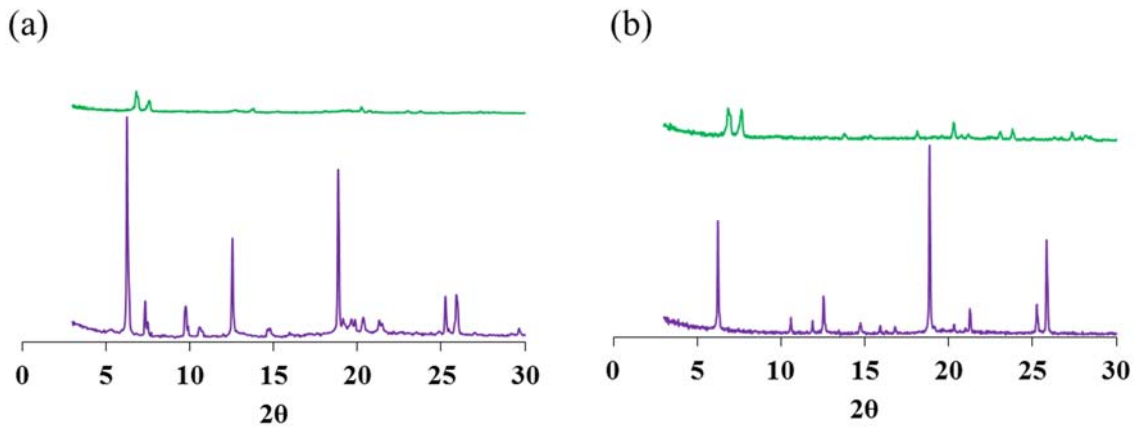

Figure A2.5 PXRD patterns for (a) PPF-5 (MnCl) and (b) PPF-5(Mn); after catalysis reaction (green) in addition to 'as-synthesised', recorded by Method 1 (purple) are shown for comparative purposes.

.

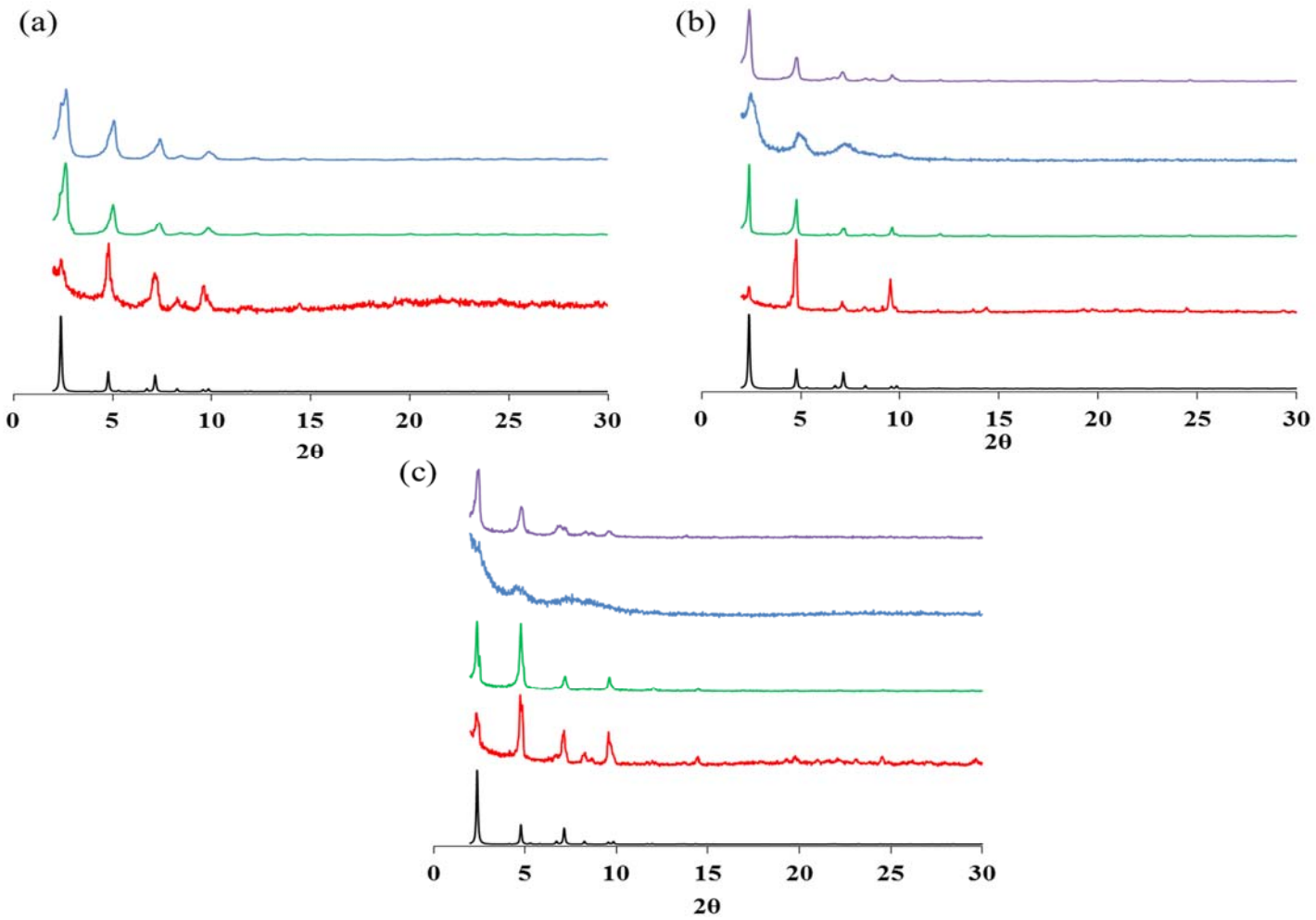

Figure A2.6 PXRD patterns for (a) PCN-222(Ni), (b) PCN-222(MnCl) and (c) PCN-222(Mn/Ni); After gas sorption measurement (blue) and after catalysis reaction (purple). In addition, as-synthesised' (red), after acid treatment (green) as well as simulated PCN-222 (black) are shown for comparative purposes.

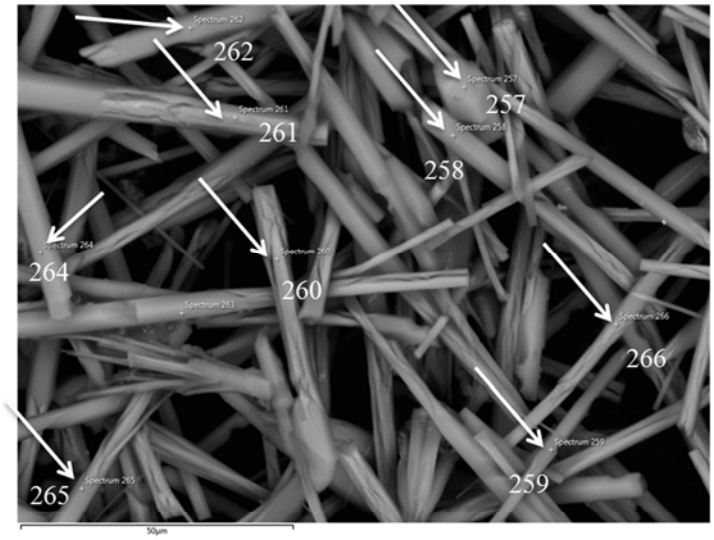

Spectrum Label	Spectrum 257 (wt%)	Spectrum 258 (wt%)	Spectrum 259 (wt%)	Spectrum 260 (wt%)	Spectrum 261 (wt%)	Spectrum 262 (wt%)	Spectrum 264 (wt%)	Spectrum 265 (wt%)	Spectrum 266 (wt%)
Mn	1.51	1.58	1.58	0.97	1.22	0.97	1.28	1.02	1.37
Ni	1.47	1.76	1.71	1.13	1.42	0.99	1.49	1.24	1.25
Zr	16.54	15.54	15.60	13.01	14.27	12.49	13.14	11.31	13.12

Figure A2.7 SEM images and EDS data of nine different spots in the sample of PCN-222(Mn/Ni).

A2.2 Thermogravimetric analysis

The thermal stability of "acid treated" PCN-222(Mn/Ni) was investigated by TGA-DTA under an atmosphere of N_2 gas. The crystals were filtered off, washed with dry acetone and transferred quickly to the instrument. The TGA-DTA traces are presented in Figure 4.25.

The TGA of PCN-222(Mn/Ni) showed weight losses between ambient temperature and 120 °C corresponding to the loss of pore solvents. The crystals had a region of stability up to approximately 400 °C, before decomposition starting at 438 °C. The reported decomposition temperature for PCN-222 materials is generally between 370–420 °C for as-synthesised samples. The DTA trace showed one weak endothermic peak, corresponding to the removal of acetone. There are exothermic peaks, indicating decomposition occurred in two steps.

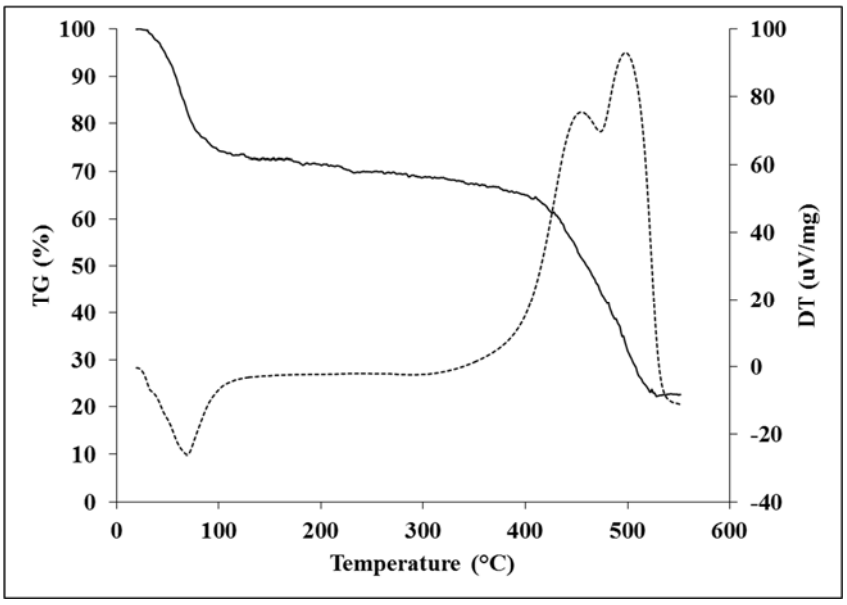

Figure A2.8 TGA-DTA traces for acid treated PCN-222(Mn/Ni) MOF. The solid lines represent the TGA and the dotted lines represent the DTA.

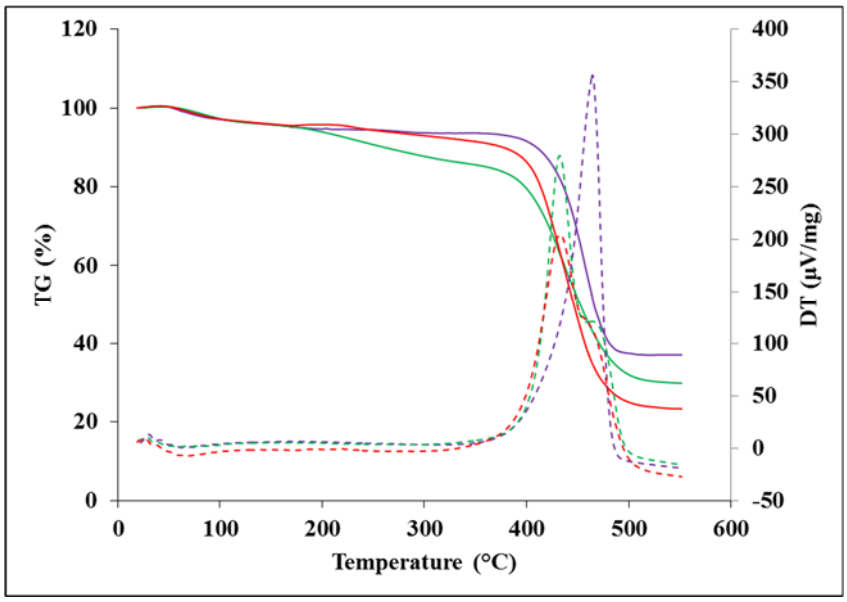

Figure A2.9 TGA-DTA traces for activated PCN-222(Ni) (green), PCN-222(MnCl) (purple) and PCN-222(Mn/Ni) (red). The solid lines represent the TGA and the dotted lines represent the DTA.

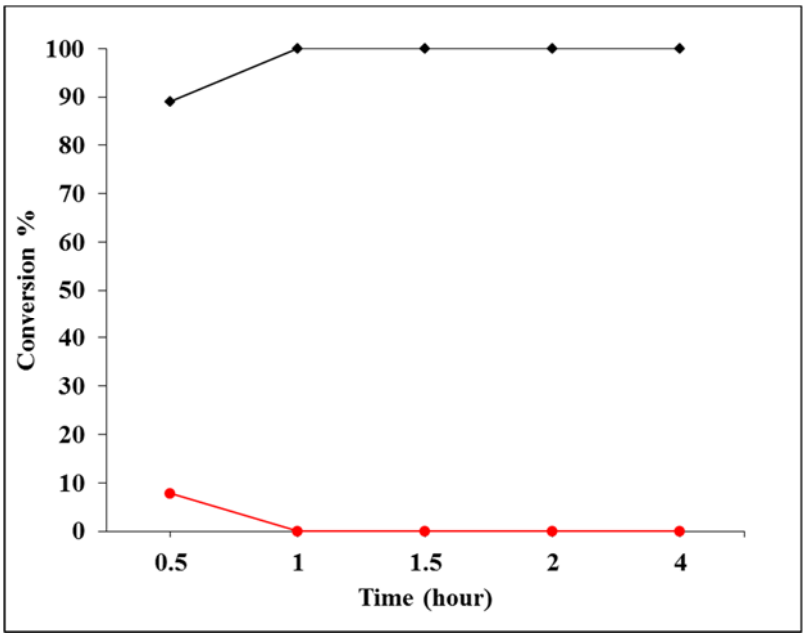

Figure A2.10 1 Kinetic traces of styrene epoxidation catalysed by PCN-222(Mn) at 5 mol% catalyst loading; styrene (red) and styrene epoxide (black).

Appendix 3

Table A3.1 Crystal and refinement data for IRMOF-NH_2, IRMOF-NHallyl, IRMOF-$N(allyl)_2$ and IRMOF-NMe_2.

	IRMOF-NH_2	**IRMOF-NHallyl**	**IRMOF-$N(allyl)_2$**	**IRMOF-NMe_2**
Empirical formula	$C_{42}H_{27}N_3O_{13}Zn_4$	$C_{51}H_{39}N_3O_{13}Zn_4$	$C_{60}H_{51}N_3O_{13}Zn_4$	$C_{48}H_{41}N_3O_{14}Zn_4$
Formula weight	1043.14	1163.33	1283.6	1145.32
Temperature/K	293	293	292	293(2)
Crystal system	tetragonal	tetragonal	tetragonal	trigonal
Space group	P-42_1m	P-42_1m	P-42_1m	R-3
a/Å	17.2045(5)	17.237(2)	17.2000(12)	24.106(3)
b/Å	17.2045(5)	17.237(2)	17.2000(12)	24.106(3)
c/Å	17.1507(12)	17.1207(17)	17.2000(12)	30.383(3)
α/°	90	90	90	90
β/°	90	90	90	90
γ/°	90	90	90	120
Volume/Å3	5076.5(5)	5086.5(14)	5088.4(8)	15290(3)
Z	2	2	2	6
ρcalcg/cm3	0.682	0.76	0.838	0.746
μ/mm-1	1.317	1.346	1.378	1.345
F(000)	1048	1180	1312	3492
Crystal size/mm3	0.2 × 0.2 × 0.15	0.1 × 0.1 × 0.08	N/A	0.12 × 0.12 × 0.05
Radiation	CuKα (λ = 1.54187)	CuKα (λ = 1.54178)	CuKα (λ = 1.54178)	CuKα (λ = 1.54178)
2Θ range for data collection/°	14.562 to 143.938	14.534 to 124.762	11.504 to 102.08	14.422 to 79.85
Index ranges	-15 ≤ h ≤ 20, -20 ≤ k ≤ 21, -20 ≤ l ≤ 20	-16 ≤ h ≤ 19, -19 ≤ k ≤ 12, -17 ≤ l ≤ 19	-9 ≤ h ≤ 8, -17 ≤ k ≤ 11, -16 ≤ l ≤ 17	-17 ≤ h ≤ 19, -20 ≤ k ≤ 20, -25 ≤ l ≤ 25
Reflections collected	25622	21880	8985	19183
Independent reflections	4898 [Rint = 0.0409, Rsigma = 0.0313]	4082 [Rint = 0.0370, Rsigma = 0.0389]	2768 [Rint = 0.0630, Rsigma = 0.0699]	2052 [Rint = 0.1110, Rsigma = 0.0693]
Data/restraints/parameters	4898/117/158	4082/140/147	2768/293/160	2052/99/196
Goodness-of-fit on F2	1.117	1.509	1.431	1.674
Final R indexes [I>=2σ (I)]	R1 = 0.0925, wR2 = 0.2772	R1 = 0.1207, wR2 = 0.3441	R1 = 0.1369, wR2 = 0.3424	R1 = 0.1330, wR2 = 0.3801
Final R indexes [all data]	R1 = 0.1074, wR2 = 0.2944	R1 = 0.1506, wR2 = 0.3930	R1 = 0.1735, wR2 = 0.3859	R1 = 0.1558, wR2 = 0.4000
Largest diff. peak/hole / e Å-3	0.61/-0.51	0.81/-1.04	0.70/-0.62	2.19/-0.63
Flack parameter	N/A	0.3(2)	0.42(2)	N/A

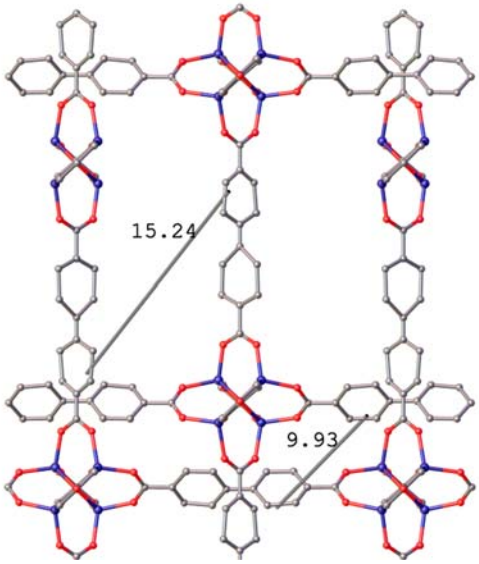

Figure A3.1 A representative view of pore size measurement for amine-functionalised IRMOFs.

A3.1 Thermogravimetric analysis

The thermal stability of 'as-synthesised' and 'activated' forms of the IRMOFs were investigated by TG-DTA under an atmosphere of N_2 gas. The results are shown in Figure A3.1 and are summarised in Table A3.2.

The TGA showed weight losses between ambient temperatures and 250 °C corresponding to the loss of all surface and pore solvents. The crystals had regions of stability up to approximately 400 °C, before decomposition sets in.

The number of DMF molecules per unit cell was calculated from the TGA data, indicated ~8, ~7 and ~7 DMF molecules per unit cell for IRMOF-NH_2, IRMOF-NHallyl and IRMOF-$N(allyl)_2$ and ~9 for IRMOF-NMe_2. From the TGA curves, it was determined that there was a correlation between the size of the pendant groups and the number of guests within the pores in IRMOF-NH_2, IRMOF-NHallyl and IRMOF-$N(allyl)_2$, which all show the same type of interpenetration. Conversion from bpdc-NH_2 into bpdc-NH(allyl) to bpdc-$N(allyl)_2$ results in a reduction in the number of DMF molecules from approximately 8 in IRMOF-NH_2 to 7 and 7 in IRMOF-NHallyl and IRMOF-$N(allyl)_2$, respectively.

The DTA traces of as-synthesised amine functionalised IRMOFs showed two weak endothermic peaks, corresponding to the loss of all solvent on the surface and pore structure. Two weak and strong exothermic peaks were observed in the DTA traces of IRMOF-NHallyl and IRMOF-$N(allyl)_2$ in the decomposition region and it is suggested that the first of the exotherms corresponds to loss of the allyl groups and the second to major decomposition of the framework. In comparison, IRMOF-NMe_2 does not display the first DTA feature and shows a very sudden mass loss and very sharp exothermic indicative of extremely rapid decomposition of the framework.

The TGA traces of the activated MOFs show very little mass losses. The DTA traces, however, show weak endothermic peaks for the samples, and this is ascribed to moisture adsorption during handling the materials in air for a short time before analysis The mass loss for IRMOF-NH_2 is the most significant, at approximately 9% between room temperature to 200 °C.

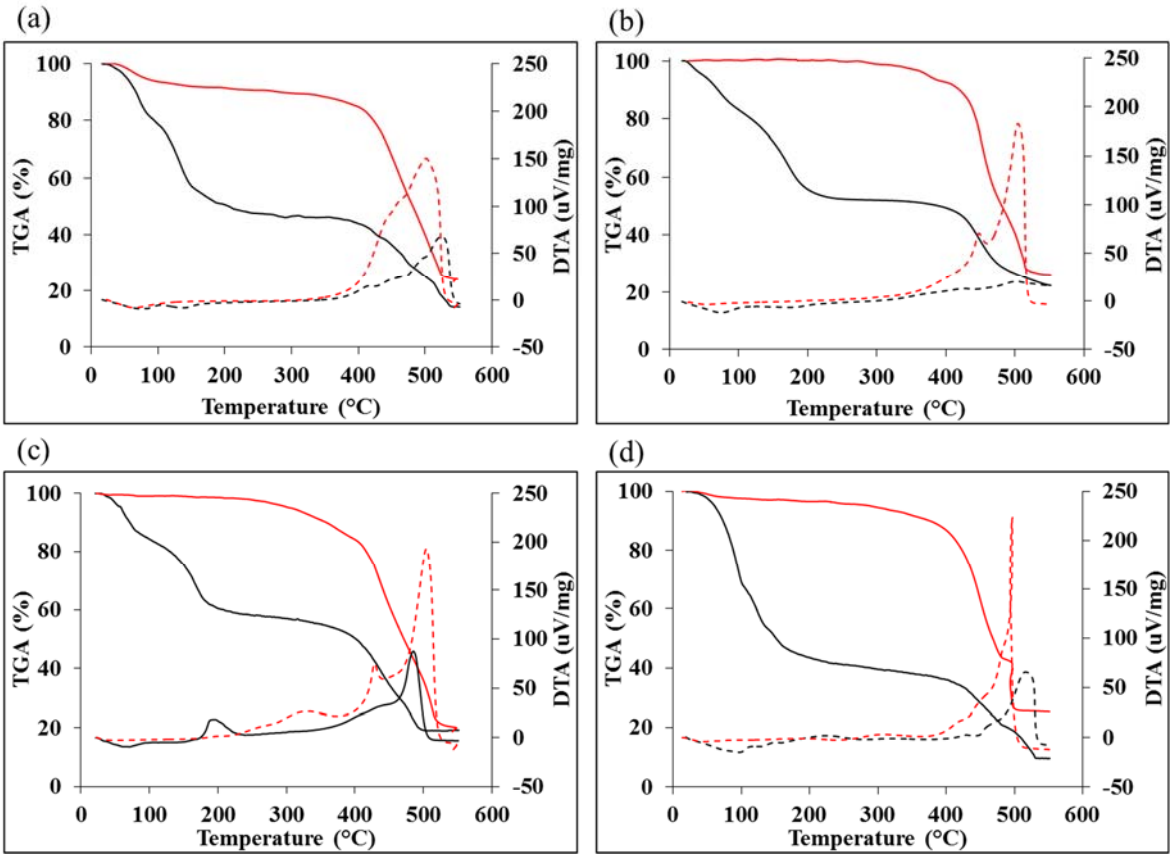

Figure A3.2 TG-DTA traces for as-synthesised (red) and activated (black); (a) IRMOF-NH_2, (b) IRMOF-NHallyl, (c) IRMOF-$N(allyl)_2$ and (d) IRMOF-NMe_2. The solid lines represent the TGA; the dotted lines represent the DTA.

Table A3.2 Thermogravimetric data of amine functionalised IRMOFs.

Structure	Solvent loss temperature	Mass loss	Decomposition temperature	Number of DMF
IRMOF-NH_2	250°C	53 %	432°C	~8
IRMOF-NHallyl	250 °C	48 %	425 °C	~7
IRMOF-$N(allyl)_2$	250 °C	42 %	420 °C	~7
IRMOF-NMe_2	250 °C	59 %	440 °C	~9

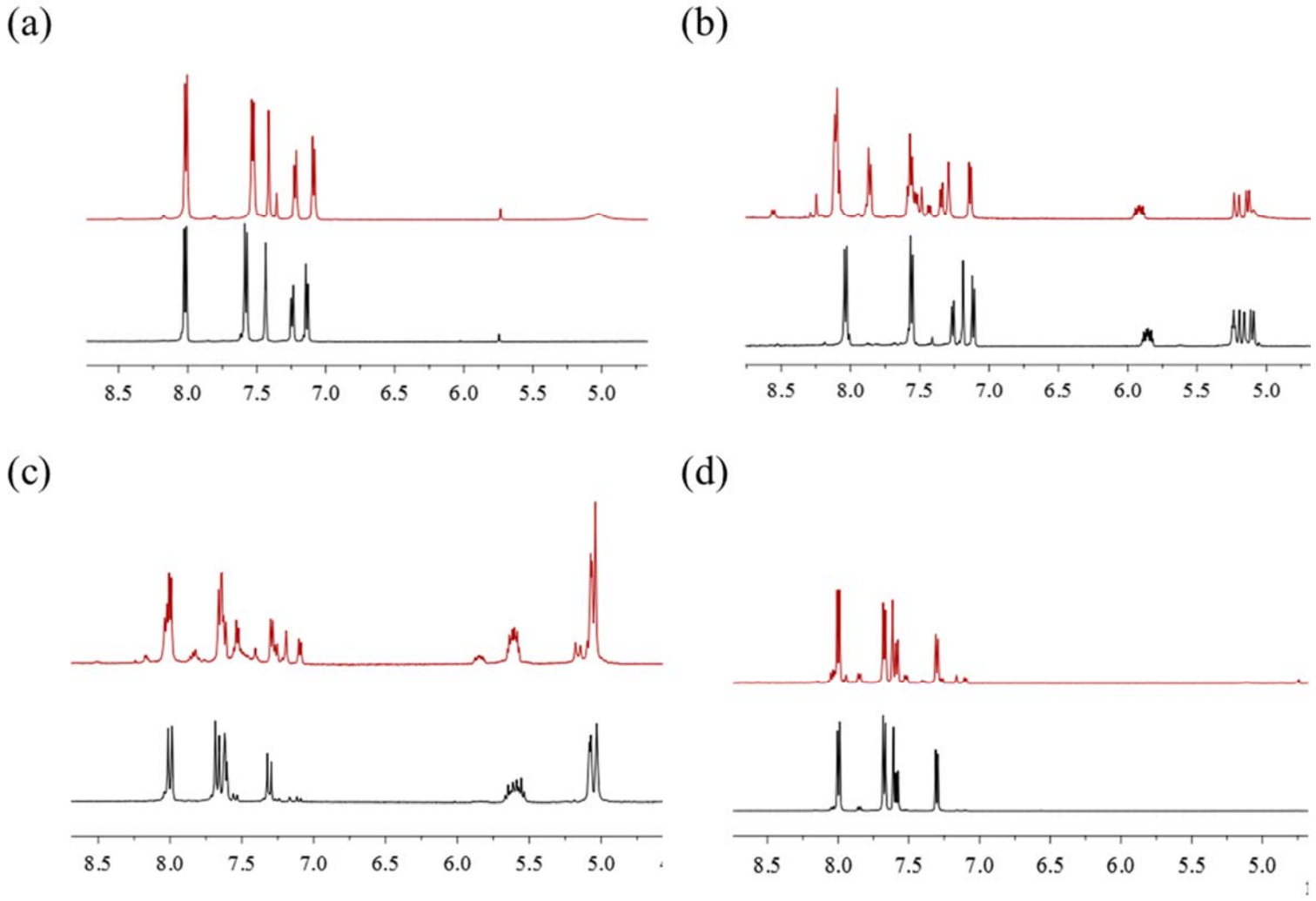

Figure A3.3 ^{1}H NMR spectra of (a) H_2bpdc-NH_2 (black) and digested IRMOF-NH_2 (red), (b) H_2bpdc-NHallyl (black) and digested IRMOF-NHallyl (red), (c) H_2bpdc-N(allyl)$_2$ (black) and digested IRMOF-N(allyl)$_2$ (red) and (d) H_2bpdc-NMe_2 (black) and digested IRMOF-NMe_2 (red).

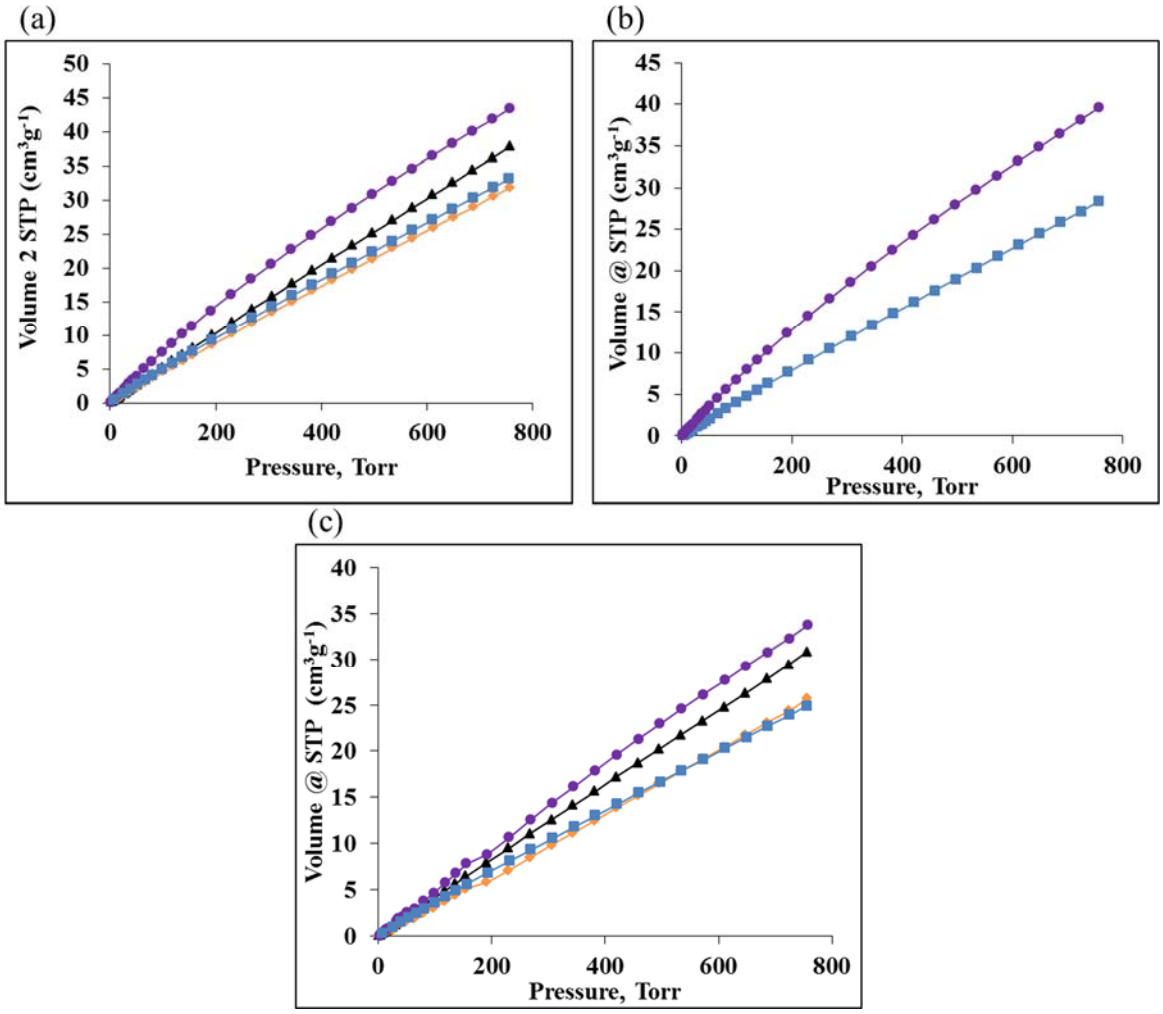

Figure A3.4 The CO_2 adsorption isotherms of CO_2 at (a) 273K, (b) 288 K and (c) 293 K for IRMOF-NH_2 (blue), IRMOF-NHallyl (black), IRMOF-$N(allyl)_2$ (brown) and IRMOF-NMe_2 (purple).

Appendix 4

Table A4.1 Crystal data and structures refinement for Sr-based coordination networks.

Identification code	$[Sr_2(bpdc\text{-}NO_2)_2(H_2O)_2]$	$[Sr_4(bpdc\text{-}(NO_2)_2)_4 \cdot 2DMF \cdot 4H_2O]$	$[Sr(bc)(H_2O)_2]$	$[Sr_3(bpdc\text{-}NH_2)_3(DMF)_2]$	$[Sr_4(bpdc\text{-}(NH_2)_2)_4(H_2O)_3]$	$[Sr(bpdc\text{-}NMe_2)(H_2O)]$
Empirical formula	$C_{14}H_{3.12}NO_6Sr$	$C_{68}H_{60}N_{12}O_{40}Sr_4$	$C_{14}H_8N_2O_6Sr$	$C_{24}H_{20}N_{2.5}O_7Sr_{1.5}$	$C_{56}H_{48}N_8O_{20}Sr_4$	$C_{16}H_{15}NO_5Sr$
Formula weight	368.92	2035.76	387.85	586.85	1503.52	371.87
Temperature/K	292(2)	293	103	113	292	113
Crystal system	orthorhombic	monoclinic	monoclinic	triclinic	triclinic	trigonal
Space group	Ima2	Cc	Cc	P-1	P-1	$P3_1$
a/Å	50.313(4)	51.8936(9)	7.8832(2)	5.7675(6)	12.4866(9)	14.7315(5)
b/Å	16.2739(4)	16.2576(3)	30.660(2)	14.6542(15)	16.2226(13)	14.7315(5)
c/Å	14.0296(6)	13.9135(10)	6.5366(2)	14.7983(17)	25.476(2)	9.7028(7)
α/°	90	90	90	68.577(6)	94.241(7)	90
β/°	90	104.182(7)	124.404(4)	79.862(7)	100.512(7)	90
γ/°	90	90	90	78.729(6)	90.380(6)	120
Volume/Å^3	11487.2(10)	11380.6(9)	1303.53(12)	1134.3(2)	5058.9(7)	1823.57(18)
Z	16	4	4	2	2	3
ρ_{calc}g/cm^3	0.853	1.188	1.9761	1.718	0.986	1.062
μ/mm^{-1}	2.752	3.036	6.116	5.198	3.105	3.231
F(000)	2882	4096	769	589	1502	588

Crystal size/mm^3	0.560 × 0.120 × 0.060	0.26 × 0.25 × 0.05	0.3 × 0.01 × 0.01	0.1 × 0.1 × 0.01	0.25 × 0.15 × 0.02	0.4 × 0.02 × 0.01
Radiation	CuKα (λ = 1.54178)	CuKα (λ = 1.54178)	Cu Kα (λ = 1.54178)	CuKα (λ = 1.54178)	CuKα (λ = 1.54178)	CuKα (λ = 1.54178)
2Θ range for data collection/°	13.102 to 144.22	13.126 to 130.16	13.92 to 144	12.336 to 74.728	11.24 to 66.82	6.928 to 144.218
Index ranges	-55 ≤ h ≤ 62, -19 ≤ k ≤ 18, -15 ≤ l ≤ 17	-60 ≤ h ≤ 60, -19 ≤ k ≤ 15, -16 ≤ l ≤ 15	-8 ≤ h ≤ 9, -37 ≤ k ≤ 37, -7 ≤ l ≤ 8	-4 ≤ h ≤ 4, -11 ≤ k ≤ 11, -11 ≤ l ≤ 11	-8 ≤ h ≤ 8, -11 ≤ k ≤ 11, -18 ≤ l ≤ 18	-16 ≤ h ≤ 16, -17 ≤ k ≤ 18, -9 ≤ l ≤ 11
Reflections collected	41232	56507	8269	5243	21377	10945
Independent reflections	10439 [R_{int} = 0.0628, R_{sigma} = 0.0625]	18140 [R_{int} = 0.0526, R_{sigma} = 0.0842]	2033 [R_{int} = 0.0736, R_{sigma} = 0.0930]	1164 [R_{int} = 0.1636, R_{sigma} = 0.1626]	3827 [R_{int} = 0.1968, R_{sigma} = 0.2312]	3944 [R_{int} = 0.0843, R_{sigma} = 0.1042]
Data/restraints/parameters	10439/7/477	18140/598/956	2033/0/93	1164/62/173	3827/137/271	3944/32/176
Goodness-of-fit on F^2	1.073	1.266	1.201	1.465	2.62	1.087
Final R indexes [I>=2σ (I)]	R_1 = 0.0762, wR_2 = 0.2306	R_1 = 0.1127, wR_2 = 0.2890	R_1 = 0.0674, wR_2 = 0.1384	R_1 = 0.1165, wR_2 = 0.2781	R_1 = 0.2223, wR_2 = 0.5102	R_1 = 0.0814, wR_2 = 0.2177
Final R indexes [all data]	R_1 = 0.0870, wR_2 = 0.2485	R_1 = 0.1473, wR_2 = 0.3488	R_1 = 0.0983, wR_2 = 0.1772	R_1 = 0.1473, wR_2 = 0.2938	R_1 = 0.2745, wR_2 = 0.5263	R_1 = 0.0921, wR_2 = 0.2300
Largest diff. peak/hole / e Å^{-3}	0.98/-0.72	1.79/-1.74	3.25/-3.39	1.39/-0.75	1.36/-0.85	0.72/-1.42

A4.1 Powder X-ray diffraction

A common sample preparation method involved taking as-synthesised crystals from DMF, crushing the damp crystals and loading on a quartz glass plate for analysis. This method worked for the majority of samples; however, in some cases, crystals with needle or plate morphologies exhibited strong preferred orientation.

A.1.1.1 PXRD studies of $[Sr_2(bpdc\text{-}NO_2)_2(H_2O)_2]$ and $[Sr_4(bpdc\text{-}(NO_2)_2)_4{\cdot}2DMF{\cdot}4H_2O]$ and $[Sr(bc)(H_2O)_2]$

The PXRD pattern of as-synthesised $[Sr_2(bpdc\text{-}NO_2)_2(H_2O)_2]$ (Figure A4.1a, red) is a good match with the calculated pattern (Figure A4.1a, black), excepting the missing low angle reflection at 3.5° (hkl=200), due to preferred orientation of the needle crystals. There are unindexed reflections with 2θ values of 6.18°, 6.98° and 8.64°. PXRD recorded after solvent exchange to wet acetone (Figure A4.1a, green) as part of the activation procedure and post-gas sorption measurements (Figure A4.1a, purple) indicated very low crystallinity of the samples and considerable change in the structure.

The experimental PXRD pattern of as-synthesised $[Sr_4(bpdc\text{-}(NO_2)_2)_4{\cdot}2DMF{\cdot}4H_2O]$ (Figure A4.1b, red) is not well matched to the calculated pattern (Figure A4.1b, black). Major 2θ peaks at 3.66°, 7.14° and 10.66° fit but with significant differences in peak intensities. Preferential orientation effects on the as-synthesised crystals results in missing peaks or significant differences in peak intensities. Low crystallinity was observed after solvent exchange to wet acetone (Figure A4.1b, green) and gas sorption measurements (Figure A4.1b, purple), as was observed for $[Sr_2(bpdc\text{-}NO_2)_2(H_2O)_2]$.

The calculated and experimental PXRD $[Sr(bc)(H_2O)_2]$ is shown in Figure A4.1c. Similar to $[Sr_4(bpdc\text{-}(NO_2)_2)_4{\cdot}2DMF{\cdot}4H_2O]$, the preferential orientation has a huge effect on the PXRD pattern of the as-synthesised $[Sr(bc)(H_2O)_2]$ versus calculated. By comparison, there exist only two major peaks at 5.72° and 11.48° in the experimental trace, compared to the calculated which has many more low intensity peaks at higher 2θ.

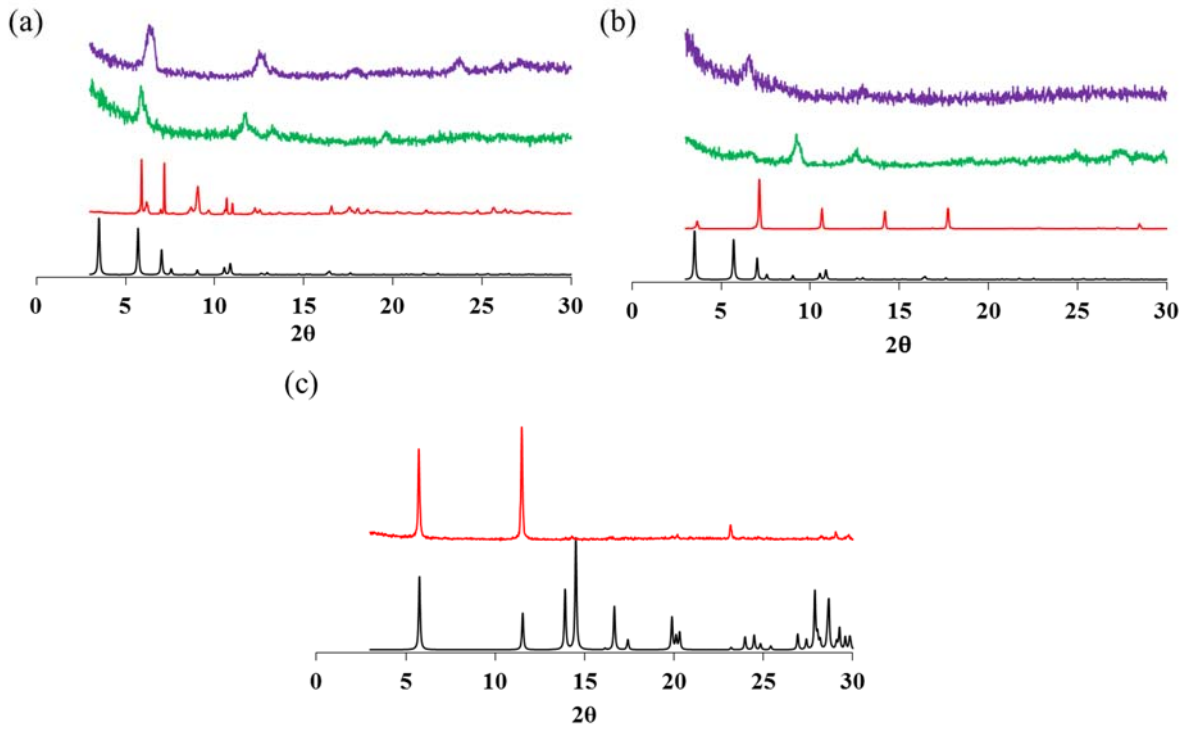

Figure A4.1 PXRD patterns for (a) $[Sr_2(bpdc\text{-}NO_2)_2(H_2O)_2]$ and (b) $[Sr_4(bpdc\text{-}(NO_2)_2)_4 \cdot 2DMF \cdot 4H_2O]$; calculated (black); 'as-synthesised' (red); solvent exchange to wet acetone containing water (green) and after gas sorption (purple) and (c) $[Sr(bc)(H_2O)_2]$; calculated (black) and 'as-synthesised' (red).

A.1.1.2 PXRD studies of $[Sr_3(bpdc\text{-}NH_2)_3(DMF)_2]$, $[Sr_4(bpdc\text{-}(NH_2)_2)_4(H_2O)_3]$ and $[Sr(bpdc\text{-}NMe_2)(H_2O)]$

The PXRD pattern of $[Sr_3(bpdc\text{-}NH_2)_3(DMF)_2]$, displayed in Figure A4.2a, shows a complete match to the calculated SCXRD pattern, implying excellent phase purity and crystallinity.

The calculated and experimental powder patterns of $[Sr_4(bpdc\text{-}NH_2)_2)_4(H_2O)_3]$ are shown in Figure A4.2b, black and red. $[Sr_4(bpdc\text{-}NH_2)_2)_4(H_2O)_3]$ showed an intense peak at 2θ value of 7.08° and two broad short peaks at 6.46° and 14.22°. The majority of the peaks are missing from the as-synthesised trace compared to the calculated. The PXRD recorded after gas sorption showed broad peaks indicating the low crystallinity of the $[Sr_4(bpdc\text{-}NH_2)_2)_4(H_2O)_3]$ after gas sorption measurements (Figure A4.2b, purple).

PXRD patterns for $[Sr(bpdc\text{-}NMe_2)(H_2O)]$ were recorded on as-synthesised, solvent exchanged, vacuum dried, and recorded material after gas sorption analysis. The PXRD data of the as-synthesised (Figure A4.2c, red), sample is near-identical to the

calculated pattern (Figure A4.2c, black) with all peak positions matching well, indicating excellent phase purity. Excellent matches were also obtained after solvent exchange (dry CH_2Cl_2) (Figure A4.2c, magenta) and vacuum drying (Figure A4.2c, blue), confirming crystallinity is retained after activation of the MOF. As shown in Figure A4.2c, purple. The PXRD pattern of [Sr(bpdc-NMe_2)(H_2O)] recorded after gas sorption measurements showed some peak splitting, which might imply there was some degradation during gas sorption studies.

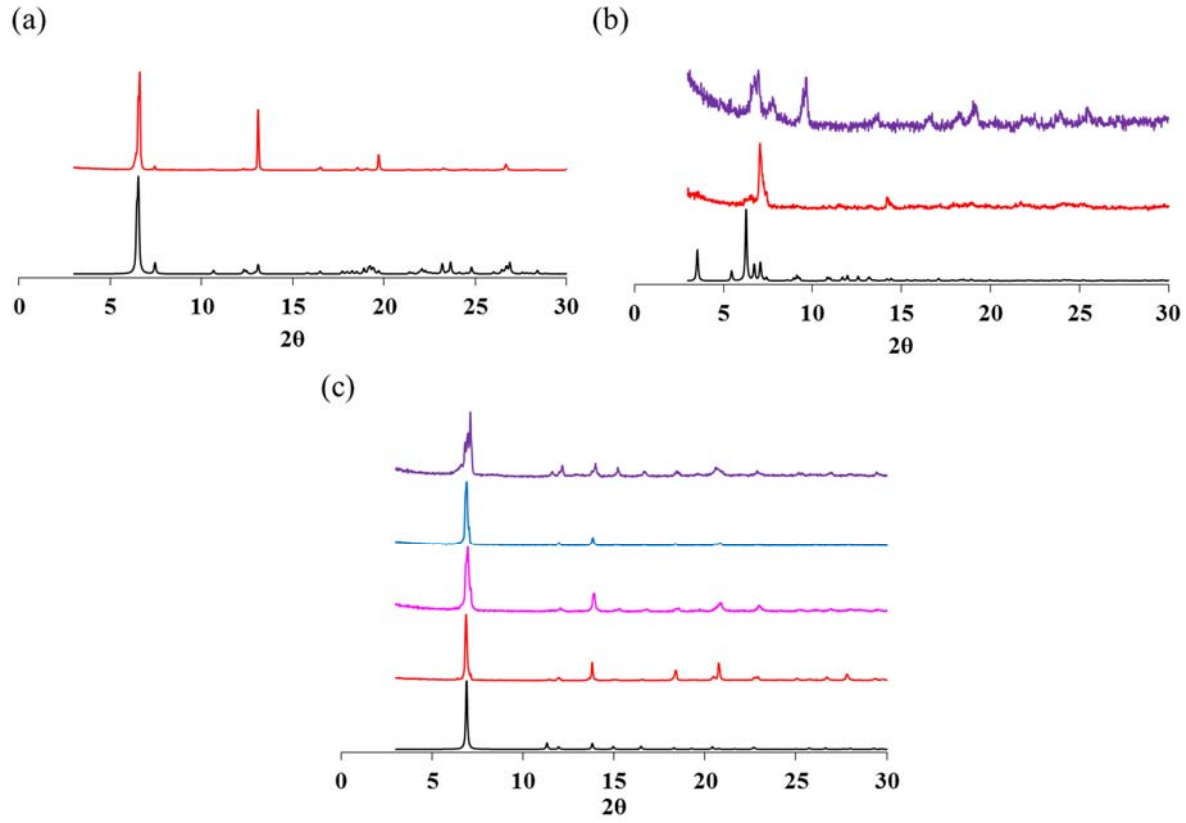

Figure A4.2 PXRD patterns for (a) [Sr_3(bpdc-NH_2)$_3$(DMF)$_2$]; calculated (black) and 'as-synthesised' (red); (b) [Sr_4(bpdc-(NH_2)$_2$)$_4$(H_2O)$_3$]; calculated (black); 'as-synthesised' (red) and after gas sorption (purple) and (c) [Sr(bpdc-NMe_2)(H_2O)] calculated (black); 'as-synthesised' (red); after solvent exchange to dry CH_2Cl_2 (magenta), after vacuuming (blue) and after gas sorption (purple).

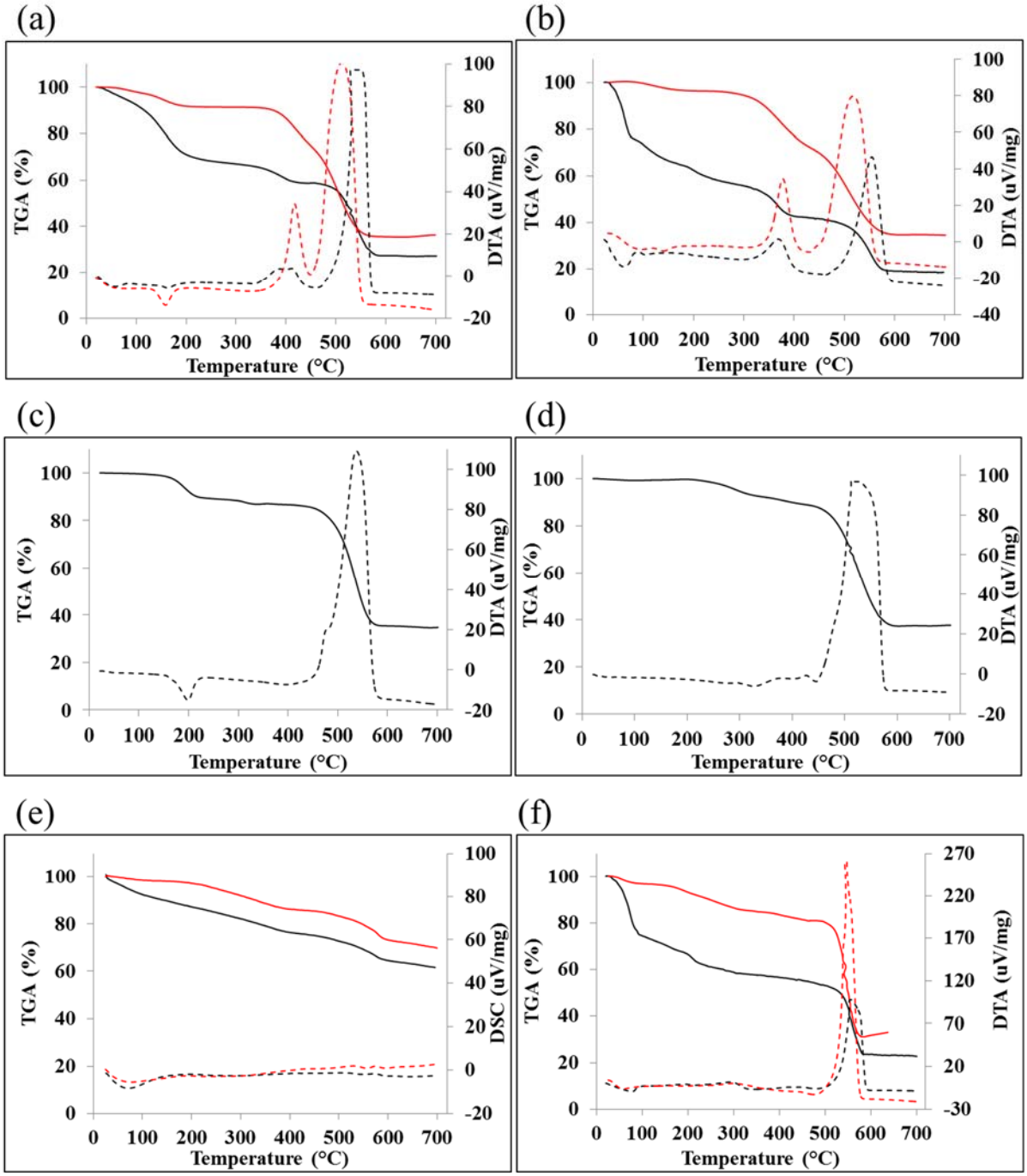

Figure A4.3 TG-DTA traces for as-synthesised (black) and activated (red); (a) $[Sr_2(bpdc\text{-}NO_2)_2(H_2O)_2]$, (b) $[Sr_4(bpdc\text{-}(NO_2)_2)_4{\cdot}2DMF{\cdot}4H_2O]$, (c) $[Sr(bc)(H_2O)]$, (d) $[Sr_3(bpdc\text{-}NH_2)_3(DMF)_2]$, (e) $[Sr_4(bpdc\text{-}(NH_2)_2)_4(H_2O)_3]$ and (f) $[Sr(bpdc\text{-}NMe_2)(H_2O)]$.The solid lines represent the TGA the dotted lines the DTA in (a), (b), (c), (d) and (f). The solid lines represent the TGA the dotted lines the DSC in (e).

Table A4.1 Solvent exchange and activation procedures on $[Sr_2(bpdc\text{-}NO_2)_2(H_2O)_2]$, $[Sr_4(bpdc\text{-}(NO_2)_2)_4 \cdot 2DMF \cdot 4H_2O]$, $[Sr_4(bpdc\text{-}NH_2)_2)_4(H_2O)_3]$ and $[Sr(bpdc\text{-}NMe_2)(H_2O)]$ and CO_2 adsorption amounts at 273 K.

Entry	Method	Solvent exchange	Activation procedure	Heating protocol under dynamic vacuum	CO_2 adsorbed at 273 K (cm^3g^{-1})			
					$[Sr_2(bpdc\text{-}NO_2)_2(H_2O)_2]$	$[Sr_4(bpdc\text{-}(NO_2)_2)_4 \cdot 2DMF \cdot 4H_2O]$	$[Sr_4(bpdc\text{-}NH_2)_2)_4(H_2O)_3]$	$[Sr(bpdc\text{-}NMe_2)(H_2O)]$
1	6.1	DMF → wet acetone	$ScCO_2$	40 °C, 16 hours	1.5	1.7		
2	6.2	DMF → wet acetone → Benzene	Freeze drying (1h)	40 °C, 16 hours	2.2	7.0		
3	6.3	DMF → wet acetone → benzene	Freeze drying (1h)	100 °C, 10 hours	4.2	6.0		
4	6.4	DMF → wet acetone → cyclohexane	Freeze drying (o/n)	40 °C, 16 hours	2.6	21.5		9.4
5	6.5	DMF → CH_2Cl_2 → cyclohexane	Freeze drying (1h)	40 °C, 16 hours			11.6	
6	6.6	DMF → CH_2Cl_2 → benzene	Freeze drying (1h)	40 °C, 6 hours				23.3
7	6.7	DMF → CH_2Cl_2	Vacuum drying	40 °C, 12 hours				26.2
8	6.8	DMF → wet acetone → cyclohexane	Freeze drying (o/n)	100 °C, 5 hours				10.4

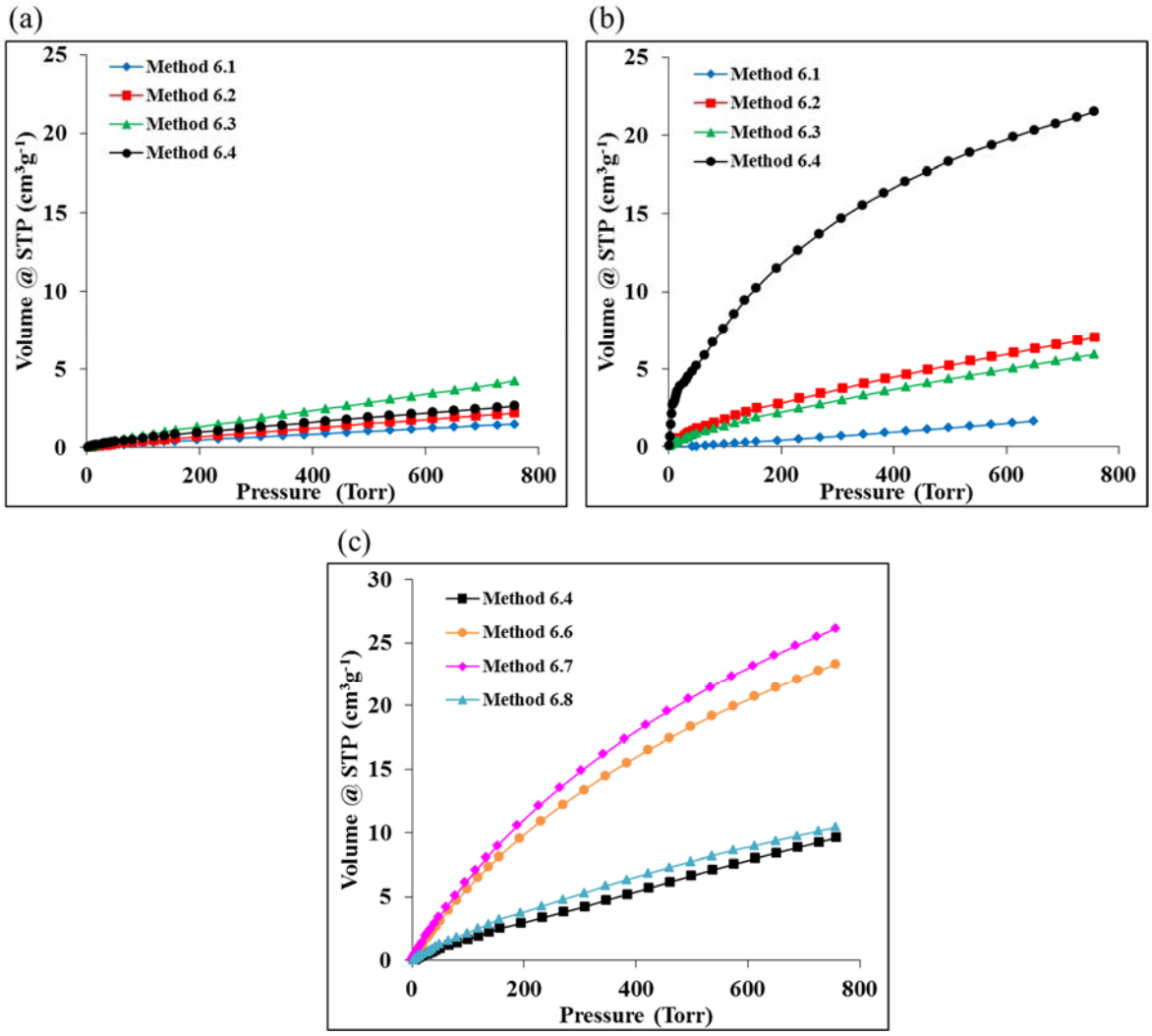

Figure A4.4 CO_2 adsorption isotherms recorded at 273 K for (a) [Sr_2(bpdc-NO_2)$_2$(H_2O)$_2$], (b) [Sr_4(bpdc-(NO_2)$_2$)$_4$·2DMF·4H_2O] and (c) [Sr(bpdc-NMe_2)(H_2O)] to assess the highest gas sorption uptake for each coordination networks.

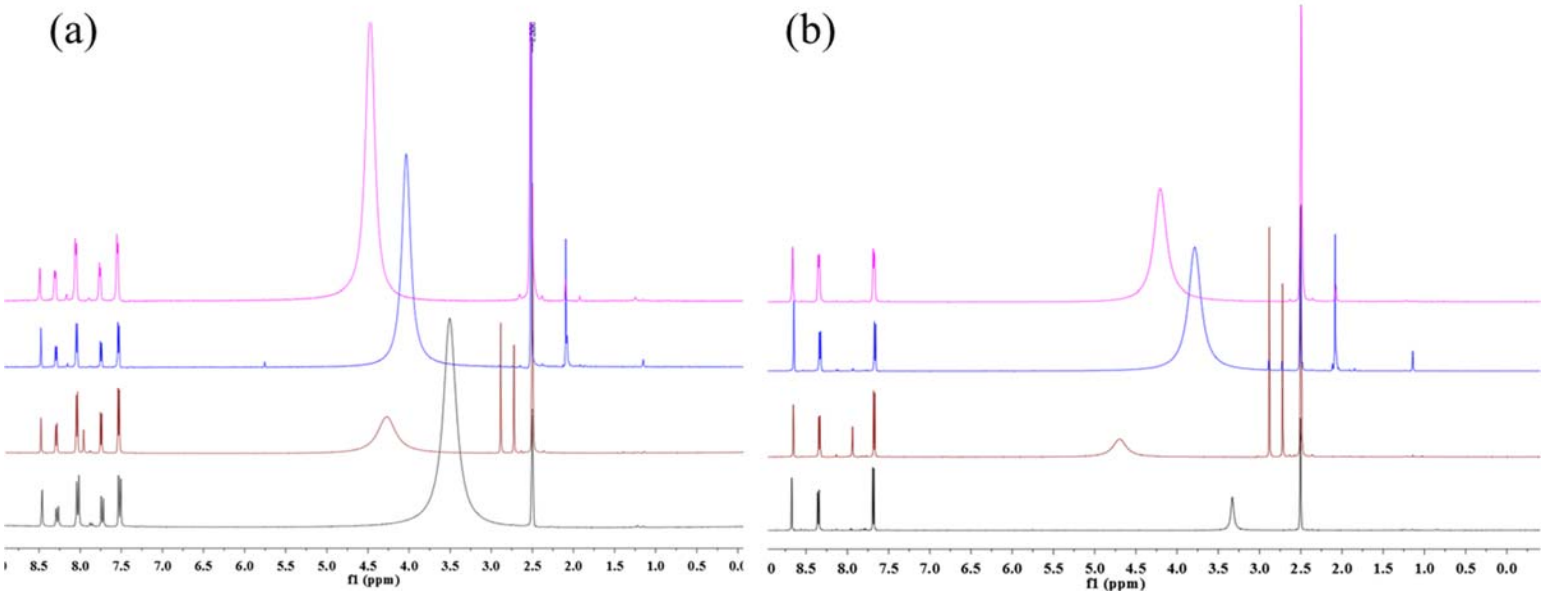

Figure A4.5 ^{1}H NMR spectra of (a) H_2bpdc-NO_2 (black), digested of [Sr_2(bpdc-NO_2)$_2$(H_2O)$_2$] after solvent exchange to dry CH_2Cl_2 (red), digested of [Sr_2(bpdc-NO_2)$_2$(H_2O)$_2$] after solvent exchange to dry acetone (blue) and digested of [Sr_2(bpdc-NO_2)$_2$(H_2O)$_2$] after solvent exchange to acetone containing 5% water (magenta), (b) H_2bpdc-(NO_2)$_2$ (black) and digested of [Sr_4(bpdc-(NO_2)$_2$)$_4$·2DMF·4H_2O] after solvent exchange to dry CH_2Cl_2 (red), digested of (b) [Sr_4(bpdc-(NO_2)$_2$)$_4$·2DMF·4H_2O] after solvent exchange to dry acetone (blue) and digested of [Sr_4(bpdc-(NO_2)$_2$)$_4$·2DMF·4H_2O] after solvent exchange to acetone containing 5% water (magenta).

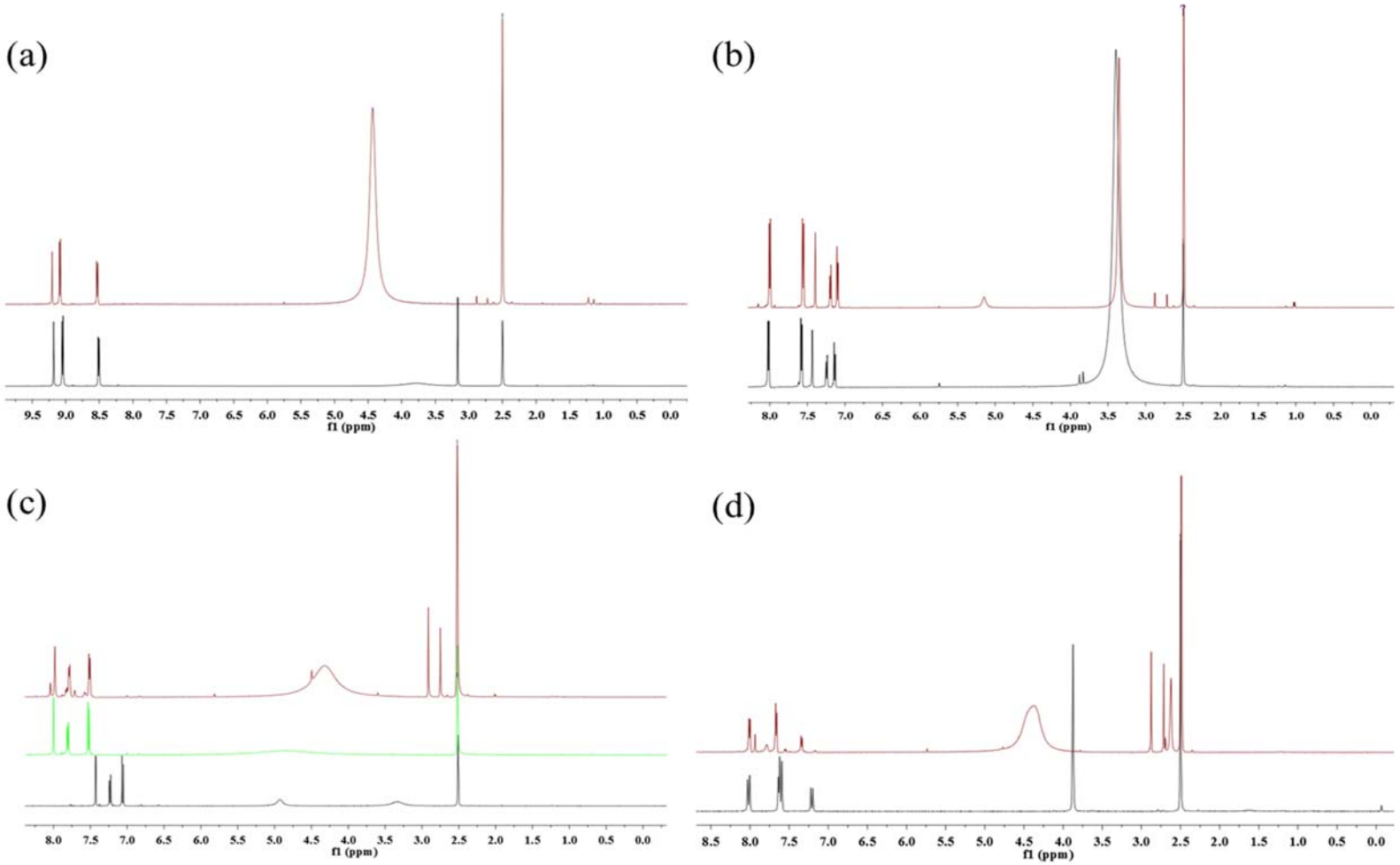

Figure A4.6 ^{1}H NMR spectra of (a) H_2bc (black) and digested of $[Sr(bc)(H_2O)]$ (red), (b) $H_2bpdc\text{-}NH_2$ (black) and digested of $[Sr_3(bpdc\text{-}NH_2)_3(DMF)_2]$ (red), $H_2bpdc\text{-}NH_2$ (black), $H_2bpdc\text{-}NH_2$ in presence of DCl/D_2O (green) and digested of $[Sr_4(bpdc\text{-}(NH_2)_2)_4(H_2O)_3]$ (red), (d) $H_2bpdc\text{-}NMe_2$ (black) and digested of $[Sr(bpdc\text{-}NMe_2)(H_2O)]$ (red)